Fakultät für Mathematik, Informatik und Naturwissenschaften | RWTH AACHEN UNIVERSITY

# Phonons in Magnetic Systems by means of Density-Functional Perturbation Theory

Von der Fakultät für Mathematik, Informatik und Naturwissenschaften der RWTH Aachen University zur Erlangung des akademischen Grades eines Doktors der Naturwissenschaften genehmigte Dissertation

vorgelegt von

Alexander Neukirchen, M.Sc.

aus

Langenfeld (Rheinland), Deutschland

Berichter*:* *Prof. Dr. rer. nat. Stefan Blügel*
*Prof. Dr. rer. nat. Carsten Honerkamp*

Tag der mündlichen Prüfung*:* *13.06.2025*

Diese Dissertation ist auf den Internetseiten der Universitätsbibliothek verfügbar.

# Abstract

Phonons are quantized vibrational excitations of the crystal lattice. These quasiparticles play a crucial role in understanding many properties of the solid-state system. In this thesis, phonons in terms of dispersion relations and density of states (DOS) are investigated on the basis of the Kohn–Sham density functional theory (DFT), the state-of-the-art ab-initio approach to the electronic structure of specific materials and a proven foundation for the study of lattice vibrations from first-principles. This work relies on the harmonic approximation, in which the properties of phonons are directly related to the second order response of the total energy of the system with respect to the displacement of the atoms in the lattice. Two complementary approaches are used to calculate this response: The first one is the finite displacement (FD) approach, that in which the second order of the energy is approximated as a difference quotient using differences in the forces acting on the atoms. The second one is the density-functional perturbation theory (DFPT), a variational approach that constructs the second order response analytically from the first order response of the wave functions obtained by the self-consistent solution of the Sternheimer equation. In this thesis, I go beyond the conventional application of DFPT to nonmagnetic systems and the conventional realization of DFPT in terms of methods representing the electron wave function in a plane wave (PW) basis and present an implementation in the all-electron full-potential linearized augmented plane-wave (FLAPW) method. This very accurate method, applicable without further ado to all nonmagnetic and magnetic chemical elements of the periodic table, comes with the challenge of an atomic position dependent basis set. I show that the subsequently arising additional matrix elements, so-called correction terms to calculate the response of wave function and energy can be determined accurately. One objective of this thesis is to advance the development of DFPT within the FLAPW method by refining and extending the existing realisation in the community code `FLEUR`. I present the general theory that leads to the existing implementation and, from this starting point, develop correction terms that improve upon previous results. I extend the framework from the minimum base version towards spin-polarized magnetic systems and systems with more than one atom per unit cell. From the viewpoint of software engineering, I demonstrate efficient integration of DFPT into the existing code, minimizing redundancy and maximizing parallelization options. I benchmark the improved implementation against FD results calculated with `FLEUR` in conjunction with the `phonopy` package and obtain an excellent agreement. The validation set spans both materials that were previously established but now show improved results, as well as materials that were previously inaccessible. I calculate both elemental and rare-earth magnets in different magnetic configurations to elucidate, how magnetism and the magnetic order impacts the phonon physics. Finally, I investigate two-dimensional (2D) layered systems and unsupported monolayers. The latter can be efficiently calculated with the thin-film implementation in `FLEUR`, for which I present an extension to the DFPT plugin.

# Kurzzusammenfassung

Phononen sind quantisierte Schwingungsanregungen des Kristallgitters. Diese Quasiteilchen spielen eine entscheidende Rolle für das Verständnis vieler Eigenschaften des Festkörpers. In dieser Arbeit werden Phononen im Hinblick auf Dispersionsbeziehungen und Zustandsdichten auf der Grundlage der Kohn–Sham-Dichtefunktionaltheorie (DFT) untersucht, dem modernsten ab-initio-Ansatz für die elektronische Struktur spezifischer Materialien und einer bewährten Grundlage für die Untersuchung von Gitterschwingungen nach ersten Prinzipien der Quantenmechanik. Diese Arbeit stützt sich auf die harmonische Näherung, bei der die Eigenschaften von Phononen direkt mit der Reaktion zweiter Ordnung der Gesamtenergie des Systems in Bezug auf die Verschiebung der Atome im Gitter zusammenhängen. Zur Berechnung dieser Reaktion werden zwei komplementäre Ansätze verwendet: Der erste ist der Ansatz der endlichen Verschiebung (FD), der die Energie zweiter Ordnung als Differenzenquotient der auf die Atome wirkenden Kräfte annähert. Der zweite Ansatz ist die Dichtefunktional-Störungstheorie (DFPT), ein Variationsansatz, der die Reaktion zweiter Ordnung analytisch aus der Reaktion erster Ordnung der Wellenfunktionen konstruiert, die durch die selbstkonsistente Lösung der Sternheimer-Gleichung erhalten wird. In dieser Arbeit gehe ich über die konventionelle Anwendung der DFPT auf nichtmagnetische Systeme und die Umsetzung in Form von Methoden, die die Elektronenwellenfunktion in einer ebenen Wellenbasis (PW) darstellen, hinaus und präsentiere eine Umsetzung in der sogenannten FLAPW-Methode mit linearisierter, erweiterter ebener Wellenbasis. Diese sehr genaue Methode, die ohne weiteres auf alle chemischen Elemente des Periodensystems anwendbar ist, bringt die Herausforderung eines atompositionsabhängigen Basissatzes mit sich. Ich zeige, dass die in der Folge entstehenden zusätzlichen Matrixelemente zur Berechnung der Reaktion von Wellenfunktion und Energie auf Änderungen der Atompositionen genau bestimmt werden können. Ein Ziel dieser Arbeit ist es, die Entwicklung von DFPT innerhalb der FLAPW-Methode voranzutreiben, indem die bestehende Umsetzung im Community-Code `FLEUR` verfeinert und erweitert wird. Ich stelle die allgemeine Theorie vor, die zu der bestehenden Implementierung führt, und entwickle von diesem Ausgangspunkt aus Korrekturterme, die die bisherigen Ergebnisse verbessern. Ich erweitere den Rahmen von der minimalen Basisversion auf spinpolarisierte magnetische Systeme und Systeme mit mehr als einem Atom pro Einheitszelle. Aus der Sicht der Softwareentwicklung demonstriere ich die effiziente Integration von DFPT in den bestehenden Code, wobei Redundanz minimiert und Parallelisierungsoptionen maximiert werden. Ich vergleiche die verbesserte Implementierung mit FD-Ergebnissen, die mit `FLEUR` in Verbindung mit dem `phonopy`-Paket berechnet wurden, und erhalte eine hervorragende Übereinstimmung. Der Validierungssatz umfasst sowohl Materialien, die bereits zuvor etabliert waren, aber nun verbesserte Ergebnisse zeigen, als auch Materialien, die zuvor unzugänglich waren. Ich berechne sowohl elementare als auch Seltene-Erden-Magnete in verschiedenen magnetischen Konfigurationen, um zu klären, die magnetische Ordnung die Phononenphysik beeinflusst. Schließlich untersuche ich zwei-dimensionale (2D)-Schichtensysteme und freitragende Monoschichten. Letztere können mit der Dünnschicht-Implementierung in `FLEUR` effizient berechnet werden, wofür ich eine Erweiterung des DFPT-Plugins vorstelle.

# Contents


List of Figures viii

List of Tables xiv

Abbreviations and Acronyms xvii

1 Introduction 1

2 Electronic Structure 5
- 2.1 The Many-Body System . . . 6
- 2.2 Kohn–Sham Density Functional Theory . . . 7
- 2.3 Exchange-Correlation Functionals . . . 9
- 2.4 State Occupation in Metals . . . 10
- 2.5 Self Consistency . . . 11
- 2.6 Spin-Density Functional Theory . . . 13
- 2.7 Extensions to and Generalizations of DFT . . . 15

3 Phonons from Electronic Structure Methods 17
- 3.1 The Periodic Lattice . . . 17
- 3.2 Phonons in the Harmonic Approximation . . . 18
- 3.3 Frozen Phonon Calculations . . . 21
- 3.4 The Finite-Displacement Method . . . 22
- 3.5 Density-Functional Perturbation Theory . . . 23

4 Density-Functional Perturbation Theory in the All-Electron Full-Potential Linearized Augmented Plane-Wave Method 29
- 4.1 The Linearized Augmented Plane-Wave Basis . . . 30
  - 4.1.1 Plane-Wave and Augmented Plane-Wave Methods . . . 30
  - 4.1.2 Full-Potential Linearized Augmented Plane-Wave Method . . . 33
  - 4.1.3 All-Electron Aspects of the FLAPW Method . . . 35
- 4.2 The Quantum Engine of FLAPW . . . 38
  - 4.2.1 Potential Generation . . . 39
  - 4.2.2 Matrix Setup and Diagonalization . . . 41
  - 4.2.3 Density Generation . . . 42

4.2.4 Total Energy and Mixing . . . 44
4.3 Adapting DFPT to FLAPW . . . 46
4.3.1 Correction Terms of the Position-Dependent Basis . . . 46
4.3.2 First Order Energy Derivatives . . . 48
4.3.3 Second Order Energy Derivatives . . . 50
4.3.4 The Sternheimer Equation in FLAPW . . . 51
4.3.5 The FLAPW-DFPT Self-Consistency Loop . . . 53

**5 Implementing DFPT in the FLEUR Code 57**
5.1 Extending the Potential Generation . . . 58
5.2 Extending the Matrix Setup . . . 62
5.3 Handling Degenerate Eigenvalues . . . 63
5.4 Extending the Density Generation . . . 68
5.5 Calculating the Second Order Energy Terms . . . 69
5.6 Scaling Behavior . . . 73

**6 Validating the Implementation 77**
6.1 Calculation Schemes and Computational Details . . . 77
6.2 Monatomic Materials . . . 80
6.3 Polyatomic Materials . . . 86
6.4 Using the q-point Interpolation . . . 92
6.5 Takeaways from the Validation . . . 96

**7 Convergence Studies in bcc Metals 97**
7.1 Supercell Convergence . . . 97
7.2 DFPT Convergence Parameters . . . 104
7.2.1 Distance Threshold Convergence . . . 105
7.2.2 Basis-Set Cutoff Convergence . . . 108
7.2.3 k-point Set Convergence . . . 109
7.3 The Case of bcc Mo . . . 110

**8 Phonons in Magnetic Materials 115**
8.1 Phonon Dispersions of Elemental Magnets . . . 115
8.1.1 Exchanging the Magnetic Textures . . . 119
8.2 Interplay of Magnetism and Phonons in Magnetic Lanthanides . . . 125
8.2.1 The Phonon Dispersion of hcp Gd . . . 125
8.2.2 The Phonon Dispersion of Collinear bcc Eu . . . 130

**9 Phonons in 2D Materials 135**
9.1 Pseudo 2D Systems . . . 136
9.2 2D Film DFPT in the FLAPW Method . . . 140
9.2.1 The FLAPW Method for Thin Films . . . 140
9.2.2 Changes to the DFPT Formalism . . . 147

**10 Conclusion 153**

**A Further Exploitation of Symmetry 157**

**B Installing and Using FLEUR with DFPT** **161**

**C Second Order Coordinate Transformation** **163**

**D Out-of-Plane Modes of the Film DFPT Implementation** **165**
D.1 Changes to the Formalism . . . . . 165
D.2 State-of-the-Art for the out-of-Plane Modes . . . . . 169

**Bibliography** **171**

# List of Figures


2.1 Sketch of the interdependent quantities after Hohenberg and Kohn. . . . . 7

2.2 Sketch of the principle workflow in a non-specific DFT calculation. The red frame highlights the self-consistent field loop. Considering the $m$-th iteration, from an input density $n_m^{\text{in}}$, the effective potential $V_{\text{eff}}$ is generated and used to set up the Hamiltonian $\mathcal{H}$. The Schrödinger equation constituted by it is solved to get a set of eigenenergies $\{\varepsilon_\nu\}$ and wave functions $\{\psi_\nu\}$. The eigenenergies are used to determine the occupation numbers $\{\tilde{f}_\nu\}$ and the Fermi energy $E_{\text{F}}$. The wave functions and occupation numbers are used to construct the output electron density $n_m^{\text{out}}$. The input and output density of an iteration are compared by a distance function to determine, whether the calculation is converged. The loop is repeated as long as this is not the case. . . . . 12

4.1 Sketch of the muffin tin sphere setup in APW methods . . . . . 31

4.2 Sketch of the DFT self-consistency workflow for a periodic basis set. On top of the general structure in 2.2, the (generalized) eigenvalue problem has to be solved for each Bloch vector $\boldsymbol{k}$ by setting up the matrix elements $H/S_{\boldsymbol{G}'\boldsymbol{G}}(\boldsymbol{k})$ for the basis set in question, *i.e.* the LAPW basis. It does not directly result in the wave functions, but in expansion coefficients $z_{\boldsymbol{k}\boldsymbol{G}\nu}$ as its eigenvectors. Aside from the resulting k-point summations for the Fermi energy and output density, the overall structure remains intact. . . . . 38

4.3 Sketch of the DFPT self-consistency workflow for the FLAPW method. The Sternheimer equation has to be solved for each Bloch vector $\boldsymbol{k}$ by setting up the matrix elements $H/S^{(1)\beta j+}_{\boldsymbol{G}'\boldsymbol{G}}(\boldsymbol{k}+\boldsymbol{q},\boldsymbol{k})$ for the basis set in question, *i.e.* the LAPW basis. The full procedure of arriving at a set of dynamical matrices involves solving the equation for each atom $\beta$, each displacement $j$, and each phonon wave vector $\boldsymbol{q}$ independently. . . . . 54

5.1 Principal workflow of the FLEUR Coulomb potential (response) generation for DFT (left hand side) and DFPT (right hand side). The dashed areas mark calls to explicitly named lower level subroutines, which needed to be adapted to the DFPT case. . . . . 60

5.2 Principal workflow of the FLEUR xc potential (response) generation for DFT (left hand side) and DFPT (right hand side). The dashed areas mark calls to explicitly named lower level subroutines, which needed to be adapted to the DFPT case. . . . . 61

6.1 Phonon dispersion for fcc Ne. The red dashed curve shows the FD reference (denoted as "sc" for supercell) and the blue squares show the DFPT data. Additionally, there are points on the $\Gamma - X$ path, that highlight separate calculations where corrections (5.24) and/or (5.28) are not applied with green crosses and a black plus, respectively. . . . . 82
6.2 Phonon dispersion for fcc Cu. The red dashed curve shows the FD reference and the blue squares show the DFPT data. . . . . 84
6.3 Phonon dispersion for fcc Ni. The red dashed curve shows the FD reference and the blue squares show the DFPT data. . . . . 85
6.4 Phonon dispersion for Si. The red dashed curve shows the FD reference and the blue squares show the DFPT data. The green cross at the second $\Gamma$-point highlights the modified result in the absence of eigenenergy response terms. The black diamonds, brown upward triangles, and yellow downward triangles belong to experimental data from references [186], [187], and [188] respectively. 88
6.5 Phonon dispersion for hcp Co. The red dashed curve shows the FD reference and the blue squares show the DFPT data. The green cross at the second $\Gamma$-point highlights the modified result in the absence of eigenenergy response terms and the black plus neglects occupation number responses. . . . . 89
6.6 Phonon dispersion for SiC. The red dashed curve shows the FD reference and the blue squares show the DFPT data. The green cross at the second $\Gamma$-point highlights the modified result in the absence of eigenenergy response terms. . 91
6.7 Phonon dispersion for fcc Cu. The red curve shows the interpolated $8 \times 8 \times 8$ reference and the blue squares show the DFPT data sampled from $16 \times 16 \times 16$. 93
6.8 Phonon density of states for fcc Cu with the histogram method. The red curve shows the FD reference and the blue curve shows the DFPT data. . . . . 94
6.9 Phonon density of states for fcc Cu with the tetrahedron method. The red curve shows the FD reference and the blue curve shows the DFPT data. . . . . 95

7.1 Phonon dispersion and DOS for bcc Fe. The red curves show the FD reference and the blue curves show the DFPT data. . . . . 98
7.2 FD Phonon dispersions for bcc Fe and different supercell configurations. The red solid curve shows the $2 \times 2 \times 2$ supercell result, while the blue dash-dotted curve represents $3 \times 3 \times 3$ and the fully dashed green one $4 \times 4 \times 4$. . . . . 99
7.3 FD Phonon dispersions for bcc Fe and different supercell configurations. The red solid curve shows the $4 \times 4 \times 4$ supercell result, while the blue dash-dotted curve represents $5 \times 5 \times 5$ and the fully dashed green one $6 \times 6 \times 6$. . . . . 100
7.4 FD Phonon dispersions for bcc Fe and different supercell configurations. The red solid curve shows the $6 \times 6 \times 6$ supercell result, while the blue dash-dotted curve represents $7 \times 7 \times 7$ and the fully dashed green one $8 \times 8 \times 8$. . . . . 101
7.5 Phonon dispersions for bcc Fe at different FD supercell configurations and for DFPT. The red solid curve shows the $2 \times 2 \times 2$ supercell result, the red dotted result has the $\pm\, 2 \times 2 \times 2$ supercell and the blue solid curve shows DFPT data. 103

7.6 Phonon dispersions for bcc Fe at different FD supercell configurations and for DFPT. The red solid curve shows the $\pm$ $4 \times 4 \times 4$ supercell result, the green dashed result has the $6 \times 6 \times 6$ supercell and the blue solid curve shows DFPT data. . . . . 104
7.7 Phonon dispersions for bcc Fe at different DFPT convergence thresholds. The black dashed curve shows the $4 \times 4 \times 4$ supercell result, while the red, green, and blue lines show the three phonon modes for specific q-points with respect to the thresholds. . . . . 105
7.8 Phonon dispersions for bcc Fe for different maximum numbers of iteration in the Sternheimer SCF cycle. The black dashed curve shows the $4 \times 4 \times 4$ supercell result, while the blue dotted lines show the three phonon modes for specific q-points with respect to the iterations. . . . . 106
7.9 First iteration distances of the Sternheimer SCF-loop for bcc Fe plotted against the Cartesian q-point component parallel to the displacement. The y-axis is given on a logarithmic scale. . . . . 107
7.10 Phonon dispersions for bcc Fe at different plane wave cutoffs. The black dashed curve shows the $4 \times 4 \times 4$ supercell result, while the blue dotted lines show the phonon frequencies for specific q-points with respect to the cutoffs. . . . . 108
7.11 Phonon dispersions for bcc Fe at different k-point meshes. The black dashed curve shows the $4 \times 4 \times 4$ supercell result, various data points show the phonon frequencies for specific q-points with respect to the sets. . . . . 109
7.12 Phonon dispersion and DOS for bcc Mo. The red curves show the FD reference and the blue curves show the DFPT data. . . . . 111
7.13 Phonon dispersion and DOS for bcc Mo. The red curves show the FD reference and the blue curves show the DFPT data. The black pluses show experimental data from [203]. . . . . 112
7.14 Phonon dispersion and DOS for bcc Mo. The red curves show the FD $4 \times 4 \times 4$ supercell, the dashed green line $8 \times 8 \times 8$, and the blue curves show the DFPT data. . . . . 114

8.1 DFPT phonon dispersions for bcc Fe expressed as a simple cubic system with a two atom basis. The blue data points belong to the FM system and the red points are those of the NM configuration. . . . . 117
8.2 DFPT phonon dispersions for bcc Fe. The blue data points belongs to the FM system expressed as a simple cubic system with a two atom basis and the red dotted lines correspond to the original bcc crystal with a single atom. . . . . 118
8.3 DFPT phonon DOS for bcc Fe. The blue curve belongs to the FM system and the red one is that of the NM state. . . . . 119
8.4 DFPT phonon dispersions for hcp Co. The blue data points belong to the FM system and the red points are those of the AFM setup that loses its magnetization in the SCF loop. . . . . 120
8.5 DFPT phonon dispersions for bcc Fe expressed as a simple cubic system with a two atom basis. The blue data points belong to the FM system with the lattice constant $a = 5.220\ a_0$ and the red points are those of the AFM setup ($a = 5.099\ a_0$) with an FM ground-state density. FMcAFM is a shorthand notation for the FM system in an AFM lattice constant. . . . . 121

8.6 DFPT phonon dispersions for bcc Fe expressed as a simple cubic system with a two atom basis. The blue data points belong to the NM system with the respective lattice constant ($a = 5.099\ a_0$) and the red points are those of the FM setup ($a = 5.220\ a_0$) with an NM ground-state density. The green data points additionally show the AFM configuration at the FM lattice constant. . . 122
8.7 DFPT phonon dispersions for hcp Co. The blue data points belong to the FM ($a = 4.606\ a_0, c = 7.356\ a_0$) and the red points are those of the NM setup ($a = 4.550\ a_0, c = 7.266\ a_0$) with an FM ground-state density. . . . . 123
8.8 DFPT phonon dispersions for hcp Co. The blue data points belong to the NM ($a = 4.550\ a_0, c = 7.266\ a_0$) and the red points are those of the FM setup ($a = 4.606\ a_0, c = 7.356\ a_0$) with a NM ground-state density. . . . . 124
8.9 Phonon dispersions for FM hcp Gd. The blue data points belong to the DFPT data and the red dashed lines represent the FD benchmark. The black crosses are from a set of experimental data in [209]. . . . . 127
8.10 Phonon dispersions for AFM hcp Gd. The blue data points belong to the DFPT data and the red dashed lines represent the FD benchmark. . . . . 128
8.11 DFPT phonon dispersions for hcp Gd. The blue data points belong to the FM and the red points are those of the AFM. . . . . 129
8.12 DFPT phonon dispersions for hcp Gd. The blue data points belong to the FM and the red points are those of the AFM setup with an FM ground-state density. 130
8.13 DFPT phonon dispersions for hcp Gd. The blue data points belong to the AFM and the red points are those of the FM setup with an AFM ground-state density. 131
8.14 DFPT phonon dispersions for bcc Eu expressed as a simple cubic system with a two atom basis. The blue data points belong to the FM and the red points are those of the AFM. . . . . 132
8.15 DFPT phonon dispersions for bcc Eu expressed as a simple cubic system with a two atom basis. The blue data points belong to the FM and the red points are those of the AFM setup with an FM ground-state density. . . . . 133
8.16 DFPT phonon dispersions for bcc Eu expressed as a simple cubic system with a two atom basis. The blue data points belong to the AFM and the red points are those of the FM setup with an AFM ground-state density. . . . . 134

9.1 Phonon dispersion for $VSe_2$. The red curve shows the FD $2 \times 2 \times 2$ supercell and the blue dots show the DFPT data. A specific $\Gamma$-point outlier far outside the range of the other values is visualized as an inlay. . . . . 137
9.2 Sketch of the unit cell setup in the film LAPW method, based on the bulk equivalent in figure 4.1. The unit cell used to construct the plane wave basis of the IR is highlighted with dashed lines while the IR-Vacuum transition is marked by the full lines. . . . . 140
9.3 Phonon dispersions for the in-plane modes of graphene. The red data points belong to the DFPT data of a bulk calculation with far apart layers. The green data points belong to a true film FLAPW calculation. . . . . 151

D.1 Phonon dispersions for graphene. The red data points belong to the DFPT data and the black dashed lines represent the FD benchmark of a bulk calculation (both with far apart layers). The green and blue data points belong to a true film FLAPW calculation, where the latter have been corrected by the offset of the $\Gamma$-point. . . . . 169
D.2 Phonon dispersions for graphene. The red data points belong to the DFPT data and the black dashed lines represent the FD benchmark of a bulk calculation (both with far apart layers). The green and blue data points belong to a true film FLAPW calculation, where the latter have been corrected by the ZO offset of the $\Gamma$-point. . . . . 170

# List of Tables


6.1 Overview of the specific calculational parameters of fcc Ne. Parameters not contained in the table are kept at the FLEUR default or are explicitly mentioned in section 6.1. . . . . 81
6.2 Overview of the acoustic Γ-point modes, $\omega$, in $cm^{-1}$ for fcc Ne. No frequency exceeds an absolute value of $0.2$ $cm^{-1}$ (or $0.025$ meV | $0.006$ THz, respectively). 82
6.3 Overview of the specific calculational parameters of fcc Cu. More parameters in section 6.1. . . . . 83
6.4 Overview of the acoustic Γ-point modes, $\omega$, in $cm^{-1}$ for fcc Cu. No frequency exceeds an absolute value of $0.4$ $cm^{-1}$ (or $0.050$ meV | $0.012$ THz, respectively). 83
6.5 Overview of the specific calculational parameters of fcc Ni. More parameters in section 6.1. . . . . 84
6.6 Overview of the acoustic Γ-point modes, $\omega$, in $cm^{-1}$ for fcc Ni. No frequency exceeds an absolute value of $0.3$ $cm^{-1}$ (or $0.037$ meV | $0.009$ THz, respectively). 85
6.7 Overview of the specific calculational parameters of Si. More parameters in section 6.1. . . . . 86
6.8 Overview of the acoustic Γ-point modes, $\omega$, in $cm^{-1}$ for Si. No frequency exceeds an absolute value of $0.1$ $cm^{-1}$ (or $0.012$ meV | $0.003$ THz, respectively). . . . . 87
6.9 Overview of the specific calculational parameters of hcp Co. More parameters in section 6.1. . . . . 88
6.10 Overview of the acoustic Γ-point modes, $\omega$, in $cm^{-1}$ for hcp Co. No frequency exceeds an absolute value of $1.7$ $cm^{-1}$ (or $0.211$ meV | $0.051$ THz, respectively). 89
6.11 Overview of the specific calculational parameters of SiC. For the atomic parameters, there are two values given each time representing the Si/C atom respectively. More parameters in section 6.1. . . . . 90
6.12 Overview of the acoustic Γ-point modes, $\omega$, in $cm^{-1}$ for SiC. No frequency exceeds an absolute value of $1.1$ $cm^{-1}$ (or $0.136$ meV | $0.033$ THz, respectively). 90

7.1 Overview of the specific calculational parameters of bcc Fe. Parameters not contained in the table are kept at the FLEUR default or are explicitly mentioned in section 6.1. . . . . 97
7.2 Overview of the acoustic Γ-point modes, $\omega$, in $cm^{-1}$ for bcc Fe. No frequency exceeds an absolute value of $0.2$ $cm^{-1}$ (or $0.025$ meV | $0.006$ THz, respectively). 98

7.3 Overview of the specific calculational parameters of bcc Mo. Parameters not contained in the table are kept at the FLEUR default or are explicitly mentioned in section 6.1. . . . . 110
7.4 Overview of the acoustic Γ-point modes, $\omega$, in $cm^{-1}$ for bcc Mo. No frequency exceeds an absolute value of $0.07$ $cm^{-1}$ (or $0.009$ meV | $0.002$ THz, respectively).111

8.1 Overview of the specific calculational parameters of (A)FM hcp Gd. Where the parameters differ for the FM and AFM structure, there are two values given. More parameters in section 6.1. . . . . 126
8.2 Overview of the acoustic Γ-point modes, $\omega$, in $cm^{-1}$ for FM hcp Gd. No frequency exceeds an absolute value of $1.4$ $cm^{-1}$ (or $0.174$ meV | $0.042$ THz, respectively).126
8.3 Overview of the acoustic Γ-point modes, $\omega$, in $cm^{-1}$ for AFM hcp Gd. No frequency exceeds an absolute value of $2.0$ $cm^{-1}$ (or $0.248$ meV | $0.060$ THz, respectively). . . . . 127
8.4 Overview of the specific calculational parameters of (A)FM bcc Eu. Where the parameters differ for the FM and AFM structure, there are two values given. More parameters in section 6.1. . . . . 130

9.1 Overview of the specific calculational parameters of $VSe_2$. For the atomic parameters, there are two values given representing the V/Se atoms respectively where they differ. More parameters in section 6.1. . . . . 136
9.2 Overview of the acoustic Γ-point modes, $\omega$, in $cm^{-1}$ for $VSe_2$. No frequency exceeds an absolute value of $3.9$ $cm^{-1}$ (or $0.484$ meV | $0.117$ THz, respectively).136
9.3 Overview of the optical Γ-point modes, $\omega$, in $cm^{-1}$ for $VSe_2$. . . . . 137
9.4 Overview of the specific calculational parameters of $MoSe_2$. More parameters in section 6.1. . . . . 138
9.5 Overview of the acoustic Γ-point modes, $\omega$, in $cm^{-1}$ for $MoSe_2$. No frequency exceeds an absolute value of $2.0$ $cm^{-1}$ (or $0.248$ meV | $0.060$ THz, respectively).138
9.6 Overview of the optical Γ-point modes, $\omega$, in $cm^{-1}$ for $MoSe_2$. The first row belongs to the supercell calculation, the second one to the DFPT run, and the third to a DFPT run, where the eigenenergy response is neglected. . . . . 139
9.7 Overview of the specific calculational parameters for graphene. More parameters in section 6.1. . . . . 150
9.8 Overview of the acoustic Γ-point modes, $\omega$, in $cm^{-1}$ for the 2D graphene film calculation. . . . . 150

# Abbreviations and Acronyms

| | |
|---|---|
| AFM | Antiferromagnet(-ic) |
| AFMcFM | Shorthand notation for a antiferromagnetic system with a ferromagnetically optimized lattice constant |
| APW | Augmented Plane-Wave |
| bcc | body-centered cubic |
| BO | Born–Oppenheimer |
| C | Coulomb |
| DFT | Density Functional Theory |
| DFPT | Density-Functional Perturbation Theory |
| DFT+U | DFT with Hubbard $U$ Corrections |
| DM | Dynamical Matrix |
| DOS | Density of States |
| eff | effective |
| el | electron |
| EOS | Equation of States |
| ext | external |
| F | Fermi |
| fcc | face-centered cubic |
| FD | Finite Displacement |
| FFT | Fast Fourier Transform |
| FLAPW | Full-Potential Linearized Augmented Plane-Wave |
| FM | Ferromagnet(-ic) |
| FMcAFM | Shorthand notation for a ferromagnetic system with an antiferromagnetically optimized lattice constant |
| GGA | Generalized Gradient Approximation |
| H | Hartree |
| Ha | Hartree |
| hcp | hexagonal close packed |
| HF | Hellmann–Feynman |
| HEG | Homogeneous Electron Gas |
| IBC | Incomplete Basis set Correction |
| (I)BZ | (Irreducible) Brillouin Zone |

| | |
|---|---|
| ii | ion-ion |
| int | integral |
| IR | Interstitial Region |
| KS | Kohn–Sham |
| LA | Longitudinal Acoustic |
| LAPW | Linearized Augmented Plane-Wave |
| LDA | Local Density Approximation |
| lin | linear |
| LO | Longitudinal Optic |
| LO | Local Orbital |
| M | Madelung |
| MT | Muffin-Tin |
| NAC | Non-Analytical term Correction |
| NM | Nonmagnetic |
| NOCO | Non-Collinear |
| nsph | non-spherical |
| op | operation |
| ps | pseudo |
| PW | Plane Wave |
| sc | supercell |
| SCF | Self-Consistent Field |
| SF | Surface |
| SOC | Spin Orbit Coupling |
| sph | spherical |
| TA | Transversal Acoustic |
| TO | Transversal Optic |
| tot | total |
| (un)occ | (un)occupied |
| xc | exchange-correlation |
| ZA | Out-of-Plane Acoustic |
| ZO | Out-of-Plane Optic |

Chapter 1

# Introduction

Phonons are quasiparticles that represent the collective vibrational modes of atoms in a crystalline material. In simpler terms, they are the elementary units of vibrational energy in a solid. The basic theory of phonons is well established and has been described in detail in text books [1, 2]. These vibrational modes play a crucial role in various physical properties of materials. Firstly, they are related to classical phenomena [1, 3–5]. The electrical and thermal transport behavior can be attributed to them. The heat-capacity and thermal expansion are related to the phonon density of states, while the speed of sound in a material is directly linked to the slope of the dispersion of the acoustic phonon mode close to the $\Gamma$-point. They are also linked to the elastic properties of the material and serve as an energy sink for scattering radiation or neutrons in the material (depending on their energy range). This gives us options to measure the phonon spectrum *e.g.* by inelastic neutron scattering [6–8], X-ray experiments [9–11], infrared [12], and Raman spectroscopy [13]. Aside from their importance in classical physics, they are involved in a wide range of semi-classical and quantum phenomena. They are a mediator of effective electron-electron interaction, hence being a key factor in the emergence of superconductivity [14]. They can couple to other (quasi-)particles to form new groups of quasiparticles that fuel model-based solid-state theory [15]. They are also of continuous interest due to their role in engineering acoustic metamaterials [16, 17], as driving force for charge-density waves [18], for the optimization of the phonon transport in thermoelectrics [19], and in the context of ferroelectric [20], 2D [21–23], and magnetic [24] materials. In the latter they contribute to spin-relaxation [25], Gilbert damping [26] and -equilibration [27], assist magnetization switching by linearly- [28] and circularly-polarized [29], or chiral phonons [30], influence the temperature dependence of the magnetocrystalline anisotropy [31], and can be of interest in the fields of orbitronics [32] and thermal Hall physics [33]. The desire to understand the various physical effects in different materials and the wealth of potential applications arising from phonons motivates the development of efficient and powerful numerical methods capable of reliably and accurately predicting the phononic properties in real materials.

The phonon calculations in this work are based on the ab-initio description of materials by means of Kohn–Sham density functional theory (DFT) [34–38]. Kohn–Sham DFT is a reliable and well-established total-energy framework, as evidenced by a huge number of applications every year, that offers valuable insights into the electronic structure especially of single crystals.

Considering that the phonon energies are small in comparison to the total energy, Kohn–Sham DFT can serve as a solid foundation to investigate phonon physics. Assuming a separation of time scales between the electronic and phononic degrees of freedom, in the harmonic approximation, the phonon dispersion relation is related to the second order derivative of the system's total energy with respect to the atomic positions. This quantity is usually computed in two ways [39]: by the finite displacement (FD) approach [40–42] or by means of density-functional perturbation theory (DFPT) [43–47]. The FD approach utilizes atomic forces (*i.e.* the first order derivatives of the energy) exerted on the atoms, which are numerically evaluated for manually displaced atoms using analytical expressions to obtain the second order derivative numerically as the difference quotient of the forces in the displaced and undisplaced system. On the other hand, the DFPT provides a fully analytical second derivative of the total energy. The FD approach is in principle easier to realize, was established earlier, and is widely used to this day [48], but comes at the cost of computing the forces in supercells of displaced atoms and of the computational uncertainty of anharmonic terms included. The implementation of the DFPT framework is much more involved, as the first-order response of the wave function with respect to the displacement is required, which is typically self-consistently obtained by the Sternheimer equation. In contrast, there is no need for the construction of supercells and phonon properties of specific and arbitrary phonon wave vectors can be addressed. Both methods are complementary, with DFPT gaining increasing attention in recent years.

Our motivation to advance computational methodologies for the description of phonons stems from the interest in the study of quantum materials and the design of quantum materials for potential devices in the area of digital, neuromorphic and quantum computing, where electron topology, associated transport properties, spin-orbit physics, spin-momentum locking and exotic magnetic textures are pivotal. Particularly, attention is drawn to materials exhibiting exotic magnetization textures or transition metal dichalcogenides (TMDCs) [30, 49, 50], known for their intriguing charge-density wave (CDW) ground-states [51]. DFPT offers insights into mechanisms at play in which phonons couple to other degrees of freedom in such materials. We mentioned, that comprehending the interplay among electrons and phonons is pivotal for electrical resistivity, electron equilibration, and superconductivity, but recently this extends to phonons with spin ensembles or magnons in magnetic materials to understand the angular momentum transfer into the lattice. A robust and practical numerical framework is essential for investigating these effects in materials effectively [52].

The computational method of choice in this thesis and the most versatile method available in general is the DFPT. The implementation has the same complexity as the Kohn–Sham quantum engine and is challenging. The implementation comes along with many important decisions, the most important of which is the choice of the basis set for the Kohn–Sham orbital. Historically, DFPT [44–47] was first implemented in a pseudopotential [53–56] context employing plane waves (PW) as basis set for electron wave functions. Even today most phonon studies using DFPT have been performed with norm-conserving pseudopotentials [57–60], but there are now also studies using ultrasoft pseudopotentials [61–63] and the projector-augmented wave (PAW) method [64]. The formalism has been expanded over the years to include both collinear [65–68] and, most recently, also non-collinear magnetism [69]. These developments were driven primarily by the communities around the `ABINIT` [57, 70] and `Quantum ESPRESSO` codes. Despite these efforts, the overall number of DFPT publications for

magnetic/spin-polarized systems is rather low[1] considering the total number of DFPT papers and there is still a lot of research to be done both for the PW community and beyond.

In this thesis we describe the implementation of DFPT in an alternative electronic structure method, an all-electron method. Characteristic to all-electron methods is the 1/r singularity caused by the atomic nuclei, which requires sophisticated atom centered basis functions to represent the Kohn–Sham orbitals. The basis functions are numerically exact solutions to this singular potential, which is often enclosed in a sphere, *e.g.* the muffin-tin sphere. One of the most precise implementations of DFT is the all-electron full-potential linearized augmented-plane-wave (FLAPW) method [71–73]. It treats valence- and core-electrons on an equal footing and adapts the degree of relativity in the physical description to the actual demands originating from the energy of the orbitals and the region of space in which the physics has to be described. With these features the FLAPW method has become the precision gold standard for electronic structure calculations, employed in community efforts to provide data sets on different physical quantities as a reference to assess the precision of other approaches [74, 75]. The LAPW basis set used by the FLAPW method to represent the valence electron orbitals not only allows for this level of precision, but is also highly efficient with respect to the number of basis functions that are needed. It allows for implementations of the FLAPW method that enable electronic structure calculations for unit cells consisting of thousands of atoms [76]. One of the great advantages of the FLAPW method is its applicability of all nonmagnetic and magnetic elements of the periodic table in structurally and electronically complex environments without much ado. The drawback of the LAPW basis, however, is that the implementation of property calculators for atom-position dependent quantities becomes challenging. In general, publications and codes combining DFPT and all-electron muffin-tin based electronic structure methods such as the augmented spherical wave (ASW) [77], linear muffin-tin orbital techniques (LMTO) [78] or Korringa–Kohn–Rostoker (KKR) Green function method [79] are scarce.

In this thesis we take on the well-acknowledged challenge of calculating phonons with the FLAPW method. The application of the FD method in combination with FLAPW requires very accurate forces [80] achieved by correction terms [81] that have been published to make the FD method successfully applicable. There were several initiatives to implement the DFPT method in the context of FLAPW [82–89]. Recently, we brought it to an implementation in the established FLAPW framework `FLEUR` [90, 91]. The implementation is on a roadmap to a full coverage of general quantum materials. These are recent developments that lead to a full theoretical framework taking all basis and surface corrections into account [92], from which a working implementation as a plugin for the `FLEUR` code was developed [93] and published [94]. This first milestone was implemented in the juPhon software package. It contained many conceptional features and correction terms induced by the basis, but was very restrictive in that it only allowed nonmagnetic, monatomic materials to be calculated with Slater's $X\alpha$ functional [95] and was tailored to a legacy version (v26) of `FLEUR` that is out of date. Furthermore, the plugin was a separately compiled program that recycled and rewrote a lot of `FLEUR` routines, which lead to a lot of redundant code that was very hard to maintain. As such, one of the main focal points of this work is the improved reintroduction of the plugin's functionality into the currently supported version of `FLEUR`, which is e.g. able

[1] A quick search on WebOfScience gives us 1822 hits for "density-functional perturbation theory" or "DFPT" or "density functional perturbation theory", but only 235 if we add "magnetism" or "magnetic" or "spin". This amounts to around 13% of the full set.

to resolve numerically induced kinks in the phonon dispersion relation that were visible in the first results [93], in a programming concept that allows a significant extension of the methodology to a broad spectrum of phonon properties and materials.

In the vein of these efforts, magnetic and polyatomic materials were made available for the first time in [94] and are used in this thesis to study materials with different magnetic orders and dimensionality, e.g. 2D materials. As mentioned before, the phonon physics in these materials are of high current interest and exactly those two classes are strong suites of FLEUR. The description of 2D materials is based on early implementations of the FLAPW formalism for thin films, *i.e.* materials with an in-plane crystal periodicity, but perfectly embedded in semi-infinite vacua normal to the film. Among the magnetic materials, our code is also well-equipped to deal with elements that have large open shells like the lanthanides. As methods that work with plane waves often have trouble describing such elements [75], an investigation of Eu and Gd and the like lends itself well to DFPT in FLEUR.

The general structure of this work is as follows: In chapter 2 the general theory of electronic structure methods with a focus on DFT is presented. From this the theory of phonons is developed for the case of the periodic lattice in chapter 3. Chapter 4 then applies the more general ideas to the specifics of the FLAPW method, which concludes the purely theoretical section. Chapter 5 deals with the specifics of the implementation in the FLEUR code, which is tested and validated in chapter 6 for several materials. Chapter 7 contains convergence studies with respect to different parameters that are relevant to the calculation of phonons both by FD and DFPT. Chapter 8 deals with the phononic properties of elemental and rare-earth magnets with special focus on the differences in behavior for ferro- and antiferromagnets to give a first glimpse of the interplay of magnetism and phonons. Finally, chapter 9 gives an overview of recent 2D calculations both of films embedded in a 3D lattice, *i.e.* a bulk calculation with large interlayer distances in the out-of-plane direction, and of an extension of the FLAPW DFPT method to thin film systems with true 2D periodicity. A conclusion and an outlook on developments and potential research planned for the future is given in chapter 10.

Chapter 2

# Electronic Structure


2.1 The Many-Body System . . . . . 6
2.2 Kohn–Sham Density Functional Theory . . . . . 7
2.3 Exchange-Correlation Functionals . . . . . 9
2.4 State Occupation in Metals . . . . . 10
2.5 Self Consistency . . . . . 11
2.6 Spin-Density Functional Theory . . . . . 13
2.7 Extensions to and Generalizations of DFT . . . . . 15


The Necessity of Numerical Approximations

Molecules and solid state systems are collections of many atoms, which in turn are made up of an atomic nucleus and a number of electrons. Calculating the properties of such a system constitutes a many-body problem. In principle, the formalism that describes the physics of such quantum mechanical objects has been well established since the early 20th century. For non-relativistic systems, the Schrödinger equation is able to accurately describe phenomena on the atomic scale. For example, the eigenstates and -energies of the hydrogen atom can be determined fully analytically by fixing the proton at the origin and describing the single electron as the only moving part (two-body problem). This property already breaks down for the Helium atom, where the interaction of the two electrons requires numerical methods (three-body problem). This train of thought continues and becomes less and less feasible for systems of many nuclei and electrons. Even when numerical methods are applied, the sheer information density of the quantum mechanical system is not containable in a realistic amount of data storage. A basic model calculation highlights this point. A single sodium atom, with one nucleus and 11 electrons, described by a wave function in three-dimensional real-space, contains 33 degrees of freedom, *i.e.* 33 coordinates for the real-space wave function. To describe this atom on a coarse real-space grid of only 10 mesh points in each spatial direction already amounts to $10^{33}$ wave function values, that when stored as double precision real numbers (8B of storage) will consume $10^{9}$YB of disk space. Walter Kohn described such behavior in his Nobel prize lecture [36] as an ”exponential wall” that the computational capacity will quickly run into.

Paul Dirac

Even before the advent of digital computers and the related understanding of the necessary storage volumes, Paul Dirac accurately described the fundamental problem of many-body quantum physics as early as 1929 [96].

> The underlying physical laws necessary for the mathematical theory of a large part of physics and the whole of chemistry are thus completely known, and the difficulty is only that the exact application of these laws leads to equations much too complicated to be soluble. It therefore becomes desirable that approximate practical methods of applying quantum mechanics should be developed, which can lead to an explanation of the main features of complex atomic systems without too much computation.

Since then, a plethora of such numerical approximations and a vast amount of models have been established to encapsulate the emergent phenomena of big groups of atoms.

Density Functional Theory

One such method is density functional theory (DFT), based on the seminal work of Hohenberg and Kohn [34]. A practical method was developed from this by Kohn and Sham [35], creating what we know today as Kohn–Sham (KS) DFT. The following chapter describes the suite of approximations that is used to go from the full many-body Hamiltonian to a set of equations that can easily be handled by modern computers.

## 2.1 The Many-Body System

As mentioned before, the properties of a quantum-mechanical system are fully contained in its wave function and governed by the (time-dependent) Schrödinger equation

$$\mathcal{H}|\Psi\rangle = i\partial_t|\Psi\rangle. \tag{2.1}$$

In the study of electronic structure, the time dependence is often separated from the spatial one and the equation constitutes an eigenvalue problem for a ground-state wave function with energy $E$. For a system of $N_{\text{ion}}$ atomic nuclei with charges $Z_\gamma$ located at $\boldsymbol{\tau}_\gamma$, $\gamma = 1, ..., N_{\text{ion}}$, and $Z_\gamma$ corresponding electrons ($N_{\text{el}}$ in total) with coordinates $\boldsymbol{r}_i$, the Hamiltonian

$$\mathcal{H} = T_{\text{el}} + T_{\text{ion}} + U_{\text{el-el}} + U_{\text{el-ion}} + U_{\text{ion-ion}} \tag{2.2}$$

contains the kinetic energy $T$ of each of these particles as well as their mutual electrostatic attraction or repulsion $U$. In practice, we are more interested in the electrons' behavior than in that of the ions. Utilizing the fact, that the ions are several orders of magnitude heavier than the electrons, we can normalize the Hamiltonian by the electron mass $m_e$ and drop the ionic kinetic energy term. The atomic positions hence take the form of external parameters to the Schrödinger equation and constitute an external potential for the electrons to move in. This is known as the Born–Oppenheimer approximation [97]. Written in atomic units ($e = m_e = \hbar = 1/(4\pi\varepsilon_0) = 1$), the corresponding Hamiltonian reads

$$\mathcal{H}_{\text{BO}}[\{\boldsymbol{\tau}\}] = \underbrace{-\frac{1}{2}\sum_{i}^{N_{\text{el}}}\nabla_i^2}_{T_{\text{el}}} + \underbrace{\frac{1}{2}\sum_{\substack{i,i'\\ i\neq i'}}^{N_{\text{el}}}\frac{1}{|\boldsymbol{r}_i - \boldsymbol{r}_{i'}|}}_{U_{\text{el-el}}} - \underbrace{\sum_{i,\gamma}\frac{Z_\gamma}{|\boldsymbol{r}_i - \boldsymbol{\tau}_\gamma|}}_{U_{\text{el-ion}}} + \underbrace{\frac{1}{2}\sum_{\substack{\gamma,\gamma'\\ \gamma\neq\gamma'}}^{N_{\text{ion}}}\frac{Z_\gamma Z_{\gamma'}}{|\boldsymbol{\tau}_\gamma - \boldsymbol{\tau}_{\gamma'}|}}_{U_{\text{ion-ion}}}, \tag{2.3}$$

where we introduced the short-hand notation $\{\boldsymbol{\tau}\} := \{\boldsymbol{\tau}_\gamma\}_{\gamma=1,\dots,N_{\text{ion}}}$. The problem is now cast into a purely electronic form. The computational effort, however, remains large, as there are at least as many electrons as ions and the electrons interact with each other through $U_{\text{el-el}}$. Aside from it, the Hamiltonian could easily be reduced to a set of $N_{\text{el}}$ separate problems by writing the many-body wave function in a product ansatz, but to arrive at such a form in spite of interacting electrons requires further approximations. One valid ansatz is the Hartree–Fock method [98]. The many-body wave function is expressed as a Slater determinant of single-particle ones, ensuring the antisymmetry required by the Pauli exclusion principle for fermions [99]. The exact form of the orbitals is determined by the minimization of the system's energy. Several refinements of this formalism exist [100–102], which commonly scale unfavorably with system size. We want to focus instead on a different approach altogether, that moves away from the many-body wave function as the central object of study.

## 2.2 Kohn–Sham Density Functional Theory

The Theorem of Hohenberg and Kohn

The essence of DFT is the reduction of the complex many-body problem to an energy minimization with respect to the electronic density, making the energy a functional of the latter. The theoretical groundwork for this was laid in 1964 by Hohenberg and Kohn [34] and is summarized in the following two statements:

i) The external potential $V_{\text{ext}}(\boldsymbol{r})$ specifying the atomic configuration of a system is a unique functional of the electronic ground-state density $n^{(0)}(\boldsymbol{r})$ of this system, apart from a constant shift in the potential. The same is true for the ground-state energy $E[n^{(0)}]$ and all other properties.

ii) The ground-state density minimizes the total-energy functional among all densities that reproduce the same number of electrons $N_{\text{el}}$, *i.e.* ,

$$E[n] > E[n^{(0)}] \; \forall n(\boldsymbol{r}) \neq n^{(0)}(\boldsymbol{r}), N_{\text{el}} = \int n(\boldsymbol{r})\mathrm{d}\boldsymbol{r} = \int n^{(0)}(\boldsymbol{r})\mathrm{d}\boldsymbol{r}. \quad (2.4)$$

Practically speaking, the first statement tells us, that the many-body wave function is too complex of an object, if one is only concerned with the ground-state of the system, as the electron density contains all necessary information. Furthermore, the external potential is fully described by said ground-state density, constituting a loop of dependencies between the central quantities in quantum mechanics and DFT:

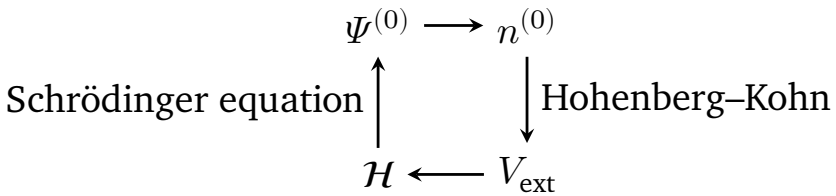



**Figure 2.1:** Sketch of the interdependent quantities after Hohenberg and Kohn.

The second statement gives us a way to construct the ground-state density: It is exactly the density, for which the total-energy functional takes on the minimal value. This density is unique.

The Kohn–Sham Formalism

At this point, we achieved the goal of reducing the data storage necessary: The electron density is a physical quantity that depends on only one coordinate, *i.e.* three degrees of freedom. This is vastly less data intensive than the initial problem, but poses the question, how the kinetic energies of the electrons and their electrostatic interactions can be expressed in terms of the ground-state density. For this, Kohn and Sham proposed setting up an auxiliary system of non-interacting electrons in an effective potential, that obeys a single-particle Schrödinger equation

$$\left(-\frac{1}{2}\nabla^2 + V_{\text{eff}}(\boldsymbol{r})\right)\psi_\nu(\boldsymbol{r}) = \varepsilon_\nu \psi_\nu(\boldsymbol{r}), \tag{2.5}$$

and correctly reproduces the density

$$n(\boldsymbol{r}) = \sum_\nu \tilde{f}_\nu |\psi_\nu(\boldsymbol{r})|^2. \tag{2.6}$$

when summed over all bands $\nu$, weighted with an occupation number $\tilde{f}_\nu$. Along with these definitions, the Born-Oppenheimer energy that corresponds to the Hamiltonian needs to be adjusted. Replacing the original kinetic energy of the electrons with a non-interacting (n-i) one, introducing an integral (with the ground-state density) for the electron-electron and electron-ion interaction, and writing everything as a functional of the ground-state density, we find

$$E_{\text{BO}}[n,\{\boldsymbol{\tau}\}] = T_{\text{el,n-i}}[n] + \frac{1}{2}\int\int \frac{n(\boldsymbol{r})n(\boldsymbol{r}')}{|\boldsymbol{r}-\boldsymbol{r}'|}\mathrm{d}\boldsymbol{r}'\mathrm{d}\boldsymbol{r} - \sum_\gamma \int \frac{Z_\gamma n(\boldsymbol{r})}{|\boldsymbol{r}-\boldsymbol{\tau}_\gamma|}\mathrm{d}\boldsymbol{r} + E_{\text{xc}} + E_{\text{ii}}, \tag{2.7}$$

where we defined the "exchange-correlation" (xc) energy

$$\begin{aligned} E_{\text{xc}}[n] :=\ & T_{\text{el}}[n] - T_{\text{el,n-i}}[n] \ + U_{\text{el-el}}[n] - \frac{1}{2}\int\int \frac{n(\boldsymbol{r})n(\boldsymbol{r}')}{|\boldsymbol{r}-\boldsymbol{r}'|}\mathrm{d}\boldsymbol{r}'\mathrm{d}\boldsymbol{r} \\ & + U_{\text{el-ion}}[n] + \sum_\gamma \int \frac{Z_\gamma n(\boldsymbol{r})}{|\boldsymbol{r}-\boldsymbol{\tau}_\gamma|}\mathrm{d}\boldsymbol{r} \end{aligned} \tag{2.8}$$

$$= \int n(\boldsymbol{r})\varepsilon_{xc}[n](\boldsymbol{r})\mathrm{d}\boldsymbol{r} \tag{2.9}$$

as the difference between the initial form and the non-interacting one and changed the notation of the ion-ion interaction from the potential term $U_{\text{ion-ion}}$ to the symbol $E_{\text{ii}}$ to highlight that it is a contribution to the total energy of the system. In doing so, we collect all terms whose dependency on the density is not known analytically into one quantity, that can be expressed as an integral over the density and an (as of yet undetermined) exchange-correlation energy density $\varepsilon_{xc}[n](\boldsymbol{r})$. In practice, an analytical approximation for this has to be made and several classes of such have been investigated. A short overview of the most prominent ones will be the topic of section 2.3. The effective potential in equation (2.5) is further specified as consisting of three parts,

$$V_{\text{eff}}[n,\{\boldsymbol{\tau}\}](\boldsymbol{r}) = V_{\text{ext}}[\{\boldsymbol{\tau}\}](\boldsymbol{r}) + V_{\text{H}}(\boldsymbol{r}) + V_{\text{xc}}[n](\boldsymbol{r}), \tag{2.10}$$

and is again a functional of the atomic positions and the density, due to the external and xc part. We omit the notation of these dependencies in the following. The external and Hartree components are often grouped into the Coulomb potential $V_\mathrm{C}$. This is due to the singular nature of the ionic term, that is compensated for by the electronic charge. The individual parts of the potential are consistent with the reformulation of the energy functional and calculated as

$$V_\mathrm{ext}(\boldsymbol{r}) = -\sum_\gamma \frac{Z_\gamma}{|\boldsymbol{r}-\boldsymbol{\tau}_\gamma|} = \sum_\gamma V_\mathrm{ext}^\gamma(\boldsymbol{r}), \tag{2.11a}$$

$$V_\mathrm{H}(\boldsymbol{r}) = \int \frac{n(\boldsymbol{r}')}{|\boldsymbol{r}-\boldsymbol{r}'|}\mathrm{d}\boldsymbol{r}', \tag{2.11b}$$

$$V_\mathrm{xc}(\boldsymbol{r}) = \frac{\delta E_\mathrm{xc}[n]}{\delta n(\boldsymbol{r})} = \varepsilon_\mathrm{xc}[n](\boldsymbol{r}) + n(\boldsymbol{r})\frac{\delta \varepsilon_\mathrm{xc}[n](\boldsymbol{r})}{\delta n(\boldsymbol{r})}. \tag{2.11c}$$

With these definitions, KS-DFT now forms a self-consistent problem, as the effective potential determines the KS eigenstates (2.5), the KS eigenstates determine the density (2.6), and the density determines the effective potential (2.10). This problem is iteratively solved by repeating the interdependent calculation steps until the density is sufficiently converged. Further detail on the procedure is provided in section 2.5.

The Kohn–Sham Total Energy

Along with the density, the total energy of the KS system is determined in each iteration. By multiplying equation (2.5) from the left with $\tilde{f}_\nu \psi_\nu^*(\boldsymbol{r})$, integrating, and summing over all states $\nu$, the resulting terms can be rearranged to replace the non-interacting kinetic energy by the KS eigenenergies and an integral of the effective potential. This is done to avoid the numerical differentiation of the wave functions in favor of reusing terms that are already present in the calculation, reducing the computational effort while increasing the numerical stability. We find:

$$T_\mathrm{el,n\text{-}i}[n] = \sum_\nu \tilde{f}_\nu \varepsilon_\nu - \int n(\boldsymbol{r}) V_\mathrm{eff}(\boldsymbol{r})\mathrm{d}\boldsymbol{r}. \tag{2.12}$$

This form can be inserted into equation (2.7) to arrive at the KS total energy, that can then be expressed in terms of quantities from the self-consistency loop as

$$E_\mathrm{tot} = \sum_\nu \tilde{f}_\nu \varepsilon_\nu + \int n(\boldsymbol{r}) \left[-V_\mathrm{eff}(\boldsymbol{r}) + \frac{1}{2}V_\mathrm{H}(\boldsymbol{r}) + V_\mathrm{ext}(\boldsymbol{r}) + \varepsilon_\mathrm{xc}[n](\boldsymbol{r})\right] \mathrm{d}\boldsymbol{r} + E_\mathrm{ii}. \tag{2.13}$$

This is the energy form that needs to be minimized, which is exactly the case for the ground-state density $n^{(0)}(\boldsymbol{r})$, as the KS system is variational with respect to it.

## 2.3 Exchange-Correlation Functionals

The Lack of a Closed Form

The exchange-correlation functional is of central importance in DFT, as it allows us to perform accurate predictions with the method. There is no closed analytical form known for this term, but in comparison to the other ingredients its energy contribution is relatively small. We can therefore already obtain very good predictions with simple approximations to $\varepsilon_\mathrm{xc}$ and a wide range of possible approximations has been explored. The following section serves to highlight

the very basic local density approximation (LDA) used in this work, while giving short nods to the most popular classes of more sophisticated functionals.

Local Density Approximation

A basic approximation to the exchange-correlation energy density, that exceeds Hartree-Fock or Mean-Field approaches where the electrons are mostly independent, is the LDA. It was established by Kohn and Sham as the first actual realization of the DFT formalism [35] and is based on the model of the homogeneous electron gas (HEG). There, the exchange-correlation energy density only depends on the averaged density of the electrons in a finite volume $n_{\text{HEG}} = N_{\text{el}}/V$. The basic statement of the LDA is, that this density can now vary in space again and yields

$$\varepsilon_{xc}^{\text{LDA}}[n](\boldsymbol{r}) = \varepsilon_{xc}^{\text{HEG}}(n(\boldsymbol{r})). \tag{2.14}$$

Parametrizations

The exchange energy [103] in LDA takes a closed analytical form ($\varepsilon_{\text{x}} = -3/4(3n/\pi)^{1/3}$), while the form of the correlation functional is determined in terms of a model for which the parameters are determined *e.g.* by quantum Monte Carlo simulations [104]. This leads to a range of slightly different parametrizations, such as that of Ceperley and Alder [105], which was based on quantum Monte Carlo simulations for several intermediate values between the limits. Among other notable variants [95, 106–108], this thesis employs the parametrization of Vosko, Wilk and Nusair [109].

Impact and Generalizations

While this approximation is, in a sense, simplistic, it has been used to resounding success in the description of many materials. It also serves as the foundation of more sophisticated methods, as they still have to be able to reproduce the HEG when a homogeneous density is inserted. Such methods include the generalized gradient approximation (GGA) [110–113], where the gradient of the density enters as a second variational parameter and takes the form

$$\varepsilon_{xc}^{\text{GGA}}[n](\boldsymbol{r}) = \varepsilon_{xc}(n(\boldsymbol{r}), \boldsymbol{\nabla} n(\boldsymbol{r})). \tag{2.15}$$

Beyond that, the approximations grow more and more accurate, but also more costly. For example, they can include the kinetic energy density of the system or the Laplacian of the density (metaGGA [114–118]) or the exact exchange formalism [119–123] that leads to hybrid functionals. A good overview of the possible approximations was given by Perdew and Schmidt [124]. The successive improvement of these approximations was likened to the rungs on a ladder towards the ultimate goal of ”chemical accuracy”. The scope of this work is confined to LDA functionals, with the possibility of future extensions.

## 2.4 State Occupation in Metals

Fractional Occupation Numbers

The boundary condition of each DFT calculation is the conservation of the total electronic charge. This translates to the requirement, that the sum of occupied states has to reflect the electron number

$$N_{\text{el}} = \sum_{\nu} \tilde{f}_{\nu} \tag{2.16}$$

accurately. The states can either be occupied or unoccupied, leading to a description of the occupation numbers $\tilde{f}_{\nu}$ by a step function $\Theta(x)$, that is 1 for values $x \geq 0$ and vanishes

otherwise. The parameter $x$ depends on the energy of the state in relation to the Fermi energy $E_\mathrm{F}$, which equals the energy of the highest occupied state. This yields

$$N_\mathrm{el} = \sum_\nu 2\Theta(x)|_{x=\varepsilon_\nu - E_\mathrm{F}}, \tag{2.17}$$

where the factor 2 accounts for spin-degeneracy and is dropped for spin-polarized calculations. The Fermi energy is determined iteratively, so that a set of $\{\tilde{f}_\nu\}$ fulfilling the condition (2.16) is found, ensuring charge neutrality of the system. In semiconductors and insulators the occupied and unoccupied bands are well separated by the band gap, with the Fermi energy at its lower end. In metals, however, bands can cross the Fermi energy and the point of this crossing is sensible to the exact system setup. Moreover, the clean distinction between the occupied and unoccupied states becomes numerically difficult. To account for this, a smearing temperature $T$ is introduced, that transforms the step function into a smooth approximation

$$\Theta(x)|_{x=\varepsilon_\nu - E_\mathrm{F}} \longrightarrow \tilde{\Theta}(x)|_{x=(\varepsilon_\nu - E_\mathrm{F})/(k_\mathrm{B}T)}. \tag{2.18}$$

The exact form of this approximation can vary. The Fermi energy determination is adjusted accordingly to find a set of fractionally occupied states to satisfy the condition (2.16).

Energy Contribution

Weinert and Davenport noted, that with such a fractional occupation number, the total energy is no longer variational to first order [125]. This can be a hindrance in the calculation of forces and likewise in the perturbation formalism presented. To remedy this, they introduce an electronic entropy term to the total energy, that depends on the state occupations and the temperature:

$$E_\mathrm{tot} \to E_\mathrm{tot} - TS \tag{2.19}$$

It is noted to be identical in form to the free energy, and was referred to as $\tilde{E} \longrightarrow E_0$ in the seminal paper. It will keep being referred to as $E_\mathrm{tot}$ in this work instead. The form of $S$ depends on the smearing function that is chosen. In this work, it is restricted to the Fermi-Dirac function. The smearing and entropy thus read

$$\tilde{\Theta}(x) = \frac{1}{\mathrm{e}^x + 1}, \qquad S = -k_\mathrm{B} \sum_\nu \left[ \tilde{f}_\nu \ln\left(\tilde{f}_\nu\right) + \left(f_\nu - \tilde{f}_\nu\right) \ln\left(f_\nu - \tilde{f}_\nu\right) \right]. \tag{2.20}$$

## 2.5 Self Consistency

The Self-Consistency Workflow

With the established self-consistency problem of the effective potential and electron density, and the basic considerations above, we can formulate a general workflow for an actual DFT implementation. We start with an adequate initial guess for the electronic density, iterate the self-consistent field (SCF) loop until the density difference between the input and output of an iteration is sufficiently close to 0, and take the resulting final density as our ground-state density $n^{(0)}$, that minimizes the energy functional.

Charge Density Mixing and Loop Structure

To talk about the notion of "convergence", we need to quantify the difference between the density input and output of an iteration. It is straight-forwardly expressed as an appropriate $L_2$-norm of the density that enters an SCF loop iteration and the new density that is generated from it:

$$\mathrm{dist}\left(n_m^\mathrm{out}, n_m^\mathrm{in}\right) = \left\| n_m^\mathrm{out} - n_m^\mathrm{in} \right\| = \sqrt{\frac{1}{V}\int_V \left(n_m^\mathrm{out} - n_m^\mathrm{in}\right)^2 \mathrm{d}\boldsymbol{r}}. \tag{2.21}$$

We call this measure the distance between the input and output density. The exact form is determined by the setup of the system and the method used. Furthermore, the input density $n^{\text{in}}_{m+1}$ for the next iteration is determined by the choice of the mixing scheme. This can be written as a function $n^{\text{in}}_{m+1} = f(n^{\text{out}}_m, \{n^{\text{in}}_m\}, \alpha_{\text{mix}})$. It is usually dependent on a mixing parameter $\alpha_{\text{mix}}$, but the details vary. The cycle of calculation steps is repeated until the distance falls below a preset threshold $\varepsilon_{\text{SCF}}$, that will be referred to as the convergence parameter of the SCF loop. The resulting SCF scheme is shown in figure 2.2.

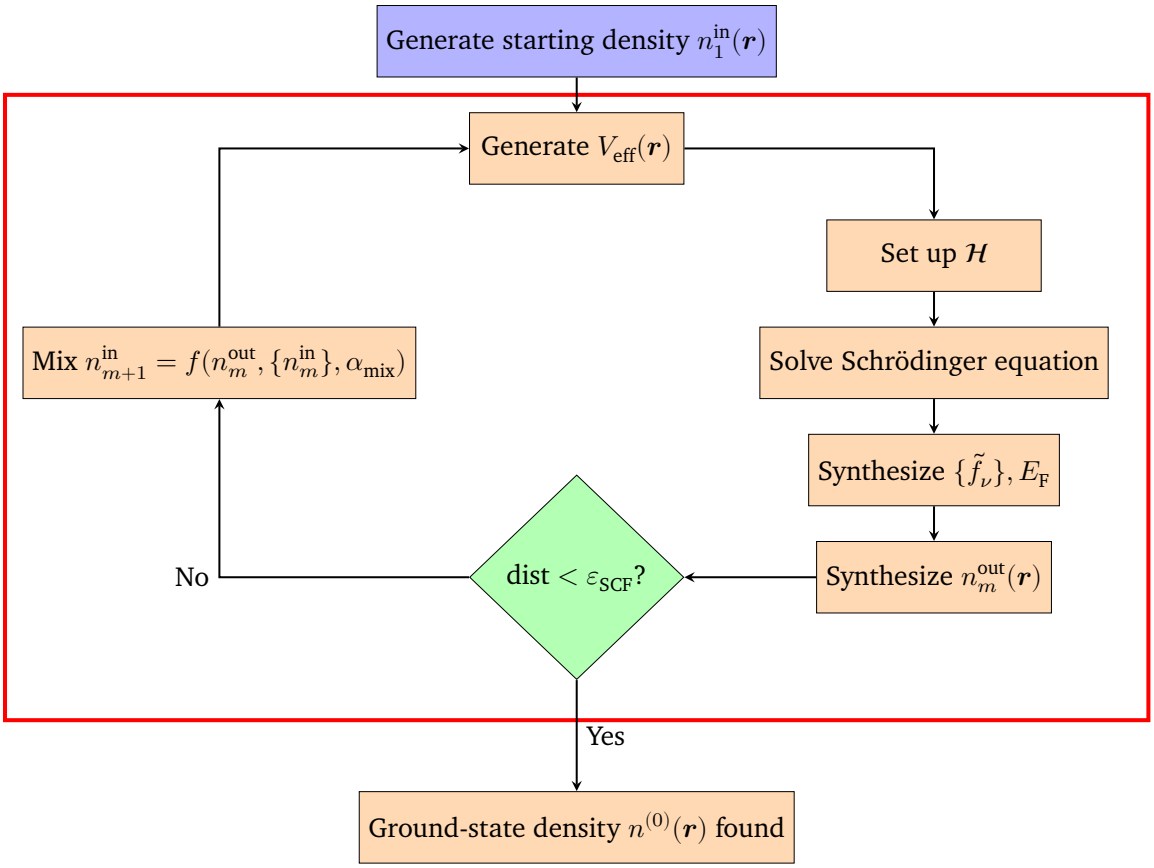



**Figure 2.2:** Sketch of the principle workflow in a non-specific DFT calculation. The red frame highlights the self-consistent field loop. Considering the $m$-th iteration, from an input density $n^{\text{in}}_m$, the effective potential $V_{\text{eff}}$ is generated and used to set up the Hamiltonian $\mathcal{H}$. The Schrödinger equation constituted by it is solved to get a set of eigenenergies $\{\varepsilon_\nu\}$ and wave functions $\{\psi_\nu\}$. The eigenenergies are used to determine the occupation numbers $\{\tilde{f}_\nu\}$ and the Fermi energy $E_{\text{F}}$. The wave functions and occupation numbers are used to construct the output electron density $n^{\text{out}}_m$. The input and output density of an iteration are compared by a distance function to determine, whether the calculation is converged. The loop is repeated as long as this is not the case.

### Mixing Schemes

In general, the mixing function can be separated into the input density and a functional $\mathcal{F}$ of the density, that converges to 0 as the density is converged. The function can be written as

$$f(n^{\text{out}}_m, n^{\text{in}}_m, \alpha_{\text{mix}}) = n^{\text{in}}_m + \alpha_{\text{mix}} \mathcal{F}_{\text{lin}}[n^{\text{out}}_m, n^{\text{in}}_m]. \tag{2.22}$$

The goal of the self-consistency procedure is to find the fixed point of this function. In the linear mixing scheme [126], the function

$$f(n_m^{\text{out}}, n_m^{\text{in}}, \alpha_{\text{mix}}) = \alpha_{\text{mix}} n_m^{\text{out}} + (1 - \alpha_{\text{mix}}) n_m^{\text{in}} = n_m^{\text{in}} + \alpha_{\text{mix}} \mathcal{F}_{\text{lin}}[n_m^{\text{out}}, n_m^{\text{in}}] \tag{2.23}$$

is very simple and depends only on the input and output density of the latest iteration. This method of mixing is (for suitably small mixing parameters) both very stable and very slow, as its convergence between iterations is bounded upwards by a constant. Other mixing schemes converge a lot more rapidly and have a bigger convergence radius. They do so by replacing the linear mixing functional $\mathcal{F}_{\text{lin}}$ by more elaborate terms. The resulting fixed point equation can be quite complicated, which is why the functional is usually linearized with respect to the input density. The linearization leads to Newton–Raphson methods, where consequently the inverse Jacobian $\mathcal{J}$ of the function needs to be taken into account. Their convergence behavior is quadratic instead of linear. This leads to a general form

$$f(n_m^{\text{out}}, n_m^{\text{in}}, \alpha_{\text{mix}}) = n_m^{\text{in}} - \mathcal{J}^{-1}[n_m^{\text{in}}]\mathcal{F}[n_m^{\text{in}}], \qquad \mathcal{J}[n_m^{\text{in}}] := \frac{\partial \mathcal{F}[n(\boldsymbol{r})]}{\partial n(\boldsymbol{r}')}|_{n_m^{\text{in}}}. \tag{2.24}$$

The computational cost of the Jacobian setup and inversion is unwieldy in practice, so Quasi-Newton methods have been developed, that approximate the differential form of the Jacobian by a difference quotient of $\mathcal{F}$ and $n$. The ramifications of dealing with this numerical construction lead to different methods, such as Broyden's approach [127, 128] or the related Anderson mixing scheme [129] which is used in this work. Due to the iterative nature of determining the Jacobian, Quasi-Newton methods involve the construction and usage of a mixing history. A comprehensive overview of different mixing methods and classes is given in [130].

## 2.6 Spin-Density Functional Theory

Spin-Polarization

When the limitation of spin-degenerate electrons is lifted and magnetism comes into play, we transition from DFT to spin-density functional theory (SDFT) [106]. In it, the wave functions becomes a two-component spinor of spin-up and -down components

$$\psi_\nu(\boldsymbol{r}) \longrightarrow \boldsymbol{\psi}_\nu(\boldsymbol{r}) = \begin{pmatrix} \psi_{\nu\uparrow}(\boldsymbol{r}) \\ \psi_{\nu\downarrow}(\boldsymbol{r}) \end{pmatrix}. \tag{2.25}$$

The total density and magnetization are written as a vector product over both spin-channels. In a general, non-collinear description this leads to a three-dimensional magnetization density vector, that incorporates the vector of Pauli matrices $\underline{\sigma}$ in its construction. They can be expressed as

$$n(\boldsymbol{r}) = \sum_\nu \tilde{f}_\nu \boldsymbol{\psi}_\nu^\dagger \cdot \boldsymbol{\psi}_\nu, \qquad \boldsymbol{m}(\boldsymbol{r}) = \sum_\nu \tilde{f}_\nu \boldsymbol{\psi}_\nu^\dagger \cdot \underline{\sigma} \cdot \boldsymbol{\psi}_\nu. \tag{2.26}$$

It is important to distinguish here between the two-dimensional spinors, the three-dimensional vector $\boldsymbol{m}$, and the three-dimensional vector of two-dimensional Pauli matrices $\underline{\sigma}$. In principle, the KS formalism can now be set up for a non-collinear system, under the condition, that appropriate xc functionals for the magnetization density can be formulated. This proves difficult in practice.

Collinear Magnetism

For a wide range of magnetic systems, such as (anti-)ferromagnets, a collinear description of the spin-polarized system suffices. It captures the physics well while lending itself better to the already established DFT formalism, as the construction of xc functionals with spin-up and spin-down densities is straightforward. It was initially established by Barth and Hedin in the form of the local spin-density approximation (LSDA) [106] and has since been extended to more elaborate classes of functionals as well. The calculatory effort roughly doubles with respect to a non spin-polarized run, because the KS equations need to be solved for both spin-channels separately, as they are decoupled, which gives us

$$\left(-\frac{1}{2}\nabla^2 + V_{\text{eff},\sigma}(\boldsymbol{r})\right)\psi_{\nu\sigma}(\boldsymbol{r}) = \varepsilon_{\nu\sigma}\psi_{\nu\sigma}(\boldsymbol{r}). \tag{2.27}$$

This also defines the independent spin-densities, that are calculated with a spin-dependent occupation factor. It is akin to the factors in equations (2.16)/(2.17) and the subsequent considerations, except for the omission of the spin-degeneracy factor of 2. We find for the spin-dependent density

$$n(\boldsymbol{r}) = \sum_{\nu\sigma} \tilde{f}_{\nu\sigma}|\psi_{\nu\sigma}(\boldsymbol{r})|^2 \equiv \sum_{\sigma} n_\sigma(\boldsymbol{r}). \tag{2.28}$$

The construction of the spin-dependent effective potential also deviates from the initial formulation. While the Coulomb potential construction remains the same, as only the total density enters, the xc part is spin-polarized. This is expressed as a functional derivative of the xc energy with respect to only the density of one spin-channel. The effective potential is

$$V_{\text{eff}}(\boldsymbol{r}) = V_{\text{C}}(\boldsymbol{r}) + V_{\text{xc},\sigma}(\boldsymbol{r}), \tag{2.29}$$

with the xc part

$$V_{\text{xc},\sigma}(\boldsymbol{r}) = \frac{\delta E_{\text{xc}}[n_\uparrow, n_\downarrow]}{\delta n_\sigma(\boldsymbol{r})} = \varepsilon_{\text{xc}}[n_\uparrow, n_\downarrow](\boldsymbol{r}) + n_\sigma(\boldsymbol{r})\frac{\delta \varepsilon_{\text{xc}}[n_\uparrow, n_\downarrow](\boldsymbol{r})}{\delta n_\sigma(\boldsymbol{r})}. \tag{2.30}$$

Lastly, the energy and entropy terms need to be modified to account for the spin-polarized effective potential, eigenenergies and occupation numbers. The generalization is straightforward and yields

$$\begin{aligned} E_{\text{tot}} = \sum_{\nu\sigma} \tilde{f}_{\nu\sigma}\varepsilon_{\nu\sigma} - \sum_{\sigma}\int n_\sigma(\boldsymbol{r})V_{\text{eff},\sigma}(\boldsymbol{r})\mathrm{d}\boldsymbol{r} - TS \\ + \int n(\boldsymbol{r})\left[\frac{1}{2}V_{\text{H}}(\boldsymbol{r}) + V_{\text{ext}}(\boldsymbol{r}) + \varepsilon_{\text{xc}}[n_\uparrow, n_\downarrow](\boldsymbol{r})\right]\mathrm{d}\boldsymbol{r} + E_{\text{ii}}, \end{aligned} \tag{2.31}$$

$$S = -k_{\text{B}}\sum_{\nu\sigma}\left[\tilde{f}_{\nu\sigma}\ln\left(\tilde{f}_{\nu\sigma}\right) + \left(f_{\nu\sigma} - \tilde{f}_{\nu\sigma}\right)\ln\left(f_{\nu\sigma} - \tilde{f}_{\nu\sigma}\right)\right]. \tag{2.32}$$

As the SCF calculations for both spin-channels are analogous to each other and decoupled, the spin index will be omitted for the rest of this work. We will also limit ourselves to this collinear restriction for the calculations involved and leave the extension to non-collinear magnetism as a future task.

## 2.7 Extensions to and Generalizations of DFT

The broad applicability and success of DFT led to a large group of extensions to the original theory. Furthermore, there are many reformulations and generalizations applying the KS formalism to entirely different classes of problems in electronic structure. We already tackled the extension from spin-degenerate to spin-polarized systems and will give a brief overview of some extensions and variations that have been investigated.

Extensions to the Existing Formalism

To describe the electronic structure of complex magnetic systems, the collinear formulation becomes insufficient. The additional formalism needed to deal with non-collinear (NOCO) magnetism [131] is straight-forward for most of the theory, but there are two main points that need extra attention. On the one hand, the two spin-channels are no longer independent from each other, but coupled in the KS equation, that now replaces the spin-polarized potential by a $2 \times 2$ potential matrix and the spin-polarized wave function by a spinor. This greatly increases the computational effort. On the other hand, the need of a functional defined in terms of the magnetization density arises. As mentioned before, this proves difficult, and a frequently used method to bypass these fully non-collinear functionals is the formulation by Kubler *et al.* [132], that uses localized rotations of the magnetization density to a collinear frame and reuses the collinear formalism for the xc potential. The spin-polarized potentials are then rotated back into the global frame to gain a three-dimensional xc magnetic field. Another spin-dependent effect is spin-orbit coupling (SOC), that becomes relevant for heavy elements like bismuth and lead. This can be either directly included to the KS equation and will give a contribution to the Hamiltonian matrix (first variation SOC) or treated as a perturbation to the established KS system (2nd variation SOC) [133, 134]. The first method introduces off-diagonal elements to the Hamiltonian in the space of spinors and is thus best described in a fully non-collinear setup to begin with. Finally, a well-established method to deal with strongly-correlated systems is DFT+U [135]. It captures the orbital dependence of the Coulomb and exchange interactions by modeling them with a parameter $U$ akin to a Hubbard model [136]. This can be used to improve the description of Mott insulators and rare-earth metal compounds both in their ground-state properties, as well as excited-state phenomena. Finally, we want to once again highlight the possibility of using more elaborate functional classes, as discussed in section 2.3, especially with respect to the implementation of hybrid functionals that mix the exact Hartree–Fock exchange with conventional DFT functionals.

Various DFT generalizations

Without much detail, we want to mention that modifications to the KS-DFT formalism can lead to exciting new frameworks and highlight some of them. Most closely related to the topic of this thesis is superconducting density-functional theory (SCDFT) [137–140], that is related to the electron-phonon interaction that can also be calculated by DFPT. Other theories include, but are not limited to:

- Reduced density-matrix functional theory (RDMFT) based on the work of Gilbert [141]
- Current-density functional theory (CDFT) [142], that tries to include magnetism even more holistically than NOCO, by constructing a full vector potential $\boldsymbol{A}_{\text{eff}}$ alongside the scalar potential
- Constrained density-functional theory (cDFT) [143], that builds on the established formalism while extending it to the lowest states compatible with arbitrary constraints

- Time-dependent density-functional theory (TDDFT) [144], where the time-dependence of the states is not dropped but instead properly evaluated

A neat overview is also given in [36]. However, none of these generalizations come into play in this work, hence we finish this brief overview as is.

Chapter 3

# Phonons from Electronic Structure Methods


3.1 The Periodic Lattice . . . . . 17
3.2 Phonons in the Harmonic Approximation . . . . . 18
3.3 Frozen Phonon Calculations . . . . . 21
3.4 The Finite-Displacement Method . . . . . 22
3.5 Density-Functional Perturbation Theory . . . . . 23


The Central Phonon Quantities

In the introduction, the many applications of phonons in solid state physics were highlighted. The multitude of related quantities is, at the lowest level, connected to the phonon dispersion and the phononic density of states. In the following chapter, the general workflow to gain knowledge about both from an electronic structure method is laid out without the specifics that stem from the choice of a basis set.

## 3.1 The Periodic Lattice

Crystals and the Bloch Theorem

Up to this point, our description of the solid-state system was very unspecific. Applying the theory to enable actual calculations requires a set of boundary conditions that set the stage for the development of electronic structure software. The first of these conditions is our restriction to the description of periodic crystals, *i.e.* solid-state systems with a defined pattern of atoms at specific positions, that is periodically repeated in space. We call this template of atoms the unit cell and the resulting system the lattice. The lattice vectors that translate between different copies of the unit cell are integer multiples of the so-called primitive vectors. The vectors form a three-dimensional matrix, referred to as the Bravais matrix

$$\underline{A} = \left(\boldsymbol{a}_1, \boldsymbol{a}_2, \boldsymbol{a}_3\right). \tag{3.1}$$

In the DFT formalism, where the atoms constitute the external potential, this can be expressed by a translation symmetry with respect to the lattice vectors $\boldsymbol{R} = \sum_{i=1}^{3} n_i \boldsymbol{a}_i$ with $n_i \in \mathbb{Z}$:

$$V_{\text{ext}}(\boldsymbol{r} + \boldsymbol{R}) = V_{\text{ext}}(\boldsymbol{r}). \tag{3.2}$$

For such a system it can be shown, that the Hamiltonian commutes with the translation operator of the lattice vectors. This inadvertently leads to a fixed behavior of the corresponding wave functions under translation, namely the wave functions at two points in space linked by a lattice vector are related by a phase

$$\psi(\boldsymbol{r}+\boldsymbol{R}) = \mathrm{e}^{\mathrm{i}\boldsymbol{k}\cdot\boldsymbol{R}}\psi(\boldsymbol{r}). \tag{3.3}$$

This is a direct consequence of the Bloch theorem [145], that states the wave functions for a periodic lattice are separable into a product of lattice-periodic functions $u(\boldsymbol{r})$ and a plane wave with a wave vector $\boldsymbol{k}$. It is referred to as the crystal momentum. Furthermore, due to the translation symmetry in reciprocal space, we can limit any calculation to momenta $\boldsymbol{k}$ in the first Brillouin zone (BZ) of the crystal. It is defined in terms of reciprocal lattice vectors $\boldsymbol{G} = \sum_{i=1}^{3} n_i \boldsymbol{b}_i$ with $n_i \in \mathbb{Z}$. As the scalar product of an arbitrary lattice vector and reciprocal lattice vector $\boldsymbol{G}$ is equal to $2\pi$, the full information is contained in a reciprocal unit cell with extent $n_i \in (-0.5, 0.5]$. The resulting Bloch functions take on the specific form

$$\psi_{\boldsymbol{k}\nu}(\boldsymbol{r}) = \mathrm{e}^{\mathrm{i}\boldsymbol{k}\cdot\boldsymbol{r}} u_{\boldsymbol{k}\nu}(\boldsymbol{r}), \tag{3.4}$$

with

$$u_{\boldsymbol{k}\nu}(\boldsymbol{r}+\boldsymbol{R}) = u_{\boldsymbol{k}\nu}(\boldsymbol{r}). \tag{3.5}$$

Consequently, the different crystal momenta constitute a second index to the already state-dependent wave functions of the system. This carries on to many different quantities in the system, *e.g.* the occupation numbers

$$\tilde{f}_\nu \longrightarrow \tilde{f}_{\boldsymbol{k}\nu} \tag{3.6}$$

previously discussed in section 2.4. We use the tilde in above the symbol to differentiate between the weight of a particular k-point $f_{\boldsymbol{k}}$ and the potentially fractional occupation number. While the index $\nu$ previously contained all information about a specific state, it now refers to many states at different k-point. Those states form a band across the BZ, which is why it is also referred to as the band index in electronic structure methods.

## 3.2 Phonons in the Harmonic Approximation

Energy Landscape of the Solid-State System

The appearance of a phonon in a solid state system corresponds to a vibrational excitation in its energy landscape. That means the initial system, that assumes minimal energy in a relaxed ground state, will be perturbed and the energy will be shifted to a higher value. This can be expressed as a small, but finite displacement of the atoms from their equilibrium positions. We express this perturbation as a set of displacements $\{\boldsymbol{w}\} = \{\boldsymbol{w}_{\alpha\boldsymbol{R}}\}_{\alpha\boldsymbol{R}=1,\ldots,N_{\text{ion}}N_{\text{u.c.}}}$ affecting each of the $N_{\text{ion}}$ atoms $\alpha$ in each of the $N_{\text{u.c.}} \longrightarrow \infty$ unit cells $\boldsymbol{R}$. We use the fact, that (i) differentiating the energy by these displacements directly corresponds to differentiating by the atomic positions and (ii) the first order vanishes, since the system is in a relaxed state and no forces act on the atoms. We can then write the perturbed energy

$$\begin{aligned} E_{\text{tot}} &= E_{\text{tot}}^{(0)} + \cancel{E_{\text{tot}}^{(1)}} + \frac{1}{2}E_{\text{tot}}^{(2)} + \ldots \\ &= E_{\text{tot}}^{(0)} + \frac{1}{2}\sum_{\beta\boldsymbol{R}'j,\alpha\boldsymbol{R}i} w_{\beta\boldsymbol{R}'j}\Phi_{\beta\boldsymbol{R}'j,\alpha\boldsymbol{R}i}w_{\alpha\boldsymbol{R}i} + \ldots \end{aligned} \tag{3.7}$$

as a Taylor series in the displacements. In this, we implicitly define the force constant matrix $\underline{\Phi}$ as the Hessian of the total energy with respect to the set of displacements. The subscripts $i, j$ indicate the Cartesian directions of the displacement vectors (leading to a size of $3N_{\text{ion}}N_{\text{u.c.}} \times 3N_{\text{ion}}N_{\text{u.c.}}$) and its matrix elements can be written as

$$\Phi_{\beta \boldsymbol{R}' j, \alpha \boldsymbol{R} i} := \frac{\partial^2 E_{\text{tot}}}{\partial w_{\beta \boldsymbol{R}' j} \partial w_{\alpha \boldsymbol{R} i}}|_{\{\boldsymbol{w}\}=\boldsymbol{0}} = \frac{\partial^2 E_{\text{tot}}}{\partial \tau_{\beta \boldsymbol{R}' j} \partial \tau_{\alpha \boldsymbol{R} i}}. \tag{3.8}$$

The force constant matrix (and its Fourier transform) are of central importance in the description of phonon physics, which will be highlighted in the next subsection.

Phononic Eigenvalue Problem

We are interested in the response of the lattice to a vibrational perturbation. If we cut of the energy after the second order, the perturbation gives us a quadratic energy dependence in the atomic displacements. This is called the harmonic approximation and naturally leads to a harmonic oscillator as the differential equation that governs the movement of the atoms. The equation for the time evolution of a specific displacement reads

$$\tilde{M}_\beta \frac{\partial^2}{\partial t^2} w_{\beta \boldsymbol{R}' j}(t) = -\sum_{\alpha \boldsymbol{R} i} \Phi_{\beta \boldsymbol{R}' j, \alpha \boldsymbol{R} i} w_{\alpha \boldsymbol{R} i}(t), \tag{3.9}$$

with $\tilde{M}_\beta$, the ionic mass expressed in multiples of the electron mass $m_e$. If we assume a perturbation, that differs between cells only by a phase factor, this leads to a plane wave Ansatz

$$w_{\beta \boldsymbol{R}' j}(t) = \frac{1}{\sqrt{\tilde{M}_\beta}} Q_{\beta j, \boldsymbol{q}} \mathrm{e}^{\mathrm{i}(\boldsymbol{q}\cdot(\boldsymbol{\tau}_\beta + \boldsymbol{R}') - \omega_{\boldsymbol{q}} t)} + \text{c.c.}\,. \tag{3.10}$$

with a complex polarization vector $\boldsymbol{Q}_{\beta, \boldsymbol{q}}$. We identify this as a monochromatic phonon, *i.e.* a plane wave with a single wave vector $\boldsymbol{q}$, that determines both the oscillation amplitude and propagation direction. The perturbation affects each atom in the lattice and the quantity of interest is the oscillation frequency $\omega_{\boldsymbol{q}}$ with respect to the wave vector, *i.e.* the phonon dispersion relation. For this we only need to look at the positive conjugate part and can eliminate the time dependence from the equation. Additionally using the translation symmetry of the lattice for shifts by a lattice vector ($\Phi_{\beta \boldsymbol{R}' j, \alpha \boldsymbol{R} i} = \Phi_{\beta(\boldsymbol{R}' - \boldsymbol{R}) j, \alpha \boldsymbol{0} i}$) we can derive:

$$\begin{aligned}
\sqrt{\tilde{M}_\beta}(-\omega_{\boldsymbol{q}}^2) Q_{\beta j, \boldsymbol{q}} \mathrm{e}^{\mathrm{i}\boldsymbol{q}\cdot(\boldsymbol{\tau}_\beta + \boldsymbol{R}')} &= -\sum_{\alpha \boldsymbol{R} i} \Phi_{\beta \boldsymbol{R}' j, \alpha \boldsymbol{R} i} \frac{1}{\sqrt{\tilde{M}_\alpha}} Q_{\alpha i, \boldsymbol{q}} \mathrm{e}^{\mathrm{i}\boldsymbol{q}\cdot(\boldsymbol{\tau}_\alpha + \boldsymbol{R})} \\
\Leftrightarrow (-\omega_{\boldsymbol{q}}^2) Q_{\beta j, \boldsymbol{q}} &= -\sum_{\alpha \boldsymbol{R} i} \mathrm{e}^{\mathrm{i}\boldsymbol{q}\cdot(\boldsymbol{\tau}_\alpha - \boldsymbol{\tau}_\beta)} \Phi_{\beta(\boldsymbol{R}' - \boldsymbol{R}) j, \alpha \boldsymbol{0} i} \frac{1}{\sqrt{\tilde{M}_\beta \tilde{M}_\alpha}} Q_{\alpha i, \boldsymbol{q}} \mathrm{e}^{-\mathrm{i}\boldsymbol{q}\cdot(\boldsymbol{R}' - \boldsymbol{R})} \\
\Leftrightarrow \omega_{\boldsymbol{q}}^2 Q_{\beta j, \boldsymbol{q}} &= \sum_{\alpha \boldsymbol{R}'' i} \mathrm{e}^{\mathrm{i}\boldsymbol{q}\cdot(\boldsymbol{\tau}_\alpha - \boldsymbol{\tau}_\beta)} \Phi_{\beta \boldsymbol{R}'' j, \alpha \boldsymbol{0} i} \frac{1}{\sqrt{\tilde{M}_\beta \tilde{M}_\alpha}} Q_{\alpha i, \boldsymbol{q}} \mathrm{e}^{-\mathrm{i}\boldsymbol{q}\cdot\boldsymbol{R}''} \\
\Leftrightarrow \omega_{\boldsymbol{q}}^2 \boldsymbol{Q}_{\boldsymbol{q}} &= \underline{D}(\boldsymbol{q}) \cdot \boldsymbol{Q}_{\boldsymbol{q}}
\end{aligned} \tag{3.11}$$

Through the introduction of the $3N_{\text{ion}}$-dimensional vector $\boldsymbol{Q}_{\boldsymbol{q}}$, we implicitly defined the dynamical matrix $\underline{D}$ as the mass-normalized Fourier transform of the force constant matrix. Finding the phonon dispersion directly corresponds to solving the eigenvalue problem of the dynamical matrix for each wave vector $\boldsymbol{q}$ in question. As the dynamical matrix is Hermitian,

the eigenvalues $\omega_{\boldsymbol{q}}^2$ are real-valued and the frequencies $\omega_{\boldsymbol{q}}$ will consequently be either real-valued or pure imaginary numbers. In the latter case, we speak of instabilities in the phonon dispersion, as they do not correspond to oscillations but to exponentially decaying so-called soft modes. They indicate, that the system is not in its ground state and the atomic positions have to be relaxed according to the direction and periodicity of the phonon mode.

Symmetry Considerations

Due to the dependence of the dynamical matrix on all atoms in the unit cell displaced in all three Cartesian directions, the computational demand quickly becomes large for a naive implementation. To at least partially remedy this, the symmetry of the system can be taken into account, to gain components of the force constant or dynamical matrix by rotating them from a representative calculation instead of directly calculating each one [146]. The first premise is of course, that the translation symmetry holds, which was already used in deriving the dynamical matrix. On top of that, we can look at symmetries that map certain atoms onto each other. If a transformation $\underline{S}$ can be used to map an atom $\alpha'$ onto $\alpha$ (and consequently $\beta'$ onto $\beta$ as well) by $\underline{S} \cdot \boldsymbol{\tau}_{\alpha'} = \boldsymbol{\tau}_{\alpha}$, the $3 \times 3$ part $\underline{\Phi}_{\beta \boldsymbol{R} j, \alpha \boldsymbol{0} i}$ of the force constant matrix associated with this atom obeys

$$\underline{\Phi}_{\beta' \boldsymbol{R}, \alpha' \boldsymbol{0}} = \underline{S}\, \underline{\Phi}_{\underline{S}(\beta' \boldsymbol{R}), \alpha \boldsymbol{0}}\, \underline{S}^T. \tag{3.12}$$

From this starting point, we can also look at the behavior of the dynamical matrix under symmetry transformation. If we define $\boldsymbol{p} = \underline{S} \cdot \boldsymbol{q}$, some quick theoretical handiwork proves

$$\underline{D}_{\beta', \alpha'}(\boldsymbol{q}) = \mathrm{e}^{\mathrm{i}\boldsymbol{q} \cdot (\boldsymbol{\tau}_{\alpha'} - \boldsymbol{\tau}_{\beta'})} \mathrm{e}^{-\mathrm{i}\boldsymbol{p} \cdot (\boldsymbol{\tau}_{\alpha} - \boldsymbol{\tau}_{\beta})}\, \underline{S}\, \underline{D}_{\beta, \alpha}(\boldsymbol{p})\, \underline{S}^T. \tag{3.13}$$

Hence, the rotation does not only affect the dynamical matrix itself, but also to which wave vector it is associated. This can be used to *e.g.* calculate the dynamical matrix on a full set of wave vectors sampling the Brillouin zone from only a considerably smaller set of representatives. Additionally, a recent implementation effort was using this formula for symmetries that leave the q-point unchanged. For such symmetries, the equation can be used to reduce the necessary calculations and drastically reduce the runtime. As the results of this thesis are not produced with this work in progress implementation in effect, we only highlight the necessary formalism and workflow in appendix A.

For the sake of completeness, the transformation behavior of forces in a system displaced from equilibrium should also be considered. It naturally transforms as a vector instead of a matrix, as it is one-dimensional instead of two-dimensional. It holds

$$\boldsymbol{F}_{\beta'} = \underline{S} \cdot \boldsymbol{F}_{\beta}. \tag{3.14}$$

Which of these symmetry relations becomes relevant depends on the method used to calculate the phonon spectrum. This will be highlighted as the respective approaches are discussed. A much more thorough discussion of symmetries and their application to normal vibrations of a crystal can be found in reference [147]. Another general property mandated by the system's symmetry is the number of phonon modes. The DM is a $3N_{\text{ion}} \times 3N_{\text{ion}}$ matrix, so it has $3N_{\text{ion}}$ possibly degenerate eigenvalues. As the sum of all the forces in the system has too vanish, as to not produce a center of mass motion of the infinite crystal, the so-called acoustic sum rule arises: The first three phonon frequencies must vanish. The branches starting at $0$ are called the acoustic branches of the spectrum, as they usually lie in an energy range that can be excited acoustically and they are linked to the speed of sound in a material. The other $3(N_{\text{ion}} - 1)$ modes are referred to as optical modes, as they are more in the energy range of optical excitations.

## 3.3 Frozen Phonon Calculations

The Frozen Phonon

To arrive at a workflow for phonon calculations, we need to define how exactly our phonon interacts with the lattice. A common approach is the frozen phonon method, where a phonon with wave vector $\boldsymbol{q}$ is directly overlayed with the system and displaces each atom accordingly. This can be written in a form with displacements as used in equation (3.7), that are now associated with a wave vector $\boldsymbol{q}$ and take the specific form

$$\begin{aligned} \boldsymbol{w}_{\alpha\boldsymbol{R},\boldsymbol{q}} &= \frac{1}{\sqrt{\tilde{M}_\alpha}} \boldsymbol{Q}_{\alpha,\boldsymbol{q}} \mathrm{e}^{\mathrm{i}\boldsymbol{q}\cdot(\boldsymbol{\tau}_\alpha+\boldsymbol{R})} + \text{c.c.} \\ &= \boldsymbol{w}^{+}_{\alpha\boldsymbol{R},\boldsymbol{q}} + \boldsymbol{w}^{-}_{\alpha\boldsymbol{R},\boldsymbol{q}}. \end{aligned} \tag{3.15}$$

With this definition, we can write down the Taylor series of a general quantity $X$ in our solid-state calculation. This can range from the density $n(\boldsymbol{r})$, to the potential or its constituents or total energy like in equation (3.7). This yields

$$\begin{aligned} X(\boldsymbol{q}) &= X^{(0)} + X^{(1)}(\boldsymbol{q}) + \frac{1}{2} X^{(2)}(\boldsymbol{q}) + \dots \\ &= X^{(0)} + \sum_{\alpha\boldsymbol{R}i\pm} \frac{\partial X}{\partial \tau_{\alpha\boldsymbol{R}i}} w^{\pm}_{\alpha\boldsymbol{R}i,\boldsymbol{q}} + \frac{1}{2} \sum_{\substack{\beta\boldsymbol{R}'j\pm' \\ \alpha\boldsymbol{R}i\pm}} w^{\pm'}_{\beta\boldsymbol{R}'j,\boldsymbol{q}} \frac{\partial^2 X}{\partial \tau_{\beta\boldsymbol{R}'j} \partial \tau_{\alpha\boldsymbol{R}i}} w^{\pm}_{\alpha\boldsymbol{R}i,\boldsymbol{q}} + \dots . \end{aligned} \tag{3.16}$$

This equation is sufficient if we want to look at a system, where the atoms are actually displaced by a finite amount and a supercell setup is used to cover the summation over $\boldsymbol{R}$. Another way to look at the response of the system to a variation is to evaluate the sum first and look at the Fourier transformed quantities

$$X^{(1)\alpha i\pm} = \sum_{\boldsymbol{R}} \mathrm{e}^{\pm\mathrm{i}\boldsymbol{q}\cdot\boldsymbol{R}} X^{(1)\alpha\boldsymbol{R}i} \equiv \sum_{\boldsymbol{R}} \mathrm{e}^{\pm\mathrm{i}\boldsymbol{q}\cdot\boldsymbol{R}} \frac{\partial X}{\partial \tau_{\alpha\boldsymbol{R}i}} \tag{3.17}$$

and

$$X^{(2)\beta j\pm'\alpha i\pm} = \sum_{\boldsymbol{R}'\boldsymbol{R}} \mathrm{e}^{\mathrm{i}\boldsymbol{q}\cdot(\pm\boldsymbol{R}\pm'\boldsymbol{R}')} X^{(2)\beta\boldsymbol{R}'j\alpha\boldsymbol{R}i} \equiv \sum_{\boldsymbol{R}'\boldsymbol{R}} \mathrm{e}^{\mathrm{i}\boldsymbol{q}\cdot(\pm\boldsymbol{R}\pm'\boldsymbol{R}')} \frac{\partial^2 X}{\partial \tau_{\beta\boldsymbol{R}'j} \partial \tau_{\alpha\boldsymbol{R}i}} \tag{3.18}$$

instead. The response of the system then depends only on these newly defined quantities, the atomic masses, and the finite polarization vectors $Q^{\pm}_{\alpha i,\boldsymbol{q}}$ (where $(-)$ corresponds to the complex conjugate of $(+)$ as above). We write this as

$$\begin{aligned} X(\boldsymbol{q}) = X^{(0)} &+ \sum_{\alpha i\pm} \frac{\mathrm{e}^{\pm\mathrm{i}\boldsymbol{q}\cdot\boldsymbol{\tau}_\alpha}}{\sqrt{\tilde{M}_\alpha}} X^{(1)\alpha i\pm} Q^{\pm}_{\alpha i,\boldsymbol{q}} \\ &+ \frac{1}{2} \sum_{\substack{\beta j\pm' \\ \alpha i\pm}} Q^{\pm'}_{\beta j,\boldsymbol{q}} \frac{\mathrm{e}^{\mathrm{i}\boldsymbol{q}\cdot(\pm'\tau_\beta\pm\tau_\alpha)}}{\sqrt{\tilde{M}_\beta \tilde{M}_\alpha}} X^{(2)\beta j\pm'\alpha i\pm} Q^{\pm}_{\alpha i,\boldsymbol{q}} + \dots . \end{aligned} \tag{3.19}$$

With this equation in mind, when we look at the total energy explicitly, we find a direct correspondence between the force constant and dynamical matrices and the newly defined

second order term

$$E_{\text{tot}}^{(2)\beta j-\alpha i+} = \sum_{\boldsymbol{R}'\boldsymbol{R}} \mathrm{e}^{-\mathrm{i}\boldsymbol{q}\cdot(\boldsymbol{R}'-\boldsymbol{R})} \Phi_{\beta\boldsymbol{R}'j,\alpha\boldsymbol{R}i} = \sum_{\boldsymbol{R}''} \mathrm{e}^{-\mathrm{i}\boldsymbol{q}\cdot\boldsymbol{R}''} \Phi_{\beta\boldsymbol{R}''j,\alpha\boldsymbol{0}i} \tag{3.20}$$

$$\Leftrightarrow D_{\beta j,\alpha i} = \frac{\mathrm{e}^{\mathrm{i}\boldsymbol{q}\cdot(\boldsymbol{\tau}_\alpha-\boldsymbol{\tau}_\beta)}}{\sqrt{\tilde{M}_\beta \tilde{M}_\alpha}} E_{\text{tot}}^{(2)\beta j-\alpha i+} \tag{3.21}$$

The second lattice vector sum technically gives an additional factor of $N_{\text{u.c.}}$, that is omitted as $N_{\text{u.c.}} \longrightarrow \infty$ and we want to look at the energy derivatives per unit cell. It can easily be shown from their definition, that the Fourier transformed quantities are no longer lattice periodic, where the ground-state quantities have been, but instead carry an additional phase dependent on the wave vector of the phonon. The same holds for the wave functions, that are Bloch waves to a specific $\boldsymbol{k}$ in the ground state. This can be summarized as

$$X^{(1)\alpha i\pm}(\boldsymbol{r}+\boldsymbol{R}) = \mathrm{e}^{\pm\mathrm{i}\boldsymbol{q}\cdot\boldsymbol{R}} X^{(1)\alpha i\pm}(\boldsymbol{r}), \tag{3.22}$$

$$X^{(2)\beta j\pm'\alpha i\pm}(\boldsymbol{r}+\boldsymbol{R}) = \mathrm{e}^{(\pm'\pm)\mathrm{i}\boldsymbol{q}\cdot\boldsymbol{R}} X^{(2)\beta j\pm'\alpha i\pm}(\boldsymbol{r}), \tag{3.23}$$

$$\psi_{\boldsymbol{k}\nu}^{(1)\alpha i\pm}(\boldsymbol{r}+\boldsymbol{R}) = \mathrm{e}^{\mathrm{i}(\boldsymbol{k}\pm\boldsymbol{q})\cdot\boldsymbol{R}} \psi_{\boldsymbol{k}\nu}^{(1)\alpha i\pm}(\boldsymbol{r}). \tag{3.24}$$

Practically speaking, each lattice periodic function becomes a Bloch wave with a Bloch vector $\boldsymbol{q}$ and each Bloch wave with vector $\boldsymbol{k}$ has it altered by $\boldsymbol{q}$ as well; the perturbation from a phonon carries a finite momentum change into the system. Another thing to note, is that the Fourier transformed first order quantities and their complex conjugates are related by the interchange of the sign of the phase $\pm$. This also follows from their definition and will be of use later. We write

$$X^{(1)\alpha i\pm *}(\boldsymbol{r}) = X^{(1)\alpha i\mp}(\boldsymbol{r}). \tag{3.25}$$

We have now established the central quantities of phonon calculations both in real (lattice vector) space, as well as in reciprocal space. Now, we will look at numerical methods that can yield the necessary quantities for the respective approach.

## 3.4 The Finite-Displacement Method

Numerical Second Derivative

If we stick to the real-space description of the second order energy perturbation, our quantity of interest is the force constant matrix. Computing it usually makes use of the finite displacement (FD) method. The first order energy responses (*i.e.* the forces on the atoms) are calculated analytically, and the second order derivative is evaluated as the numerical derivative between the forces of a lattice with a displaced atom and the equilibrium one. Using the definition of the Hellmann–Feynman forces, this gives us

$$E_{\text{tot}}^{(1)\alpha\boldsymbol{R}i} = \int n(\boldsymbol{r}) V_{\text{ext}}^{(1)\alpha\boldsymbol{R}i}(\boldsymbol{r})\mathrm{d}\boldsymbol{r} + E_{\text{ii}}^{(1)\alpha\boldsymbol{R}i} = -F_{\alpha\boldsymbol{R}i}. \tag{3.26}$$

It can be derived from equation (2.13) by straight-forward differentiation and evaluation of the eigenenergy derivative that will emerge, as shown *e.g.* in [92]. The derivative of the occupation numbers cancels out with the entropy term, keeping the first order energy derivative variational in the unperturbed quantities [92, 125]. The resulting formula is in

a sense complete for any approach, where we do not have any dependence of the basis on the atomic positions. Such a dependence exists for the FLAPW method, however, and will be discussed in section 4.1. The numerical differentiation for the second order response reads

$$E_{\text{tot}}^{(2)\beta\boldsymbol{R}'j\alpha\boldsymbol{R}i} \approx -\frac{F_{\alpha\boldsymbol{R}i}[\tau_{\beta\boldsymbol{R}'j} + w_{\beta\boldsymbol{R}'j}] - F_{\alpha\boldsymbol{R}i}[\tau_{\beta\boldsymbol{R}'j}]}{w_{\beta\boldsymbol{R}'j}}. \tag{3.27}$$

This derivative delivers the correct quadratic energy dependence in second order, provided that the finite displacement is small as compared to the distance between neighboring atoms. Otherwise, anharmonic effects will be taken into account as well, which makes the description as a harmonic oscillator invalid.

Supercells

For the finite displacement method to deliver accurate results, we need to think about the construction of supercells. There are two aspects: On the one hand, the force on an atom, as the result of shifting one in another unit cell, will diminish with distance. A supercell for a phonon calculation must be at least big enough, so that this force is sufficiently decayed in relation to the scale of phononic energy differences. On the other hand, the frozen phonon approach will be displacing atoms in different cells by different amounts to imprint the wave form onto the lattice. To correctly describe this, the extent of the supercell needs to be at least big enough, that a full period of oscillation fits into it, *i.e.* $1 = \boldsymbol{q} \cdot \boldsymbol{R}$.

Phonopy

In practice, the second of these requirements is relaxed to a certain extent. For the calculations in this work, we make use of the `phonopy` code [148–150]. The package has interfaces to several popular DFT codes and can, in theory, be interfaced to any electronic structure software, that provides structural input and accurate forces. We programmed a `FLEUR` [90, 91] interface for it, to be able to accurately benchmark the results of our own phonon calculations against those from `phonopy`. From a basic unit cell input and information on the desired supercell, it will generate the corresponding supercell input. It is broken down to the bare minimum of necessary displacements according to the symmetry considerations in section 3.2. We can feed the input back into `FLEUR` to calculate the forces induced by the atomic displacement. Once this is done for each displacement, `phonopy` can read the force data files to generate the force constant matrix. From there, several thermodynamic quantities can be accessed. For our purposes, it is most important that the phonon dispersion can be interpolated from the force constant matrix by Fourier transform.

## 3.5 Density-Functional Perturbation Theory

Analytical Second Derivative

While the phonon spectra in an FD approach are a necessary benchmark and a reliable way to gain insight about the vibrational properties of a system, the main focus of this work is the complementary method of density-functional perturbation theory (DFPT) [43–47]. It distinguishes itself from FD in the way we investigate the second order energy derivative. Whereas it was half-analytical, half-numerical before, we now derive an analytic expression for the second order as well. Using the notation we established in section 3.3 and applying the derivative in a second atom to equation (3.26) yields

$$E_{\text{tot}}^{(2)\beta\boldsymbol{R}'j\alpha\boldsymbol{R}i} = \int \left[ n^{(1)\beta\boldsymbol{R}'j}(\boldsymbol{r}) V_{\text{ext}}^{(1)\alpha\boldsymbol{R}i}(\boldsymbol{r}) + n(\boldsymbol{r}) V_{\text{ext}}^{(2)\beta\boldsymbol{R}'j\alpha\boldsymbol{R}i}(\boldsymbol{r}) \right] \mathrm{d}\boldsymbol{r} + E_{\text{ii}}^{(2)\beta\boldsymbol{R}'j\alpha\boldsymbol{R}i} \tag{3.28}$$

or in the subsequent notation with Fourier transformed quantities

$$E_{\text{tot}}^{(2)\beta j-\alpha i+} = \int_{\Omega} \left[ n^{(1)\beta j-}(\boldsymbol{r}) V_{\text{ext}}^{(1)\alpha i+}(\boldsymbol{r}) + n(\boldsymbol{r}) V_{\text{ext}}^{(2)\beta j-\alpha i+}(\boldsymbol{r}) \right] \mathrm{d}\boldsymbol{r} + E_{\text{ii}}^{(2)\beta j-\alpha i+}. \quad (3.29)$$

Again, we omit a factor $N_{\text{u.c.}}$ from the unit cell summation and explicitly introduce the integration domain as the unit cell with volume $\Omega$. This is due to the nature of the Fourier transformed quantities involved. If their phases add up to $0$, as it does for a combination of real-space quantities with superscripts $+$ and $-$, their product is the same in each unit cell. This means we only need the integral over the representative unit cell. If the phases do not match, the integral vanishes instead.

The Sternheimer Equation

Due to the relation of the dynamical matrix to the energy derivative in equation (3.29), we now know all quantities needed to calculate it. These quantities, however, are no longer all available or can be constructed solely from a ground-state density SCF calculation, as they were for the forces. Instead, the response of the density and thus the response of the wave functions needs to be calculated explicitly. It obeys a first order equivalent of the KS Schrödinger equation, that is widely known as the Sternheimer equation [151]. It is obtained by perturbing equation (2.5) with respect to atom $\beta$ in the $j$ direction for a positive q-point $+\boldsymbol{q}$ $(\beta j+)$:

$$\left( -\frac{1}{2}\nabla^2 + V_{\text{eff}}(\boldsymbol{r}) - \varepsilon_{\boldsymbol{k}\nu} \right) \psi_{\boldsymbol{k}\nu}^{(1)\beta j+}(\boldsymbol{r}) = -\left( V_{\text{eff}}^{(1)\beta j+}(\boldsymbol{r}) - \varepsilon_{\boldsymbol{k}\nu}^{(1)\beta j+} \right) \psi_{\boldsymbol{k}\nu}(\boldsymbol{r}). \quad (3.30)$$

This equation needs to be solved self-consistently, just like the KS equations before. This is again due to the relations between the potential, density, and wave function responses. The first order density

$$\begin{aligned} n^{(1)\beta j+}(\boldsymbol{r}) = \sum_{\boldsymbol{k}\nu} [ & \tilde{f}_{\boldsymbol{k}\nu}^{(1)\beta j+} |\psi_{\boldsymbol{k}\nu}(\boldsymbol{r})|^2 \\ & + \tilde{f}_{\boldsymbol{k}\nu} \psi_{\boldsymbol{k}\nu}^{*(1)\beta j+}(\boldsymbol{r}) \psi_{\boldsymbol{k}\nu}(\boldsymbol{r}) + \tilde{f}_{\boldsymbol{k}\nu} \psi_{\boldsymbol{k}\nu}^{*}(\boldsymbol{r}) \psi_{\boldsymbol{k}\nu}^{(1)\beta j+}(\boldsymbol{r}) ]. \end{aligned} \quad (3.31)$$

is constructed from the first order wave functions and occupation numbers. For the scope of this thesis, we will always assume our lattice to be symmetric under inversion or time-inversion, which consequently means the following relations for the wave functions and eigenenergies hold:

$$\psi_{\boldsymbol{k}\nu}^{*} = \psi_{-\boldsymbol{k}\nu}, \qquad \varepsilon_{\boldsymbol{k}\nu} = \varepsilon_{-\boldsymbol{k}\nu}. \quad (3.32)$$

Inversion symmetry is the stronger condition of the two, in that it additionally enforces real-valued wave functions. The latter equation also translates to the occupation numbers. With some sum manipulation, this means we can simplify the form of the first order density

$$n^{(1)\beta j+}(\boldsymbol{r}) = \sum_{\boldsymbol{k}\nu} \left[ \tilde{f}_{\boldsymbol{k}\nu}^{(1)\beta j+} |\psi_{\boldsymbol{k}\nu}(\boldsymbol{r})|^2 + 2 \tilde{f}_{\boldsymbol{k}\nu} \psi_{\boldsymbol{k}\nu}^{*}(\boldsymbol{r}) \psi_{\boldsymbol{k}\nu}^{(1)\beta j+}(\boldsymbol{r}) \right], \quad (3.33)$$

which limits the calculation to the perturbation for $+\boldsymbol{q}$. Moving on to the next step of the workflow, the response of the effective potential (through its constituents) depends on the density response just like the effective potential depends on the density:

$$V_{\text{eff}}^{(1)\beta j+}(\boldsymbol{r}) = V_{\text{ext}}^{(1)\beta j+}(\boldsymbol{r}) + V_{\text{H}}^{(1)\beta j+}(\boldsymbol{r}) + V_{\text{xc}}^{(1)\beta j+}(\boldsymbol{r}), \quad (3.34)$$

$$V_{\text{ext}}^{(1)\beta j+}(\boldsymbol{r}) = -\sum_{\boldsymbol{R}} \mathrm{e}^{\mathrm{i}\boldsymbol{q}\cdot\boldsymbol{R}} \nabla_j V_{\text{ext}}^{\beta\boldsymbol{R}}, \tag{3.35a}$$

$$V_{\text{H}}^{(1)\beta j+}(\boldsymbol{r}) = \int \frac{n^{(1)\beta j+}(\boldsymbol{r}')}{|\boldsymbol{r}-\boldsymbol{r}'|} \mathrm{d}\boldsymbol{r}', \tag{3.35b}$$

$$V_{\text{xc}}^{(1)\beta j+}(\boldsymbol{r}) = n^{(1)\beta j+}(\boldsymbol{r}) \frac{\delta^2 E_{\text{xc}}[n]}{\delta n(\boldsymbol{r})^2} = n^{(1)\beta j+}(\boldsymbol{r}) K_{\text{xc}}[n](\boldsymbol{r}). \tag{3.35c}$$

Here we implicitly used the fact, that we restrict ourselves to LDA functionals, for which the xc Kernel $K_{xc}$ only needs to be multiplied with the density response. This form becomes more complicated *e.g.* for GGA functionals. In the case of a spin-polarized system, the equation assumes a slightly different form,

$$V_{\text{xc},\sigma}^{(1)\beta j+}(\boldsymbol{r}) = \sum_{\sigma'} n_{\sigma'}^{(1)\beta j+}(\boldsymbol{r}) \frac{\delta^2 E_{\text{xc}}[n_\uparrow, n_\downarrow]}{\delta n_{\sigma'}(\boldsymbol{r}) \delta n_\sigma(\boldsymbol{r})}, \tag{3.36}$$

where each spin channel requires the xc Kernel for the mixed spin derivative and the corresponding second derivative in its own spin. This gives us terms for the first order quantities, that are very alike to their ground-state counterparts. This also means that the first order SCF loop can be run in a similar setup as the ground-state one, though with modifications at various points.

Perturbed Occupation Numbers

In equation (3.33) we need not only the perturbed wave functions, but also the response of the occupation numbers. It will only contribute in metallic materials, where the step function cutting off the unoccupied state is smeared into a smooth form as stated in section 2.4. Assuming the smearing function to be Fermi–Dirac like again, they can be gained by differentiating the explicit form of the occupation numbers,

$$\tilde{f}_{\boldsymbol{k}\nu} = \frac{f_{\boldsymbol{k}}}{\mathrm{e}^x + 1}\Big|_{x=(\varepsilon_{\boldsymbol{k}\nu}-E_{\text{F}})/(k_{\text{B}}T)}, \tag{3.37}$$

with the weight $f_{\boldsymbol{k}}$ of each k-point. This gives us a form for the first order occupations

$$\tilde{f}_{\boldsymbol{k}\nu}^{(1)\beta j+} = -\frac{\tilde{f}_{\boldsymbol{k}}}{\mathrm{e}^{-x} + 1}\Big|_{x=(\varepsilon_{\boldsymbol{k}\nu}-E_{\text{F}})/(k_{\text{B}}T)} \frac{\varepsilon_{\boldsymbol{k}\nu}^{(1)\beta j+} - E_{\text{F}}^{(1)\beta j+}}{k_{\text{B}}T}, \tag{3.38}$$

that is not yet fully soluble, as it depends on the first order Fermi energy that is at this point undetermined. We can find a closed form for it by differentiating equation (2.16) under the assumption, that the electron count does not vary and thus the left hand side derivative is $0$. This yields

$$E_{\text{F}}^{(1)\beta j+} = \frac{\sum_{\boldsymbol{k}\nu} \tilde{f}_{\boldsymbol{k}\nu} \varepsilon_{\boldsymbol{k}\nu}^{(1)\beta j+} / (\mathrm{e}^{-x}+1)|_{x=(\varepsilon_{\boldsymbol{k}\nu}-E_{\text{F}})/(k_{\text{B}}T)}}{\sum_{\boldsymbol{k}\nu} \tilde{f}_{\boldsymbol{k}\nu} / (\mathrm{e}^{-x}+1)|_{x=(\varepsilon_{\boldsymbol{k}\nu}-E_{\text{F}})/(k_{\text{B}}T)}}. \tag{3.39}$$

In the case of semiconductors and insulators, the calculation is skipped and this quantity is set to $0$ to avoid divisions by very small numbers.

Analytic Second Order Quantities

The remaining terms in equation (3.29) that are yet to be discussed are the second order responses of the external potential and the ion-ion interaction. Both of these quantities are

analytical and completely independent of both the ground-state and first-order density SCF calculations. The best way to calculate them depends on the basis set chosen for the electronic structure calculation, but we want to introduce their analytical form here for the sake of completeness of the chapter. The second order external potential perturbation is independent of $\boldsymbol{q}$ and directly follows from the first order in equation (3.35a) and reads

$$V_{\text{ext}}^{(2)\beta j-\alpha i+}(\boldsymbol{r}) = \delta_{\beta\alpha} \sum_{\boldsymbol{R}} \nabla_j \nabla_i V_{\text{ext}}^{\alpha\boldsymbol{R}}(\boldsymbol{r}). \tag{3.40}$$

The formula for the second order ion-ion interaction is more involved. This stems from the fact that we look at a double sum that excludes one specific combination of atoms that would make the Coulomb singularity diverge. It reads

$$\begin{aligned} E_{\text{ii}}^{(2)\beta j-\alpha i+} = &-\delta_{\beta\alpha} Z_\alpha \sum_{\boldsymbol{R}} \sum_{\gamma\boldsymbol{R}''\neq\alpha\boldsymbol{R}} \nabla_j \nabla_i V_{\text{ext}}^{\gamma\boldsymbol{R}''}(\boldsymbol{r})|_{\boldsymbol{r}=\boldsymbol{\tau}_{\alpha\boldsymbol{R}}} \\ &+ Z_\alpha \sum_{\substack{\boldsymbol{R}'\boldsymbol{R} \\ \beta\boldsymbol{R}'\neq\alpha\boldsymbol{R}}} \mathrm{e}^{-\mathrm{i}\boldsymbol{q}\cdot(\boldsymbol{R}'-\boldsymbol{R})} \nabla_j \nabla_i V_{\text{ext}}^{\beta\boldsymbol{R}'}(\boldsymbol{r})|_{\boldsymbol{r}=\boldsymbol{\tau}_{\alpha\boldsymbol{R}}}. \end{aligned} \tag{3.41}$$

The first term is a second spatial derivative of the external potential of all atoms except the one at $\boldsymbol{\tau}_{\alpha\boldsymbol{R}}$ evaluated at the position of this exact atom. The second term is similar, but gains a dependence on the phonon wave vector and is restricted to the displaced atom with the row index. A similar form, that lacked the sum over all atoms in the first term was established in [92] and elaborated on in [93]. The exact calculation of these elements and the second order external potential response in the FLAPW framework will be discussed in the next chapter.

**Other Types of Perturbations**

The general formalism of DFPT was introduced in this chapter on the specific example of phononic perturbations. It should be noted, that this is by no means the only type of perturbation that can be applied, *i.e.* other important response quantities are related to different perturbations like mechanical strain or external fields. The general form for such perturbations (aside from the initial potential perturbation and the ion-ion interaction response) as well as the resulting Sternheimer equation are all quite similar in nature, as long as they do not create responses that lie outside the Hilbert space of the original wave functions. In the specific case of DFPT for vibrational excitations in a linearized augmented plane-wave basis, such terms indeed exist which make the theory and implementation a lot more complicated. This will be discussed in detail in section 4.3, while allusions to other response quantities are given where they are adequate.

**Variationality and 2n+1 Theorem**

From equations (3.26) and the related quantities it can be seen that for a phononic perturbation, the first order response only depends on self-consistent quantities form the ground-state calculation as well as an analytic expression for the external potential response. The same does not hold for the second order energy response in equation and (3.29), where the first order density response is incorporated as well. These dependencies of response terms on lower order expressions is a general consequence of the $2n+1$-theorem. It states, that the responses of physical quantities up to $(2n+1)$th order can be expressed through the responses of the wave functions and eigenenergies up to only $n$th order. The proof of this theorem relies on the varitationality of such quantities up to arbitrary order [45, 152–154]. The general fact, that the second order energy response is variational with respect to the ground-state density and the first order wave function response also mandates a good convergence behaviour. The

numerical consequence of variationality is that the total energy of the KS system converges more quickly than the ground-state density itself, *i.e.* middling accuracy of the density already gives good accuracy of the energy - the convergence is stable with respect to the basis set chosen. As the second order energy response is variational as well with respect to the first order density response, a similar relation between the accuracy of the phonon dispersion and the degree of convergence in the Sternheimer SCF cycle can be expected.

Chapter 4

# Density-Functional Perturbation Theory in the All-Electron Full-Potential Linearized Augmented Plane-Wave Method


4.1 The Linearized Augmented Plane-Wave Basis . . . . . 30
4.2 The Quantum Engine of FLAPW . . . . . 38
4.3 Adapting DFPT to FLAPW . . . . . 46


The Choice of Basis

To this point, the only assumption we made about the solid state system under consideration has been the periodicity of the lattice. This dictates the general form of the wave functions, being Bloch waves with crystal momentum $\boldsymbol{k}$, but not the specific form of the lattice periodic functions $u_{\boldsymbol{k}\nu}(\boldsymbol{r})$. The space of possible functions is vast and a common approach is to define a set of basis functions in which the wave functions

$$\psi_{\boldsymbol{k}\nu}(\boldsymbol{r}) = \sum_{\boldsymbol{G}} z_{\boldsymbol{k}\boldsymbol{G}\nu}\phi_{\boldsymbol{k}\boldsymbol{G}}(\boldsymbol{r}) = \sum_{\boldsymbol{G}} z_{\boldsymbol{k}\boldsymbol{G}\nu}\mathrm{e}^{\mathrm{i}\boldsymbol{k}\cdot\boldsymbol{r}}u_{\boldsymbol{k}\boldsymbol{G}}(\boldsymbol{r}) \tag{4.1}$$

can be expanded. Each basis function $\phi_{\boldsymbol{k}\boldsymbol{G}}$ and expansion coefficient $z_{\boldsymbol{k}\boldsymbol{G}\nu}$ is associated with a vector $\boldsymbol{k}+\boldsymbol{G}$, where $\boldsymbol{G}$ is a reciprocal lattice vector. The computational setup is dictated by the exact choice of basis and its ramifications. Aside from this, some other factors come into play. The choice of the xc functional greatly influences the ground-state density. The kinetic energy operator in the KS equations can be handled non-relativistically, in a scalar-relativistic approximation (SRA) or in a fully relativistic fashion. The potential can be approximated by a smooth pseudopotential to deal with the Coulomb singularities at the atomic nuclei, and lastly, the shape of the potential across the unit cell can be fixed to be spherical around the atoms and flat farther away from them. Generally, the expansion into a basis set transforms the KS equations into a (possibly generalized) eigenvalue problem

$$\boldsymbol{0} = (\underline{H}(\boldsymbol{k}) - \varepsilon_{\boldsymbol{k}\nu}\underline{S}(\boldsymbol{k}))\cdot\boldsymbol{z}_{\boldsymbol{k}\nu}, \tag{4.2}$$

with a Hamiltonian and overlap matrix

$$H_{\boldsymbol{G}',\boldsymbol{G}} = \langle\phi_{\boldsymbol{k}\boldsymbol{G}'}|\mathcal{H}|\phi_{\boldsymbol{k}\boldsymbol{G}}\rangle_\Omega, \tag{4.3}$$

$$S_{\boldsymbol{G}',\boldsymbol{G}} = \langle\phi_{\boldsymbol{k}\boldsymbol{G}'}|\phi_{\boldsymbol{k}\boldsymbol{G}}\rangle_\Omega, \tag{4.4}$$

where the expansion coefficients have been written as a vector with components labeled by the reciprocal lattice vectors $\boldsymbol{G}$. The subscript $\Omega$ on the brakets indicates an integration over a single unit cell and equation (4.2) needs to be solved for each k-point in the Brillouin zone. The following sections highlight our method of choice, the all-electron full-potential linearized augmented-plane wave method (FLAPW) as implemented in the electronic structure code FLEUR, the theoretical considerations that lead to its development, as well as its application to the DFPT formalism. The last point encompasses the main focus of this thesis. The FLAPW framework was specifically constructed to deal with the ionic $1/r$-singularities in a way that does not require any shape approximations and contains in its setup not only the valence electrons, but the core electrons, too. References to methods, that are also common, but unrelated to FLAPW will be given where appropriate.

## 4.1 The Linearized Augmented Plane-Wave Basis

### 4.1.1 Plane-Wave and Augmented Plane-Wave Methods

PW Methods

Historically, the FLAPW method is based on the successive improvement upon more simple ideas, that have preceded it. We start with the natural choice for the description of a periodic lattice - an orthonormalized plane wave (PW) basis function

$$\phi^{\text{PW}}_{\boldsymbol{k}\boldsymbol{G}}(\boldsymbol{r}) = \frac{1}{\sqrt{\Omega}} \mathrm{e}^{\mathrm{i}(\boldsymbol{k}+\boldsymbol{G})\cdot\boldsymbol{r}}. \tag{4.5}$$

With this basis, the overlap matrix becomes unity ($S_{\boldsymbol{G}',\boldsymbol{G}} = \delta_{\boldsymbol{G}',\boldsymbol{G}}$) and the Hamiltonian matrix is equivalent to a Fourier transform of the potential $\hat{V}_{\text{eff}}(\boldsymbol{G}' - \boldsymbol{G})$ plus a diagonal kinetic energy term $\delta_{\boldsymbol{G},\boldsymbol{G}'}(\boldsymbol{k}+\boldsymbol{G})^2/2$. The basis introduces a cutoff parameter $K_{\text{max}}$ that limits the set of plane waves by demanding that $|\boldsymbol{k}+\boldsymbol{G}| < K_{\text{max}}$. This effectively limits the kinetic energy of the electrons. The method is straight-forward to implement [155], but has a set of drawbacks. The most significant of them is the treatment of the Coulomb singularities at the nuclei. In practice, the divergent nature of the ionic term will lead to high-frequency oscillations in the wave functions, which can only be captured in plane waves with a very large cutoff parameter ($K_{\text{max}} \longrightarrow \infty$), which is of course detrimental in terms of computational effort. Therefore, PW codes often opt to substitute the $1/r$-term with a smooth pseudopotential, that matches the true form away from the singularity but replaces the divergent term by a flat one with similar scattering properties. This method has been in use for a very long time and is still used to great success today [156]. Another way to mitigate the issues is to use the projector-augmented wave method [157].

APW Methods

A natural way to account for the Coulomb singularities is to consider their spherical nature and to treat the radial part numerically or in a basis. It would be fitting to have basis functions, that share that same radial nature close to the ions, but are nevertheless lattice periodic, *i.e.* match to plane waves at a proper distance from them. This led Slater to develop the class of augmented-plane wave (APW) basis sets [158, 159]. In a preset radius around each nucleus $\gamma$, the basis set is changed to an expansion in radial functions and spherical harmonics, that depend on the polar coordinates with the origin at the atom's position $\boldsymbol{\tau}_\gamma$. The resulting position vector is $\boldsymbol{r}_\gamma := \boldsymbol{r} - \boldsymbol{\tau}_\gamma$. This leads to a separation into a set of spheres, that optimally take up most of the unit cell [160], and interstitial region (IR) between them, where the

plane wave description still applies. Visualizing this idea in a two-dimensional space leads to a picture resembling a muffin tin, hence the radii of these spheres are known as muffin-tin (MT) radii. The basis takes the following read

$$\begin{aligned}\phi^{\mathrm{APW}}_{\boldsymbol{kG}}(\boldsymbol{r}) &= \begin{cases} \frac{1}{\sqrt{\Omega}} \mathrm{e}^{\mathrm{i}(\boldsymbol{k}+\boldsymbol{G})\cdot\boldsymbol{r}}, & \boldsymbol{r} \in \mathrm{IR} \\ \sum_{\ell m} a^{\boldsymbol{k}+\boldsymbol{G},\gamma}_{\ell m} u^{\gamma}_{\ell}(r_\gamma) Y^m_\ell(\hat{\boldsymbol{r}}_\gamma) & \boldsymbol{r} \in \mathrm{MT}^\gamma \end{cases} \\ &= \Theta_{\mathrm{IR}}(\boldsymbol{r}) \phi^{\mathrm{IR}}_{\boldsymbol{kG}}(\boldsymbol{r}) + \sum_\gamma \Theta_\gamma(\boldsymbol{r}) \phi^{\gamma}_{\boldsymbol{kG}}(\boldsymbol{r}), \end{aligned} \tag{4.6}$$

where we defined the step function $\Theta_{\mathrm{IR}}$, that cuts out the MT spheres and leaves only the interstitial region as

$$\Theta_\gamma(\boldsymbol{r}) := \Theta(R_{\mathrm{MT}^\gamma} - |\boldsymbol{r} - \boldsymbol{\tau}_\gamma|), \tag{4.7}$$

$$\Theta_{\mathrm{IR}}(\boldsymbol{r}) := 1 - \sum_\gamma \Theta_\gamma(\boldsymbol{r}) = \sum_{\boldsymbol{G}} \hat{\Theta}(\boldsymbol{G}) \mathrm{e}^{\mathrm{i}\boldsymbol{G}\cdot\boldsymbol{r}}, \tag{4.8}$$

$$\hat{\Theta}(\boldsymbol{G}) := \delta_{\boldsymbol{G},\boldsymbol{0}} - \sum_\gamma \frac{4\pi R^3_{\mathrm{MT}^\gamma}}{\Omega} \frac{j_1(G R_{\mathrm{MT}^\gamma})}{G R_{\mathrm{MT}^\gamma}} \mathrm{e}^{-\mathrm{i}\boldsymbol{G}\cdot\boldsymbol{\tau}_\gamma}, \tag{4.9}$$

as found in [133]. The setup is clarified in figure 4.1. It explicitly shows several MT spheres with the respective atomic positions and MT radii $R_{\mathrm{MT}}$, and the interstitial region.

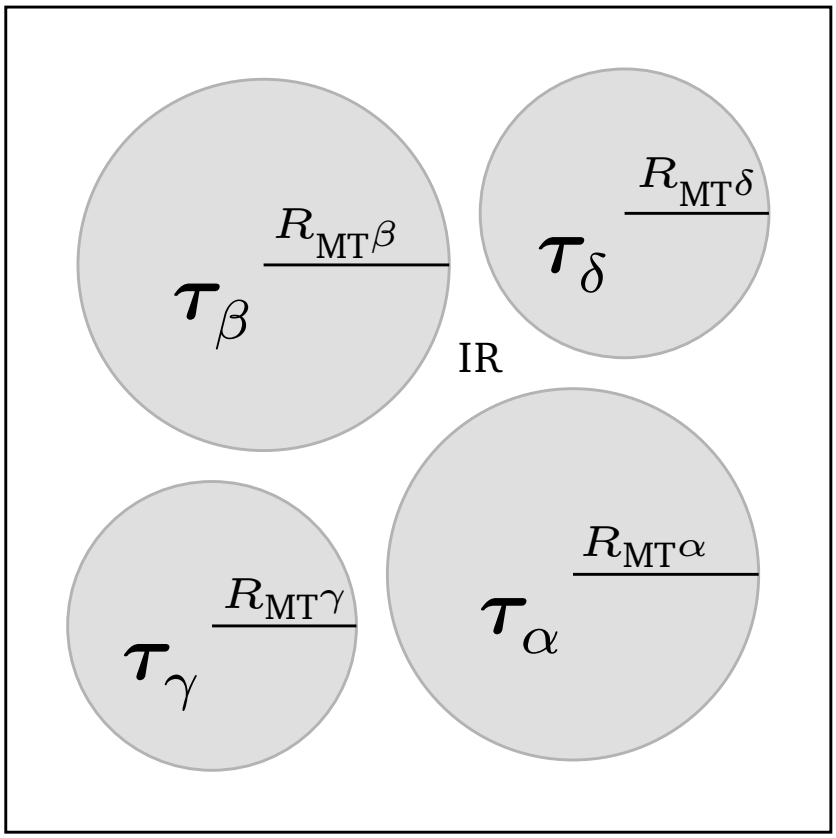



**Figure 4.1:** Sketch of the muffin tin sphere setup in APW methods

Due to the choice of a segmented basis set, the radial part needs to be multiplied by a matching coefficient $a^{\boldsymbol{k}+\boldsymbol{G},\gamma}_{\ell m}$, that is determined in a way that ensures continuity at the MT boundary.

Thus it takes the form

$$a_{\ell m}^{\boldsymbol{k}+\boldsymbol{G},\gamma} = \frac{4\pi \mathrm{i}^{\ell}}{\sqrt{\Omega}} \mathrm{e}^{\mathrm{i}(\boldsymbol{k}+\boldsymbol{G})\cdot\boldsymbol{\tau}_\gamma} \frac{j_\ell\left(|\boldsymbol{k}+\boldsymbol{G}|\, R_{\mathrm{MT}\gamma}\right)}{u_\ell^\gamma(R_{\mathrm{MT}\gamma})} Y_\ell^{m*}\left(\widehat{\boldsymbol{k}+\boldsymbol{G}}\right), \tag{4.10}$$

due to the expansion of the plane waves into spherical harmonics. It includes spherical Bessel functions of the first kind $j_\ell$. The radial expansion of the basis set is obviously not infinite, but also cut off by a maximum angular momentum number $\ell_{\mathrm{max}}^\gamma$, that can in principle vary for each atom. The radial functions in the MT spheres are as of yet unspecified. They were defined first by Slater as the solutions to the radial part of the KS equation, *i.e.* solving

$$\mathcal{H}_{\mathrm{sph}} r_\gamma u_\ell^\gamma(r_\gamma) = \left(-\frac{1}{2}\partial_{r_\gamma}^2 + \frac{\ell(\ell+1)}{2r_\gamma^2} + V_{\mathrm{eff,sph}}^\gamma(r_\gamma)\right) r_\gamma u_\ell^\gamma(r_\gamma) = E_\ell^\gamma r_\gamma u_\ell^\gamma(r_\gamma) \tag{4.11}$$

with an energy parameter $E_\ell^\gamma$ [158]. The equation is solved self-consistently for $r_\gamma u_\ell^\gamma$ for the sake of numerical convenience. The radial functions are normalized according to

$$1 = \langle u_\ell^\gamma | u_\ell^\gamma \rangle_{\mathrm{MT}\gamma} = \int_0^{R_{\mathrm{MT}\gamma}} r_\gamma^2 u_\ell^\gamma(r_\gamma) u_\ell^\gamma(r_\gamma) \mathrm{d}r_\gamma. \tag{4.12}$$

With this separation and the corresponding definitions, the Hamiltonian and overlap matrix elements of the APW method get additional contributions as opposed to the PW case. The MT Hamiltonian can be split up into the spherical part and the non-spherical potential. The spherical part can be expressed solely through the overlap and the eigenenergies, while the radial part of the non-spherical potential is neglected. The details on this will be discussed in the following part dealing with the LAPW basis, where the setup becomes more involved. For now, the Hamiltonian and overlap take the general form

$$\begin{aligned} H_{\boldsymbol{G}',\boldsymbol{G}}(\boldsymbol{k}) &= \sum_\gamma \langle \phi_{\boldsymbol{k}\boldsymbol{G}'}^\gamma | \mathcal{H}_{\mathrm{sph}}^\gamma | \phi_{\boldsymbol{k}\boldsymbol{G}}^\gamma \rangle_\gamma + \langle \phi_{\boldsymbol{k}\boldsymbol{G}'}^{\mathrm{IR}} | \Theta_{\mathrm{IR}} \mathcal{H} | \phi_{\boldsymbol{k}\boldsymbol{G}}^{\mathrm{IR}} \rangle_\Omega \\ S_{\boldsymbol{G}',\boldsymbol{G}}(\boldsymbol{k}) &= \sum_\gamma \langle \phi_{\boldsymbol{k}\boldsymbol{G}'}^\gamma | \phi_{\boldsymbol{k}\boldsymbol{G}}^\gamma \rangle_\gamma + \langle \phi_{\boldsymbol{k}\boldsymbol{G}'}^{\mathrm{IR}} | \Theta_{\mathrm{IR}} | \phi_{\boldsymbol{k}\boldsymbol{G}}^{\mathrm{IR}} \rangle_\Omega. \end{aligned} \tag{4.13}$$

The MT part of the Hamiltonian can be expressed through the overlap matrix elements and the energy parameters $E_\ell^\gamma$, which will be discussed in more detail for the implementation of the LAPW basis. In the APW method, the IR potential is often assumed to be a constant and the MT potential a spherical function. This is referred to as the atomic sphere approximation (ASA). Otherwise the wave functions are not well-described by the radial basis. The basis is only flexible enough when the energy parameters match the initially unknown band energies $\varepsilon_{\boldsymbol{k}\nu}$ closely. But these energies are a quantity that should be a result of the calculation, not an input. So an initial energy guess $E_\ell^\gamma$ is made, leading to a secular equation for the eigenenergies, where the Hamiltonian and overlap depend on $E_\ell^\gamma$ as well. This problem is non-linear and its solution is a state, where $E_\ell^\gamma$ equals the final eigenenergy determined. The calculation is highly involved and has to be repeated for each state, which makes it computationally expensive. Another drawback is the so-called asymptote problem. Certain combinations of energy parameters and MT radii can make the radial functions vanish at the MT boundary, which makes matching them against the plane waves impossible. In equation (4.10), this corresponds to divergent matching coefficients. The next successive improvement to this method will remedy both of these problems.

### 4.1.2 Full-Potential Linearized Augmented Plane-Wave Method

LAPW Method

The linearized augmented plane-wave basis was introduced by Marcus [161] and expanded upon by Andersen [71], Koelling, and Arbman [72] to deal with the shortcomings of the plain APW approach. It is motivated by a linearization of the radial eigenfunctions around the preset energy parameter:

$$u_\ell^\gamma(r_\gamma,\varepsilon) \approx u_\ell^\gamma(r_\gamma,E_\ell^\gamma) + \frac{\partial u_\ell^\gamma}{\partial\varepsilon}(r_\gamma,E_\ell^\gamma)(\varepsilon - E_\ell). \tag{4.14}$$

This leads to an improved description of radial functions at arbitrary energies $\varepsilon$ close to the chosen energy parameter instead of only directly at it. We take the radial eigenfunctions and their energy derivatives $\dot{u}_\ell^\gamma(r_\gamma,E_\ell^\gamma)$ together as the new radial part of the basis set. The energy derivatives are determined by a differentiated version of equation (4.11):

$$\mathcal{H}_{\text{sph}} r_\gamma \dot{u}_\ell^\gamma(r_\gamma) = r_\gamma u_\ell^\gamma(r_\gamma) + E_\ell^\gamma r_\gamma \dot{u}_\ell^\gamma(r_\gamma) \tag{4.15}$$

The equation contains the radial solutions and the energy derivatives are thus created after them. The energy derivatives are usually made orthogonal to the initial radial functions ($\langle \dot{u}_{\ell'}^\gamma | u_\ell^\gamma \rangle_{\text{MT}^\gamma} = 0$) and are not normalized ($\langle \dot{u}_{\ell'}^\gamma | \dot{u}_\ell^\gamma \rangle_{\text{MT}^\gamma} = c_{\ell'\ell}^\gamma$). The latter property needs to be taken into account *e.g.* when the matrix elements are evaluated. With the radial functions and their energy derivatives, the LAPW basis functions now look as follows:

$$\phi_{\boldsymbol{k}\boldsymbol{G}}^{\text{LAPW}}(\boldsymbol{r}) = \begin{cases} \frac{1}{\sqrt{\Omega}} \mathrm{e}^{\mathrm{i}(\boldsymbol{k}+\boldsymbol{G})\cdot\boldsymbol{r}}, & \boldsymbol{r} \in \text{IR} \\ \sum_{\ell m} \left( a_{\ell m}^{\boldsymbol{k}+\boldsymbol{G},\gamma} u_\ell^\gamma(r_\gamma) + b_{\ell m}^{\boldsymbol{k}+\boldsymbol{G},\gamma} \dot{u}_\ell^\gamma(r_\gamma) \right) Y_\ell^m(\hat{\boldsymbol{r}}_\gamma), & \boldsymbol{r} \in \text{MT}^\gamma \end{cases} \tag{4.16}$$

We need two sets of matching coefficients $a_{\ell m}^{\boldsymbol{k}+\boldsymbol{G},\gamma}$ and $b_{\ell m}^{\boldsymbol{k}+\boldsymbol{G},\gamma}$ for this new basis. They are determined by again requiring the continuity of the basis at the MT boundary, but now with the added stipulation of being continuously differentiable there as well. This leads to a vector-matrix equation for the matching coefficients,

$$\begin{pmatrix} a_{\ell m}^{\boldsymbol{k}+\boldsymbol{G},\gamma} \\ b_{\ell m}^{\boldsymbol{k}+\boldsymbol{G},\gamma} \end{pmatrix} = \frac{4\pi \mathrm{i}^\ell}{\sqrt{\Omega}} \mathrm{e}^{\mathrm{i}(\boldsymbol{k}+\boldsymbol{G})\cdot\boldsymbol{\tau}_\gamma} Y_\ell^{m*}\left(\widehat{\boldsymbol{k}+\boldsymbol{G}}\right) \underline{U}_{\ell\gamma}^{-1} \cdot \begin{pmatrix} j_\ell\left(|\boldsymbol{k}+\boldsymbol{G}|\, R_{\text{MT}^\gamma}\right) \\ |\boldsymbol{k}+\boldsymbol{G}|\, j_\ell'\left(|\boldsymbol{k}+\boldsymbol{G}|\, R_{\text{MT}^\gamma}\right) \end{pmatrix}, \tag{4.17}$$

that involves inverting the matrix

$$\underline{U}_{\ell\gamma} = \begin{pmatrix} u_\ell^\gamma(R_{\text{MT}^\gamma}) & \dot{u}_\ell^\gamma(R_{\text{MT}^\gamma}) \\ u_\ell'^\gamma(R_{\text{MT}^\gamma}) & \dot{u}_\ell'^\gamma(R_{\text{MT}^\gamma}) \end{pmatrix} \tag{4.18}$$

of radial boundary values. The required matrix is easily found by the standard way of inverting a $2 \times 2$-matrix. With the determinant of the boundary value matrix $W_\ell^\gamma$, it can be written as

$$\underline{U}_{\ell\gamma}^{-1} = \frac{1}{W_\ell^\gamma} \begin{pmatrix} \dot{u}_\ell'^\gamma(R_{\text{MT}^\gamma}) & -\dot{u}_\ell^\gamma(R_{\text{MT}^\gamma}) \\ -u_\ell'^\gamma(R_{\text{MT}^\gamma}) & u_\ell^\gamma(R_{\text{MT}^\gamma}) \end{pmatrix}. \tag{4.19}$$

This way of determining the matching coefficients by matrix inversion can always be done, as long as the matrix determinant, *i.e.* the Wronskian of the radial functions, is finite. It can easily be shown, that this is always the case, as the Wronskian

$$W_\ell^\gamma = u_\ell^\gamma(R_{\text{MT}^\gamma})\dot{u}_\ell'^\gamma(R_{\text{MT}^\gamma}) - \dot{u}_\ell^\gamma(R_{\text{MT}^\gamma})u_\ell'^\gamma(R_{\text{MT}^\gamma}) = -\frac{2}{R_{\text{MT}^\gamma}^2} \neq 0 \tag{4.20}$$

takes on a finite value independent of the form of the radial functions. Please note, that the Wronskian that is written out by FLEUR is defined with an additional negative prefactor, yielding a finite positive value. In many parts of the method, that involve radial integrals (in particular the DFPT implementation), it is convenient to rewrite the matching coefficients. They are usually paired up with the basis expansion coefficients, to get a new set of parameters, where the reciprocal vector dependency is already summed over. To distinguish between the matching coefficients with and without the contraction with the expansion coefficients, we will refer to them as the large and the small matching coefficients. The large coefficients

$$\begin{pmatrix} A_{\ell m}^{\boldsymbol{k}\nu\gamma} \\ B_{\ell m}^{\boldsymbol{k}\nu\gamma} \end{pmatrix} = \sum_{\boldsymbol{G}} z_{\boldsymbol{k}\boldsymbol{G}\nu} \begin{pmatrix} a_{\ell m}^{\boldsymbol{k}+\boldsymbol{G},\gamma} \\ b_{\ell m}^{\boldsymbol{k}+\boldsymbol{G},\gamma} \end{pmatrix} \tag{4.21}$$

take up less space and make the formalism more elegant on paper as well. To summarize, the LAPW basis cures both the asymptote problem and the non-linear nature of the APW eigenvalue problem. The linearization provides enough variational freedom that the energy parameters no longer need to be set strictly to the band energies. They provide an energy window in which the eigenenergies will be described accurately enough in most cases. The computational method is reduced to a single generalized eigenvalue equation for each k-point. The variational freedom also allows us to lift the shape approximations made before.

FLAPW

In the FLAPW [73] method, not only the basis determines the computational workflow and effort, but also the choice of our expressions for the density and potential. In general, it makes no restrictions to the shape the potential can take, but rather allows a full expansion of the MT functions into spherical harmonics and the IR function into plane waves. This enables the accurate description of atomic quantities and the basis expansion takes the form

$$n(\boldsymbol{r}) = \begin{cases} \sum_{\boldsymbol{G}} n_{\text{IR}}(\boldsymbol{G}) \mathrm{e}^{\mathrm{i}\boldsymbol{G}\cdot\boldsymbol{r}}, & \boldsymbol{r} \in \text{IR} \\ \sum_{\ell m} n_{\gamma\ell m}(r_\gamma) Y_\ell^m(\hat{\boldsymbol{r}}_\gamma) & \boldsymbol{r} \in \text{MT}^\gamma \end{cases}, \tag{4.22}$$

$$V_{\text{eff}}(\boldsymbol{r}) = \begin{cases} \sum_{\boldsymbol{G}} V_{\text{eff,IR}}(\boldsymbol{G}) \mathrm{e}^{\mathrm{i}\boldsymbol{G}\cdot\boldsymbol{r}}, & \boldsymbol{r} \in \text{IR} \\ \sum_{\ell m} V_{\text{eff},\gamma\ell m}(r_\gamma) Y_\ell^m(\hat{\boldsymbol{r}}_\gamma) & \boldsymbol{r} \in \text{MT}^\gamma \end{cases}. \tag{4.23}$$

The IR part is cut off at an additional parameter $G_{\text{max}}$ that limits the amount of plane waves taken into account ($|\boldsymbol{G}| < G_{\text{max}}$). It needs to be at least twice as big as the basis cutoff $K_{\text{max}}$ and is taken to be $3K_{\text{max}}$ for accuracy, if not specified otherwise. Along with taking both core and valence electrons into account in the calculation, this description of the density and potential constitutes the full-potential part of the all-electron FLAPW method [54, 73, 160]. In the FLEUR code, this expansion of the density and the potential is further broken down into a symmetrized set of functions, the so-called star-functions [133] in the IR, and symmetrized spherical harmonics, so-called lattice harmonics [162], in the MT. The stars are constructed as the sum of all symmetry-equivalent reciprocal lattice vectors, that thus share the same expansion coefficient up to a phase. They read

$$f_s(\boldsymbol{r}) = \frac{1}{N_{\text{op}}} \sum_{\text{op}} \mathrm{e}^{\mathrm{i}(\underline{S}\boldsymbol{G}_s)(\boldsymbol{r}-\boldsymbol{t})}, \tag{4.24}$$

for a set of $N_{\text{op}}$ symmetry operations $\{\underline{S}, \boldsymbol{t}\}$. The rotation matrices $\underline{S}$ transform a representative reciprocal lattice vector $\boldsymbol{G}_s$ into a set of symmetry equivalents. The lattice harmonics are

constructed as real-valued combinations of the spherical harmonics exclusively for orbitals $(\ell, m)$ that are allowed under the symmetry of the lattice. They read

$$Y_{\gamma L}((\hat{\boldsymbol{r}}_\gamma)) = \sum_{\mu(L)} c^{\gamma}_{L\mu} Y^{m(L,\mu)}_{\ell(L)}((\hat{\boldsymbol{r}}_\gamma)). \tag{4.25}$$

The index $L$ enumerates the lattice harmonics and $\mu(L)$ is the index of the members of one specific lattice harmonic. With this, the symmetrized density or potential can be expanded as

$$X(\boldsymbol{r}) = \begin{cases} \sum_s X_{\text{IR}}(s) f_s(\boldsymbol{r}), & \boldsymbol{r} \in \text{IR} \\ \sum_L X_{\gamma L}(r_\gamma) Y_{\gamma L}(\hat{\text{r}}_\gamma) & \boldsymbol{r} \in \text{MT}^\gamma \end{cases}. \tag{4.26}$$

It should be noted, that the symmetry of quantities perturbed in first order like the density response generally differs from that of the ground-state system. Due to this, we treat them without symmetry. In practice, this makes the stars expand back into plane waves (as only the identity matrix is present as a symmetry operation), while the MT functions are still described by real-valued $(m, -m)$ combinations of spherical harmonics, albeit all orbitals up to $\ell_{\text{max}}$ will be allowed. This needs to be taken into account, by keeping track of the lattice harmonic coefficients $c^{\gamma}_{L\mu}$. The density and potential constructions for the FLAPW method will be discussed in later sections. For now we deal with some additional considerations of the electrons and the basis set at hand.

### 4.1.3 All-Electron Aspects of the FLAPW Method

Relativism

Up to this point, our description of the electrons and the corresponding radial basis was strictly non-relativistic. It assumed a Schrödinger-like form for the KS equation for a single particle (2.5), which will break down *e.g.* for heavy nuclei that lead to high kinetic energies for the atoms. In such a case, the more general equation to study is the KS Dirac equation for a spherical potential [134], that can be written as

$$\left[c\underline{\boldsymbol{\alpha}}\boldsymbol{p} + (\underline{\beta} - \underline{I}_4)c^2 + V^{\gamma}_{\text{eff,sph}}\right] \boldsymbol{\Psi} = E_n \boldsymbol{\Psi}, \tag{4.27}$$

with the main quantum number $n$ and the matrices

$$\underline{\boldsymbol{\alpha}} = \sum_{i=1}^{3} \hat{\boldsymbol{e}}_i \begin{pmatrix} \underline{0}_2 & \underline{\sigma}_i \\ \underline{\sigma}_i & \underline{0}_2 \end{pmatrix}, \; \underline{\beta} = \text{diag}(1, 1, -1, -1), \; \underline{I}_4 = \text{diag}(1, 1, 1, 1). \tag{4.28}$$

This equation contains relativistic effects, that are usually split-up into *e.g.* a Darwin term, the mass-velocity term, and a spin-orbit interaction. It forms a set of four coupled first order differential equations for the large and small components $g_\kappa$ and $f_\kappa$ of both spins. Furthermore, the total angular momentum $\kappa$ is taken into account instead of $\ell$. The additional effort for the core electrons is insignificant in this regard, as their radial functions are determined from the current potential in each iteration, but the valence electrons are a different case. Their self-consistent calculation for a four-component wave function instead of a scalar one increases the size of the Hamiltonian by a factor of $4$ in each dimension and thus leads to a diagonalization step that is $4^3$ times as costly as in a nonmagnetic non-relativistic calculation. This factor reduces to by half for a collinear calculation and to $2^3$ in a non-collinear setup, where the spin-channels are already coupled. The coupling is numerically expensive [163],

which is why we turn to the scalar relativistic approximation (SRA) [164]. It neglects the spin-orbit interaction of the Dirac equation, separating the spin channels and thus decoupling the majority and minority spin contributions. This reduces the increase in effort from a factor of $4^3$ to $2 \times 2^3$, which is a lot more feasible. In an already spin-polarized setup, this reduces down from $32$ to only a factor of $8$. Spin-orbit coupling can either be reintroduced by an additional off-diagonal contribution to the Hamiltonian in spin space for a non-collinear setup or be treated as a small perturbation in second variation, as described in section 2.7. In this SRA, we want to calculate the relativistic equivalents of the radial basis functions and energy derivatives determined by equations (4.11) and (4.15) for the valence electrons. We replace the small component $f_\kappa$ by $\Phi_\kappa = f_\kappa + (\kappa+1)g_\kappa/(2Mcr)$ and identify that in the SRA, the total angular momentum can be replaced by $\ell$ due to the relation $\kappa(\kappa+1) = \ell(\ell+1)$. The scalar relativistic equation for the radial functions then reads

$$\begin{pmatrix} -\partial_{r_\gamma} & 2Mc \\ \frac{1}{2Mc}\frac{\ell(\ell+1)}{r_\gamma^2} + \frac{1}{c}(V^\gamma_{\text{eff,sph}} - E^\gamma_\ell) & -\frac{2}{r_\gamma} - \partial_{r_\gamma} \end{pmatrix} \begin{pmatrix} g^\gamma_\ell \\ \phi^\gamma_\ell \end{pmatrix} (r_\gamma) = 0, \tag{4.29}$$

while that for the corresponding energy derivatives is

$$\begin{pmatrix} -\partial_{r_\gamma} & 2Mc \\ \frac{1}{2Mc}\frac{\ell(\ell+1)}{r_\gamma^2} + \frac{1}{c}(V^\gamma_{\text{eff,sph}} - E^\gamma_\ell) & -\frac{2}{r_\gamma} - \partial_{r_\gamma} \end{pmatrix} \begin{pmatrix} \dot{g}^\gamma_\ell \\ \dot{\phi}^\gamma_\ell \end{pmatrix} (r_\gamma) + \begin{pmatrix} 0 & \frac{1}{c} \\ -\frac{1}{4M^2c^3}\frac{\ell(\ell+1)}{r_\gamma^2} - \frac{1}{c} & 0 \end{pmatrix} \begin{pmatrix} g^\gamma_\ell \\ \phi^\gamma_\ell \end{pmatrix} (r_\gamma) = 0. \tag{4.30}$$

In these equations, we introduced a relativistic mass term $M(r_\gamma) = 1 + (E^\gamma_\ell - V^\gamma_{\text{eff,sph}}(r_\gamma))/(2c^2)$. The resulting functions are normalized akin to the non-relativisitic case and the energy derivatives are again made orthogonal to them:

$$\left\langle \begin{pmatrix} g^\gamma_\ell \\ \phi^\gamma_\ell \end{pmatrix} \middle| \begin{pmatrix} g^\gamma_\ell \\ \phi^\gamma_\ell \end{pmatrix} \right\rangle_{\text{MT}^\gamma} = 1, \left\langle \begin{pmatrix} \dot{g}^\gamma_\ell \\ \dot{\phi}^\gamma_\ell \end{pmatrix} \middle| \begin{pmatrix} g^\gamma_\ell \\ \phi^\gamma_\ell \end{pmatrix} \right\rangle_{\text{MT}^\gamma} = 0. \tag{4.31}$$

From the solutions, we can recover the large component of the SRA directly and the small component as a linear combination of $\Phi_\ell$ and the large one. These large and small components then replace the scalar solution $u_\ell$ in all further calculations. The scalar-relativistic equivalents of the matching coefficients equation (4.17) should technically get another dimension to cover the large and small part of the spinor in the KS Dirac equation. Due to the scalar nature of the IR basis, however, only the large component is matched against the plane waves, neglecting the small one.

**Core Electrons** As mentioned in the previous section, the core electrons are treated fully relativistically due to a negligible rise in computational effort and their proximity to the nuclei. They give an additional spherical contribution to the MT density, which will be discussed in the next chapter. There are no expansion coefficients that are calculated self-consistently for them; they are solely determined by their energy parameters and the spherical potential. Their wave functions can be written with a factor containing the Bloch wave vector $\boldsymbol{k}$, but this does not carry a real functional dependence. We will continue the discussion of core electrons in section 4.2.3 about the density generation.

**Local Orbitals** A well explored way to improve the convergence and quality of (FL)APW calculations is supplementing the radial basis with additional functions, the so-called local orbitals (LO) [133,

165, 166]. They can be constructed in different ways for different purposes and have been used to reduce the linearization error [167, 168], to improve the description of high-lying unoccupied states [169], and to deal with core electrons, that are high in energy and not strongly confined. Such semi-core electrons are prominent in the complete left side of the periodic table and when dealing with heavy elements, as *e.g.* the $f$-electrons have an energy range that is not well-described by the low energy parameters of the core electrons. There are different classes of LOs to combat the different problems arising. An exhaustive study on them can be found in [168], where the terms "higher derivative local orbital" (HDLO) and "higher energy local orbital" (HELO) were coined. The former can be used to go to higher orders of energy differentiation for the radial functions to both reduce the linearization error and enlarging the window of well-described energies. The latter, in contrast, forego the original energy parameters to construct radial functions at a different, higher energy or $\ell$. This effectively opens up a second range of energies, where the electronic structure is well captured. The LOs are constructed from a radial differential equation similarly to the existing $u_\ell^\gamma$ and $\dot{u}_\ell^\gamma$ of a particular $\ell$ and $E_\ell$ and added onto them, to form radial terms

$$R_\ell^{\gamma,\mathrm{LO}}(r_\gamma) = a_\ell^{\gamma,\mathrm{LO}} u_\ell^\gamma(r_\gamma) + b_\ell^{\gamma,\mathrm{LO}} \dot{u}_\ell^\gamma(r_\gamma) + c_\ell^{\gamma,\mathrm{LO}} u_\ell^{\gamma,\mathrm{LO}}(r_\gamma). \tag{4.32}$$

The LO coefficients $a_\ell^{\gamma,\mathrm{LO}}, b_\ell^{\gamma,\mathrm{LO}}, c_\ell^{\gamma,\mathrm{LO}}$ are chosen, such that the radial function and its radial derivative vanish at the MT boundary and the function is normalized akin to equation (4.12). Furthermore, in the `FLEUR` code, these coefficients are multiplied by a phase factor. This means, *e.g.* for the first coefficient

$$a_{\ell m}^{\boldsymbol{k}+\boldsymbol{G}^{\mathrm{LO}},\gamma} = 4\pi \mathrm{i}^\ell \mathrm{e}^{\mathrm{i}(\boldsymbol{k}+\boldsymbol{G}^{\mathrm{LO}})\cdot\boldsymbol{\tau}_\gamma} Y_\ell^{m*}\left(\widehat{\boldsymbol{k}+\boldsymbol{G}^{\mathrm{LO}}}\right) a_\ell^{\gamma,\mathrm{LO}} / W_\ell^\gamma. \tag{4.33}$$

They are matched against a virtual plane wave with reciprocal lattice vector $\boldsymbol{G}^{\mathrm{LO}}$. Each LO enlarges the number of radial basis functions by $2\ell+1$, due to the dependence on the magnetic quantum number $m$. This ensures more variational freedom and makes LOs a remedy for the aforementioned problems. The added matching coefficients ensure their linear independence and restore the inversion symmetry (if the system exhibits it) by combining several LOs into real-valued combinations. Furthermore, they gain the same Bloch character with Bloch vector $\boldsymbol{k}$ that the rest of the basis has.

## 4.2 The Quantum Engine of FLAPW

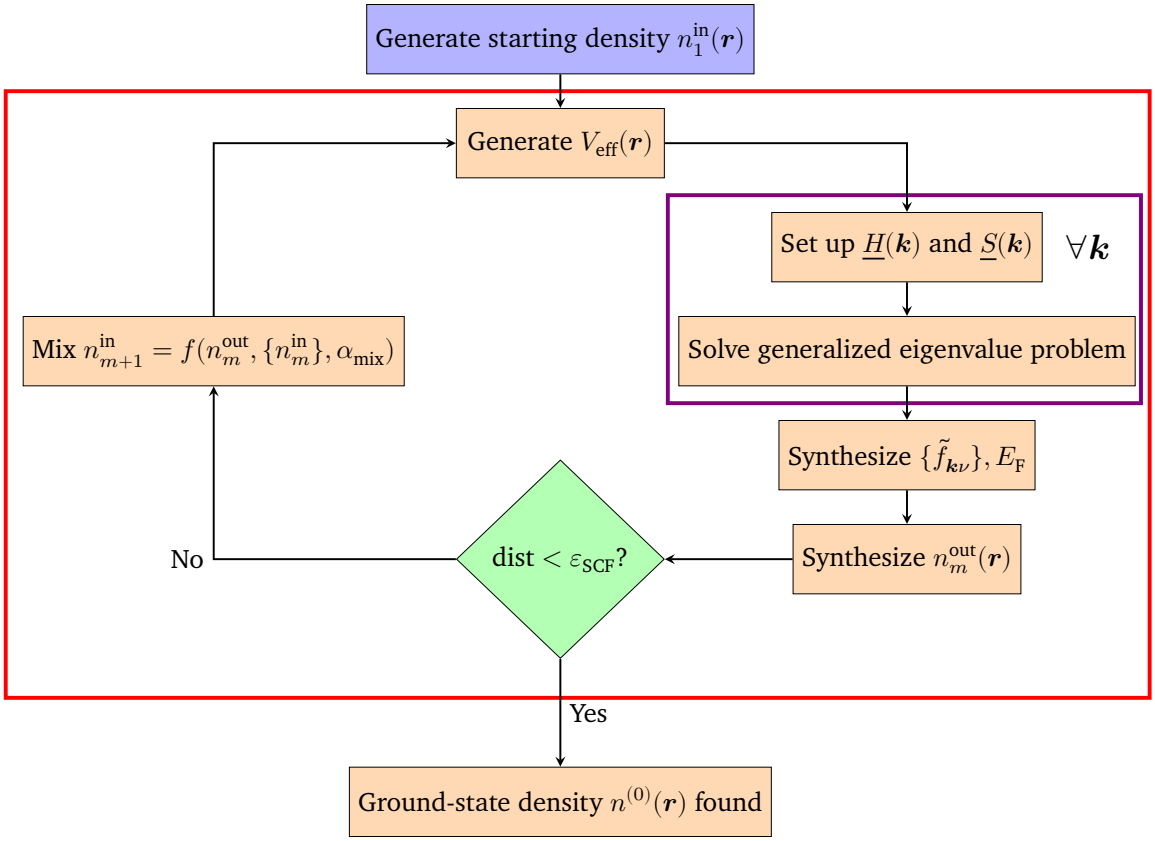



**Figure 4.2:** Sketch of the DFT self-consistency workflow for a periodic basis set. On top of the general structure in 2.2, the (generalized) eigenvalue problem has to be solved for each Bloch vector $\boldsymbol{k}$ by setting up the matrix elements $H/S_{\boldsymbol{G}'\boldsymbol{G}}(\boldsymbol{k})$ for the basis set in question, *i.e.* the LAPW basis. It does not directly result in the wave functions, but in expansion coefficients $z_{\boldsymbol{k}\boldsymbol{G}\nu}$ as its eigenvectors. Aside from the resulting k-point summations for the Fermi energy and output density, the overall structure remains intact.

The Loop Structure

Now that we have provided detailed information on each of the facets of the FLAPW method, from the all-electron character, to the lack of shape approximations, and lastly the form of the (LO supplemented) basis, it is time to move on to actually providing numerical recipes. From figure 2.2, the SCF-loop has to be adjusted to contain the loop over the Bloch vectors $\boldsymbol{k}$ and the construction of the basis specific Hamiltonian and overlap matrices. The result of this is shown in figure 4.2. We refer to the SCF-loop of the FLAPW-DFT method as the quantum engine of the code, as opposed to the property calculator that takes the results of the ground-state run to output physical results. For the next section, we will deal with the FLAPW centered specifications of each step shown in the scheme, starting with the generation of the potential.

### 4.2.1 Potential Generation

Coulomb Potential Generation

The difficulty of constructing a potential from a given charge density strongly depends on the underlying method of choice. Specifically, the shape approximations that are or are not made and the basis in which the quantities are expanded determine the degree of effort. For the Coulomb part, the central equation to solve is Poisson's equation

$$\Delta V_C(\boldsymbol{r}) = -4\pi n(\boldsymbol{r}), \tag{4.34}$$

where the second spatial derivative of the Coulomb potential (*cf.* equation (2.10) and the consequent text section) is proportional to the density. If we were to work in a PW basis, we could easily expand both sides and calculate the Fourier coefficients of the potential from those of the density. Due to the augmentation with the MT spheres, however, the problem becomes a lot more involved. Weinert proposed a cohesive recipe to deal with this challenge [170] and his method of solving Poisson's equation will be frequently highlighted as a solution to different problems in the scope of this thesis. It is based on the construction of a pseudodensity $n_{\text{ps}}(\boldsymbol{r})$, such that the straight-forward PW solution for the IR can be applied to its Fourier coefficients

$$V_{\text{C,IR}}(\boldsymbol{G}) = (1 - \delta_{\boldsymbol{G},\boldsymbol{0}}) \frac{4\pi n_{\text{ps}}(\boldsymbol{G})}{G^2}. \tag{4.35}$$

Consequently, the potential inside a specific MT can be calculated by solving equation (4.34) as a Dirichlet boundary value problem with the IR potential already fixed. This leads to a formula with the appropriate Green's function for the spherical problem and the MT density, and a surface integral over the MT boundary with the normal derivative of said Green's function and the IR potential. Evaluating the angular integrals gives a form for the MT potential coefficients

$$\begin{aligned} V_{\text{C},\gamma\ell m}(r_\gamma) =& \frac{4\pi}{2\ell+1} \int_0^{R_{\text{MT}\gamma}} r'^2 n_{\gamma\ell m}(r') \frac{r_<^\ell}{r_>^{\ell+1}} \left(1 - \left(\frac{r_>}{R_{\text{MT}\gamma}}\right)^{2\ell+1}\right) \mathrm{d}r' \\ &+ \left(\frac{r_\gamma}{R_{\text{MT}\gamma}}\right)^\ell 4\pi \mathrm{i}^\ell \sum_{\boldsymbol{G}\neq\boldsymbol{0}} \mathrm{e}^{\mathrm{i}\boldsymbol{G}\cdot\boldsymbol{\tau}_\gamma} j_\ell(GR_{\text{MT}\gamma}) Y_\ell^{m*}\left(\hat{\boldsymbol{G}}\right) V_{\text{C,IR}}(\boldsymbol{G}), \end{aligned} \tag{4.36}$$

that is only dependent on a radial integration with the variables $r_{</>} = \min / \max\{r', r_\gamma\}$. This provides an easy way to calculate the Coulomb potential. But we have yet to discuss the construction of the pseudodensity for the interstitial potential generation. It is based on the idea of slightly refactoring the density and subsequently representing it as a Fourier series. In practice, the reformulation looks as follows:

$$\begin{aligned} n(\boldsymbol{r}) &= \Theta_{\text{IR}}(\boldsymbol{r}) n_{\text{IR}}(\boldsymbol{r}) + \sum_\gamma \Theta_\gamma(\boldsymbol{r}) n_\gamma(\boldsymbol{r}) \\ &= n_{\text{IR}}(\boldsymbol{r}) + \sum_\gamma \Theta_\gamma(\boldsymbol{r}) (n_\gamma(\boldsymbol{r}) - n_{\text{IR}}(\boldsymbol{r})) \\ &\to n_{\text{IR}}(\boldsymbol{r}) + n_{\text{MT,ps}}(\boldsymbol{r}) = \sum_{\boldsymbol{G}} \left(n_{\text{IR}}(\boldsymbol{G}) + n_{\text{MT,ps}}(\boldsymbol{G})\right) \mathrm{e}^{\mathrm{i}\boldsymbol{G}\cdot\boldsymbol{r}}. \end{aligned} \tag{4.37}$$

In this we introduced a pseudodensity for the MT region, that can be smoothly expanded into plane waves and reproduces the correct multipole moments of the true MT density. This kind of pseudodensity can be inserted into equation (4.35). The only task remaining is to

express it in a closed form. This can be done by expressing the charge in the MT through multipole moments of the MT density and multipole moments of the IR density continued to the MT region, so the pseudodensity will reproduce the same moments by construction. The necessary equations are

$$n_{\mathrm{MT,ps}}(\boldsymbol{G}) = \delta_{\boldsymbol{G},\mathbf{0}}\frac{\sqrt{4\pi}}{\Omega}\sum_{\gamma}\tilde{q}^{\gamma}_{00} \tag{4.38}$$
$$+(1-\delta_{\boldsymbol{G},\mathbf{0}})\frac{4\pi}{\Omega}\sum_{\gamma\ell m}(-\mathrm{i})^{\ell}\frac{(2\ell+2N+3)!!}{(2\ell+1)!!}\frac{j_{\ell+N+1}(GR_{\mathrm{MT}\gamma})}{(GR_{\mathrm{MT}\gamma})^{N+1}}\tilde{q}^{\gamma}_{\ell m}\mathrm{e}^{-\mathrm{i}\boldsymbol{G}\cdot\boldsymbol{\tau}_{\gamma}}Y^{m}_{\ell}\left(\hat{\boldsymbol{G}}\right)$$
$$\tilde{q}^{\gamma}_{\ell m} = q^{\gamma}_{\ell m} - q^{\gamma,\mathrm{ps}}_{\ell m} \tag{4.39}$$
$$q^{\gamma}_{\ell m} = \int_{\mathrm{MT}\gamma} Y^{m*}_{\ell}\left(\hat{\boldsymbol{r}}_{\gamma}\right) r^{\ell}_{\gamma} n(\boldsymbol{r})\mathrm{d}\boldsymbol{r}_{\gamma} \tag{4.40}$$
$$q^{\gamma,\mathrm{ps}}_{\ell m} = \delta_{\ell,0}\frac{\sqrt{4\pi}}{3}R^{3}_{\mathrm{MT}\gamma}n_{\mathrm{IR}}(\mathbf{0})$$
$$+4\pi\sum_{\boldsymbol{G}\neq\mathbf{0}}\mathrm{i}^{\ell}R^{\ell+3}_{\mathrm{MT}\gamma}\frac{j_{\ell+1}(GR_{\mathrm{MT}\gamma})}{GR_{\mathrm{MT}\gamma}}n_{\mathrm{IR}}(\boldsymbol{G})\mathrm{e}^{\mathrm{i}\boldsymbol{G}\cdot\boldsymbol{\tau}_{\gamma}}Y^{m*}_{\ell}\left(\hat{\boldsymbol{G}}\right) \tag{4.41}$$

The derivation of these quantities requires repeated expansions of plane waves into spherical harmonics (like for the construction of the matching coefficients) and a study of the numerical properties of the convergence factor (*i.e.* the fractions) in the pseudodensity sum. It is influenced by the freely adjustable parameter $N$, for which Weinert gives a table of suitable values [170]. `FLEUR` automatically provides such values without the need of specifying them in the input. For the construction of the true multipole moments and the MT boundary value problem, the full density needs to be considered, the electronic and ionic part that is. That means the point charges at the MT centers also contribute.

The xc Potential

Now that the Coulomb part of the potential is well described, we turn to the description of the exchange-correlation potential. It was defined in equation (2.11c) as the functional derivative of the xc energy functional with respect to the density. For the LDA, that we use in this work, the result of this differentiation is straight-forward:

$$V_{\mathrm{xc}}(\boldsymbol{r}) = \varepsilon_{\mathrm{xc}}(n(\boldsymbol{r})) + n(\boldsymbol{r})\frac{\partial\varepsilon_{\mathrm{xc}}(n(\boldsymbol{r}))}{\partial n(\boldsymbol{r})}. \tag{4.42}$$

This means, that the exact form of the potential solely depends on the functional dependence of the xc energy density on the density and, consequently, its derivative. This can of course be a non-trivial function to differentiate (`FLEUR` provides only a selection of the most popular LDA and GGA functionals that are hardcoded), but this task is simplified greatly, when the `libxc` library of functionals is employed [171]. For a given density (or in the case of more advanced functionals additional input like the density gradient *etc.*) in real space, it constructs both the xc energy density and its derivative analytically and returns the corresponding values at the same real space points. The xc potential is thus constructed from the density in three steps. i) Transforming the density from coefficient space into real space by multiplying it with the lattice harmonics in the MT regions on a grid of points in the sphere and Fourier transforming the Fourier components in the IR on a dense real space grid. ii) Evaluating the xc quantities in real space with the use of `libxc`. iii) Transforming the real space quantities back into coefficient space. These coefficients can then be added onto those of the Coulomb

potential to gain the full effective potential. This concludes our summary of the potential generation and we move on to the next step of the SCF loop.

### 4.2.2 Matrix Setup and Diagonalization

As shown in equation (4.13), the setup of the Hamiltonian and overlap matrices in an (L)APW basis consists of more terms than the simple PW potential integral. Here we highlight the fully evaluated form these contributions take, starting with terms that stem from the IR quantities. The unit cell integral involving the IR potential amounts to a convolution of it and the step function in reciprocal space, as it is a product of the same in real space. In practice, the step function and potential are actually Fourier transformed onto a real space grid, multiplied into a warped potential $\tilde{V}_{\text{eff}}(\boldsymbol{r}) = \Theta_{\text{IR}}(\boldsymbol{r})V_{\text{eff}}(\boldsymbol{r})$, and then transformed back - akin to the procedure for the xc potential generation. The integration results in a contribution $\tilde{V}(\boldsymbol{G}-\boldsymbol{G}')$ to the Hamiltonian matrix element. The second contribution is the kinetic energy term, that involves the application of the Laplace operator to the plane wave and the evaluation of the step function. The same evaluation needs to be done for the overlap matrix, yielding the IR matrix elements

$$H^{\text{IR}}_{\boldsymbol{G}',\boldsymbol{G}}(\boldsymbol{k}) = \tilde{V}(\boldsymbol{G}-\boldsymbol{G}') + \frac{|\boldsymbol{k}+\boldsymbol{G}|^2}{2}\Theta_{\text{IR}}(\boldsymbol{G}-\boldsymbol{G}'), \tag{4.43}$$

$$S^{\text{IR}}_{\boldsymbol{G}',\boldsymbol{G}}(\boldsymbol{k}) = \Theta_{\text{IR}}(\boldsymbol{G}-\boldsymbol{G}'). \tag{4.44}$$

The MT contributions to the matrices decompose into a spherical part and a non-spherical one, the latter of which only contributes to the Hamiltonian. Evaluating the MT integral of the basis functions gives an overlap contribution

$$S^{\text{MT}}_{\boldsymbol{G}',\boldsymbol{G}}(\boldsymbol{k}) = \sum_{\gamma\ell m} a^{\boldsymbol{k}+\boldsymbol{G}',\gamma *}_{\ell m} a^{\boldsymbol{k}+\boldsymbol{G},\gamma}_{\ell m} + b^{\boldsymbol{k}+\boldsymbol{G}',\gamma *}_{\ell m} b^{\boldsymbol{k}+\boldsymbol{G},\gamma}_{\ell m} \langle \dot{u}^{\gamma}_{\ell} | \dot{u}^{\gamma}_{\ell} \rangle_{\text{MT}^{\gamma}}. \tag{4.45}$$

The spherical Hamiltonian looks similar. We make use of the defining differential equations of the radial functions (4.11) and energy derivatives (4.15), to find

$$\begin{aligned} H^{\text{MT,sph}}_{\boldsymbol{G}',\boldsymbol{G}}(\boldsymbol{k}) = \sum_{\gamma\ell m} & E^{\gamma}_{\ell} a^{\boldsymbol{k}+\boldsymbol{G}',\gamma *}_{\ell m} a^{\boldsymbol{k}+\boldsymbol{G},\gamma}_{\ell m} + a^{\boldsymbol{k}+\boldsymbol{G}',\gamma *}_{\ell m} b^{\boldsymbol{k}+\boldsymbol{G},\gamma}_{\ell m} \\ & + E^{\gamma}_{\ell} b^{\boldsymbol{k}+\boldsymbol{G}',\gamma *}_{\ell m} b^{\boldsymbol{k}+\boldsymbol{G},\gamma}_{\ell m} \langle \dot{u}^{\gamma}_{\ell} | \dot{u}^{\gamma}_{\ell} \rangle_{\text{MT}^{\gamma}}. \end{aligned} \tag{4.46}$$

In the non-spherical part, the integral over the spherical harmonics in the basis does not directly collapse the sum, as there is a third factor from the potential term. This is tantamount to saying that the three spherical harmonics form Gaunt coefficients instead of Kronecker deltas when integrated. For the purposes of this thesis, we define them by

$$G^{m',m'',m}_{\ell',\ell'',\ell} := \oint_{\partial B_1(\boldsymbol{0})} Y^{m'*}_{\ell'}(\hat{\mathrm{r}}) Y^{m''}_{\ell''}(\hat{\mathrm{r}}) Y^{m}_{\ell}(\hat{\mathrm{r}}) \mathrm{d}S. \tag{4.47}$$

The integration domain is the ball of radius $1$ around the origin. They only have a finite value, when a) the relation $m' = m + m''$ and b) the triangle inequality $|\ell - \ell''| \leq \ell' \leq \ell + \ell''$ are fulfilled. We use the coefficients to first integrate out the radial dependencies of the non-spherical Hamiltonian matrix:

$$t^{\gamma(\cdot)(\cdot)}_{\ell' m' \ell m} := \langle u^{(\cdot)\gamma}_{\ell'} Y^{m'}_{\ell'} | V^{\gamma}_{\text{eff,nsph}} | u^{(\cdot)\gamma}_{\ell} Y^{m}_{\ell} \rangle_{\gamma} = \sum_{\ell''\geq 1, m''} G^{m',m'',m}_{\ell',\ell'',\ell} \langle u^{(\cdot)\gamma}_{\ell'} | V_{\text{eff},\gamma\ell''m''} | u^{(\cdot)\gamma}_{\ell} \rangle_{\gamma}. \tag{4.48}$$

These t-coefficients form a matrix $\underline{t}$ in the space spanned by the superindices $(\ell m(\cdot))$, where the $(\cdot)$ discriminates between radial functions and their energy derivatives. If we define a supervector in these same indices from the matching coefficients of both the radial functions and energy derivatives, $\boldsymbol{a}^{\boldsymbol{k}+\boldsymbol{G},\gamma} = (a_{00}^{\boldsymbol{k}+\boldsymbol{G},\gamma}, ..., a_{\ell_{\max}\ell_{\max}}^{\boldsymbol{k}+\boldsymbol{G},\gamma}, b_{00}^{\boldsymbol{k}+\boldsymbol{G},\gamma}, ..., b_{\ell_{\max}\ell_{\max}}^{\boldsymbol{k}+\boldsymbol{G},\gamma})^\top$, we can efficiently cast the Hamiltonian matrix elements as the result of a linear algebra problem and write

$$H^{\text{MT,nsph}}_{\boldsymbol{G}',\boldsymbol{G}}(\boldsymbol{k}) = \sum_\gamma \boldsymbol{a}^{\boldsymbol{k}+\boldsymbol{G}',\gamma\dagger} \cdot \underline{t}^\gamma \cdot \boldsymbol{a}^{\boldsymbol{k}+\boldsymbol{G},\gamma}. \tag{4.49}$$

This constitutes a problem with big matrices and vectors well-suited for the application of GPU computing power. In practice, the higher $\ell$ contributions will contribute less and less to the matrix element and in FLEUR, an additional cutoff $\ell_{\text{nsph}}$ is introduced, that limits the extent of $\underline{t}$.

LO Contributions

Until now, only the radial functions and energy derivatives to the MT matrices were discussed. There will be combinations of these functions with local orbitals and LO-LO combinations that contribute as well. They are constructed in a very similar way to the MT part of the basic Hamiltonian. But there is one key difference: The local orbitals are only artificially matched to the IR, as their radial part vanishes at the MT boundaries. This means they are completely independent of the plane waves and each LO constitutes an additional linearly independent basis function. This means the number of possible states in the system is also increased. The LOs are thus not summed onto the rest of the Hamiltonian and overlap, but rather extend its size in each dimension by the total number of LOs in the system $N_{\text{LO}} = \sum_{\text{LO}}(2\ell_{\text{LO}} + 1)$.

Symmetrization and Occupations

The Hamiltonian of a solid state system should by definition be a self-adjoint operator and thus the constructed matrix is to be Hermitian. In practice, FLEUR ensures this by calculating parts of the Hamiltonian slightly differently. In particular, the Laplace operator in the KS equation is made to not only apply to the basis function on its right, but averaged between working to the left and to the right. This modifies the kinetic energy term in the IR (4.43) and the spherical Hamiltonian term in the MT (4.46):

$$\frac{|\boldsymbol{k}+\boldsymbol{G}|^2}{2} \longrightarrow \frac{|\boldsymbol{k}+\boldsymbol{G}'|^2 + |\boldsymbol{k}+\boldsymbol{G}|^2}{4}, \tag{4.50}$$

$$a_{\ell m}^{\boldsymbol{k}+\boldsymbol{G}',\gamma *} b_{\ell m}^{\boldsymbol{k}+\boldsymbol{G},\gamma} \longrightarrow \frac{1}{2}\left(a_{\ell m}^{\boldsymbol{k}+\boldsymbol{G}',\gamma *} b_{\ell m}^{\boldsymbol{k}+\boldsymbol{G},\gamma} + b_{\ell m}^{\boldsymbol{k}+\boldsymbol{G}',\gamma *} a_{\ell m}^{\boldsymbol{k}+\boldsymbol{G},\gamma}\right). \tag{4.51}$$

Once all eigenenergies and expansion coefficients are determined by solving equation (4.2) for the symmetrized Hamiltonian, the state-dependent information for the iteration is fully determined. From the eigenenergy spectrum, the Fermi energy and the occupation of each state is determined by iterating from an initial guess $E_{\text{F}} = \max\{\varepsilon_{\boldsymbol{k}\nu}\}$ as described in section 2.4. The index $\nu$ counts all states ordered by energy, that sum up to just below the electron count, when no smearing is applied. The only amendment is, that now the (fractionally) occupied states for all Bloch vectors need to add up to the total electron count, adding an additional index to the occupation numbers $\tilde{f}_{\boldsymbol{k}\nu}$ as discussed for equation (3.6).

### 4.2.3 Density Generation

Valence Electron Density

The determination of the expansion coefficients and occupation numbers enables the calculation of the electron density of the system. For this we once again look at the IR and MT region

separately. For the plane wave functions, the expansion coefficients are Fourier transformed (FT) onto a real space grid and normalized with the volume of the unit cell, to find the wave functions

$$\psi_{\boldsymbol{k}\nu}(\boldsymbol{r}) = \frac{1}{\sqrt{\Omega}}\mathrm{FT}[z_{\boldsymbol{k}\boldsymbol{G}\nu}] = \frac{1}{\sqrt{\Omega}}\sum_{\boldsymbol{G}} z_{\boldsymbol{k}\boldsymbol{G}\nu} \mathrm{e}^{\mathrm{i}\boldsymbol{G}\cdot\boldsymbol{r}}, \tag{4.52}$$

which are then squared, weighted with the occupation numbers, and summed up for each Bloch vector. The phase factor from the k-point itself is neglected, as it vanishes through this procedure. This yields the Fourier coefficients for the density of a specific $\boldsymbol{k}$

$$n_{\mathrm{IR},\boldsymbol{k}}(\boldsymbol{G}) = \mathrm{IFT}[\sum_{\nu} \tilde{f}_{\boldsymbol{k}\nu} |\psi_{\boldsymbol{k}\nu}(\boldsymbol{r})|^2] \tag{4.53}$$

when transformed back (inverse Fourier transform IFT) into coefficient space. Evaluating the sum over all Bloch vectors then yields the Fourier coefficients of the full valence electron density. The same contribution for the MT spheres is constructed in a different way. First, the wave function in a specific MT $\gamma$

$$\psi^{\gamma}_{\boldsymbol{k}\nu}(\boldsymbol{r}) = \sum_{\boldsymbol{G}} z_{\boldsymbol{k}\boldsymbol{G}\nu}\phi^{\gamma}_{\boldsymbol{k}\boldsymbol{G}}(\boldsymbol{r}) = \sum_{\ell m}\left(A^{\boldsymbol{k}\nu\gamma}_{\ell m} u^{\gamma}_{\ell}(r_\gamma) + B^{\boldsymbol{k}\nu\gamma}_{\ell m}\dot{u}^{\gamma}_{\ell}(r_\gamma)\right) Y^{m}_{\ell}(\hat{\mathrm{r}}_\gamma) \tag{4.54}$$

is expressed in terms of the large matching coefficients. From there, the idea is to reduce the formula down to a sum of weighted radial functions and energy derivatives, *i.e.* summing over all indices besides the angular quantum numbers for each Bloch vector and then evaluating the sum over all Bloch vectors as it is done in the IR case. In this spirit, the full density coefficient of atom $\gamma$ can be written with the summed prefactors $d^{\boldsymbol{k}\gamma}_{\ell'\ell\ell''(\cdot)'(\cdot)}$ as

$$\begin{aligned} n_{\gamma\ell''m''}(r_\gamma) &= \sum_{\boldsymbol{k}\nu}\tilde{f}_{\boldsymbol{k}\nu}\sum_{\substack{\ell' m'(\cdot)' \\ \ell m(\cdot)}} A^{\boldsymbol{k}\nu\gamma *}_{\ell' m'(\cdot)'} \overset{(\cdot)'\gamma}{u}_{\ell'}(r_\gamma) A^{\boldsymbol{k}\nu\gamma}_{\ell m(\cdot)} \overset{(\cdot)\gamma}{u}_{\ell}(r_\gamma) G^{m,m'',m'}_{\ell,\ell'',\ell'} \\ &= \sum_{\boldsymbol{k}}\sum_{\substack{\ell'(\cdot)' \\ \ell(\cdot)}} d^{\boldsymbol{k}\gamma}_{\ell'\ell\ell''(\cdot)'(\cdot)} \overset{(\cdot)'\gamma}{u}_{\ell'}(r_\gamma)\overset{(\cdot)\gamma}{u}_{\ell}(r_\gamma). \end{aligned} \tag{4.55}$$

As was the case when constructing the matrix elements, the selection of certain channels $(\ell'' m'')$ leads to integrals over three spherical harmonics and consequently to the evaluation of Gaunt coefficients. With these formulae, the valence density coefficients can be constructed component wise within the Bloch vector loop, alongside the IR Fourier coefficients. The summation over the radial functions can be done after the loop and is computationally cheap.

Core Electron Density

The core electron density $n_{\mathrm{core}}$ is constructed separately from the valence contribution. As mentioned before, the core electrons are assumed to be confined to their respective MT sphere and to have their radial functions vanish at the MT boundary. This leads to a description of the MT through spherically symmetric functions, when the (occupied) core states are summed over all relevant quantum numbers (expressed as a composite index $c = (n\ell m_\ell)$ for the quantum numbers of the Schrödinger equation or $c = (njm_j)$ for the relativistic Dirac case). The corresponding MT coefficients read

$$n_{\mathrm{core},\gamma 00}(r_\gamma) = \sqrt{4\pi}\sum_{c} |\psi_c(r_\gamma)|^2. \tag{4.56}$$

Here, there is once again a distinction between large and small components due to the relativistic nature of the Dirac equation, which we omit for the sake of brevity. If the core electrons are sufficiently confined to their MT spheres, this description is enough to describe their contribution to the density. Conversely, if there are high-lying core states that are not properly modeled by taking additional LOs into account there can be a leakage of charge into the interstitial region. Usually, when the leakage is small, the resulting leaked charge can be subtracted from the overall charge $Q_{\text{core}}$ of the core electrons and then smoothly distributed by averaging it with respect to the IR volume. This gives an additional $\boldsymbol{G} = \boldsymbol{0}$ contribution to the Fourier coefficients

$$n_{\text{core,IR}}(\boldsymbol{G} = \boldsymbol{0}) = \left( Q_{\text{core}} - \sum_{\gamma} \int_0^{R_{\text{MT}^\gamma}} r_\gamma^2 n_{\text{core},\gamma 00}(r_\gamma) Y_0^0 \mathrm{d}r_\gamma \right) / \Omega_{\text{IR}}. \tag{4.57}$$

Another way to deal with cases of bigger leakage is the proper description of the leaking core-tails [172] through a proper Fourier transform onto the IR density coefficients and a subsequent continuation into the other MT spheres. For this, the core density is first modeled by a Gaussian in the MT as

$$\tilde{n}_{\text{core}}^{\gamma}(\boldsymbol{r}_\gamma) = \begin{cases} A_\gamma \mathrm{e}^{-a_\gamma r_\gamma^2}, & r_\gamma \leq R_{\text{MT}^\gamma} \\ n_{\text{core},\gamma 00}(r_\gamma) Y_0^0, & \text{else} \end{cases}, \tag{4.58}$$

where the coefficients are determined as to ensure a continuous and differentiable function at the MT boundary. $\tilde{n}_{\text{core}}^{\gamma}$ can be seen as the density of the core-tails leaking into the interstitial and other MT spheres. The Fourier coefficients of the resulting IR core-tail density are

$$n_{\text{ct,IR}}(\boldsymbol{G}) = \sum_{\gamma} \underbrace{\mathrm{e}^{-\mathrm{i}\boldsymbol{G}\cdot\boldsymbol{\tau}_\gamma}}_{S_\gamma(\boldsymbol{G})} \underbrace{\frac{1}{\Omega} \int_\gamma \tilde{n}_{\text{core}}^{\gamma}(\boldsymbol{r}_\gamma) \mathrm{d}\boldsymbol{r}_\gamma}_{F_\gamma(\boldsymbol{G})}, \tag{4.59}$$

where we defined the structure factor $S_\gamma(\boldsymbol{G})$ and the form factor $F_\gamma(\boldsymbol{G})$. Once the latter is determined, they can be used to calculate the density

$$\tilde{n}_{\text{ct},\gamma'\ell m}^{\gamma}(\boldsymbol{r}_\gamma) = 4\pi \mathrm{i}^\ell \sum_{\boldsymbol{G}} S_\gamma(\boldsymbol{G}) F_\gamma(\boldsymbol{G}) S_{\gamma'}^*(\boldsymbol{G}) Y_\ell^{m*}(\hat{\mathrm{G}}) j_\ell(G r_{\gamma'}) \tag{4.60}$$

induced in a MT sphere $\gamma' \neq \gamma$ by the core-tail of atom $\gamma$. Adding the core electron density to the valence contribution finally gives the full density of the electrons. To ensure the charge neutrality of the system, at this point it is normally checked that the unit cell integral of the charge density reproduces the total electronic charge. If there are slight deviations, the density is corrected by a global factor on all coefficients, so the condition is met.

### 4.2.4 Total Energy and Mixing

Calculating the Total Energy

In contrast to the general and unspecific total energy calculation in KS DFT (equation (2.13)), the application of the FLAPW method in a periodic lattice directly affects the evaluation of the density-potential and xc integral terms, as well as the ion-ion interaction. A way of dealing with the latter term, that has to explicitly avoid self-interaction by prohibiting the combination of an atom with itself in the summation, was proposed by Weinert, Wimmer, and

Freeman [173]. In their seminal paper, the electron-ion and ion-ion interaction are grouped into a Madelung term, that can be used to construct a boundary problem and cancel out the divergent ionic self-interaction. Thus, the total energy reduces to a form

$$\begin{aligned} E_{\text{tot}} = &\sum_{\boldsymbol{k}\nu} \tilde{f}_{\boldsymbol{k}\nu}\varepsilon_{\boldsymbol{k}\nu} - \frac{1}{2}\left[\int_\Omega n(\boldsymbol{r})V_{\text{C}}(\boldsymbol{r})\mathrm{d}\boldsymbol{r} + \sum_\gamma Z_\gamma \left\langle \frac{n(\boldsymbol{r}_\gamma)}{r_\gamma}\right\rangle_\gamma\right] \\ &-\frac{1}{2}\sum_\gamma \frac{Z_\gamma}{R_{\text{MT}\gamma}}\left[R_{\text{MT}\gamma}\bar{V}_{\text{C}}(R_{\text{MT}\gamma}) + Z_\gamma - Q_\gamma\right] \\ &+\int_\Omega n(\boldsymbol{r})\left[\varepsilon_{\text{xc}}[n](\boldsymbol{r}) - V_{\text{xc}}(\boldsymbol{r})\right]\mathrm{d}\boldsymbol{r} - TS, \end{aligned} \tag{4.61}$$

where the average Coulomb potential $\bar{V}_{\text{C}}(R_{\text{MT}\gamma})$ at the boundary of the MT sphere $\gamma$ and the electronic charge $Q_\gamma$ in said sphere were introduced. $\langle ...\rangle$ indicates the radial integral of a function in the same sphere. This form can easily be handled numerically and relies solely on quantities that are already calculated during the iteration. Only the evaluation of the unit cell integrals needs to be discussed. For this we recall the representation of the density (equation (4.22)) and potential (equation (4.23)) in plane waves and spherical harmonics, or rather the symmetrized form of stars and lattice harmonics in equation (4.26). The integral over a product of two such functions reduces to a scalar product of their respective coefficients due the orthogonality of the basis in which they are expanded. Hence we can write for two arbitrary functions $X, Y$ in this representation

$$\int_\Omega X_{\text{IR}}(\boldsymbol{r})Y_{\text{IR}}(\boldsymbol{r})\mathrm{d}\boldsymbol{r} = \Omega\sum_s X^*_{\text{IR}}(s)Y_{\text{IR}}(s), \tag{4.62}$$

$$\int_\gamma X_\gamma(\boldsymbol{r}_\gamma)Y_\gamma(\boldsymbol{r}_\gamma)\mathrm{d}\boldsymbol{r}_\gamma = \sum_L \int_\gamma r_\gamma^2 X_{\gamma L}(r_\gamma)Y_{\gamma L}(r_\gamma)\mathrm{d}r_\gamma. \tag{4.63}$$

In practice, the IR integral will contain the step function $\Theta_{\text{IR}}$ as well to cut out the MT region and we need a proper way to execute the radial integration there. These points will be addressed in the following section on mixing, where the general form is further evaluated to reduce unit cell integrals to a matrix-vector operation with real coefficients.

Mixing in the FLAPW Method

To conclude the discussion of the SCF iteration, there needs to be a specification of the general mixing scheme in section 2.5, that is tailored to the representation of the charge density in the FLAPW method. That means finding a closed form for the distance in equation (2.21) expressed in the star and lattice harmonic coefficients. If we define the difference between the input and output densities of iteration $m$ as a function $\Delta(\boldsymbol{r})$, we find

$$\text{dist}\left(n_m^{\text{out}}, n_m^{\text{in}}\right) = \sqrt{\frac{1}{\Omega}\int_\Omega \Delta^2(\boldsymbol{r})\mathrm{d}\boldsymbol{r}} \tag{4.64}$$

for the unit cell volume $\Omega$ and the task at hand is the solution of a unit cell integral

$$\int_\Omega \Delta^2(\boldsymbol{r})\mathrm{d}\boldsymbol{r} = \int_\Omega \Theta_{\text{IR}}(\boldsymbol{r})\Delta^2(\boldsymbol{r})\mathrm{d}\boldsymbol{r} + \sum_\gamma \int_\gamma \Delta^2(\boldsymbol{r}_\gamma)\mathrm{d}\boldsymbol{r}_\gamma. \tag{4.65}$$

Let us first investigate the IR contribution. It is expanded in stars and weighted with the IR step function, that is expanded the same way. This can be rewritten as a product of only

two star function, when the coefficients of the step function and one of the $\Delta$ functions are convoluted. It can be seen as applying a metric $g$ to the star coefficients of $\Delta$. We implicitly define the function $\tilde{\Delta}$, where this is already done, and use the orthogonality of the stars to write

$$\int_\Omega \Theta_{\mathrm{IR}}(\boldsymbol{r})\Delta^2(\boldsymbol{r})\mathrm{d}\boldsymbol{r} = \int_\Omega \Delta^*(\boldsymbol{r}) \underbrace{(\Theta_{\mathrm{IR}}\Delta)}_{\tilde{\Delta}}(\boldsymbol{r})\mathrm{d}\boldsymbol{r} = \sum_s \Delta^*(s)\tilde{\Delta}_{\mathrm{IR}}(s). \tag{4.66}$$

In the MT, the procedure is analogous. The integration over the spheres is transformed into numerical integration with function values and integration weights at the radial grid points $r_\gamma^i$, that can also be seen as a metric $g$ to multiply with $\Delta$, and the orthogonality of the lattice harmonics is used. This leads to

$$\int_\gamma \Delta^2(\boldsymbol{r}_\gamma)\mathrm{d}\boldsymbol{r}_\gamma = \sum_{Li} \Delta_{\gamma L}^{(*)}(r_\gamma^i) \underbrace{g(r_\gamma^i)\Delta_{\gamma L}(r_\gamma^i)}_{\tilde{\Delta}} = \sum_{Li} \Delta_{\gamma L}(r_\gamma^i)\tilde{\Delta}_{\gamma L}(r_\gamma^i). \tag{4.67}$$

The two complementary descriptions of IR and MT allow for an elegant description of the mixing procedure: A real-valued mixing vector $\boldsymbol{\Delta}$ is defined, that contains all the star and lattice harmonic coefficients (the former of which are split into their real and imaginary part and the latter are evaluated at the radial grid points). The metric is applied to it and then the scalar product with the initial mixvector is calculated. Formally, this can be written as a multiplication of vectors with a matrix $\underline{g}$ representing the metric:

$$\int_\Omega \Delta^2(\boldsymbol{r})\mathrm{d}\boldsymbol{r} = \boldsymbol{\Delta}^\top \underline{g}\boldsymbol{\Delta}. \tag{4.68}$$

From this, the distance between two charge density iterations can finally be calculated. It gives a measure of convergence of the SCF procedure and allows for the supervision of the process. After the densities are mixed, the resulting new input density enters the loop in the next iteration and all the steps in this section are repeated, until the distance falls under a preset threshold. This closes the discussion of the FLAPW SCF loop.

## 4.3 Adapting DFPT to FLAPW

### 4.3.1 Correction Terms of the Position-Dependent Basis

Correction Terms

After specifying the workflow for a ground-state density calculation to the FLAPW method, the same needs to be done for the DFPT framework. In the self-consistent workflow that links the wave function, density, and potential responses, each step has to be tailored to the specifics of the formalism. This becomes prominent for the first time in the LAPW basis functions (4.16) that are used to expand the wave functions in equation (4.1). The difficulty, as opposed to the basic formalism outlined in section 3.5, is the dependency of the LAPW basis set on the atomic positions. They are directly related to the phononic perturbation at hand, which is reflected in the wave functions subdividing into two parts: a part that can be expressed in the original set of basis functions, *i.e.* living in the same Hilbert space and thus marked with a subscript $||$, and a part that is orthogonal to the original basis, with a subscript $\perp$:

$$\begin{aligned}\psi_{\boldsymbol{kq}\nu}^{(1)\beta j+}(\boldsymbol{r}) &= \sum_{\boldsymbol{G}} z_{\boldsymbol{kGq}\nu}^{(1)\beta j+}\phi_{\boldsymbol{kGq}}(\boldsymbol{r}) + z_{\boldsymbol{kG}\nu}\sum_{\boldsymbol{R}} \mathrm{e}^{\mathrm{i}\boldsymbol{q}\cdot\boldsymbol{R}}\phi_{\boldsymbol{kG}}^{(1)\beta\boldsymbol{R}j}(\boldsymbol{r}) \\ &= \psi_{||,\boldsymbol{kq}\nu}^{(1)\beta j+}(\boldsymbol{r}) + \psi_{\perp,\boldsymbol{kq}\nu}^{(1)\beta j+}(\boldsymbol{r}).\end{aligned} \tag{4.69}$$

The part outside the original Hilbert space directly follows from the response of the basis to a shift of the atomic positions. It can be analytically derived from equation (4.16). The perturbation only acts on the basis function in the specific MT and unit cell, where the displaced atom is located. It consists of three parts: i) a derivative of the matching coefficients, that gives an imaginary prefactor, ii) a response term linked to the perturbation of the radial basis functions and energy derivatives, and iii) a gradient term, that stems from the differentiation of the spatial dependency of the basis function. The latter two form the incomplete basis set correction (IBC). The second term is assumed to be negligible, which leads to the so-called frozen-augmentation approximation [80] to the basis response. It is equivalent to taking the Pulay corrections [174] to the basis into account, while neglecting the radial basis response [175]:

$$\phi^{(1)\beta\boldsymbol{R}j}_{\boldsymbol{kG}}(\boldsymbol{r}) = \Theta_{\beta\boldsymbol{R}}(\boldsymbol{r})(\mathrm{i}(\boldsymbol{k}+\boldsymbol{G}) - \nabla)_j \phi^{\beta\boldsymbol{R}}_{\boldsymbol{kG}}(\boldsymbol{r}). \tag{4.70}$$

The part of the response not contained in the original basis is solely the gradient term, which will be of further interest at different points in the calculation.

The shift of the atomic coordinates has another side effect, however. It changes the range of integration for integrals over the unit cell, when they contain the displaced MT. This means, if such an integral is differentiated with respect to the perturbation, there will be additional surface terms arising. These are dependent on the normal vector $\hat{\boldsymbol{e}}_r$ of the MT surface and consist of an MT contribution as well as an interstitial term with a negative prefactor. This can be expressed as a surface integral of the discontinuity at the MT boundary:

$$\frac{\partial}{\partial\tau_{\beta\boldsymbol{R}j}}\int X(\boldsymbol{r})\mathrm{d}\boldsymbol{r} = \int \frac{\partial X(\boldsymbol{r})}{\partial\tau_{\beta\boldsymbol{R}j}}\mathrm{d}\boldsymbol{r} + \oint_{\partial\beta\boldsymbol{R}} [X(\boldsymbol{r})]_{\mathrm{SF}}\hat{\boldsymbol{e}}_{r,j}\mathrm{d}S, \tag{4.71}$$

$$[X(\boldsymbol{r})]_{\mathrm{SF}} \coloneqq X_{\mathrm{MT}}(\boldsymbol{r}) - X_{\mathrm{IR}}(\boldsymbol{r}). \tag{4.72}$$

Such terms appear frequently both in solving the Sternheimer equation and in calculating the dynamical matrix.

It is useful to keep two reformulations in mind. Firstly, through a variant of Gauss' theorem, the integral over a closed surface of a scalar function can be rewritten into an integral over the contained volume of the function's gradient. Secondly, splitting the unit cell integral into the MT and IR before differentiating and expressing the IR as an integration over the original function modulated with the IR step function, the IR surface integral can be associated with the differentiated term, that contains a perturbation of said step function. The resulting formulae are

$$\oint_{\partial\beta\boldsymbol{R}} X_{\mathrm{MT}}(\boldsymbol{r})\hat{\boldsymbol{e}}_{r,j}\mathrm{d}S = \int_{\beta\boldsymbol{R}} \nabla_j X(\boldsymbol{r})\mathrm{d}\boldsymbol{r}, \tag{4.73a}$$

$$-\oint_{\partial\beta\boldsymbol{R}} X_{\mathrm{IR}}(\boldsymbol{r})\hat{\boldsymbol{e}}_{r,j}\mathrm{d}S = \int \frac{\partial\Theta_{\mathrm{IR}}(\boldsymbol{r})}{\partial\tau_{\beta\boldsymbol{R}j}} X(\boldsymbol{r})\mathrm{d}\boldsymbol{r} = \int \Theta^{(1)\beta\boldsymbol{R}j}_{\mathrm{IR}}(\boldsymbol{r})X(\boldsymbol{r})\mathrm{d}\boldsymbol{r}. \tag{4.73b}$$

These identities will be used frequently to recast MT surface integrals into gradient terms, that can then be used to cancel out those stemming from the basis response. This improves the algorithm's stability, as the numerical handling (*e.g.* integration) of such gradient terms can be problematic. This is due to the fact, that *e.g.* the gradient of the density has to be calculated numerically which can lead to problems both near the core, where the density becomes negligible, and near the MT boundary, where the spacing between the radial grid

points is largest due to the choice of a logarithmic grid. Furthermore, something of note about the first order responses of real-space quantities is their similarity to a gradient of the same function. Their calculation involves differentiation with respect to the atomic positions, which *e.g.* for the external potential is exactly the same as taking its gradient (baring a minus sign). While this similarity is more implicit in other quantities, this gives them something like a "gradient character" in the MT of the displaced atom. They are therefore best handled numerically, when the gradient is added in this MT for the same displacement direction. As this will be done frequently, *e.g.* in the evaluation of matrix elements in equation (4.89), we introduce a notation for this grouping of responses and gradients:

$$X^{(1)\beta \boldsymbol{R} j \nabla}(\boldsymbol{r}) := X^{(1)\beta \boldsymbol{R} j}(\boldsymbol{r}) + \Theta_{\beta \boldsymbol{R}}(\boldsymbol{r}) \nabla_j X(\boldsymbol{r}). \tag{4.74}$$

### 4.3.2 First Order Energy Derivatives

Now that the general numerical and conceptional difficulties have been pointed out, it is time to figure out which quantities need to be calculated for the construction of the dynamical matrix. For this calculation, as given in equation (3.21), the second order energy derivative is required. This section gives a short derivation of its closed form. Starting from equation (2.13) with the added entropy term, the construction of the first order energy response for a displacement of atom $\alpha \boldsymbol{R}$ into the $i$-direction leads to a long assortment of terms, due to both the application of the product rule in integral contributions and the explicit treatment of the resulting surface corrections:

$$\begin{aligned}
E_{\text{tot}}^{(1)\alpha \boldsymbol{R} i} = & \sum_{\boldsymbol{k}\nu} [\tilde{f}_{\boldsymbol{k}\nu}^{(1)\alpha \boldsymbol{R} i} \varepsilon_{\boldsymbol{k}\nu} + \tilde{f}_{\boldsymbol{k}\nu} \varepsilon_{\boldsymbol{k}\nu}^{(1)\alpha \boldsymbol{R} i}] - T S^{(1)\alpha \boldsymbol{R} i} && \text{(4.75a)} \\
& + \int n^{(1)\alpha \boldsymbol{R} i}(\boldsymbol{r}) \left[ -V_{\text{eff}}(\boldsymbol{r}) + \frac{1}{2} V_{\text{H}}(\boldsymbol{r}) + V_{\text{ext}}(\boldsymbol{r}) + \varepsilon_{\text{xc}}[n](\boldsymbol{r}) \right] \mathrm{d}\boldsymbol{r} && \text{(4.75b)} \\
& + \int n(\boldsymbol{r}) \left[ -V_{\text{eff}}(\boldsymbol{r}) + \frac{1}{2} V_{\text{H}}(\boldsymbol{r}) + V_{\text{ext}}(\boldsymbol{r}) + \varepsilon_{\text{xc}}[n](\boldsymbol{r}) \right]^{(1)\alpha \boldsymbol{R} i} \mathrm{d}\boldsymbol{r} && \text{(4.75c)} \\
& + \oint_{\partial \alpha \boldsymbol{R}} \left[ n(\boldsymbol{r}) \left[ -V_{\text{eff}}(\boldsymbol{r}) + \frac{1}{2} V_{\text{H}}(\boldsymbol{r}) + V_{\text{ext}}(\boldsymbol{r}) + \varepsilon_{\text{xc}}[n](\boldsymbol{r}) \right] \right]_{\text{SF}} \hat{\boldsymbol{e}}_{r,i} \mathrm{d}S && \text{(4.75d)} \\
& + E_{\text{ii}}^{(1)\alpha \boldsymbol{R} i}. && \text{(4.75e)}
\end{aligned}$$

This lengthy formula can be reduced piece by piece by employing identities that either hold for the system or can be easily derived. Firstly, the contributions from the occupation number and entropy responses in line (4.75a) directly cancel out. This is what the entropy term was introduced for in [125], as making

$$\sum_{\boldsymbol{k}\nu} \tilde{f}_{\boldsymbol{k}\nu}^{(1)\alpha \boldsymbol{R} i} \varepsilon_{\boldsymbol{k}\nu} - T S^{(1)\alpha \boldsymbol{R} i} = 0. \tag{4.76}$$

vanish keeps the formulation variational to first order. Secondly, an explicit form for the perturbed Hartree potential can be constructed. It takes on a Hartree-like form again, only with respect to the density response instead of the density itself:

$$\begin{aligned}
V_{\text{H}}^{(1)\alpha \boldsymbol{R} i}(\boldsymbol{r}) &= \frac{\partial}{\partial \tau_{\alpha \boldsymbol{R} i}} \int \frac{n(\boldsymbol{r}')}{|\boldsymbol{r} - \boldsymbol{r}'|} \mathrm{d}\boldsymbol{r}' \\
&= \int \frac{n^{(1)\alpha \boldsymbol{R} i}(\boldsymbol{r}')}{|\boldsymbol{r} - \boldsymbol{r}'|} \mathrm{d}\boldsymbol{r}' + \oint_{\partial \alpha \boldsymbol{R}} \frac{[n(\boldsymbol{r}')]_{\text{SF}}}{|\boldsymbol{r} - \boldsymbol{r}'|} \hat{\boldsymbol{e}}_{r,i} \mathrm{d}S'.
\end{aligned} \tag{4.77}$$

As this form is integrated over once more in line (4.75c), the integrations can be interchanged to reveal a form very alike to the rest of the integral contributions in lines (4.75b) and (4.75d):

$$\int n(\boldsymbol{r}) V_{\mathrm{H}}^{(1)\alpha\boldsymbol{R}i}(\boldsymbol{r}) \mathrm{d}\boldsymbol{r} = \int n^{(1)\alpha\boldsymbol{R}i}(\boldsymbol{r}) V_{\mathrm{H}}(\boldsymbol{r}) \mathrm{d}\boldsymbol{r} + \oint_{\partial\alpha\boldsymbol{R}} [n(\boldsymbol{r}) V_{\mathrm{H}}(\boldsymbol{r})]_{\mathrm{SF}} \hat{\boldsymbol{e}}_{r,i} \mathrm{d}S. \tag{4.78}$$

In a similar way, the response of the xc energy density in line (4.75c) is recast into a form dependent on the density response. This is done by applying the chain rule of differentiation and leads to

$$(\varepsilon_{\mathrm{xc}}[n](\boldsymbol{r}))^{(1)\alpha\boldsymbol{R}i} = n^{(1)\alpha\boldsymbol{R}i}(\boldsymbol{r}) \frac{\delta \varepsilon_{\mathrm{xc}}[n]}{\delta n(\boldsymbol{r})}. \tag{4.79}$$

This can be grouped with the xc term from line (4.75b), to instead find an integral of $n^{(1)\alpha\boldsymbol{R}i}(\boldsymbol{r}) V_{\mathrm{xc}}(\boldsymbol{r})$. With these considerations, equation (4.75) can be drastically simplified, yielding

$$\begin{aligned}
E_{\mathrm{tot}}^{(1)\alpha\boldsymbol{R}i} &= \sum_{\nu\boldsymbol{k}} \tilde{f}_{\nu\boldsymbol{k}} \varepsilon_{\nu\boldsymbol{k}}^{(1)\alpha\boldsymbol{R}i} && \text{(4.80a)} \\
&+ \int n(\boldsymbol{r}) \left[ -V_{\mathrm{eff}}(\boldsymbol{r}) + V_{\mathrm{ext}}(\boldsymbol{r}) \right]^{(1)\alpha\boldsymbol{R}i} \mathrm{d}\boldsymbol{r} && \text{(4.80b)} \\
&+ \oint_{\partial\alpha\boldsymbol{R}} \left[ n(\boldsymbol{r}) \left\{ \varepsilon_{\mathrm{xc}}[n](\boldsymbol{r}) - V_{\mathrm{xc}}(\boldsymbol{r}) \right\} \right]_{\mathrm{SF}} \hat{\boldsymbol{e}}_{r,i} \mathrm{d}S && \text{(4.80c)} \\
&+ E_{\mathrm{ii}}^{(1)\alpha\boldsymbol{R}i}. && \text{(4.80d)}
\end{aligned}$$

The next step is to find a closed form for the eigenenergy response. Starting from the KS eigenvalue equation,

$$\langle \psi_{\boldsymbol{k}\nu} | H - \varepsilon_{\boldsymbol{k}\nu} | \psi_{\boldsymbol{k}\nu} \rangle = 0, \tag{4.81}$$

and summing over all states, we quickly arrive at a first order term, where the potential response part can be separated from the rest:

$$\begin{aligned}
\sum_{\boldsymbol{k}\nu} \tilde{f}_{\boldsymbol{k}\nu} \varepsilon_{\boldsymbol{k}\nu}^{(1)\alpha\boldsymbol{R}i} = \sum_{\boldsymbol{k}\nu} \tilde{f}_{\boldsymbol{k}\nu} \Big\{ & \langle \psi_{\boldsymbol{k}\nu,\phi}^{(1)\alpha\boldsymbol{R}i} | H - \varepsilon_{\boldsymbol{k}\nu} | \psi_{\boldsymbol{k}\nu} \rangle + \langle \psi_{\boldsymbol{k}\nu} | H - \varepsilon_{\boldsymbol{k}\nu} | \psi_{\boldsymbol{k}\nu,\phi}^{(1)\alpha\boldsymbol{R}i} \rangle && \text{(4.82a)} \\
& + \oint_{\partial\alpha\boldsymbol{R}} \left[ \psi_{\boldsymbol{k}\nu}^{*} (H - \varepsilon_{\boldsymbol{k}\nu}) \psi_{\boldsymbol{k}\nu} \right]_{\mathrm{SF}} \hat{\boldsymbol{e}}_{r,i} \mathrm{d}S \Big\} && \text{(4.82b)} \\
& + \int n(\boldsymbol{r}) V_{\mathrm{eff}}^{(1)\alpha\boldsymbol{R}i}(\boldsymbol{r}) \mathrm{d}\boldsymbol{r}. && \text{(4.82c)}
\end{aligned}$$

Here, the subscript $\phi$ on the wave function response indicates that only the part with the basis function response in equation (4.69) is considered. This is because the integral over the expansion coefficient response vanishes; it is tantamount to evaluating the original eigenvalue problem at a specific basis function. We can go one step further and use the reformulation (4.73a) of the surface terms in line (4.82b) to cancel out the gradient part of the response and define

$$\tilde{\psi}_{\boldsymbol{k}\nu}^{(1)\alpha\boldsymbol{R}i}(\boldsymbol{r}) := \Theta_{\alpha\boldsymbol{R}}(\boldsymbol{r}) \sum_{\boldsymbol{G}} z_{\boldsymbol{k}\boldsymbol{G}\nu} \mathrm{i}(\boldsymbol{k} + \boldsymbol{G})_i \phi_{\boldsymbol{k}\boldsymbol{G}}^{\alpha\boldsymbol{R}}(\boldsymbol{r}). \tag{4.83}$$

With the additional insight, that the last line (4.82c) exactly cancels the effective potential part of line (4.80b), inserting equation (4.82) into (4.80) leads to a preliminary final form of

the first order energy response. Using the established notation and collecting all remaining terms yields

$$E_{\text{tot}}^{(1)\alpha\boldsymbol{R}i} = \int n(\boldsymbol{r}) V_{\text{ext}}^{(1)\alpha\boldsymbol{R}i}(\boldsymbol{r}) \mathrm{d}\boldsymbol{r} + E_{\text{ii}}^{(1)\alpha\boldsymbol{R}i} \tag{4.84a}$$

$$+ \sum_{\boldsymbol{k}\nu} \tilde{f}_{\boldsymbol{k}\nu} \Big\{ \langle \tilde{\psi}_{\boldsymbol{k}\nu}^{(1)\alpha\boldsymbol{R}i} | H - \varepsilon_{\boldsymbol{k}\nu} | \psi_{\boldsymbol{k}\nu} \rangle + \langle \psi_{\boldsymbol{k}\nu} | H - \varepsilon_{\boldsymbol{k}\nu} | \tilde{\psi}_{\boldsymbol{k}\nu}^{(1)\alpha\boldsymbol{R}i} \rangle \tag{4.84b}$$

$$- \oint_{\partial\alpha\boldsymbol{R}} \left[ \psi_{\boldsymbol{k}\nu}^{*} (T - \varepsilon_{\boldsymbol{k}\nu}) \psi_{\boldsymbol{k}\nu}(\boldsymbol{r}) \right]_{\text{IR}} \hat{\boldsymbol{e}}_{r,i} \mathrm{d}S \Big\} \tag{4.84c}$$

$$+ \oint_{\partial\alpha\boldsymbol{R}} \left[ n(\boldsymbol{r}) \left\{ \varepsilon_{\text{xc}}[n](\boldsymbol{r}) - V_{\text{xc}}(\boldsymbol{r}) \right\} \right]_{\text{SF}} \hat{\boldsymbol{e}}_{r,i} \mathrm{d}S \tag{4.84d}$$

$$+ \int_{\alpha\boldsymbol{R}} n(\boldsymbol{r}) \nabla_i V_{\text{eff}}(\boldsymbol{r}) \mathrm{d}\boldsymbol{r} - \oint_{\partial\alpha\boldsymbol{R}} \left[ n(\boldsymbol{r}) V_{\text{eff}}(\boldsymbol{r}) \right]_{\text{IR}} \hat{\boldsymbol{e}}_{r,i} \mathrm{d}S. \tag{4.84e}$$

The terms in the last line (4.84e) stem from the remainder of the surface integral in line (4.82b), after the basis function gradients are canceled and the IR Hamiltonian is separated into the kinetic energy (4.84c) and potential parts. The present form is i) the FLAPW equivalent to equation (3.26), ii) very similar to what is derived in the seminal paper on forces in the LAPW basis [80], and iii) completely variational with respect to the ground state, as all first order terms that appear are fully analytical and do not depend on the solution of a self-consistency problem to first order. This is in stark contrast to the second order energy response.

### 4.3.3 Second Order Energy Derivatives

We can write the terms in lines (4.84b)/(4.84c), that are summed with the occupation numbers over all states, as coefficients $C_{\boldsymbol{k}\nu}^{(1)\alpha\boldsymbol{R}i}$. With this, we find a more concise form for equation (4.84) in

$$E_{\text{tot}}^{(1)\alpha\boldsymbol{R}i} = \int n(\boldsymbol{r}) V_{\text{ext}}^{(1)\alpha\boldsymbol{R}i}(\boldsymbol{r}) \mathrm{d}\boldsymbol{r} + E_{\text{ii}}^{(1)\alpha\boldsymbol{R}i} \tag{4.85a}$$

$$+ \sum_{\boldsymbol{k}\nu} \tilde{f}_{\boldsymbol{k}\nu} C_{\boldsymbol{k}\nu}^{(1)\alpha\boldsymbol{R}i} \tag{4.85b}$$

$$+ \oint_{\partial\alpha\boldsymbol{R}} \left[ n(\boldsymbol{r}) \left\{ \varepsilon_{\text{xc}}[n](\boldsymbol{r}) - V_{\text{xc}}(\boldsymbol{r}) \right\} \right]_{\text{SF}} \hat{\boldsymbol{e}}_{r,i} \mathrm{d}S \tag{4.85c}$$

$$+ \int_{\alpha\boldsymbol{R}} n(\boldsymbol{r}) \nabla_i V_{\text{eff}}(\boldsymbol{r}) \mathrm{d}\boldsymbol{r} - \oint_{\partial\alpha\boldsymbol{R}} \left[ n(\boldsymbol{r}) V_{\text{eff}}(\boldsymbol{r}) \right]_{\text{IR}} \hat{\boldsymbol{e}}_{r,i} \mathrm{d}S. \tag{4.85d}$$

To continue, we need to consider how a second perturbation in an atomic perturbation acts on the existing surface terms to first order. By first transforming the surface integrals to volume integrals of gradients, executing the second derivative, and finally transforming the inner derivative back to a surface integral, we can show that

$$\frac{\partial}{\partial \tau_{\beta\boldsymbol{R}'j}} \oint_{\partial\alpha\boldsymbol{R}} [X(\boldsymbol{r})]_{\text{SF}} \hat{\boldsymbol{e}}_{r,i} \mathrm{d}S = \oint_{\partial\alpha\boldsymbol{R}} [X^{\beta\boldsymbol{R}'j}(\boldsymbol{r}) + \delta_{\beta\alpha}\delta_{\boldsymbol{R}'\boldsymbol{R}} \nabla_j X(\boldsymbol{r})]_{\text{SF}} \hat{\boldsymbol{e}}_{r,i} \mathrm{d}S. \tag{4.86}$$

Additionally, we keep in mind how the xc energy density transforms under differentiation to deal with the xc part of the first order energy response (4.85c). From this we can easily find a

first formulation of the second order energy response. With the equation numbers set in a way that directly reflects were each terms stems from in the first order form, we derive

$$
\begin{aligned}
E_{\text{tot}}^{(2)\beta\boldsymbol{R}'j\alpha\boldsymbol{R}i} = &\int \left[ n^{(1)\beta\boldsymbol{R}'j}(\boldsymbol{r}) V_{\text{ext}}^{(1)\alpha\boldsymbol{R}i}(\boldsymbol{r}) + n(\boldsymbol{r}) V_{\text{ext}}^{(2)\beta\boldsymbol{R}'j\alpha\boldsymbol{R}i}(\boldsymbol{r}) \right] \mathrm{d}\boldsymbol{r} + E_{\text{ii}}^{(2)\beta\boldsymbol{R}'j\alpha\boldsymbol{R}i} \\
&+ \oint_{\partial\beta\boldsymbol{R}'} \left[ n(\boldsymbol{r}) V_{\text{ext}}^{(1)\alpha\boldsymbol{R}i}(\boldsymbol{r}) \right]_{\text{SF}} \hat{\boldsymbol{e}}_{r,j} \mathrm{d}S && \text{(4.87a)} \\
&+ \sum_{\boldsymbol{k}\nu} \left\{ \tilde{f}_{\boldsymbol{k}\nu}^{(1)\beta\boldsymbol{R}'j} C_{\boldsymbol{k}\nu}^{(1)\alpha\boldsymbol{R}i} + \tilde{f}_{\boldsymbol{k}\nu} C_{\boldsymbol{k}\nu}^{(2)\beta\boldsymbol{R}'j\alpha\boldsymbol{R}i} \right\} && \text{(4.87b)} \\
&- \oint_{\partial\alpha\boldsymbol{R}} \left[ n(\boldsymbol{r}) V_{\text{xc}}^{(1)\beta\boldsymbol{R}'j}(\boldsymbol{r}) \right]_{\text{SF}} \hat{\boldsymbol{e}}_{r,i} \mathrm{d}S \\
&- \delta_{\beta\alpha}\delta_{\boldsymbol{R}'\boldsymbol{R}} \oint_{\partial\alpha\boldsymbol{R}} \left[ n(\boldsymbol{r}) \nabla_j V_{\text{xc}}(\boldsymbol{r}) \right]_{\text{SF}} \hat{\boldsymbol{e}}_{r,i} \mathrm{d}S && \text{(4.87c)} \\
&+ \int_{\alpha\boldsymbol{R}} \left[ n^{(1)\beta\boldsymbol{R}'j}(\boldsymbol{r}) \nabla_i V_{\text{eff}}(\boldsymbol{r}) + n(\boldsymbol{r}) \nabla_i V_{\text{eff}}^{(1)\beta\boldsymbol{R}'j}(\boldsymbol{r}) \right] \mathrm{d}\boldsymbol{r} \\
&+ \oint_{\partial\beta\boldsymbol{R}'} \left[ n(\boldsymbol{r}) \nabla_i V_{\text{eff}}(\boldsymbol{r}) \right]_{\text{MT}} \hat{\boldsymbol{e}}_{r,j} \mathrm{d}S \\
&- \oint_{\partial\alpha\boldsymbol{R}} \left[ n^{(1)\beta\boldsymbol{R}'j}(\boldsymbol{r}) V_{\text{eff}}(\boldsymbol{r}) + n(\boldsymbol{r}) V_{\text{eff}}^{(1)\beta\boldsymbol{R}'j}(\boldsymbol{r}) \right]_{\text{IR}} \hat{\boldsymbol{e}}_{r,i} \mathrm{d}S \\
&- \delta_{\beta\alpha}\delta_{\boldsymbol{R}'\boldsymbol{R}} \oint_{\partial\alpha\boldsymbol{R}} \left[ \nabla_j (n(\boldsymbol{r}) V_{\text{eff}}(\boldsymbol{r})) \right]_{\text{IR}} \hat{\boldsymbol{e}}_{r,i} \mathrm{d}S. && \text{(4.87d)}
\end{aligned}
$$

This form is the FLAPW equivalent of equation (3.28) and comes with a lot of contributions. A main effort in the implementation of DFPT in FLAPW was the thorough numerical taming of this lengthy equation and the subsequent cancellation of terms that appear in it. By multiplying it with the phase $\mathrm{e}^{-\mathrm{i}\boldsymbol{q}\cdot(\boldsymbol{R}-\boldsymbol{R}')}$ and summing over the lattice vectors $\boldsymbol{R}(')$ we arrive at the Fourier transformed quantity $E_{\text{tot}}^{(2)\beta j+\alpha i-}$ that is needed for the dynamical matrix in equation (3.21).

### 4.3.4 The Sternheimer Equation in FLAPW

We will not go into further detail here, but rather revisit the second order energy terms and consequently the dynamical matrix setup in chapter 5. For now, it serves to note that the coefficients $C_{\boldsymbol{k}\nu}^{(2)\beta\boldsymbol{R}'j\alpha\boldsymbol{R}i}$ will necessarily contain non-analytical first order quantities, like the response of the expansion coefficients. Hence we have to solve an FLAPW-adapted Sternheimer equation. It can be derived in a similar way to equation (4.82), but coming from the generalized eigenvalue equation (4.2). In general, it can be written in a form, where the Hamiltonian/overlap derivative and the basis response come together to constitute a first order Hamiltonian and overlap:

$$
\begin{aligned}
\left(\underline{H}(\boldsymbol{k}+\boldsymbol{q}) - \varepsilon_{\boldsymbol{k}\nu}\underline{S}(\boldsymbol{k}+\boldsymbol{q})\right) \cdot \boldsymbol{z}_{\boldsymbol{k}+\boldsymbol{q},\nu}^{(1)\beta\boldsymbol{R}'j} = &\Big(\underline{H}^{(1)\beta\boldsymbol{R}'j}(\boldsymbol{k}+\boldsymbol{q},\boldsymbol{k}) - \varepsilon_{\boldsymbol{k}\nu}^{(1)\beta\boldsymbol{R}'j}\underline{S}(\boldsymbol{k}) \\
&- \varepsilon_{\boldsymbol{k}\nu}\underline{S}^{(1)\beta\boldsymbol{R}'j}(\boldsymbol{k}+\boldsymbol{q},\boldsymbol{k})\Big) \cdot \boldsymbol{z}_{\boldsymbol{k}\nu}. \qquad \text{(4.88)}
\end{aligned}
$$

To solve this equation self-consistently, we need to consider several things. Firstly, the matrices appearing on the right hand side are no longer quadratic, but can become rectangular, as the number of basis functions for the Bloch vector $\boldsymbol{k}+\boldsymbol{q}$ is not necessarily the same as for $\boldsymbol{k}$ (hence the notation with both vectors). We also need to take all terms, including the basis

derivative, into account correctly. After some rearrangement and cancellation (writing it in a form, where the lattice vector sum is carried out as in equation (3.30)) this leads to the following form for the Hamiltonian and overlap response:

$$H^{(1)\beta j+,\mathrm{MT}}_{\boldsymbol{G}',\boldsymbol{G}} = \sum_{\gamma} \langle \phi_{\boldsymbol{k}\boldsymbol{G}'\boldsymbol{q}} | V^{(1)\beta j+\nabla}_{\mathrm{eff}} | \phi_{\boldsymbol{k}\boldsymbol{G}} \rangle_{\gamma} + \mathrm{i}(G - G' - q)_j \langle \phi_{\boldsymbol{k}\boldsymbol{G}'\boldsymbol{q}} | \mathcal{H} | \phi_{\boldsymbol{k}\boldsymbol{G}} \rangle_{\beta}, \tag{4.89}$$

$$S^{(1)\beta j+,\mathrm{MT}}_{\boldsymbol{G}',\boldsymbol{G}} = \mathrm{i}(G - G' - q) \langle \phi_{\boldsymbol{k}\boldsymbol{G}'\boldsymbol{q}} | \phi_{\boldsymbol{k}\boldsymbol{G}} \rangle_{\beta}, \tag{4.90}$$

$$H^{(1)\beta j+,\mathrm{IR}}_{\boldsymbol{G}',\boldsymbol{G}} = \langle \phi_{\boldsymbol{k}\boldsymbol{G}'\boldsymbol{q}} | \Theta_{\mathrm{IR}} V^{(1)\beta j+}_{\mathrm{eff}} + \Theta^{(1)\beta j+}_{\mathrm{IR}} V_{\mathrm{eff}} + \Theta^{(1)\beta j+}_{\mathrm{IR}} T | \phi_{\boldsymbol{k}\boldsymbol{G}} \rangle_{\Omega}, \tag{4.91}$$

$$S^{(1)\beta j+,\mathrm{IR}}_{\boldsymbol{G}',\boldsymbol{G}} = \langle \phi_{\boldsymbol{k}\boldsymbol{G}'\boldsymbol{q}} | \Theta^{(1)\beta j+}_{\mathrm{IR}} | \phi_{\boldsymbol{k}\boldsymbol{G}} \rangle_{\Omega}. \tag{4.92}$$

This form is numerically convenient, as it once again does not contain any unpaired gradient terms (which was noted as beneficial before) and groups the IR contributions in a way, that is very similar to the ground-state calculation. This makes the implementation elegant in terms of reusing and adapting existing code instead of rewriting or duplicating parts of it. Next, we need an expression for the first order eigenvalue response expressed through the matrix responses. Due to the nature of the perturbation, that shifts the Bloch vector of the basis functions by $\boldsymbol{q}$, it will only contribute in the case $\boldsymbol{q} = \boldsymbol{0}$. Otherwise the dimensions of the matrices would not match on the right hand side of the Sternheimer equation (4.88) (a more thorough explanation can be found *e.g.* in [92]). In the non-vanishing case, the response can be found by multiplying from the left with the expansion coefficient vector of the same state $\nu$ as on the right. This makes the left hand side of the equation equal 0 and yields

$$\varepsilon^{(1)\beta j}_{\boldsymbol{k}\nu} = \varepsilon^{(1)\beta j}_{\boldsymbol{k}\nu} \boldsymbol{z}^{\dagger}_{\boldsymbol{k}\nu} \underline{S}(\boldsymbol{k}) \boldsymbol{z}_{\boldsymbol{k}\nu} = \boldsymbol{z}^{\dagger}_{\boldsymbol{k}\nu} \left( \underline{H}^{(1)\beta j+}(\boldsymbol{k}, \boldsymbol{k}) - \varepsilon_{\boldsymbol{k}\nu} \underline{S}^{(1)\beta j+}(\boldsymbol{k}, \boldsymbol{k}) \right) \boldsymbol{z}_{\boldsymbol{k}\nu} \tag{4.93}$$

The last point is dealing with the inversion of the left hand side of equation (4.88). A numerical inversion proves very difficult, as the left hand side becomes very large for certain contributions to the Hamiltonian. This can be seen, when we represent it by its eigenvalue spectrum (written as a diagonal matrix $\underline{\varepsilon}_{\boldsymbol{k}+\boldsymbol{q}}$) and the eigenvector matrices $\underline{z}^{(\dagger)}_{\boldsymbol{k}+\boldsymbol{q}}$:

$$\underline{H}(\boldsymbol{k} + \boldsymbol{q}) = \underline{z}^{\dagger -1}_{\boldsymbol{k}+\boldsymbol{q}} \underline{\varepsilon}_{\boldsymbol{k}+\boldsymbol{q}} \underline{z}^{-1}_{\boldsymbol{k}+\boldsymbol{q}}, \tag{4.94}$$

$$\underline{S}(\boldsymbol{k} + \boldsymbol{q}) = \underline{z}^{\dagger -1}_{\boldsymbol{k}+\boldsymbol{q}} \underline{z}^{-1}_{\boldsymbol{k}+\boldsymbol{q}}. \tag{4.95}$$

A numerical inversion of the full left hand side term would skim over the fact, that the subtraction of $\varepsilon_{\boldsymbol{k}\nu}$ from the eigenvalue matrix can lead to vanishing contributions, that in turn lead to a singular matrix. We postpone the discussion of how to remedy this until chapter 5 and formally note the solution to the Sternheimer equation as an analytical inversion through the eigenvalue spectrum:

$$\boldsymbol{z}^{(1)\beta j+}_{\boldsymbol{k}+\boldsymbol{q},\nu} = -\underline{z}_{\boldsymbol{k}+\boldsymbol{q}} (\underline{\varepsilon}_{\boldsymbol{k}+\boldsymbol{q}} - \varepsilon_{\boldsymbol{k}\nu})^{-1} \underline{z}^{\dagger}_{\boldsymbol{k}+\boldsymbol{q}} \left( \underline{H}^{(1)\beta j+}(\boldsymbol{k} + \boldsymbol{q}, \boldsymbol{k}) - \varepsilon_{\boldsymbol{k}\nu} \underline{S}^{(1)\beta j+}(\boldsymbol{k} + \boldsymbol{q}, \boldsymbol{k}) \right) \cdot \boldsymbol{z}_{\boldsymbol{k}\nu}. \tag{4.96}$$

This means, that solving the Sternheimer equation is on a lower level of complexity than solving the KS eigenvalue equation in the ground-state calculation, as it only constitutes successive matrix multiplications instead of a diagonalization. This is in contrast to the other steps of the calculation like the potential response generation and the matrix element setup, that are very similar to the original calculation. We will investigate the analogy to the ground state in more detail in chapter 5, that deals with the implementation aspect of the FLAPW-DFPT framework in FLEUR. We close this chapter with only a brief overview on how the SCF structure changes in this context.

### 4.3.5 The FLAPW-DFPT Self-Consistency Loop

The goal of the DFPT self-consistency workflow is to calculate the dynamical matrix of a lattice for a phonon of wave vector $\boldsymbol{q}$. In practice, this is done for several vectors successively, to either sample the phonon dispersion at various points or to gain a mesh of q-points, from which more highly resolved quantities can be interpolated. Either way, this constitutes a first additional layer as compared to the DFT SCF loop: an outer loop over the q-points. Next we need to consider the setup of the dynamical matrix. It consists of $3N_{\text{ion}} \times 3N_{\text{ion}}$ entries, that in principle are all independent of each other (baring the requirement, that the dynamical matrix is Hermitian). As before, the indices of the matrix columns are labeled with $(\alpha i)$ for a displaced atom $\alpha$ and Cartesian direction $i$, while the rows are labeled $(\beta j)$. We refer to this as the perturbation index. As a consequence of the matrix setup, there appear only a small set of different contributions. There are analytical quantities, like the external potential response in first and second order, and the ion–ion interaction in second order. These are only dependent on the atomic positions, the unit cell size, and the setup parameters, making them fully unrelated to the SCF problem. These quantities can be calculated once for each $\boldsymbol{q}$ and then be stored and used repeatedly. The second group of contributions, however, does directly depend on the SCF cycle. There are contributions from the first order density and potential responses, as well as state dependent eigenenergy and occupation terms. Fortunately, in accordance with the $2n+1$-theorem [45, 152–154], such terms never combine two first order SCF contributions - neither for the same atom and direction, nor for different ones. That means each perturbation index can be handled separately and we choose to work through the rows of the dynamical matrix one after another (this is, however, only a convention - the opposite case of working through the columns is equally viable). This adds another layer of $3N_{\text{ion}}$ self-consistency loops for each dynamical matrix. Regarding each separate SCF loop, they make use of the quantities that were calculated in the ground-state run (as well as the gradients of the respective density and potentials) and the external potential perturbation in first order to calculate the first guess for the density response. This is done by going through a modified form of the SCF iteration, where only $V_{\text{ext}}^{(1)\beta j+}(\boldsymbol{r})$ enters instead of $V_{\text{eff}}^{(1)\beta j+}(\boldsymbol{r})$.

Aside from this, the SCF procedure for the density response is very similar to that of the ground-state calculation. The potential generation is replaced by the potential response generation and the Hamiltonian and overlap setup is replaced by the setup for the corresponding response matrices. The diagonalization, as mentioned before, is replaced by the solution of the Sternheimer equation, which involves a series of matrix multiplications. Instead of the occupation numbers and Fermi energy, their responses are calculated and from them, we construct a new output density response. The mixing can, in theory, be done the same way as before, but additional care needs to be taken, because it is no longer guaranteed, that $n^{(1)\beta j+}(\boldsymbol{r})$ is a real-valued quantity. Especially in the MT spheres, where the density and potentials are expressed in terms of real-valued lattice harmonics, the imaginary part that can arise needs to be explicitly carried through the calculation as an additional variable. Once an SCF calculation is finished, the corresponding contribution to the dynamical matrix is evaluated and the next perturbation index is treated. When this is done for all indices, the dynamical matrix is fully set up and can be diagonalized, yielding a set of eigenvalues and eigenvectors. After that, the calculation for the next q-point is started and finally, when all specified q-points are handled, the results can be evaluated. This lengthy workflow exceeds the computational effort of the ground-state run by several times, at least by a factor of $3N_{\text{ion}}N_{\boldsymbol{q}}$,

which does not yet take into account other factors slowing down the calculation. The resulting run times and scaling behavior will be discussed in a later chapter. For now, this concludes the discussion of the DFPT workflow and it is summarized in figure 4.3.

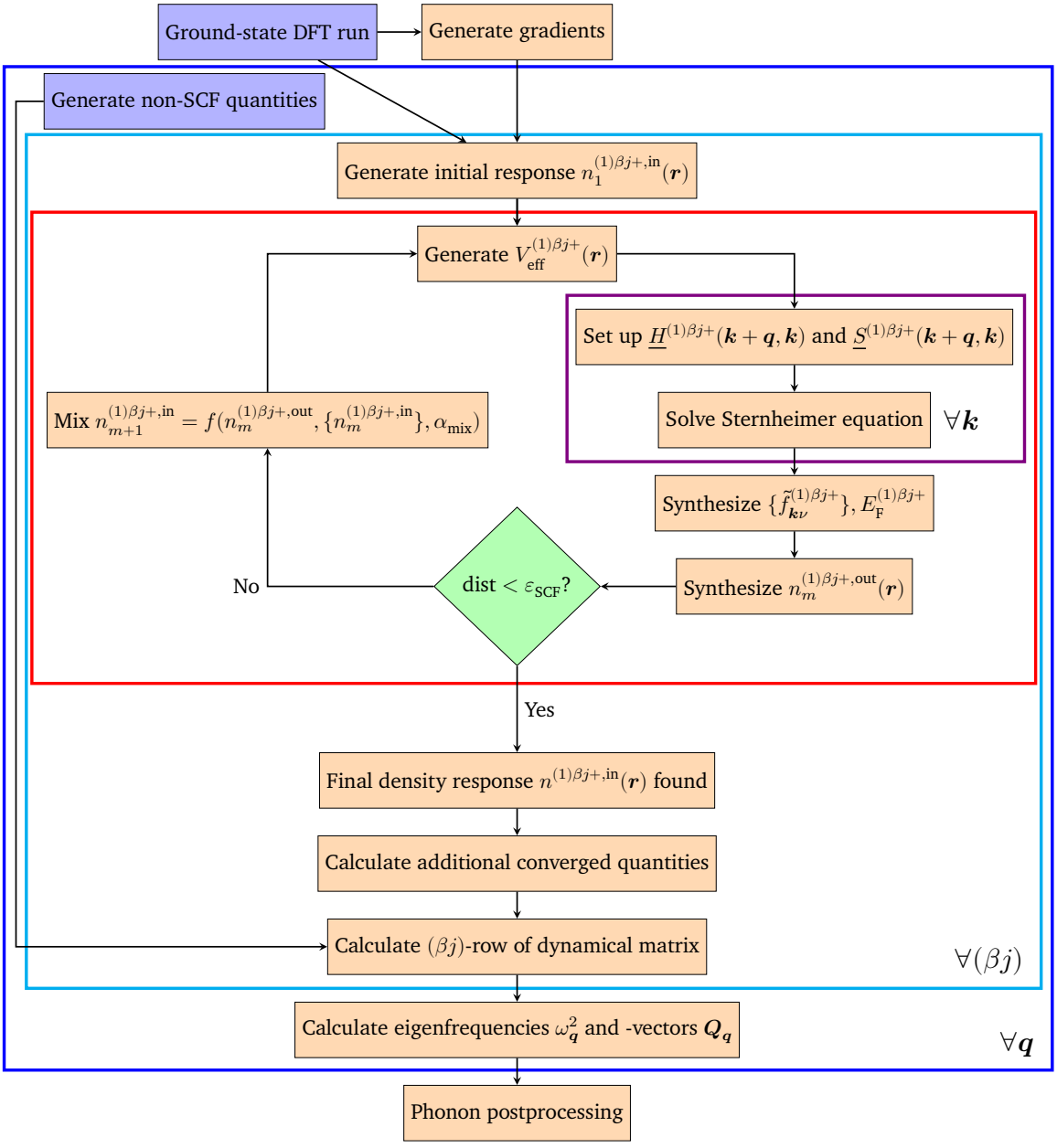



**Figure 4.3:** Sketch of the DFPT self-consistency workflow for the FLAPW method. The Sternheimer equation has to be solved for each Bloch vector $\boldsymbol{k}$ by setting up the matrix elements $H/S_{\boldsymbol{G}'\boldsymbol{G}}^{(1)\beta j+}(\boldsymbol{k}+\boldsymbol{q},\boldsymbol{k})$ for the basis set in question, *i.e.* the LAPW basis. The full procedure of arriving at a set of dynamical matrices involves solving the equation for each atom $\beta$, each displacement $j$, and each phonon wave vector $\boldsymbol{q}$ independently.

There are some steps in this workflow, that are not self-explanatory from the knowledge provided in this chapter and the general terminology established in figures 2.2 and 4.2. ”Gen-

erate non-SCF quantities" refers to quantities, that are calculated before the Sternheimer self-consistency loop is started for a specific calculation $(\beta j \boldsymbol{q})$. This encompasses the eigenvectors $\boldsymbol{z}_{\boldsymbol{k}\boldsymbol{q}\nu'}$ and eigenvalues $\varepsilon_{\boldsymbol{k}\boldsymbol{q}\nu'}$ for all occupied and unoccupied states $\nu'$ at the shifted Bloch vector $\boldsymbol{k}+\boldsymbol{q}$ as well as the analytical second order quantities $V_{\text{ext}}^{(2)\beta j-\alpha i+}(\boldsymbol{r})$ and $E_{\text{ii}}^{(2)\beta j-\alpha i+}$, which are needed for the second order energy response in equation (4.87) and will be discussed in more detail in section 5.5. "Calculate additional converged quantities" highlights the need to calculate quantities for the second order energy response, that were not needed in the Sternheimer loop itself and thus need to be calculated once after the density response is converged. Such quantities will be highlighted in the next chapter. "Generate initial response $n_1^{(1)\beta j+,\text{in}}(\boldsymbol{r})$" marks the calculation that needs to be done before we can start the Sternheimer loop proper. An iteration "0" of the loop is started for the external potential response instead of the effective one to gain access to a first set of response matrices, eigenvalues/expansion coefficients, and finally the desired density response. It is inserted into the SCF cycle as the first "true" density response without being mixed (as there is no other density to mix it with). Finally, "Phonon postprocessing" covers everything that can be done with the results of a dynamical matrix construction and diagonalization. This can range from in-code manipulations such as the interpolation of a smooth phonon bandstructure or density of states from a set of sampled q-points, to the graphical output of the resulting data as it is often provided in the later chapters of this work.

Chapter 5

# Implementing DFPT in the FLEUR Code


5.1 Extending the Potential Generation . . . . . 58
5.2 Extending the Matrix Setup . . . . . 62
5.3 Handling Degenerate Eigenvalues . . . . . 63
5.4 Extending the Density Generation . . . . . 68
5.5 Calculating the Second Order Energy Terms . . . . . 69
5.6 Scaling Behavior . . . . . 73


The implementation of DFPT into the FLAPW method is of the same, if not a higher order of complexity as the ground-state DFT formalism. As highlighted in the previous chapter, all the calculation steps get replaced by a similar but different operations, which generally receive more complex and less symmetric input. The theoretical groundwork for such an implementation is well established [82, 83, 86, 87], but there is a distinct lack of publications on the implementation of the formalism, especially in comparison to pseudopotential codes and other related methods [46, 47, 176, 177]. The implementation in this work is based on the initial work of Klüppelberg [92], from which Gerhorst developed the `juPhon` plugin based on a previous version of FLEUR [93]. The resulting code showed promising first results, but was limited in a multitude of ways. Basically, due to the implementation as a stand-alone product with a separate compilation and modules from an old version of the FLEUR code, the plugin did not outgrow the level of monatomic, spin-degenerate test systems. Moreover, the divergent nature of the code made it hard to maintain alongside an ever-growing and constantly evolving electronic structure package like FLEUR. Hence one of the main goals of this thesis is refactoring the DFPT functionality back into the main code and streamlining it according to the modern programming philosophy behind it. The main focus in this respect was on two key aspects. For one, there was the aspect of usability. This means making the code usable on top of a regular ground-state calculation performed in FLEUR, without the need to artificially modify the input to an unrecognizable level. An additional aspect in this context was to provide the necessary input for a DFPT calculation in the regular input file. The second and more important aspect of the rework is the elimination of redundant code. This was done by reworking the feature into the existing routines with optional switches

wherever possible. The advantages of this are threefold. i) It ensures maintainability of the feature, as it is directly woven into code that is by necessity tested and maintained as long as FLEUR is in use. ii) Extensions to other functionalities that the code already provides are more easily accessible. This is used in this thesis to enable the calculation of spin-polarized materials, polyatomic unit cells, systems with local orbitals, and interfacing the feature to the `libxc` [171] library of xc functionals. Each of these steps in and of itself would be a big effort in a separate code, but their implementation becomes somewhat natural in a code that already works with these concepts. iii) The parallelizations and optimizations done in the base code can be easily adapted and used to speed up the DFPT implementation. In summary: The rework back into the FLEUR code avoids redundancy on each level from implementation, to maintenance, to usage. The following chapter serves to highlight each computational aspect that needs to be considered. This covers both adaptions that need to be made and, *e.g.* for the dynamical matrix setup, additions to the original code. The concepts, as well as the respective routines and some pseudocode to highlight the program's logic are shown. Explicit references to the subroutines and variables of the code are given. Technical details on the usage of the feature as well as the version used to produce the results can be found in appendix B. We begin with the adaption of the potential generation.

## 5.1 Extending the Potential Generation

The Potential Components

To generate the potential response in the FLAPW method, we need to look at its three constituents (the external, Hartree, and xc parts) in equation (3.34). We want to construct the potential response analogously to the base case, *i.e.* the Coulomb potential response with the method developed by Weinert [170] amended with some adaptions and the xc potential response through the direct evaluation of the xc Kernel on a real space grid, as opposed to the xc potential itself.

The Coulomb Potential Response

The construction of the Coulomb potential response differs from the original potential as described in section 4.2 in several key ways. The first is a general property of the response quantities in real space. Looking at equations (4.22)/(4.23), we remark that the first order density and potentials carry an additional phase factor determined by the phonon wave vector. This yields

$$X^{(1)\beta j+}(\boldsymbol{r}) = \begin{cases} \sum_{\boldsymbol{G}+\boldsymbol{q}} X^{(1)\beta j+}_{\text{IR}}(\boldsymbol{G}+\boldsymbol{q}) \mathrm{e}^{\mathrm{i}(\boldsymbol{G}+\boldsymbol{q})\cdot\boldsymbol{r}}, & \boldsymbol{r} \in \text{IR} \\ \sum_{\ell m} X^{(1)\beta j+}_{\gamma\ell m}(r_\gamma) Y^m_\ell(\hat{\boldsymbol{r}}_\gamma) & \boldsymbol{r} \in \text{MT}^\gamma \end{cases}. \tag{5.1}$$

for the representation of the density and potential responses in plane waves and spherical harmonics. This additional phase necessarily influences the Coulomb potential construction as well. In every formula that contains the reciprocal lattice vectors $\boldsymbol{G}$, there will appear a vector shifted by $\boldsymbol{q}$ instead, leading to the following set of modified equations

$$V^{(1)\beta j+}_{\text{C,IR}}(\boldsymbol{G}+\boldsymbol{q}) = (1-\delta_{\boldsymbol{G}+\boldsymbol{q},\boldsymbol{0}}) \frac{4\pi n_{\text{ps}}(\boldsymbol{G}+\boldsymbol{q})}{|\boldsymbol{G}+\boldsymbol{q}|^2}, \tag{5.2}$$

$$V^{(1)\beta j+}_{\mathrm{C},\gamma\ell m}(r_\gamma) = \frac{4\pi}{2\ell+1}\int_0^{R_{\mathrm{MT}\gamma}} r'^2 n^{(1)\beta j+}_{\gamma\ell m}(r')\frac{r_<^\ell}{r_>^{\ell+1}}\left(1-\left(\frac{r_>}{R_{\mathrm{MT}\gamma}}\right)^{2\ell+1}\right)\mathrm{d}r' \tag{5.3}$$
$$+\left(\frac{r_\gamma}{R_{\mathrm{MT}\gamma}}\right)^\ell 4\pi \mathrm{i}^\ell \sum_{\boldsymbol{G}+\boldsymbol{q}\neq\boldsymbol{0}} \mathrm{e}^{\mathrm{i}(\boldsymbol{G}+\boldsymbol{q})\cdot\boldsymbol{\tau}_\gamma} j_\ell(|\boldsymbol{G}+\boldsymbol{q}|R_{\mathrm{MT}\gamma}) Y_\ell^{m*}\left(\widehat{\boldsymbol{G}+\boldsymbol{q}}\right) V^{(1)\beta j+}_{\mathrm{C,IR}}(\boldsymbol{G}+\boldsymbol{q}),$$

$$n_{\mathrm{MT,ps}}(\boldsymbol{G}+\boldsymbol{q}) = \delta_{\boldsymbol{G}+\boldsymbol{q},\boldsymbol{0}}\frac{\sqrt{4\pi}}{\Omega}\tilde{q}^\gamma_{00}$$
$$+(1-\delta_{\boldsymbol{G}+\boldsymbol{q},\boldsymbol{0}})\frac{4\pi}{\Omega}\sum_{\gamma\ell m}(-\mathrm{i})^\ell\frac{(2\ell+2N+3)!!}{(2\ell+1)!!}\frac{j_{\ell+N+1}(|\boldsymbol{G}+\boldsymbol{q}|R_{\mathrm{MT}\gamma})}{(|\boldsymbol{G}+\boldsymbol{q}|R_{\mathrm{MT}\gamma})^{N+1}} \tag{5.4}$$
$$\times\tilde{q}^{\gamma,(1)\beta j+}_{\ell m}\mathrm{e}^{-\mathrm{i}(\boldsymbol{G}+\boldsymbol{q})\cdot\boldsymbol{\tau}_\gamma}Y_\ell^m\left(\widehat{\boldsymbol{G}+\boldsymbol{q}}\right).$$

Aside from the shift in the vectors and the fact, that the density response can explicitly take on complex values and thus produce a complex result for the Coulomb potential response, the formulae remain unchanged. It is worth noting, however, that the special treatment for $\boldsymbol{G}=\boldsymbol{0}$ will only apply for $\boldsymbol{q}=\boldsymbol{0}$ now. Any q-point in the first BZ is at most $0.5$ in any direction in internal coordinates, while the reciprocal lattice vectors take integer values, thus the $\boldsymbol{G}+\boldsymbol{q}=\boldsymbol{q}$ component is constructed in the same way that the coefficients for $\boldsymbol{G}\neq\boldsymbol{0}$ were before. The shift of the vector also influences the (pseudo-)multipole moments in a similar fashion.

The second difference to the ground-state calculation is that due to the position dependence of the basis set, the Hartree potential response is slightly modified, as highlighted in equation (4.77). The surface discontinuity term in this equation can be expressed by surface multipole moments and directly added onto the original ones. This leads to

$$\tilde{q}^{\gamma,(1)\beta j+}_{\ell m} = q^{\gamma,(1)\beta j+}_{\ell m} - q^{\gamma,(1)\beta j+,\mathrm{ps}}_{\ell m} + q^{\gamma,\beta j+|\mathrm{SF}}_{\ell m} - q^{\gamma,\beta j+|\mathrm{SF,ps}}_{\ell m} \tag{5.5}$$

with the multipole terms

$$q^{\gamma,(1)\beta j+}_{\ell m} = \int_{\mathrm{MT}\gamma} Y_\ell^{m*}\left(\hat{\boldsymbol{r}}_\gamma\right) r_\gamma^\ell n^{(1)\beta j+}(\boldsymbol{r})\mathrm{d}\boldsymbol{r}_\gamma, \tag{5.6}$$

$$q^{\gamma,(1)\beta j+,\mathrm{ps}}_{\ell m} = \delta_{\boldsymbol{G}+\boldsymbol{q},\boldsymbol{0}}\delta_{\ell,0}\frac{\sqrt{4\pi}}{3}R^3_{\mathrm{MT}\gamma}n^{(1)\beta j+}_{\mathrm{IR}}(\boldsymbol{0})$$
$$+4\pi\sum_{\boldsymbol{G}\neq\boldsymbol{0}}\mathrm{i}^\ell R^{\ell+3}_{\mathrm{MT}\gamma}\frac{j_{\ell+1}(|\boldsymbol{G}+\boldsymbol{q}|R_{\mathrm{MT}\gamma})}{|\boldsymbol{G}+\boldsymbol{q}|R_{\mathrm{MT}\gamma}}n^{(1)\beta j+}_{\mathrm{IR}}(\boldsymbol{G}+\boldsymbol{q})\mathrm{e}^{\mathrm{i}(\boldsymbol{G}+\boldsymbol{q})\cdot\boldsymbol{\tau}_\gamma}Y_\ell^{m*}\left(\widehat{\boldsymbol{G}+\boldsymbol{q}}\right), \tag{5.7}$$

$$q^{\gamma,\beta j+|\mathrm{SF}}_{\ell m} = \delta_{\gamma\beta}R^{\ell+2}_{\mathrm{MT}\gamma}\sum_{\ell' m'}n_{\gamma\ell' m'}(R_{\mathrm{MT}\gamma})\sum_{m''=-1}^{1}\zeta_{j,m''}G^{m,m',m''}_{\ell,\ell',1}, \tag{5.8a}$$

and

$$q^{\gamma,\beta j+|\mathrm{SF,ps}}_{\ell m} = \delta_{\gamma\beta}\sum_{\ell' m'}4\pi\mathrm{i}^{\ell'}\sum_{\boldsymbol{G}}\mathrm{e}^{\mathrm{i}\boldsymbol{G}\cdot\boldsymbol{\tau}_\gamma}n_{\mathrm{IR}}(\boldsymbol{G}) \tag{5.8b}$$
$$\times\,\mathrm{Y}^*_{\ell' m'}(\hat{\boldsymbol{G}})\mathrm{j}_{\ell'}(|\boldsymbol{G}|\,R_{\mathrm{MT}\gamma})\sum_{m''=-1}^{1}\zeta_{j,m''}G^{m,m',m''}_{\ell,\ell',1},$$

where the matrix $\underline{\zeta}$, that links the Cartesian to the natural coordinates has been defined as

$$\underline{\zeta} = \sqrt{\frac{2\pi}{3}} \begin{pmatrix} 1 & 0 & -1 \\ \mathrm{i} & 0 & \mathrm{i} \\ 0 & \sqrt{2} & 0 \end{pmatrix}. \tag{5.9}$$

A last variation on the base formalism is the contribution of the ionic charge $Z_\gamma$. Where it only contributed to the spherical component before ($q_{00}^{\gamma,\mathrm{ext}} = -Z_\gamma/\sqrt{4\pi}$), it is now related to the dipole channels with $\ell = 1$:

$$q_{1m}^{\beta j+|\gamma,\mathrm{ext}} = -\delta_{\gamma\beta}\frac{3}{4\pi} Z_\gamma \zeta_{j,m}. \tag{5.10}$$

As mentioned before, there will be parts of the calculation where responses and gradients of the same quantity are added together in the displaced MT (*cf.* equation (4.74)). To make this numerically accurate for the potentials, their gradients are constructed in the same way as the response through the potential generation, instead of numerically differentiating them. In this case, the above formulae hold, but the density response is replaced by the gradient of the density in each one of them. Additionally, the $\delta_{\gamma\beta}$ prefactors for the surface elements vanish and are replaced by a negative prefactor, yielding *e.g.* for the ionic contribution:

$$q_{1m}^{\gamma,\mathrm{ext}} = \frac{3}{4\pi} Z_\gamma \zeta_{j,m}. \tag{5.11}$$

In FLEUR, the generation of the Coulomb potential is handled in the subroutine `vgen_coulomb`. The analogous nature of the DFPT implementation to the standard DFT one motivates the usage of the same subroutine, but for different input and slightly different logic. This is pictured in figure 5.1.

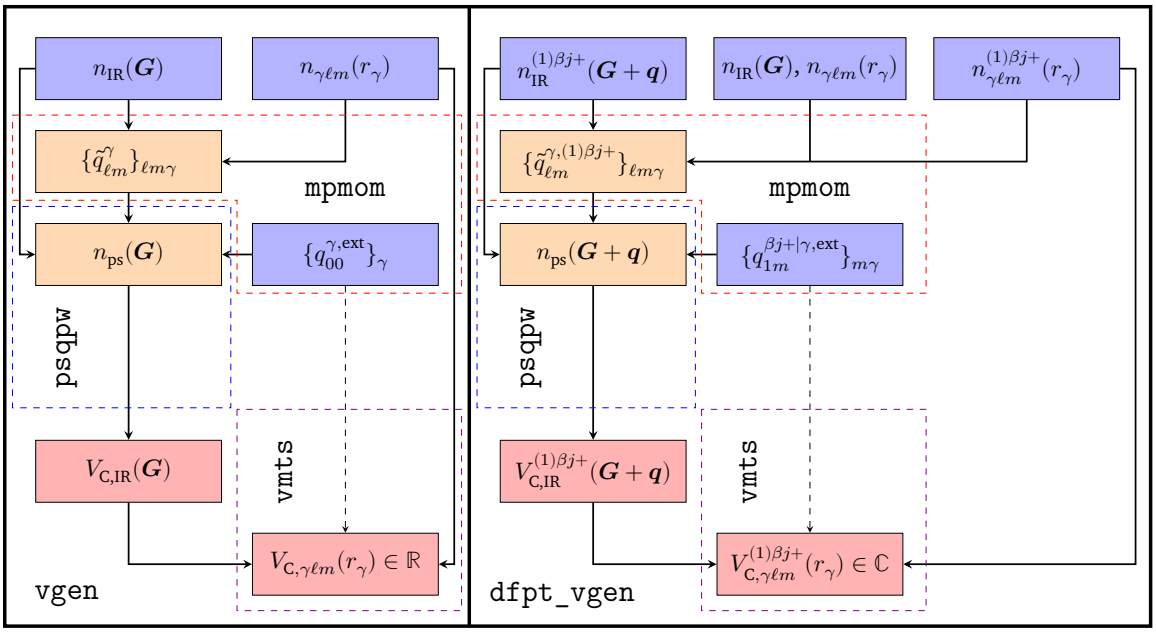



**Figure 5.1:** Principal workflow of the FLEUR Coulomb potential (response) generation for DFT (left hand side) and DFPT (right hand side). The dashed areas mark calls to explicitly named lower level subroutines, which needed to be adapted to the DFPT case.

Due to the selection of the LDA for the xc functional, the form of the xc kernel $K_{\text{xc}}$ in equation (3.35c) becomes very simple. Where the functional derivative of the xc energy functional became just the partial derivative of the xc energy density with respect to to the density, the same holds true for the second derivative. This directly gives us

The xc Potential Response

$$V_{\text{xc}}^{(1)\beta j+}(\boldsymbol{r}) = n^{(1)\beta j+}(\boldsymbol{r}) \left( 2\frac{\partial \varepsilon_{\text{xc}}(n(\boldsymbol{r}))}{\partial n(\boldsymbol{r})} + n(\boldsymbol{r}) \frac{\partial^2 \varepsilon_{\text{xc}}(n(\boldsymbol{r}))}{\partial n(\boldsymbol{r})^2} \right). \tag{5.12}$$

Whereas in the base case, the density was transformed into real space to calculate the xc potential and then transform it back, the same now has to be done for both the density and the density response or gradient of the density. The concept, however, remains the same. The top-level routine governing the calculation is `vgen_xcpot`, while the real space transformations and calculations are found in subroutines `vis_xc` and `vmt_xc` or `dfpt_vis_xc` and `dfpt_vmt_xc` respectively. The xc calculations are handled by an interface to `libxc` [171] in both cases to ensure consistency. The resulting workflow is highlighted in figure 5.2.

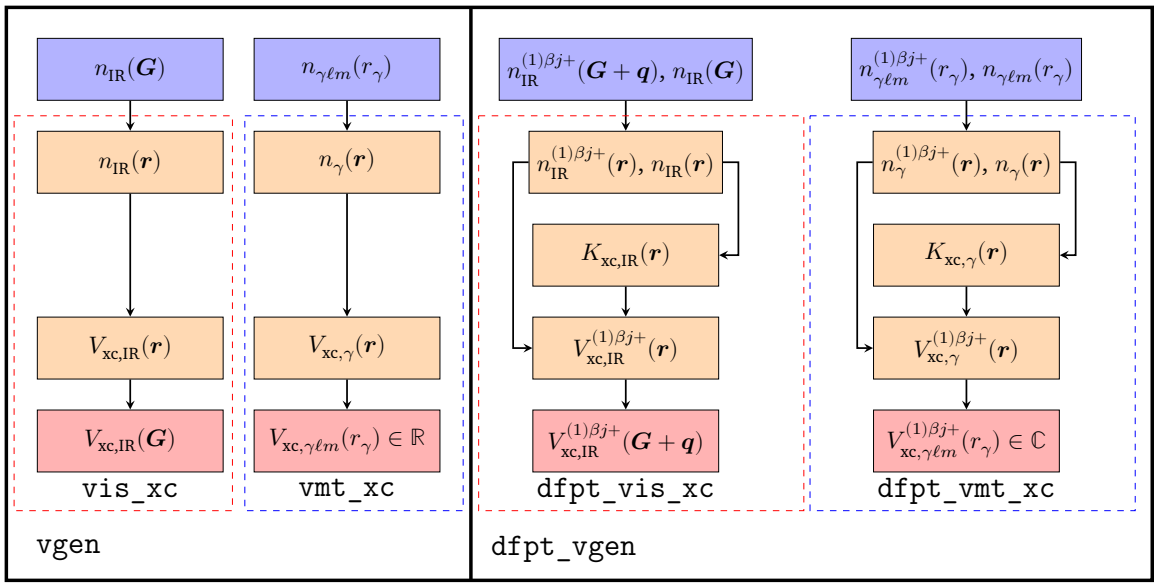



**Figure 5.2:** Principal workflow of the `FLEUR` xc potential (response) generation for DFT (left hand side) and DFPT (right hand side). The dashed areas mark calls to explicitly named lower level subroutines, which needed to be adapted to the DFPT case.

Finalization Steps

After the Coulomb and xc steps, we found the potential response/gradient expressed in Fourier coefficients and radial functions. In a normal potential calculation, the IR part would now be convoluted with the step function by transforming both onto the real space grid, multiplying them, and transforming back. In the code, the initial potential is designated as the variable `pw` in the `potden` data type for density and potentials, while the warped part (*i.e.* the convolution of the potential and the step function) is saved as `pw_w`. This is done, because the evaluation of integrals in the IR always involves taking the step function into account, *e.g.* when the matrix elements are calculated. As we have already noted in equation (4.91), the IR matrix Hamiltonian has terms combining the potential and step function to first order. To work in analogy to the base case, we thus combine the potential response and step function with the potential and step function response in real space and transform the resulting sum back

into Fourier coefficients. We save this combined quantity into the `pw_w` part of the potential response `potden` variable. This will become handy in the next step of the calculation.

## 5.2 Extending the Matrix Setup

In the ground-state calculation, the Hamiltonian and overlap matrices are Hermitian and are constructed by evaluating the Hamiltonian operator (or unity for the overlap) from both sides with the same set of basis function at Bloch vector $\boldsymbol{k}$. This symmetry breaks down for the DFPT use case. The left basis functions are evaluated at a shifted vector $\boldsymbol{k}+\boldsymbol{q}$, which makes the response matrices rectangular (in general) and necessitates the modification of the routines used by optional input. The basic logic is to use the same routines to evaluate the numerous contributions as before, but to provide the second set of basis functions and, based on its existence, calling the subroutines in a different fashion. Especially, since the routines usually only have to calculate the lower triangle of the Hamiltonian and overlap matrices (they are Hermitian), the calculation of the upper part needs to be actively enforced. This will be highlighted in the following.

**The Interstitial Matrix Response**

The interstitial matrices get three contributions. The warped potential and the kinetic energy with the step function are evaluated for the Hamiltonian and the step function alone is evaluated for the overlap. The response matrices get three analogous contributions, but the input differs. Aside from the two sets of basis functions, the `pw_w` part of the potential is replaced by that of the potential response as described in the previous chapter (equation (4.91)) and each occurrence of the step function is replaced by its response. It can be directly derived from equation (4.9) and has the Fourier coefficients

$$\hat{\Theta}^{(1)\beta j+}(\boldsymbol{G}+\boldsymbol{q}) = \mathrm{i}(\boldsymbol{G}+\boldsymbol{q})_j \frac{4\pi R_{\mathrm{MT}^\beta}^3}{\Omega} \frac{j_1(|\boldsymbol{G}+\boldsymbol{q}|R_{\mathrm{MT}^\beta})}{|\boldsymbol{G}+\boldsymbol{q}|R_{\mathrm{MT}^\beta}} \mathrm{e}^{-\mathrm{i}(\boldsymbol{G}+\boldsymbol{q})\cdot\boldsymbol{\tau}_\beta}. \tag{5.13}$$

With this, the IR and Hamiltonian can be quickly written down as

$$H_{\boldsymbol{G}',\boldsymbol{G}}^{(1)\beta j+,\mathrm{IR}}(\boldsymbol{k}+\boldsymbol{q},\boldsymbol{k}) = \tilde{V}_{\mathrm{eff}}^{(1)\beta j+}(\boldsymbol{G}-\boldsymbol{G}') + \frac{|\boldsymbol{k}+\boldsymbol{G}'+\boldsymbol{q}|^2 + |\boldsymbol{k}+\boldsymbol{G}|^2}{4} \Theta_{\mathrm{IR}}^{(1)\beta j+}(\boldsymbol{G}-\boldsymbol{G}'), \tag{5.14}$$

$$S_{\boldsymbol{G}',\boldsymbol{G}}^{(1)\beta j+,\mathrm{IR}}(\boldsymbol{k}+\boldsymbol{q},\boldsymbol{k}) = \Theta_{\mathrm{IR}}^{(1)\beta j+}(\boldsymbol{G}-\boldsymbol{G}'). \tag{5.15}$$

In FLEUR, the evaluation step is programmed into `hs_int_direct`, while the respective control routines that provide the correct input and variables are `hs_int` and `dfpt_hs_int`. The main effort in implementing DFPT for this area is applying the correct logic to the $\boldsymbol{G}^{(\prime)}$ selection in the evaluation step. The two different sets of reciprocal lattice vectors are chosen according to $|\boldsymbol{k}+\boldsymbol{G}'+\boldsymbol{q}| < K_{\mathrm{max}}$ and $|\boldsymbol{k}+\boldsymbol{G}| < K_{\mathrm{max}}$, respectively. `dfpt_hs_int` is tasked with passing both sets into `hs_int_direct`, whereas `hs_int` passes two copies of the same set.

**The Muffin-Tin Matrix Response**

The same necessity of passing two sets of reciprocal lattice vectors arises for the MT contribution, but there is more to be taken into consideration. For one, in the base case calculation, the MT Hamiltonian is separated into the spherical and non-spherical contribution. For the evaluation of the potential response, such a separation is not necessary and the evaluation is done by constructing the matrix $\underline{t}$ as described in equation (4.48), but for the potential response and for $\ell'' \geq 0$. In contrast to the ground-state setup, this matrix is not Hermitian even for a spin-degenerate system, where usually some computation time can be saved by

using only its upper triangular part in constructing the matrix elements. There is also no separate spherical part or kinetic energy term. The contribution to the matrix response is

$$V_{\text{eff},\boldsymbol{G}',\boldsymbol{G}}^{(1)\beta j+,\text{MT}}(\boldsymbol{k}+\boldsymbol{q},\boldsymbol{k}) = \sum_{\gamma} \boldsymbol{a}^{\boldsymbol{k}+\boldsymbol{G}'+\boldsymbol{q},\gamma\dagger} \cdot \underline{t}^{(1)\beta j+,\gamma} \cdot \boldsymbol{a}^{\boldsymbol{k}+\boldsymbol{G},\gamma}. \tag{5.16}$$

Additionally, the unperturbed Hamiltonian and overlap elements for the displaced atom are calculated and added onto the respective response matrices. *E.g.* for equation (4.89), first the matrix element $\langle\phi_{\boldsymbol{k}\boldsymbol{G}'\boldsymbol{q}}|\mathcal{H}|\phi_{\boldsymbol{k}\boldsymbol{G}}\rangle_\beta$ is calculated in the same way as for the base case and then subsequently multiplied with the imaginary prefactor $\mathrm{i}(G-G'-q)_j$ and added onto the Hamiltonian response. For each of the contributions above, local orbitals have to be taken into account as well. The analogous control routines to the IR case are `hsmt` and `dfpt_hsmt`, while the routines called for the particular contributions are `hsmt_sph`, `hsmt_nonsph`, and `hsmt_lo`. The matrix setup of the radial terms is handled by `tlmplm`, which is called with the necessary logic either by `tlmplm_cholesky` or `dfpt_tlmplm`.

## 5.3 Handling Degenerate Eigenvalues

Solving the Sternheimer Equation

The solution of the Sternheimer equation (4.96) is represented by a series of consecutive matrix multiplications, that transform the ground-state expansion coefficients of the wave functions to the corresponding response. The response matrix setup in the previous chapter serves to set up the solution in analogy to the eigenvalue problem of the base case calculation. The analytical inversion of the ground-state matrices will lead to additional problems for degenerate eigenvalues in the reciprocal energy difference, as such terms would become singular if they are not dealt with separately. Preceding works [92, 93] opted to drop the contributions to the expansion coefficients for energy differences below $10^{-7}$ Ha and set them to $0$. In this work, we want to go beyond this neglect. Instead, to analyze and avoid this problem, we look at the equation in the space of eigenstates, meaning we evaluate the rightmost matrices for the states at $\boldsymbol{k}$ and $\boldsymbol{k}+\boldsymbol{q}$ and look at the expansion vectors coefficient wise, to find

$$\boldsymbol{z}_{\boldsymbol{k}\boldsymbol{G}\boldsymbol{q},\nu}^{(1)\beta j+} = -\sum_{\nu'} z_{\boldsymbol{k}\boldsymbol{G}\boldsymbol{q}\nu'} \frac{H_{\nu'\nu}^{(1)\beta j+}(\boldsymbol{k}+\boldsymbol{q},\boldsymbol{k}) - \varepsilon_{\boldsymbol{k}\nu} S_{\nu'\nu}^{(1)\beta j+}(\boldsymbol{k}+\boldsymbol{q},\boldsymbol{k})}{\varepsilon_{\boldsymbol{k}+\boldsymbol{q},\nu'} - \varepsilon_{\boldsymbol{k}\nu}}. \tag{5.17}$$

The key to making the reciprocal term less volatile is looking at how this equation is used. It most importantly enters the calculation of the first order density response and secondly gives a contribution to the dynamical matrix through the terms $C_{\boldsymbol{k}\nu}^{(2)\beta\boldsymbol{R}'j\alpha\boldsymbol{R}i}$ in equation (4.87). We look at the first use case first and write

$$\begin{aligned}
n^{(1)\beta j+}(\boldsymbol{r}) &= \sum_{\boldsymbol{k}\nu} 2\tilde{f}_{\boldsymbol{k}\nu} \psi_{\boldsymbol{k}\boldsymbol{q}\nu}^*(\boldsymbol{r}) \psi_{\boldsymbol{k}\nu}^{(1)\beta j+}(\boldsymbol{r}) \\
&= \sum_{\boldsymbol{k}\nu} 2\tilde{f}_{\boldsymbol{k}\nu} \psi_{\boldsymbol{k}\nu}^*(\boldsymbol{r}) \sum_{\boldsymbol{G}} z_{\boldsymbol{k}\boldsymbol{G}\boldsymbol{q}\nu}^{(1)\beta j+} \phi_{\boldsymbol{k}\boldsymbol{G}\boldsymbol{q}}(\boldsymbol{r}) \\
&= -\sum_{\boldsymbol{k}\nu} 2\tilde{f}_{\boldsymbol{k}\nu} \psi_{\boldsymbol{k}\nu}^*(\boldsymbol{r}) \sum_{\nu'} \psi_{\boldsymbol{k}\boldsymbol{q}\nu'}(\boldsymbol{r}) (\varepsilon_{\boldsymbol{k}+\boldsymbol{q},\nu'} - \varepsilon_{\boldsymbol{k}\nu})^{-1} \times \\
&\quad \left( H_{\nu'\nu}^{(1)\beta j+}(\boldsymbol{k}+\boldsymbol{q},\boldsymbol{k}) - \varepsilon_{\boldsymbol{k}\nu} S_{\nu'\nu}^{(1)\beta j+}(\boldsymbol{k}+\boldsymbol{q},\boldsymbol{k}) \right),
\end{aligned} \tag{5.18}$$

neglecting the basis correction and occupation number response for now. We insert a factor of $1 = 1 - \tilde{f}_{\boldsymbol{kq}\nu'} + \tilde{f}_{\boldsymbol{kq}\nu'}$ into the rightmost sum and look at the resulting term, that contains both occupation numbers (without the prefactors):

$$\begin{aligned} a^{(1)\beta j+} = \sum_{\boldsymbol{k}\nu\nu'} \tilde{f}_{\boldsymbol{k}\nu}\tilde{f}_{\boldsymbol{kq}\nu'}\psi^*_{\boldsymbol{k}\nu}(\boldsymbol{r})\psi_{\boldsymbol{kq}\nu'}(\boldsymbol{r})(\varepsilon_{\boldsymbol{k}+\boldsymbol{q},\nu'} - \varepsilon_{\boldsymbol{k}\nu})^{-1}\times \\ \left(H^{(1)\beta j+}_{\nu'\nu}(\boldsymbol{k}+\boldsymbol{q},\boldsymbol{k}) - \varepsilon_{\boldsymbol{k}\nu}S^{(1)\beta j+}_{\nu'\nu}(\boldsymbol{k}+\boldsymbol{q},\boldsymbol{k})\right) \end{aligned} \tag{5.19}$$

Under the assumption of time reversal or inversion symmetry (*cf.* the density response generation in section 3.5), this term can be reformulated for a pair of occupied states. The derivation, which is very similar to early considerations in [82], hinges on the manipulation of the k-point and state sums. We first identify the shifted Bloch vector $\boldsymbol{k}+\boldsymbol{q}$ as another $\boldsymbol{k}'$. Then we factor out a negative sign from the resulting (shifted) Bloch vectors and apply the symmetry that we required above. Finally, we once again identify a new Bloch vector (written as the original one) in $\boldsymbol{k} = -\boldsymbol{k}'$. As a chain of equations, this yields

$$\begin{aligned} &\sum_{\boldsymbol{k}\nu\nu'} \tilde{f}_{\boldsymbol{k}\nu}\tilde{f}_{\boldsymbol{kq}\nu'}\psi^*_{\boldsymbol{k}\nu}(\boldsymbol{r})\psi_{\boldsymbol{kq}\nu'}(\boldsymbol{r})(\varepsilon_{\boldsymbol{k}+\boldsymbol{q},\nu'} - \varepsilon_{\boldsymbol{k}\nu})^{-1}\times \\ &\left(H^{(1)\beta j+}_{\nu'\nu}(\boldsymbol{k}+\boldsymbol{q},\boldsymbol{k}) - \varepsilon_{\boldsymbol{k}\nu}S^{(1)\beta j+}_{\nu'\nu}(\boldsymbol{k}+\boldsymbol{q},\boldsymbol{k})\right) \\ \overset{\boldsymbol{k}'=\boldsymbol{k}+\boldsymbol{q}}{=}&\sum_{\boldsymbol{k}'\nu\nu'} \tilde{f}_{\boldsymbol{k}'-\boldsymbol{q},\nu}\tilde{f}_{\boldsymbol{k}'\nu'}\psi^*_{\boldsymbol{k}'-\boldsymbol{q},\nu}(\boldsymbol{r})\psi_{\boldsymbol{k}'\nu'}(\boldsymbol{r})(\varepsilon_{\boldsymbol{k}',\nu'} - \varepsilon_{\boldsymbol{k}'-\boldsymbol{q},\nu})^{-1}\times \\ &\left(H^{(1)\beta j+}_{\nu'\nu}(\boldsymbol{k}',\boldsymbol{k}'-\boldsymbol{q}) - \varepsilon_{\boldsymbol{k}'-\boldsymbol{q},\nu}S^{(1)\beta j+}_{\nu'\nu}(\boldsymbol{k}',\boldsymbol{k}'-\boldsymbol{q})\right) \\ =&\sum_{\boldsymbol{k}'\nu\nu'} \tilde{f}_{-(-\boldsymbol{k}'+\boldsymbol{q}),\nu}\tilde{f}_{-(-\boldsymbol{k}')\nu'}\psi^*_{-(-\boldsymbol{k}'+\boldsymbol{q}),\nu}(\boldsymbol{r})\psi_{-(-\boldsymbol{k}')\nu'}(\boldsymbol{r})(\varepsilon_{-(-\boldsymbol{k}'),\nu'} - \varepsilon_{-(-\boldsymbol{k}'+\boldsymbol{q}),\nu})^{-1}\times \\ &\left(H^{(1)\beta j+}_{\nu'\nu}(-(-\boldsymbol{k}'),-(-\boldsymbol{k}'+\boldsymbol{q})) - \varepsilon_{-(-\boldsymbol{k}'+\boldsymbol{q}),\nu}S^{(1)\beta j+}_{\nu'\nu}(-(-\boldsymbol{k}'),-(-\boldsymbol{k}'+\boldsymbol{q}))\right) \\ \overset{\text{sym}}{=}&\sum_{\boldsymbol{k}'\nu\nu'} \tilde{f}_{-\boldsymbol{k}'+\boldsymbol{q},\nu}\tilde{f}_{-\boldsymbol{k}'\nu'}\psi^*_{-\boldsymbol{k}'+\boldsymbol{q},\nu}(\boldsymbol{r})\psi_{-\boldsymbol{k}'\nu'}(\boldsymbol{r})(\varepsilon_{-\boldsymbol{k}',\nu'} - \varepsilon_{-\boldsymbol{k}'+\boldsymbol{q},\nu})^{-1}\times \\ &\left(H^{(1)\beta j+}_{\nu'\nu}(-\boldsymbol{k}',-\boldsymbol{k}'+\boldsymbol{q}) - \varepsilon_{-\boldsymbol{k}'+\boldsymbol{q},\nu}S^{(1)\beta j+}_{\nu'\nu}(-\boldsymbol{k}',-\boldsymbol{k}'+\boldsymbol{q})\right) \\ \overset{\boldsymbol{k}=-\boldsymbol{k}'}{=}&\sum_{\boldsymbol{k}\nu\nu'} \tilde{f}_{\boldsymbol{k}+\boldsymbol{q},\nu}\tilde{f}_{\boldsymbol{k}\nu'}\psi^*_{\boldsymbol{k}+\boldsymbol{q},\nu}(\boldsymbol{r})\psi_{\boldsymbol{k}\nu'}(\boldsymbol{r})(\varepsilon_{\boldsymbol{k},\nu'} - \varepsilon_{\boldsymbol{k}+\boldsymbol{q},\nu})^{-1}\times \\ &\left(H^{(1)\beta j+}_{\nu'\nu}(\boldsymbol{k},\boldsymbol{k}+\boldsymbol{q}) - \varepsilon_{\boldsymbol{k}+\boldsymbol{q},\nu}S^{(1)\beta j+}_{\nu'\nu}(\boldsymbol{k},\boldsymbol{k}+\boldsymbol{q})\right) = b^{(1)\beta j+}. \end{aligned} \tag{5.20}$$

We identify this reformulation as a new coefficient $b^{(1)\beta j+}$, that looks very similar to the $a^{(1)\beta j+}$ we defined in equation (5.19), up to a negative sign and a switch of the indices $\nu'$ and $\nu$. The latter is arbitrary and can be lifted by renaming the states, which yields

$$\begin{aligned} b^{(1)\beta j+} = -\sum_{\boldsymbol{k}\nu\nu'} \tilde{f}_{\boldsymbol{k}\nu}\tilde{f}_{\boldsymbol{kq}\nu'}\psi^*_{\boldsymbol{k}\nu}(\boldsymbol{r})\psi_{\boldsymbol{kq}\nu'}(\boldsymbol{r})(\varepsilon_{\boldsymbol{k}+\boldsymbol{q},\nu'} - \varepsilon_{\boldsymbol{k}\nu})^{-1}\times \\ \left(H^{(1)\beta j+}_{\nu'\nu}(\boldsymbol{k}+\boldsymbol{q},\boldsymbol{k}) - \varepsilon_{\boldsymbol{k}+\boldsymbol{q},\nu'}S^{(1)\beta j+}_{\nu'\nu}(\boldsymbol{k}+\boldsymbol{q},\boldsymbol{k})\right) = a^{(1)\beta j+}. \end{aligned} \tag{5.21}$$

Replacing the initial term $a^{(1)\beta j+}$ by the arithmetic mean of it and the reformulation $b^{(1)\beta j+}$, the reciprocal energy difference can be canceled out and the Hamiltonian term vanishes, which gives us

$$a^{(1)\beta j+} = \frac{a^{(1)\beta j+} + b^{(1)\beta j+}}{2} = \sum_{\boldsymbol{k}\nu\nu'} \tilde{f}_{\boldsymbol{k}\nu}\tilde{f}_{\boldsymbol{kq}\nu'}\psi^*_{\boldsymbol{k}\nu}(\boldsymbol{r})\psi_{\boldsymbol{kq}\nu'}(\boldsymbol{r})\frac{S^{(1)\beta j+}_{\nu'\nu}(\boldsymbol{k}+\boldsymbol{q},\boldsymbol{k})}{2}. \tag{5.22}$$

We want to provide this as a modified expansion coefficient response $\boldsymbol{z}^{(1)\beta j+}_{\boldsymbol{kGq},\nu}$. To do so we need to reintroduce the neglected prefactors, cover the remaining portion $1-\tilde{f}_{\boldsymbol{kq}\nu'}$ of the factor we introduced, and look only at the part, that does not come from the density construction itself. If we write the coefficients as a contraction of the unperturbed expansion coefficients at $\boldsymbol{k}+\boldsymbol{q}$ and a band representation of the responses,

$$\boldsymbol{z}^{(1)\beta j+}_{\boldsymbol{kGq},\nu} = -\sum_{\nu'} z_{\boldsymbol{kGq}\nu'} z^{(1)\beta j+}_{\boldsymbol{q}\nu',\boldsymbol{k}\nu}, \tag{5.23}$$

the result can be written as a modification of the band part. First, however, we additionally look at the case of vanishing energy differences. In that case (or when the energy difference is at least negligibly small) we can follow an analogous derivation without inserting the factor first, to find a complementary result. Summing up the results, we can write

$$z^{(1)\beta j+}_{\boldsymbol{q}\nu',\boldsymbol{k}\nu} = \begin{cases} S^{(1)\beta j+}_{\nu'\nu}(\boldsymbol{k}+\boldsymbol{q},\boldsymbol{k})/2, & \varepsilon_{\boldsymbol{k}+\boldsymbol{q},\nu'} - \varepsilon_{\boldsymbol{k}\nu} = 0 \\ \frac{1-\tilde{f}_{\boldsymbol{kq}\nu'}}{\varepsilon_{\boldsymbol{k}+\boldsymbol{q},\nu'}-\varepsilon_{\boldsymbol{k}\nu}} \left( H^{(1)\beta j+}_{\nu'\nu}(\boldsymbol{k}+\boldsymbol{q},\boldsymbol{k}) - \varepsilon_{\boldsymbol{k}\nu} S^{(1)\beta j+}_{\nu'\nu}(\boldsymbol{k}+\boldsymbol{q},\boldsymbol{k}) \right) & \\ +\tilde{f}_{\boldsymbol{kq}\nu'} S^{(1)\beta j+}_{\nu'\nu}(\boldsymbol{k}+\boldsymbol{q},\boldsymbol{k})/2, & \text{occ-occ} \\ (\varepsilon_{\boldsymbol{k}+\boldsymbol{q},\nu'} - \varepsilon_{\boldsymbol{k}\nu})^{-1} \left( H^{(1)\beta j+}_{\nu'\nu}(\boldsymbol{k}+\boldsymbol{q},\boldsymbol{k}) - \varepsilon_{\boldsymbol{k}\nu} S^{(1)\beta j+}_{\nu'\nu}(\boldsymbol{k}+\boldsymbol{q},\boldsymbol{k}) \right), & \text{else} \end{cases} \tag{5.24}$$

and thus arrive at the desired form. The modification corresponds to the elimination of occupied-occupied combinations, which are reduced to an overlap term. This can be seen from the factor $1-\tilde{f}_{\boldsymbol{kq}\nu'}$ in the occ-occ case. Moving on to the second use of the coefficients, the contribution to $C^{(2)\beta j-\alpha i+}_{\boldsymbol{k}\nu}$ that is related to them can be transformed as well. The relevant contribution (that once again makes use of the same symmetry as before) is

$$\begin{aligned} C^{(2)\beta j-\alpha i+}_{\boldsymbol{k}\nu} = \ldots + 2 \sum_{\boldsymbol{G}'\boldsymbol{G}} z^{(1)\beta j+*}_{\boldsymbol{kG}'\boldsymbol{q},\nu} \{ &\mathrm{i}(G-G'-q)_i (H^{\alpha}_{\boldsymbol{G}',\boldsymbol{G}}(\boldsymbol{k}+\boldsymbol{q},\boldsymbol{k}) - \varepsilon_{\boldsymbol{k}\nu} S^{\alpha}_{\boldsymbol{G}',\boldsymbol{G}}(\boldsymbol{k}+\boldsymbol{q},\boldsymbol{k})) \\ &+ \langle \phi_{\boldsymbol{kG}'\boldsymbol{q}} | \Theta^{(1)\alpha i+}_{\mathrm{IR}}(\boldsymbol{\mathcal{H}} - \varepsilon_{\boldsymbol{k}\nu}) | \phi_{\boldsymbol{kG}\nu} \rangle_{\Omega} \} z_{\boldsymbol{kG}\nu}. \end{aligned} \tag{5.25}$$

Summing up to $\sum_{\boldsymbol{k}\nu} \tilde{f}_{\boldsymbol{k}\nu} C^{(2)\beta j-\alpha i+}_{\boldsymbol{k}\nu}$ and writing the evaluated matrix elements as a pseudo Hamiltonian and overlap, we can do a similar derivation as before. For an analogous coefficient to that in equation (5.19) that corresponds to the use case of the DM, we find the identity

$$\begin{aligned} a^{(2)\beta j-\alpha i+}_{\mathrm{DM}} &= \sum_{\boldsymbol{k}\nu\nu'} \tilde{f}_{\boldsymbol{k}\nu} \tilde{f}_{\boldsymbol{kq}\nu'} (\varepsilon_{\boldsymbol{k}+\boldsymbol{q},\nu'} - \varepsilon_{\boldsymbol{k}\nu})^{-1} \left( H^{(1)\beta j+}_{\nu'\nu}(\boldsymbol{k}+\boldsymbol{q},\boldsymbol{k}) - \varepsilon_{\boldsymbol{k}\nu} S^{(1)\beta j+}_{\nu'\nu}(\boldsymbol{k}+\boldsymbol{q},\boldsymbol{k}) \right)^* \times \\ &\qquad \left( \tilde{H}_{\nu'\nu}(\boldsymbol{k}+\boldsymbol{q},\boldsymbol{k}) - \varepsilon_{\boldsymbol{k}\nu} \tilde{S}_{\nu'\nu}(\boldsymbol{k}+\boldsymbol{q},\boldsymbol{k}) \right) \\ &= -\sum_{\boldsymbol{k}\nu\nu'} \tilde{f}_{\boldsymbol{k}\nu} \tilde{f}_{\boldsymbol{kq}\nu'} (\varepsilon_{\boldsymbol{k}+\boldsymbol{q},\nu'} - \varepsilon_{\boldsymbol{k}\nu})^{-1} \left( H^{(1)\beta j+}_{\nu'\nu}(\boldsymbol{k}+\boldsymbol{q},\boldsymbol{k}) - \varepsilon_{\boldsymbol{k}+\boldsymbol{q},\nu'} S^{(1)\beta j+}_{\nu'\nu}(\boldsymbol{k}+\boldsymbol{q},\boldsymbol{k}) \right)^* \times \\ &\qquad \left( \tilde{H}_{\nu'\nu}(\boldsymbol{k}+\boldsymbol{q},\boldsymbol{k}) - \varepsilon_{\boldsymbol{k}+\boldsymbol{q},\nu'} \tilde{S}_{\nu'\nu}(\boldsymbol{k}+\boldsymbol{q},\boldsymbol{k}) \right). \end{aligned} \tag{5.26}$$

Using the same mean as before and rearranging some terms gives a form, that is very reminiscent of the transformation for the density case, but has an additional contribution that needs to be evaluated for the final iteration of the SCF cycle:

$$a^{(2)\beta j-\alpha i+}_{\mathrm{DM}} = \sum_{\boldsymbol{k}\nu\nu'} \tilde{f}_{\boldsymbol{k}\nu} \tilde{f}_{\boldsymbol{kq}\nu'} \{ \frac{S^{(1)\beta j+*}_{\nu'\nu}(\boldsymbol{k}+\boldsymbol{q},\boldsymbol{k})}{2} \left( \tilde{H}_{\nu'\nu}(\boldsymbol{k}+\boldsymbol{q},\boldsymbol{k}) - \varepsilon_{\boldsymbol{k}\nu} \tilde{S}_{\nu'\nu}(\boldsymbol{k}+\boldsymbol{q},\boldsymbol{k}) \right) \tag{5.27a}$$

$$+ \left( H^{(1)\beta j+}_{\nu'\nu}(\boldsymbol{k}+\boldsymbol{q},\boldsymbol{k}) - \varepsilon_{\boldsymbol{k}+\boldsymbol{q},\nu'} S^{(1)\beta j+}_{\nu'\nu}(\boldsymbol{k}+\boldsymbol{q},\boldsymbol{k}) \right)^* \frac{\tilde{S}_{\nu'\nu}(\boldsymbol{k}+\boldsymbol{q},\boldsymbol{k})}{2} \}. \tag{5.27b}$$

The same analogy holds for a contribution with vanishing energy difference, and we can write the second part (5.27b) as an additional expansion coefficient that must be calculated. Its band resolved form reads

$$z^{(1)\beta j+}_{\boldsymbol{q}\nu',\boldsymbol{k}\nu,\mathrm{DM}} = \begin{cases} \left(H^{(1)\beta j+}_{\nu'\nu}(\boldsymbol{k}+\boldsymbol{q},\boldsymbol{k}) - \varepsilon_{\boldsymbol{k}\nu} S^{(1)\beta j+}_{\nu'\nu}(\boldsymbol{k}+\boldsymbol{q},\boldsymbol{k})\right)/2, & \varepsilon_{\boldsymbol{k}+\boldsymbol{q},\nu'} - \varepsilon_{\boldsymbol{k}\nu} = 0 \\ \tilde{f}_{\boldsymbol{k}\boldsymbol{q}\nu'}\left(H^{(1)\beta j+}_{\nu'\nu}(\boldsymbol{k}+\boldsymbol{q},\boldsymbol{k}) - \varepsilon_{\boldsymbol{k}+\boldsymbol{q},\nu'} S^{(1)\beta j+}_{\nu'\nu}(\boldsymbol{k}+\boldsymbol{q},\boldsymbol{k})\right)/2, & \text{occ-occ} \\ 0, & \text{else} \end{cases} \tag{5.28}$$

With this, we gained a numerically stable form that avoids the division by small energy differences. In practice, it is not applied at a difference of 0, but tied to a cutoff parameter `eDiffcut`, below which the correction is applied. It can be set in the `juPhon` tag of the input file and is set to $10^{-7}$ Ha by default. The importance of such a modification is shown in chapter 6, where it massively influences the dispersion relation of fcc Ne. The necessary logic of equations (5.24) and (5.28) is implemented in the `dfpt_eigen` subroutine and the workflow is elucidated for a specific k-point in algorithm 1.

Aside from the expansion coefficient response, we need the response of the eigenenergies and of the occupation numbers. The eigenenergy calculation is resolved before the division over the energy difference is done and hence does not need to be modified from equation (4.93). Similarly, the calculation for $\tilde{f}^{(1)\beta j+}_{\boldsymbol{k}\nu}$ does not need to be modified from equations (3.38) and (3.39), as there are no additional corrections from the use of the FLAPW method. We do, however, keep in mind that the eigenenergies are only perturbed to first order for $\boldsymbol{q} = \boldsymbol{0}$, which translates to the Fermi energy and occupation numbers.

**Algorithm 1:** Selection logic for the calculation of the first order expansion coefficients for a specific k-point.

**Input:** $H^{(1)\beta j+}_{\nu'\nu}(\boldsymbol{k}+\boldsymbol{q},\boldsymbol{k})$, $S^{(1)\beta j+}_{\nu'\nu}(\boldsymbol{k}+\boldsymbol{q},\boldsymbol{k})$, $\varepsilon_{\boldsymbol{k}+\boldsymbol{q},\nu'}$, $\varepsilon_{\boldsymbol{k},\nu}$
**Output:** $z^{(1)\beta j+}_{\boldsymbol{q}\nu',\boldsymbol{k}\nu}$, $z^{(1)\beta j+}_{\boldsymbol{q}\nu',\boldsymbol{k}\nu,\mathrm{DM}}$, $\varepsilon^{(1)\beta j}_{\boldsymbol{k}\nu}$
**for** $\nu$ **do**
  **if** $\boldsymbol{q}=0$ **then**
    eigs1($\nu$) $\leftarrow\left(H^{(1)\beta j+}_{\nu'\nu}(\boldsymbol{k}+\boldsymbol{q},\boldsymbol{k})-\varepsilon_{\boldsymbol{k}\nu}S^{(1)\beta j+}_{\nu'\nu}(\boldsymbol{k}+\boldsymbol{q},\boldsymbol{k})\right)$;
  **else**
    eigs1($\nu$) $\leftarrow 0$;
  **end if**
  **for** $\nu'$ **do**
    **if** $\boldsymbol{q}=\boldsymbol{0}$ *and* $\nu'=\nu$ **then**
      tempMat2($\nu'$) $\leftarrow 0$;
      **if** *Sternheimer converged* **then**
        tempMat3($\nu'$) $\leftarrow 0$;
      **end if**
    **else if** $\varepsilon_{\boldsymbol{k}+\boldsymbol{q},\nu'}-\varepsilon_{\boldsymbol{k},\nu}<$ `eDiffcut` **then**
      tempMat2($\nu'$) $\leftarrow S^{(1)\beta j+}_{\nu'\nu}(\boldsymbol{k}+\boldsymbol{q},\boldsymbol{k})/2$;
      **if** *Sternheimer converged* **then**
        tempMat3($\nu'$) $\leftarrow\left(H^{(1)\beta j+}_{\nu'\nu}(\boldsymbol{k}+\boldsymbol{q},\boldsymbol{k})-\varepsilon_{\boldsymbol{k}\nu}S^{(1)\beta j+}_{\nu'\nu}(\boldsymbol{k}+\boldsymbol{q},\boldsymbol{k})\right)/2$;
      **end if**
    **else if** $\nu',\nu$ *occupied* **then**
      tempMat2($\nu'$) $\leftarrow\frac{1-\tilde{f}_{\boldsymbol{k}\boldsymbol{q}\nu'}}{\varepsilon_{\boldsymbol{k}+\boldsymbol{q},\nu'}-\varepsilon_{\boldsymbol{k}\nu}}\left(H^{(1)\beta j+}_{\nu'\nu}(\boldsymbol{k}+\boldsymbol{q},\boldsymbol{k})-\varepsilon_{\boldsymbol{k}\nu}S^{(1)\beta j+}_{\nu'\nu}(\boldsymbol{k}+\boldsymbol{q},\boldsymbol{k})\right)$;
      tempMat2($\nu'$) $\leftarrow$tempMat2($\nu'$)$+\tilde{f}_{\boldsymbol{k}\boldsymbol{q}\nu'}S^{(1)\beta j+}_{\nu'\nu}(\boldsymbol{k}+\boldsymbol{q},\boldsymbol{k})/2$;
      **if** *Sternheimer converged* **then**
        tempMat3($\nu'$) $\leftarrow\tilde{f}_{\boldsymbol{k}\boldsymbol{q}\nu'}\left(H^{(1)\beta j+}_{\nu'\nu}(\boldsymbol{k}+\boldsymbol{q},\boldsymbol{k})-\varepsilon_{\boldsymbol{k}+\boldsymbol{q},\nu'}S^{(1)\beta j+}_{\nu'\nu}(\boldsymbol{k}+\boldsymbol{q},\boldsymbol{k})\right)/2$;
      **end if**
    **else**
      tempMat2($\nu'$)
       $\leftarrow(\varepsilon_{\boldsymbol{k}+\boldsymbol{q},\nu'}-\varepsilon_{\boldsymbol{k}\nu})^{-1}\left(H^{(1)\beta j+}_{\nu'\nu}(\boldsymbol{k}+\boldsymbol{q},\boldsymbol{k})-\varepsilon_{\boldsymbol{k}\nu}S^{(1)\beta j+}_{\nu'\nu}(\boldsymbol{k}+\boldsymbol{q},\boldsymbol{k})\right)$;
      **if** *Sternheimer converged* **then**
        tempMat3($\nu'$) $\leftarrow 0$;
      **end if**
    **end if**
  **end for**
  $\{z^{(1)\beta j+}_{\boldsymbol{q}\nu',\boldsymbol{k}\nu}\}_{\nu'}\leftarrow$tempMat2;
  $\{z^{(1)\beta j+}_{\boldsymbol{q}\nu',\boldsymbol{k}\nu,\mathrm{DM}}\}_{\nu'}\leftarrow$tempMat3;
**end for**
$\varepsilon^{(1)\beta j}_{\boldsymbol{k}\nu}\leftarrow$eigs1

## 5.4 Extending the Density Generation

The Interstitial Response

With the expansion coefficient and occupation number responses covered, we have all the ingredients to deal with the first order density response. Here, we again separate the calculation into the IR and MT contributions. The interstitial case is very similar to the ground-state calculation, only that both the expansion coefficients and their responses need to be transformed into real space, where the density response can then be constructed from equation (3.33) with the same scheme as described along equations (4.52) and (4.53). The only thing to keep in mind, is that we operate at a shifted Bloch vector $\boldsymbol{k}+\boldsymbol{q}$ for one of the wave functions and $\boldsymbol{G}+\boldsymbol{q}$ for the density response Fourier coefficients. For this we adapt the routine `pwden`, that contains calls to the `FLEUR` FFT interface. The MT response proves to be a bit more complicated to implement.

The Muffin-Tin Response

For this part, we want to construct the response by first summing up all matching and expansion coefficients into a coefficient, that only depends on the $(\ell'' m'')$-channel of the radial function $n^{(1)\beta j+}_{\gamma\ell'' m''}(r_\gamma)$ and the orbital quantum numbers $\ell, \ell'$ and orders $(\cdot), (\cdot)'$ of the radial functions it is multiplied with. This can then be evaluated exactly like equation (4.55). The FLAPW-DFPT specific correction in this procedure affects the construction of the coefficient $d^{\boldsymbol{k}\gamma}_{\ell'\ell\ell''(\cdot)'(\cdot)}$. It will contain the response of both the expansion and the matching coefficients and the occupation numbers, and thus have extra terms for the displaced MT. Furthermore, the density gradient part of the basis response in equation (4.70) is compounded into one term that represents the gradient of the density. All in all, this yields for the representation of the density response in the MT

$$n^{(1)\beta j+}_{\gamma\ell'' m''}(r_\gamma) = \sum_{\boldsymbol{k}} \sum_{\substack{\ell'(\cdot)' \\ \ell(\cdot)}} d^{(1)\beta j+,\boldsymbol{k}\gamma}_{\ell'\ell\ell''(\cdot)'(\cdot)} u^{(\cdot)'\gamma}_{\ell'}(r_\gamma) u^{(\cdot)\gamma}_{\ell}(r_\gamma) - \delta_{\gamma\beta} \left(\nabla_j n\right)_{\gamma\ell'' m''}(r_\gamma). \tag{5.29}$$

In it, we defined the adjusted d-coefficients

$$\begin{aligned} d^{(1)\beta j+,\boldsymbol{k}\gamma}_{\ell'\ell\ell''(\cdot)'(\cdot)} = &\sum_{\nu} \tilde{f}_{\boldsymbol{k}\nu} \sum_{m',m} A^{\boldsymbol{k}\nu\gamma *}_{\ell' m'(\cdot)'} A^{(1)\beta j+,\boldsymbol{k}\nu\gamma}_{\ell m(\cdot)} G^{m,m'',m'}_{\ell,\ell'',\ell'} \\ &+ \sum_{\nu} \tilde{f}^{(1)\beta j+}_{\boldsymbol{k}\nu} \sum_{m',m} A^{\boldsymbol{k}\nu\gamma *}_{\ell' m'(\cdot)'} A^{\boldsymbol{k}\nu\gamma}_{\ell m(\cdot)} G^{m,m'',m'}_{\ell,\ell'',\ell'} \end{aligned} \tag{5.30}$$

and the corresponding adjusted matching coefficients

$$A^{(1)\beta j+,\boldsymbol{k}\nu\gamma}_{\ell m(\cdot)} = \sum_{\boldsymbol{G}} 2 z^{(1)\beta j+}_{\boldsymbol{k}\boldsymbol{G}\boldsymbol{q}\nu} a^{\boldsymbol{k}+\boldsymbol{G}+\boldsymbol{q},\gamma}_{\ell m(\cdot)} + \delta_{\gamma\beta} z_{\boldsymbol{k}\boldsymbol{G}\nu} \mathrm{i}(\boldsymbol{k}+\boldsymbol{G})_j a^{\boldsymbol{k}+\boldsymbol{G},\gamma}_{\ell m(\cdot)}. \tag{5.31}$$

The program logic is identical to the base case, only with additional optional parameters passed through the subroutines. The calculation of the d-coefficients is contained in a group of routines `rho(n)mt(lo)`, while the final summation of the coefficients and radial functions is found in `cdnmt`. It is used in the same way as it was for the ground-state calculation, aside from providing the adjusted d-coefficients as input, constructing the imaginary part of the density response as well, and skipping the calculation of some output that is meaningless for the DFPT case, but not for the ground state.

Density Response Mixing

The mixing procedure remains largely unchanged by the switch from the density to its response. One thing to keep in mind, however, is the imaginary part of the MT part. Where the density

was expanded into real-valued lattice harmonics, doing so for the density response necessitates the creation of a second MT variable that stores the information of the imaginary part as a real variable as well. This leads to more separate terms in the calculation of equation (4.67). When the mixvector is set up, the components add to its length and must not be neglected. Their metric is the same as for the real part coefficients.

## 5.5 Calculating the Second Order Energy Terms

Rearranging and Evaluating the Second Order Energy

In principle, we have already established a closed form for the second order response of the total energy in equation (4.87). With the previous sections, we already provided most of the necessary quantities to evaluate it, but there are certain problems yet to be addressed. i) The state dependent coefficients $C^{(2)\beta j-\alpha i+}_{\boldsymbol{k}\nu}$ were only alluded to in the section on expansion coefficients, but contain many more terms than were pictured there. ii) A closed form for the calculation of Hellmann–Feynman terms, *i.e.* the second order in the external potential and ion-ion interaction needs to be derived. iii) There appear gradient terms of response quantities and, *e.g.* for $V^{(2)\beta j-\alpha i+}_{\text{ext}}(\boldsymbol{r})$, double gradient terms, that proved to be numerically unwieldy in testing. All these problems will lead to some reformulations and cancellations of specific terms to make the resulting scheme for the dynamical matrix as numerically stable as possible.

State Dependent Coefficients

The contributions to the second order energy derivative can be broadly grouped into three types. There is Hellmann–Feynman contribution, that contains only the density (responses) and the external potential (responses) and would appear as well in a method with no position dependence of the basis. There are also additional terms, that contain the xc and full effective potential in the integrals and stem form the corrections due to the FLAPW basis. The third group is the sum of state dependent coefficients, that are multiplied with the occupation numbers and their responses. To derive the required second order coefficients, we first look at a rearranged and $\boldsymbol{G}$-resolved form of the first order terms,

$$\begin{aligned} C^{(1)\alpha i+}_{\boldsymbol{k}\nu} &= \sum_{\boldsymbol{G}'\boldsymbol{G}} z^*_{\boldsymbol{k}\boldsymbol{G}'\boldsymbol{q},\nu}\{\mathrm{i}(G-G'-q)_i\langle\phi_{\boldsymbol{k}\boldsymbol{G}'\boldsymbol{q}}|H-\varepsilon_{\nu\boldsymbol{k}}|\phi_{\boldsymbol{k}\boldsymbol{G}}\rangle_\alpha \\ &\quad +\langle\phi_{\boldsymbol{k}\boldsymbol{G}'\boldsymbol{q}}|\Theta^{(1)\alpha i+}(T-\varepsilon_{\nu\boldsymbol{k}})|\phi_{\boldsymbol{k}\boldsymbol{G}}\rangle_\Omega\} z_{\boldsymbol{k}\boldsymbol{G}\nu} \\ &= \sum_{\boldsymbol{G}'\boldsymbol{G}} z^*_{\boldsymbol{k}\boldsymbol{G}'\boldsymbol{q},\nu}(\tilde{H}_{\boldsymbol{G}'\boldsymbol{G}}(\boldsymbol{k}+\boldsymbol{q},\boldsymbol{k})-\varepsilon_{\nu\boldsymbol{k}}\tilde{S}_{\boldsymbol{G}'\boldsymbol{G}}(\boldsymbol{k}+\boldsymbol{q},\boldsymbol{k}))z_{\boldsymbol{k}\boldsymbol{G}\nu}, \end{aligned} \tag{5.32}$$

where we grouped Hamiltonian- and overlap-like terms in the last line and explicitly defined them as matrices $\underline{\tilde{H}}$ and $\underline{\tilde{S}}$. Differentiating this equation to second order involves taking the derivative of every component involved, *i.e.* of the Hamiltonian terms, the overlaps, the eigenenergies, and the expansion coefficients. We start from the left with the expansion coefficients. Differentiating them on both ends of the equation leads to a pair of complex conjugate terms with the expansion coefficient response and the matrix part left unchanged. In the same vein as the density response being reduced from equation (3.31) to equation (3.33), they are grouped together by exploiting symmetry to find

$$C^{(2)\beta j-\alpha i+}_{\boldsymbol{k}\nu,\mathrm{z1}} = 2\sum_{\boldsymbol{G}'\boldsymbol{G}} z^{(1)\beta j+*}_{\boldsymbol{k}\boldsymbol{G}'\boldsymbol{q},\nu}(\tilde{H}_{\boldsymbol{G}'\boldsymbol{G}}(\boldsymbol{k}+\boldsymbol{q},\boldsymbol{k})-\varepsilon_{\nu\boldsymbol{k}}\tilde{S}_{\boldsymbol{G}'\boldsymbol{G}}(\boldsymbol{k}+\boldsymbol{q},\boldsymbol{k}))z_{\boldsymbol{k}\boldsymbol{G}\nu}, \tag{5.33}$$

which was already discussed in section 5.3, where it takes a slightly different form due to the modified expansion coefficients. For the overlap part, taking the second derivative is the

same as adding another prefactor and a selection of the displaced MT, as can be seen from *e.g.* equation (5.13). The terms stem from the first order step function and basis correction terms in the MT, that both give a prefactor of the reciprocal lattice vectors and the imaginary unit. Only the already displaced MT can give another contribution due to the derivative of the structure factor. This yields

$$C^{(2)\beta j-\alpha i+}_{\boldsymbol{k}\nu,\mathrm{S}} = -\sum_{\boldsymbol{G}'\boldsymbol{G}} z^*_{\boldsymbol{k}\boldsymbol{G}'\boldsymbol{q},\nu}(\varepsilon_{\nu\boldsymbol{k}}\tilde{S}^{(1)\beta j-}_{\boldsymbol{G}'\boldsymbol{G}}(\boldsymbol{k},\boldsymbol{k}) + \varepsilon^{(1)\beta j-}_{\nu\boldsymbol{k}}\tilde{S}_{\boldsymbol{G}'\boldsymbol{G}}(\boldsymbol{k},\boldsymbol{k}))z_{\boldsymbol{k}\boldsymbol{G}\nu}, \tag{5.34}$$

$$\tilde{S}^{(1)\beta j-}_{\boldsymbol{G}'\boldsymbol{G}}(\boldsymbol{k},\boldsymbol{k}) = \delta_{\beta\alpha}\mathrm{i}(G-G')_j\tilde{S}_{\boldsymbol{G}'\boldsymbol{G}}(\boldsymbol{k},\boldsymbol{k}). \tag{5.35}$$

A similar form translates directly to the Hamiltonian part, albeit with the kinetic energy term added in. Additionally, the effective potential response appears from the direct differentiation of the Hamiltonian matrix. We find

$$C^{(2)\beta j-\alpha i+}_{\boldsymbol{k}\nu,\mathrm{H}} = \sum_{\boldsymbol{G}'\boldsymbol{G}} z^*_{\boldsymbol{k}\boldsymbol{G}'\boldsymbol{q},\nu}\tilde{H}^{(1)\beta j-}_{\boldsymbol{G}'\boldsymbol{G}}(\boldsymbol{k},\boldsymbol{k})z_{\boldsymbol{k}\boldsymbol{G}\nu}, \tag{5.36}$$

$$\tilde{H}^{(1)\beta j-}_{\boldsymbol{G}'\boldsymbol{G}}(\boldsymbol{k},\boldsymbol{k}) = \delta_{\beta\alpha}\mathrm{i}(G-G')_j\tilde{H}_{\boldsymbol{G}'\boldsymbol{G}}(\boldsymbol{k},\boldsymbol{k}) + \mathrm{i}(G-G')_i V^{(1)\beta j-,\mathrm{MT}}_{\mathrm{eff},\boldsymbol{G}'\boldsymbol{G}}(\boldsymbol{k},\boldsymbol{k}). \tag{5.37}$$

With these equations and the insights from section 5.3, we can finally write down the full form of the state dependent dynamical matrix contributions as

$$E^{(2)\beta j-\alpha i+}_{\mathrm{state}} = \sum_{\boldsymbol{k}\nu}\left\{\tilde{f}^{(1)\beta j-}_{\nu\boldsymbol{k}}C^{(1)\alpha i+}_{\boldsymbol{k}\nu} + \tilde{f}_{\nu\boldsymbol{k}}C^{(2)\beta j-\alpha i+}_{\boldsymbol{k}\nu}\right\} \tag{5.38}$$

with the second order coefficients

$$\begin{aligned} C^{(2)\beta j-\alpha i+}_{\boldsymbol{k}\nu} = \sum_{\boldsymbol{G}'\boldsymbol{G}}\{\, & z^{(1)\beta j+*}_{\boldsymbol{k}\boldsymbol{G}'\boldsymbol{q},\nu}\left(\tilde{H}_{\boldsymbol{G}'\boldsymbol{G}}(\boldsymbol{k}+\boldsymbol{q},\boldsymbol{k}) - \varepsilon_{\nu\boldsymbol{k}}\tilde{S}_{\boldsymbol{G}'\boldsymbol{G}}(\boldsymbol{k}+\boldsymbol{q},\boldsymbol{k})\right) \\ & + z^*_{\boldsymbol{k}\boldsymbol{G}',\nu}\left[\tilde{H}^{(1)\beta j-}_{\boldsymbol{G}'\boldsymbol{G}}(\boldsymbol{k},\boldsymbol{k}) - \varepsilon_{\nu\boldsymbol{k}}\tilde{S}^{(1)\beta j-}_{\boldsymbol{G}'\boldsymbol{G}}(\boldsymbol{k},\boldsymbol{k}) - \varepsilon^{(1)\beta j-}_{\nu\boldsymbol{k}}\tilde{S}_{\boldsymbol{G}'\boldsymbol{G}}(\boldsymbol{k},\boldsymbol{k})\right]\Big\} z_{\boldsymbol{k}\boldsymbol{G}\nu}. \end{aligned} \tag{5.39}$$

Regrouping Non-HF Integral Terms

We look next at the integral terms, that are not related to the external potential. Specifically, the MT integrals of the effective potential in equation (4.87d) are of interest. We can reformulate the loose MT surface integral to find a form, that only contains terms with canceled gradient character:

$$\begin{aligned} & \int_\alpha \left[n^{(1)\beta j-}(\boldsymbol{r})\nabla_i V_{\mathrm{eff}}(\boldsymbol{r}) + n(\boldsymbol{r})\nabla_i V^{(1)\beta j-}_{\mathrm{eff}}(\boldsymbol{r})\right]\mathrm{d}\boldsymbol{r} + \oint_{\partial\beta}\left[n(\boldsymbol{r})\nabla_i V_{\mathrm{eff}}(\boldsymbol{r})\right]_{\mathrm{MT}}\hat{\boldsymbol{e}}_{r,j}\mathrm{d}S \\ =& \int_\alpha \left[n^{(1)\beta j-\nabla}(\boldsymbol{r})\nabla_i V_{\mathrm{eff}}(\boldsymbol{r}) + n(\boldsymbol{r})\nabla_i V^{(1)\beta j-\nabla}_{\mathrm{eff}}(\boldsymbol{r})\right]\mathrm{d}\boldsymbol{r}. \end{aligned} \tag{5.40}$$

The first term appearing is numerically stable, while the second one contains the gradient of a potential response. We want to recast this into a form, where the gradient instead applies to the density:

$$\begin{aligned} & \int_\alpha n(\boldsymbol{r})\nabla_i V^{(1)\beta j-\nabla}_{\mathrm{eff}}(\boldsymbol{r})\mathrm{d}\boldsymbol{r} \\ =& -\int_\alpha (\nabla_i n(\boldsymbol{r}))V^{(1)\beta j-\nabla}_{\mathrm{eff}}(\boldsymbol{r})\mathrm{d}\boldsymbol{r} + \oint_{\partial\alpha}\left[n(\boldsymbol{r})V^{(1)\beta j-\nabla}_{\mathrm{eff}}(\boldsymbol{r})\right]_{\mathrm{MT}}\hat{\boldsymbol{e}}_{r,i}\mathrm{d}S. \end{aligned} \tag{5.41}$$

We keep this form in mind and move on to the surface integral terms containing the xc potential in equation (4.87c). We want to recast them according to the identities in equation (4.73), to

obtain integrals of the step function response and benevolent MT (surface) integrals. They are rewritten as

$$\begin{aligned} &-\oint_{\partial\alpha}\left[n(\boldsymbol{r})V_{\text{xc}}^{(1)\beta j-}(\boldsymbol{r})\right]_{\text{SF}}\hat{\boldsymbol{e}}_{r,i}\mathrm{d}S-\delta_{\beta\alpha}\oint_{\partial\alpha}\left[n(\boldsymbol{r})\nabla_j V_{\text{xc}}(\boldsymbol{r})\right]_{\text{SF}}\hat{\boldsymbol{e}}_{r,i}\mathrm{d}S \\ =&-\oint_{\partial\alpha}\left[n(\boldsymbol{r})V_{\text{xc}}^{(1)\beta j-\nabla}(\boldsymbol{r})\right]_{\text{MT}}\hat{\boldsymbol{e}}_{r,i}\mathrm{d}S-\int\Theta_{\text{IR}}^{(1)\alpha i+}(\boldsymbol{r})n(\boldsymbol{r})\left[V_{\text{xc}}^{(1)\beta j-}(\boldsymbol{r})+\delta_{\beta\alpha}\nabla_j V_{\text{xc}}(\boldsymbol{r})\right]\mathrm{d}\boldsymbol{r}. \end{aligned} \tag{5.42}$$

Finally, we look at the preexisting interstitial surface elements in equation (4.87d), that contain the effective potential. They can be reformulated into step function response terms as well, to yield

$$\begin{aligned} &-\oint_{\partial\alpha}\left[n^{(1)\beta j-}(\boldsymbol{r})V_{\text{eff}}(\boldsymbol{r})+n(\boldsymbol{r})V_{\text{eff}}^{(1)\beta j-}(\boldsymbol{r})\right]_{\text{IR}}\hat{\boldsymbol{e}}_{r,i}\mathrm{d}S-\delta_{\beta\alpha}\oint_{\partial\alpha}\left[\nabla_j(n(\boldsymbol{r})V_{\text{eff}}(\boldsymbol{r}))\right]_{\text{IR}}\hat{\boldsymbol{e}}_{r,i}\mathrm{d}S \\ =&\int\Theta_{\text{IR}}^{(1)\alpha i+}(\boldsymbol{r})n(\boldsymbol{r})\left[V_{\text{eff}}^{(1)\beta j-}(\boldsymbol{r})+\delta_{\beta\alpha}\nabla_j V_{\text{eff}}(\boldsymbol{r})\right]\mathrm{d}\boldsymbol{r} \\ +&\int\Theta_{\text{IR}}^{(1)\alpha i+}(\boldsymbol{r})\left[n^{(1)\beta j-}(\boldsymbol{r})+\delta_{\beta\alpha}\nabla_j n(\boldsymbol{r})\right]V_{\text{eff}}(\boldsymbol{r})\mathrm{d}\boldsymbol{r}. \end{aligned} \tag{5.43}$$

The resulting terms now all have a very similar form and can be grouped into an integral contribution to the dynamical matrix. In doing so, some terms cancel out and we finally arrive at

$$\begin{aligned} E_{\text{int}}^{(2)\beta j-\alpha i+}=&\int_{\alpha}\left[n^{(1)\beta j-\nabla}(\boldsymbol{r})\nabla_i V_{\text{eff}}(\boldsymbol{r})-(\nabla_i n(\boldsymbol{r}))V_{\text{eff}}^{(1)\beta j-\nabla}(\boldsymbol{r})\right]\mathrm{d}\boldsymbol{r} \\ &+\oint_{\partial\alpha}\left[n(\boldsymbol{r})V_{\text{C}}^{(1)\beta j-\nabla}(\boldsymbol{r})\right]_{\text{MT}}\hat{\boldsymbol{e}}_{r,i}\mathrm{d}S \\ &+\int\Theta_{\text{IR}}^{(1)\alpha i+}(\boldsymbol{r})n(\boldsymbol{r})\left[V_{\text{C}}^{(1)\beta j-}(\boldsymbol{r})+\delta_{\beta\alpha}\nabla_j V_{\text{C}}(\boldsymbol{r})\right]\mathrm{d}\boldsymbol{r} \\ &+\int\Theta_{\text{IR}}^{(1)\alpha i+}(\boldsymbol{r})\left[n^{(1)\beta j-}(\boldsymbol{r})+\delta_{\beta\alpha}\nabla_j n(\boldsymbol{r})\right]V_{\text{eff}}(\boldsymbol{r})\mathrm{d}\boldsymbol{r}. \end{aligned} \tag{5.44}$$

The Hellmann–Feynman Contribution

The final dynamical matrix terms to be discussed are the contributions from the external potential responses. They prove tricky to deal with, due to the ion-ion interaction term explicitly prohibiting particular combination of atoms in the summation. There are different ways to mitigate this, one being the Ewald summation [178], that is used *e.g.* in the `ABINIT` code [57, 179]. Another way is the construction through the FLAPW-adjusted Weinert construction [170], that was developed in part for exactly the purpose of being an alternative to the Ewald summation. This was implemented and tested against the `ABINIT` results in [93]. The corresponding usage for the total energy was discussed already in section 4.2 and is based on reference [173]. For this work, we investigate an analogous construction for the second order Hellmann–Feynman energy terms, that in opposition to the implementation described in [93] directly handles both the second order external potential and the ion-ion term. We start from

$$\begin{aligned} E_{\text{HF}}^{(2)\beta j-\alpha i+}=&\int\left[n^{(1)\beta j-}(\boldsymbol{r})V_{\text{ext}}^{(1)\alpha i+}(\boldsymbol{r})+n(\boldsymbol{r})V_{\text{ext}}^{(2)\beta j-\alpha i+}(\boldsymbol{r})\right]\mathrm{d}\boldsymbol{r} \\ &+E_{\text{ii}}^{(2)\beta j-\alpha i+}+\oint_{\partial\beta}\left[n(\boldsymbol{r})V_{\text{ext}}^{(1)\alpha i+}(\boldsymbol{r})\right]_{\text{SF}}\hat{\boldsymbol{e}}_{r,j}\mathrm{d}S, \end{aligned} \tag{5.45}$$

$$\int_{\Omega}n(\boldsymbol{r})V_{\text{ext}}^{(2)\beta j-\alpha i+}(\boldsymbol{r})\mathrm{d}\boldsymbol{r}=-\delta_{\beta\alpha}\sum_{\boldsymbol{R}}Z_\alpha\nabla_j\nabla_i V_{\text{H}}(\boldsymbol{r})|_{\boldsymbol{r}=\boldsymbol{\tau}_{\alpha\boldsymbol{R}}}, \tag{5.46}$$

and

$$E_{\text{ii}}^{(2)\beta j-\alpha i+} = -\delta_{\beta\alpha}\sum_{\boldsymbol{R}}\sum_{\gamma\boldsymbol{R}''\neq\alpha\boldsymbol{R}} Z_\alpha \nabla_j\nabla_i V_{\text{ext}}^{\gamma\boldsymbol{R}''}(\boldsymbol{r})|_{\boldsymbol{r}=\boldsymbol{\tau}_{\alpha\boldsymbol{R}}} + \sum_{\boldsymbol{R}'\boldsymbol{R}} \mathrm{e}^{-\mathrm{i}\boldsymbol{q}\cdot(\boldsymbol{R}'-\boldsymbol{R})}(1-\delta_{\beta\alpha}\delta_{\boldsymbol{R}'\boldsymbol{R}})Z_\alpha\nabla_j\nabla_i V_{\text{ext}}^{\beta\boldsymbol{R}'}(\boldsymbol{r})|_{\boldsymbol{r}=\boldsymbol{\tau}_{\alpha\boldsymbol{R}}}. \tag{5.47}$$

The second order potential term can be grouped with the q-independent part of the ion-ion interaction. Doing so yields a form that is very akin to the Madelung potential in [173], *i.e.* it represents the energy of a point charge in the second derivative of the Coulomb potential without its own charge contributing. Explicitly defining this as a Madelung term $-\delta_{\beta\alpha}Z_\alpha V_{\text{M}}^{(2)\alpha ji}(\boldsymbol{\tau}_\alpha)$ we find

$$\begin{aligned}&-\delta_{\beta\alpha}\sum_{\boldsymbol{R}} Z_\alpha\nabla_j\nabla_i V_{\text{H}}(\boldsymbol{r})|_{\boldsymbol{r}=\boldsymbol{\tau}_{\alpha\boldsymbol{R}}} - \delta_{\beta\alpha}\sum_{\boldsymbol{R}}\sum_{\gamma\boldsymbol{R}''\neq\alpha\boldsymbol{R}} Z_\alpha\nabla_j\nabla_i V_{\text{ext}}^{\gamma\boldsymbol{R}''}(\boldsymbol{r})|_{\boldsymbol{r}=\boldsymbol{\tau}_{\alpha\boldsymbol{R}}}\\ =&-\delta_{\beta\alpha}Z_\alpha\nabla_j\nabla_i V_{\text{C}}^{\setminus\alpha}(\boldsymbol{r})|_{\boldsymbol{r}=\boldsymbol{\tau}_\alpha} = -\delta_{\beta\alpha}Z_\alpha V_{\text{M}}^{(2)\alpha ji}(\boldsymbol{\tau}_\alpha).\end{aligned} \tag{5.48}$$

This term can be evaluated directly through the same method applied to the Madelung potential in [173]: The second derivative of the full Coulomb Potential is evaluated on the boundary of the MT of atom $\alpha$ and then solved for its origin by a boundary value problem. The second derivative of the atom itself has to be subtracted, but its spherical average is $0$. Sticking to the notation of the original paper, this gives

$$V_{\text{M}}^{(2)\alpha ji}(\boldsymbol{\tau}_\alpha) = \frac{1}{R_{\text{MT}^\alpha}}\left[R_{\text{MT}^\alpha}S_0(R_{\text{MT}^\alpha}) - \left\langle\nabla_j\nabla_i n(\boldsymbol{r})\right\rangle_\alpha\right] + \left\langle\frac{1}{r}\nabla_j\nabla_i n(\boldsymbol{r})\right\rangle_\alpha. \tag{5.49}$$

For this, the standard potential generator can be used, provided we supply it with the second order density derivative instead of the density itself and modify the multipole moments of the ions accordingly. The latter will now contribute for $\ell = 2$ instead of $\ell = 1$ (potential response) or only $\ell = 0$ (potential). Combining the terms in such a way leaves the q-dependent part of the ion-ion term. It can be split into the cases where the evaluation is at the same atom $\beta = \alpha$ and where they are different. For the first case another Madelung term for a q-dependent second potential derivative can be constructed, while for the latter we only need said derivative evaluated at a point, where it is non-singular. This gives

$$\begin{aligned}&\sum_{\boldsymbol{R}'\boldsymbol{R}}\mathrm{e}^{-\mathrm{i}\boldsymbol{q}\cdot(\boldsymbol{R}'-\boldsymbol{R})}(1-\delta_{\beta\alpha}\delta_{\boldsymbol{R}'\boldsymbol{R}})Z_\alpha\nabla_j\nabla_i V_{\text{ext}}^{\beta\boldsymbol{R}'}(\boldsymbol{r})|_{\boldsymbol{r}=\boldsymbol{\tau}_{\alpha\boldsymbol{R}}}\\ =&\,\delta_{\beta\alpha}Z_\beta V_{\text{M}}^{(2)\alpha ji+}(\boldsymbol{\tau}_\alpha) + (1-\delta_{\beta\alpha})Z_\beta V_{\text{M}}^{(2)\alpha ji+}(\boldsymbol{\tau}_\beta),\end{aligned} \tag{5.50}$$

where we defined the q-dependent Madelung term

$$V_{\text{M}}^{(2)\alpha ji+}(\boldsymbol{r}) = \sum_{\boldsymbol{R}}\mathrm{e}^{\mathrm{i}\boldsymbol{q}\cdot\boldsymbol{R}}\nabla_j\nabla_i V_{\text{ext}}^{\alpha\boldsymbol{R}}(\boldsymbol{r}). \tag{5.51}$$

This potential can again be constructed with the Weinert method, keeping in mind the additional q-dependency as was the case for the calculation of the potential response in section 5.1. As was the case for the multipole moments there, the ions contribute modified coefficients dependent on the atomic charge and a transformation $\boldsymbol{\chi}$ between the natural and Cartesian coordinates, that now depends on two directional indices instead of one. This makes it a tensor with three indices and yields

$$q_{2m}^{\alpha ji+|\gamma,\text{ext}} = -\delta_{\gamma\alpha}\frac{5}{4\pi}Z_\gamma\chi_{j,i,m}. \tag{5.52}$$

Once again, for the case of the q-independent second potential derivative, the $\delta_{\gamma\alpha}$ vanishes. The full matrix can be found in appendix C.



The Weinert construction for the ion-ion interaction and second order external potential that was described above is analytically sound and an elegant way to describe these two terms as a unified contribution to the dynamical matrix. It turns out, however, that the corresponding implementation runs into two problems. First off, the second numerical derivative of the density that is needed is not the most stable quantity and thus not well suited to produce accurate results. For the $V_{\text{ext}}^{(2)\beta j-\alpha i+}$ part of the Hellmann–Feynman terms, it is better to use partial integration to remove one gradient from the external potential and shift it to the density instead. This produces a set of surface integrals, whose interstitial contribution can be reformulated in the same way as before:

$$\begin{aligned}\int_\Omega n(\boldsymbol{r})V_{\text{ext}}^{(2)\beta j-\alpha i+}(\boldsymbol{r})\mathrm{d}\boldsymbol{r} &= \int_\Omega n(\boldsymbol{r})\delta_{\beta\alpha}\sum_{\boldsymbol{R}}\nabla_j\nabla_i V_{\text{ext}}^{\alpha\boldsymbol{R}}(\boldsymbol{r})\mathrm{d}\boldsymbol{r} &(5.53)\\ &= -\int_\Omega n(\boldsymbol{r})\delta_{\beta\alpha}\nabla_j V_{\text{ext}}^{(1)\alpha i\boldsymbol{0}}(\boldsymbol{r})\mathrm{d}\boldsymbol{r} &(5.54)\\ &= \int_\Omega (\nabla_j n(\boldsymbol{r}))\delta_{\beta\alpha}V_{\text{ext}}^{(1)\alpha i\boldsymbol{0}}(\boldsymbol{r})\mathrm{d}\boldsymbol{r} &(5.55)\\ &\quad -\sum_\gamma \oint_{\partial\gamma}\left[n(\boldsymbol{r})V_{\text{ext}}^{(1)\alpha i\boldsymbol{0}}(\boldsymbol{r})\right]_{\text{SF}}\hat{\boldsymbol{e}}_{r,j}\mathrm{d}S. &(5.56)\end{aligned}$$

Secondly, implementing the pure ion-ion part showed, that $V_{\text{ext}}^{(2)\beta j\alpha i\boldsymbol{0}}$ did not correctly reproduce the second order numerical derivative in the interstitial region for the Cartesian diagonal contributions in a monatomic material. *I.e.* we found

$$V_{\text{ext}}^{(2)\alpha i\alpha i\boldsymbol{0}}(\boldsymbol{G}) \neq -G_i^2 V_{\text{ext}}(\boldsymbol{G}), \tag{5.57}$$

which should hold as an analytical relation. This is akin to something already observed in [93], where a set of theoretically sound diagonal terms lead to discrepancies in the previous form of the ion-ion interaction. At the moment, we still do not know why a correction needs to be done here, but it can be handily implemented as one line of code by adding the following term to the pseudodensity, from which the potential response is constructed:

$$n_{\text{ps}}(\boldsymbol{G}) \longrightarrow n_{\text{ps}}(\boldsymbol{G}) + Z_\gamma\frac{(2N+7)!!}{3\Omega}\mathrm{e}^{\mathrm{i}\boldsymbol{G}\cdot\boldsymbol{\tau}_\gamma}\frac{j_{N+3}(GR_\gamma)}{G^{N+1}}. \tag{5.58}$$

Just as with the previous implementation, this term suffices to correct the pseudodensity. $N$ is the Weinert convergence parameter associated with the angular quantum number $\ell = 2$. If this method is used to calculate the second spatial derivative of the potential, it needs to be added for each atom. For the external potential response, it only appears for the displaced atom.

## 5.6 Scaling Behavior

The DFPT algorithm comes on top of a ground-state calculation for which a detailed discussion can be found in [76]. Its scaling behavior is dominated by the diagonalization of the

Hamiltonian for each k-point to solve the generalized eigenvalue problem in equation (4.2). Since the diagonalization scales with the third power of the matrix size (*i.e.* the number of basis functions $N_\mathrm{B}$ as determined by $K_\mathrm{max}$), this step of the algorithm is of the order $\mathcal{O}(N_{\boldsymbol{k}} N_\mathrm{B}^3)$ in computational effort. The analogous runtime determining step of the DFPT algorithm is the iterative solution of the Sternheimer equation (5.17) for each wave vector $\boldsymbol{q}$, for all three Cartesian coordinates of the displacement perturbation, all $N_\mathrm{ion}$ atoms in the unit cell, and all $N_{\boldsymbol{k}}$ k-points in the BZ. In practice, this is done by a series of matrix multiplications and thus the computational effort is bounded by the largest among them. This is already the first one, where we multiply the perturbed Hamiltonian and overlap matrices ($N_\mathrm{B} \times N_\mathrm{B}$) with the matrix of unperturbed expansion coefficients in the occupied subspace ($N_\mathrm{B} \times N_\mathrm{o}$), where $N_\mathrm{o}$ is the number of occupied states. The order of operations for this multiplication is at most $\mathcal{O}(N_\mathrm{o} N_\mathrm{B}^2)$. It should be noted, that this is for the most naive approach, while matrix multiplication algorithms have long been optimized to below $\mathcal{O}(N^{2.5})$ for quadratic $N \times N$ matrices [180, 181]. The other matrix multiplications are of the same order, as the dimension of the occupied subspace gets passed on with each product, and there is no proper matrix inversion necessary for the initial Hamiltonian and overlap, as we use the spectral representation for a quasi-analytic inversion. This is of the order $\mathcal{O}(N_\mathrm{o} N_\mathrm{B})$.

Summarizing, the runtime of the DFPT algorithm scales as $\propto 3 N_{\boldsymbol{k}} N_\mathrm{ion} N_\mathrm{o} N_\mathrm{B}^2$ for each wave vector $\boldsymbol{q}$. Since the number of occupied states as well as the number of basis functions scale with the number of atoms, the DFPT has a volume scaling (*i.e.* scaling with respect to the number of atoms) of $\mathcal{O}(N_\mathrm{ion}^4)$ and the precision scaling is of $\mathcal{O}(N_{\boldsymbol{k}} N_\mathrm{B}^2)$ in the number of basis functions. Although in the DFPT approach, the volume scaling is worse than for the conventional DFT self-consistency cycle ($\propto N_\mathrm{ion}^3$), in the FLAPW method the number of occupied states are only a fraction of all $N_\mathrm{B}$, *e.g.* in fcc Ne we find 4 occupied states for 162 to 177 states overall (depending on the k-point). This is at most 2.5%. In general we expect a maximum occupancy in the order of 5-10%. Thus, $N_\mathrm{o}$ produces a prefactor that is a fraction of $N_B$ and an iteration of the Sternheimer loop is faster than that of a conventional DFT calculation with no symmetry. Currently we use all available unoccupied states ($N_\mathrm{B} - N_\mathrm{o} \simeq N_\mathrm{B}$) in calculating the band-resolved response matrices $H/S^{(1)\beta j+}_{\nu'\nu}(\boldsymbol{k}+\boldsymbol{q}, \boldsymbol{k})$ and the subsequent multiplications. Investigating the influence of high-lying unoccupied states and introducing the cutoff on the number of them we take into account can further reduce the time consumption of the matrix multiplication steps. Such a move is planned to further improve the DFPT implementation, but has as of yet not been executed. The memory requirement, as opposed to the ground-state calculation, is more than tripled. This is due to the necessity of not only keeping the occupied unperturbed eigenvalues $\varepsilon_{\boldsymbol{k}\nu}$ and eigenvectors $\boldsymbol{z}_{\boldsymbol{k}\nu}$ in storage, but also the full set of unperturbed $\varepsilon_{\boldsymbol{k}+\boldsymbol{q},\nu'}$ and $\boldsymbol{z}_{\boldsymbol{k}+\boldsymbol{q},\nu'}$, as well as the occupied perturbed quantities $\varepsilon^{(1)\beta j}_{\boldsymbol{k}+\boldsymbol{q},\nu}$ and $\boldsymbol{z}^{(1)\beta j}_{\boldsymbol{k}+\boldsymbol{q},\nu}$. The q-dependent quantities, however, can be deleted once a specific q-point calculation is finished.

Parallelization

Due to the increased computational complexity of DFPT as opposed to the ground-state DFT calculation, the method is an excellent target for strong parallelization efforts. Due to the software engineering approach of weaving DFPT calculations into the ground-state code, it can make full use of already established parallelization schemes. This means that especially the calculations for different k-points can be handled independently, reducing the load on a single node and drastically speeding up the algorithm. Additionally, a top-level parallelization of the displaced atoms, displacement directions, and q-points is quite natural.

The k-point parallelization in FLEUR is handled by an MPI interface and is currently the only form implemented for DFPT parallelism, aside from low-level OMP loops in the subroutines it shares with the main code.

### Reducing the Computational Effort

Currently, the implementation of DFPT in FLEUR is very naive in the sense, that it has the maximum possible computational effort for the calculation of each q-point. Although the system may hold certain symmetries, that make sets of displacements or k-points equivalent, these symmetries are currently only used to reduce the BZ of q-points into a smaller irreducible set. As stated in section 3.2, there is a lot that can still be exploited here, but these considerations are postponed to future work with the DFPT implementation. This thesis serves to document the working basic implementation, which will be explored in the next chapter.

Chapter 6

# Validating the Implementation


6.1 Calculation Schemes and Computational Details . . . . . 77
6.2 Monatomic Materials . . . . . 80
6.3 Polyatomic Materials . . . . . 86
6.4 Using the q-point Interpolation . . . . . 92
6.5 Takeaways from the Validation . . . . . 96


The implementation of DFPT in the FLEUR code [90, 91] as it stands today has gone through a lot of development and several reiterations of key routines. It evolved from a standalone program based on the output of a legacy version of the code, to a plugin that relied a lot on redundant code, to a full part of the latest code versions. Consolidating the current state-of-the-art, including refactoring and the tricks highlighted in chapter 5, was only possible due to the meticulous study of a select group of test materials, for which the DFPT results were benchmarked against those from FD calculations with the phonopy code [149, 150]. This chapter serves to illuminate the full workflow from the ground-state calculation in a crystal to the adaptations that need to be done for the supercell and DFPT runs. Subsequently, the DFPT results are validated against the formalism based on force calculations, which have been implemented before [80, 81].

## 6.1 Calculation Schemes and Computational Details

Notes on the Ground-State Run

To ensure comparable phonon calculations from the two methods, some things need to be kept in mind with respect to the ground-state calculation, as there are limitations to the materials that can be investigated. Section 2.7 lists a plethora of extensions to the basic DFT formalism, that are partially implemented in the FLEUR code, but are not all adapted to the DFPT formalism. Such as the implementation of non-collinear magnetism, the spin-orbit interaction, DFT+U and related schemes, and the usage of hybrid functionals. Moreover, due to the direct way of calculating the xc potential response from the density response (equation (5.12)), only LDA functionals are correctly applicable at the moment. Choosing a material that does not rely

on these extensions provides a valid candidate to use the DFPT implementation. Before the actual phonon run, the material has to be fully optimized with respect to its ground-state energy. That means the lattice constant $a_{\text{latt}}$ needs to be optimized by finding the equilibrium value, that minimizes the crystals energy as expressed in an equation of states (EOS), such as that of Birch and Murnaghan [182]. Additionally, if the system has any free parameters, such as the z-position of certain atoms in a layered system, these will have to be optimized to find the actual minimum of the energy landscape and thus the ground state the system will assume. Only from such an optimized system can a phonon calculation be started, as it relies on the harmonic approximation to the energy landscape around a minimum. We set a convergence threshold of $\varepsilon_{\text{SCF}} = 10^{-5}\ a_0^{-3}$ for the distance (as defined in section 4.2) in all ground-state calculations in the validation set. It applies to the ground-state EOS runs, the supercell ground-states for the force calculations, and the DFPT density perturbations (unit: $a_0^{-4}$) as well.

**Common Parameters and Calculation Profile**

The space of tuneable parameters in the FLAPW method is vast. To restrict it to a manageable size for our purposes, we opted to use the capability of using preset profiles in `FLEUR`, that set most parameters for us. When no profile is used, the code automatically adjusts the cutoff parameters for the systems according to its constituents and a set of hard coded default data. We created the `dfpt_01` profile, that sets the plane-wave cutoff $K_{\text{max}}$ to $4.5\ a_0^{-1}$ and the density and potential cutoff $G_{\text{max}}$ to $3K_{\text{max}}$, and reduces the predetermined MT radii, that are chosen as big as possible without making the spheres overlap, to 95% of its original value. This is done to avoid overlapping the MT as soon as we chose a slightly smaller lattice constant in the EOS calculation. In each of the inputs, the xc functional is chosen to be that of Vosko, Wilk, and Nusair [109] (VWN) and the Fermi smearing energy is $k_B T = 0.001$ Ha.

**Generating the Supercell Input**

As mentioned before, we rely on the `phonopy` code for the FD phonon calculation steps that are not directly related to a `FLEUR` run. We programmed an interface for `phonopy`, that allows it to read the `FLEUR` input file and extend it into a supercell input, that can again be read by `FLEUR`. For this, the input needs to have a specific form. While there is a multitude of ways to specify the basic input file for the input generator (`inpgen`) in `FLEUR`, the interface searches for specific tags in it and the file thus has to take the following form:

```
Comment line

xxx yyy zzz ! a1
xxx yyy zzz ! a2
xxx yyy zzz ! a3
scale0
scalexxx scaleyyy scalezzz

n ! num atoms
Z1 x y z
Z2 x y z
...

&exco xctyp='vwn' /
```

Specifically, the interface searches for the tags that follow the exclamation marks. The set of floats xxx/yyy/zzz represents the lattice vectors of the crystal. It is globally scaled by the float

scale0 and each column has another specific scaling factor. n represents the number of atoms in the unit cell. The numbers Z1,Z2... represent the atomic numbers of the constituents and x/y/z their coordinates in terms of the lattice vectors. The exco tag at the bottom of the file ensures, that the VWN functional will be used. A specific example for this kind of input will be given in appendix B. From this, we invoke `phonopy` with a command line, that specifies the construction of a supercell input with displaced atoms. It is specified by a supercell matrix $\underline{M}_S$, that relates the unit cell Bravais matrix $\underline{A}_u$ to that of the supercell by $\underline{A}_S = \underline{M}_S \underline{A}_u$. For a $2 \times 2 \times 2$ supercell to be constructed, the command line for `phonopy` with a unit cell input file `input.in` would look like

phonopy --fleur -c input.in -d --dim="2 0 0 0 2 0 0 0 2",

where the rightmost command represents the supercell matrix. From this, new input files `supercell-XXX.in` will be generated according to the minimum amount of necessary displacements to accurately describe the full phonon spectrum. While the lattice vectors, scales and atom list are transformed and extended according to the supercell matrix, the lowermost input is simply copied over, so that the other system parameters stay the same.

Running the Force Calculations

For each of the displaced supercells, additional `FLEUR` calculations have to be performed. They start with a ground-state run of each supercell, followed by a force calculation. For this, the `FLEUR` input file `inp.xml` file has to be modified. The tag `l_f` is set to `"T"` to enable force calculations and a tag `f_level="0"` [81] is added to generate the necessary output. Specifically, it creates an output file `FORCES_SORT` that contains a list of the forces acting on all atoms (instead of only for the representative atom for each symmetrized atom group) and is sorted in the same way the atoms in the supercell input file were. The last relevant tag in this context is the force convergence threshold `epsforce` in units of Ha/$a_0$. In the force calculation, `FLEUR` keeps repeating the SCF loop and calculating the forces in each iteration. Once their difference between two steps falls below the threshold, the converged force is written out. The convergence parameter is set to $\varepsilon_{\text{force}} = 10^{-5}$ Ha/$a_0$ for all FD calculations. Once this is done for all supercells, the main part of the calculation is finished.

Evaluating the Phonon Spectrum

To begin the post-processing of the force files, they have to be read by the interface. With a command line

phonopy --fleur -f FORCES_SORT_001 FORCES_SORT_002 ...

a file `FORCE_SETS` is generated. This file serves as the starting point for all thermodynamical calculations with `phonopy`. We are specifically interested in the phonon dispersion and can thus invoke the program with a path to follow for the phonon band structure. It takes the form of a list of 3-tuples that represent the internal coordinates of the phonon wave vectors. At and between those vectors the dispersion relation is calculated. For our previous example input (with a shorthand notation for the diagonal supercell matrix) and a set of high-symmetry points $\left\{\begin{pmatrix}0 & 1/2 & 1/2\end{pmatrix}^T, \begin{pmatrix}0 & 0 & 0\end{pmatrix}^T, \begin{pmatrix}1/2 & 1/2 & 1/2\end{pmatrix}^T\right\}$ we write

phonopy --fleur -c input.in --dim="2 2 2" -p --band="0 1/2 1/2 0 0 0 1/2 1/2 1/2",

representing *e.g.* the $X - \Gamma - L$ path in an fcc crystal. The output is written into a file `bands.yaml`, that can then be read and plotted using a simple output program. There are many parameters that can be set individually to influence the calculation, such as the amplitude of the

atomic displacement. We chose to keep it at the default size of $0.02\ a_0$ hard coded into the interface. We do, however, directly provide a conversion factor of `--factor=5140.48767176083` to change the unit of the frequencies into $\mathrm{cm}^{-1}$. It should also be noted, that `phonopy` applies the acoustic sum rule by default, which means that the forces on all atoms are summed up and the residual force is subtracted [81] from each single one. This results in three clean acoustic modes with a frequency of $0\ \mathrm{cm}^{-1}$ at the $\Gamma$-point.

DFPT Input

For the DFPT calculation, the same input that was provided for the FD supercell generation can be used. When running it through the input generator, we additionally provide the argument `-nosym` to generate an `inp.xml` that does not make use of the crystal symmetries. Otherwise, the response quantities would not be accurately calculated, as they do not adhere to the same symmetries as the ground state (*cf.* section 3.2). We also have to generate an additional k-point set, that is ensured to be a regular mesh and contain the $\Gamma$-point. We modify the input file to use the new k-point set and set the xc functional to VWN from `libxc` [171] (to have access to the functional derivative) and converge the ground-state calculation. The other parameters, like the cutoffs and convergence threshold, stay the same as in the ground-state run. Afterward, we modify the input to calculate and save all states in the KS eigenvalue equation, as they are needed to solve the Sternheimer equation, and add a list of q-points that are to be calculated.

Running and Evaluating the DFPT Calculations

The result of each SCF loop in the DFPT calculation is a converged set of response quantities. The expansion coefficients, density, and potential responses form the building blocks of the dynamical matrix and each run will write exactly one row of it into an output file. After all rows of a single q-point are calculated, the dynamical matrix is diagonalized and the eigenvalues and eigenvectors are written to the output file as well. Plotting the output of these files takes little effort and overlaying the data points with the interpolated curves from the FD simulation gives us a great tool to judge the quality of the DFPT implementation. The validation results are the subject of the next section.

## 6.2 Monatomic Materials

Analytical Solution

We start the investigation with the most simple case: a single atom that is repeated in each unit cell. For such a system, we can make certain predictions. There are exactly three (possibly degenerate) acoustic phonon branches that have zero frequency at the $\Gamma$-point. Aside from this being a physical reality, it can be directly inferred from the Sternheimer equation and the constituents of the dynamical matrix by finding its analytical solution [93]. It takes the form

$$\boldsymbol{z}^{(1)\beta j}_{\boldsymbol{kG},\nu} = -\mathrm{i}(\boldsymbol{k}+\boldsymbol{G})_j \boldsymbol{z}_{\boldsymbol{kG},\nu}. \tag{6.1}$$

This analytical expression, when applied to the wave function, directly causes the prefactor term in the sole MT sphere to be canceled out, while being exactly equivalent to the gradient of the wave function in the interstitial. Hence, we find for the wave function and density responses:

$$\Psi^{(1)\beta j}_{\boldsymbol{k}\nu}(\boldsymbol{r}) = -\nabla_j \Psi_{\boldsymbol{k}\nu}(\boldsymbol{r}), \tag{6.2}$$

$$n^{(1)\beta j}(\boldsymbol{r}) = -\nabla_j n(\boldsymbol{r}). \tag{6.3}$$

Working through the potential response generation, it can also be found, that

$$V_{\text{eff}}^{(1)\beta j}(\boldsymbol{r}) = -\nabla_j V_{\text{eff}}(\boldsymbol{r}). \tag{6.4}$$

A last thing to keep in mind, is that this kind of system will not exhibit any response of the eigenenergies at $\Gamma$. This is due to the fact, that displacing a single atom in each unit cell by the same amount does not create any relative displacement between them. Thus, the energy of each state is unaffected. Consequently, the occupation numbers are not changed. Using all this information and inserting it into the dynamical matrix constituents in section 5.5 neatly cancels all of them [93] and thus gives a matrix of zeros and the desired acoustic modes starting at $0$ cm$^{-1}$, hence making them gapless Goldstone modes [183]. The accuracy with which this analytical requirement is fulfilled gives us a good measure for the quality of our DFPT implementation.

fcc Ne

The first test system in our validation efforts is fcc Ne. While this at first seems to be an unorthodox choice, seeing how exotic noble gas lattices are, it is a proper test case if we can construct it in a ground-state run. It is

i) monatomic,

ii) isolating,

iii) nonmagnetic,

iv) not heavy enough to make spin-orbit interactions relevant, and

v) does not require any core-tail or LO corrections, as the electrons are strongly bound to the ion.

Additionally, fcc Ne has a large lattice constant due to it being bound by van der Waals forces [184]. This gives us phonon frequencies on a small scale, where numerical problems become easily visible. We investigate the system with the aforementioned common input and find the following set of parameters for the equilibrium lattice constant:

**Table 6.1:** Overview of the specific calculational parameters of fcc Ne. Parameters not contained in the table are kept at the FLEUR default or are explicitly mentioned in section 6.1.

| $N_{k_{x/y/z}}$ | $\ell_{\max}$ | $\ell_{\max,\text{nsph}}$ | $N_{\text{MT}}$ | $R_{\text{MT}}$ | $dx$ | $a_{\text{latt}}$ |
|---|---|---|---|---|---|---|
| 16 | 11 | 8 | 803 | 2.43 $a_0$ | 0.014 | 7.536 $a_0$ |

Aside from parameters that were already mentioned and explained in section 4.1, we denote the number of k-points along each reciprocal lattice vector as $N_{k_{x/y/z}}$, the number of radial grid points as $N_{\text{MT}}$, and the logarithmic increment of the radial grid as $dx$. The FD calculation for this simple system requires only one displacement in a $2\times2\times2$ supercell. The DFPT calculation is also relatively tame, taking at most 10 iterations for any q-point and displacement direction. Table 6.2 summarizes the Goldstone modes for both cases to assess their precision.

The values are in such close proximity to $0$ cm$^{-1}$, that there is no need to enforce the acoustic sum rule and correct the DFPT dispersion curve by them. They are less than $0.2\%$ of the dispersion curve maximum and thus negligible on the created energy scale. The relevant high-symmetry points for the dispersion curve aside from $\Gamma$ are given in internal coordinates by $X = (0, 1/2, 1/2)^T$, $X' = (1/2, 1/2, 1)^T$, and $L = (1/2, 1/2, 1/2)^T$. Another relevant intermediary point is $K = (3/8, 3/8, 3/4)^T$. We look at the high-symmetry paths $\Gamma - X$,

**Table 6.2:** Overview of the acoustic Γ-point modes, $\omega$, in $\mathrm{cm}^{-1}$ for fcc Ne. No frequency exceeds an absolute value of $0.2\ \mathrm{cm}^{-1}$ (or $0.025$ meV | $0.006$ THz, respectively).

| | $\omega_1$ | $\omega_2$ | $\omega_3$ |
|---|---|---|---|
| FD | $1.36 \times 10^{-1}$ | $1.36 \times 10^{-1}$ | $1.36 \times 10^{-1}$ |
| DFPT | $-1.59 \times 10^{-1}$ | $-1.59 \times 10^{-1}$ | $-1.59 \times 10^{-1}$ |

$X' - \Gamma$, and $\Gamma - L$ which are parallel to the wave vector directions $(1,0,0)^T$, $(1,1,0)^T$, and $(1,1,1)^T$ in Cartesian coordinates. For the first path, we expect two degenerate transversal branches (associated to the y-/z-direction for the chosen point) and one longitudinal branch. The second path is non-degenerate and the third path should once again show the same 2+1 splitting as the first one.

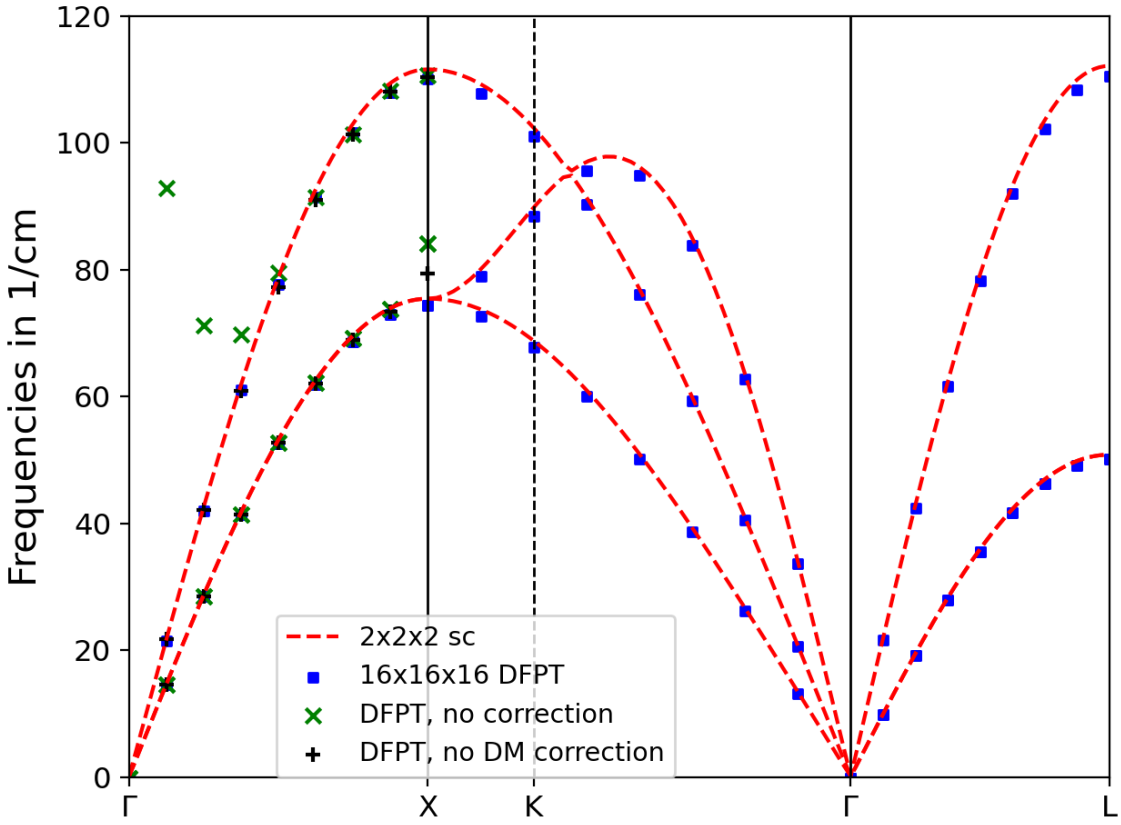



**Figure 6.1:** Phonon dispersion for fcc Ne. The red dashed curve shows the FD reference (denoted as "sc" for supercell) and the blue squares show the DFPT data. Additionally, there are points on the $\Gamma - X$ path, that highlight separate calculations where corrections (5.24) and/or (5.28) are not applied with green crosses and a black plus, respectively.

During the study of fcc Ne, some peculiarities were observed in certain modes that spurred a lot of investigation into the behavior of degenerate states and how they need to be treated. Particularly, there was a steep increase of the longitudinal phonon mode (uppermost branch) towards the $\Gamma$-point, instead of a smooth linear descent to $0$, and the slope of the degenerate

transversal lower branches going towards the high-symmetry point X. Moreover, investigating both problems for denser and denser k-point sets and q-point paths revealed, that the latter slope was actually a jump from a smooth curve to a point shifted slightly upwards. Both problems decreased in magnitude with the denser choice of reciprocal lattices and were a major factor in motivating the development of the correction terms in equation (5.24) and furthermore in equation (5.28) (DM correction). Having said this, the resulting phonon dispersions with and without both corrections can be found in figure 6.1, where they are plotted against the `phonopy` FD curve, neatly highlighting the original problems and their solution. The curve shows good agreement between the phonons calculated by both methods. It is also a good benchmark for their precision, as it exhibits frequencies of only slightly above $100\ \mathrm{cm}^{-1}$. Considering the results as a whole, they show the overall form that is to be expected for fcc materials, which can be solved analytically [185] and only depends on the nearest neighbor force constant due to the system's symmetry. This is a satisfying result and allows us to move on to the next material.

For the next validation, we chose fcc Cu. It is a transition metal with a rather full outer electron shell, which means it lifts restriction (ii) as opposed to fcc Ne, but without a need to supplement it with LOs, making it a logical next step. Table 6.3 summarizes the parameter set for the equilibrium lattice constant. fcc Cu

**Table 6.3:** Overview of the specific calculational parameters of fcc Cu. More parameters in section 6.1.

| $N_{k_{x/y/z}}$ | $\ell_{\mathrm{max}}$ | $\ell_{\mathrm{max,nsph}}$ | $N_{\mathrm{MT}}$ | $R_{\mathrm{MT}}$ | dx | $a_{\mathrm{latt}}$ |
|---|---|---|---|---|---|---|
| 16 | 10 | 8 | 741 | 2.24 $a_0$ | 0.017 | 6.647 $a_0$ |

Compared with fcc Ne, the lattice is a bit more densely packed, motivating higher overall phonon frequencies. This reflects in the Goldstone modes of the DFPT phonons, as shown in table 6.4.

**Table 6.4:** Overview of the acoustic $\Gamma$-point modes, $\omega$, in $\mathrm{cm}^{-1}$ for fcc Cu. No frequency exceeds an absolute value of $0.4\ \mathrm{cm}^{-1}$ (or $0.050$ meV | $0.012$ THz, respectively).

| | $\omega_1$ | $\omega_2$ | $\omega_3$ |
|---|---|---|---|
| FD | $-4.78 \times 10^{-6}$ | $-1.70 \times 10^{-6}$ | $1.12 \times 10^{-6}$ |
| DFPT | $-3.16 \times 10^{-1}$ | $-3.14 \times 10^{-1}$ | $-3.10 \times 10^{-1}$ |

In contrast to the previous calculation, there is a large difference between the magnitude of the FD and DFPT Goldstone modes. While the latter sit at roughly the same size in relation to the maximum frequency (figure 6.2), the FD modes are several orders of magnitude smaller. This result, however, seems rather arbitrary and is solely dependent on how good the subtraction of residual forces works in the `phonopy` interface. Previous results for a different set of parameters [94] show the same behavior for fcc Ne and it seems to be sensitive to the exact choice of cutoffs and precision parameters. We keep the evaluation of the mode quality for all further investigated materials in mind and discuss the full spectrum of fcc Cu in figure 6.2.

As was the case for fcc Ne, we find good agreement between the phonon dispersions of both methods. Looking at the iteration count that is needed to converge the calculation, it is worth

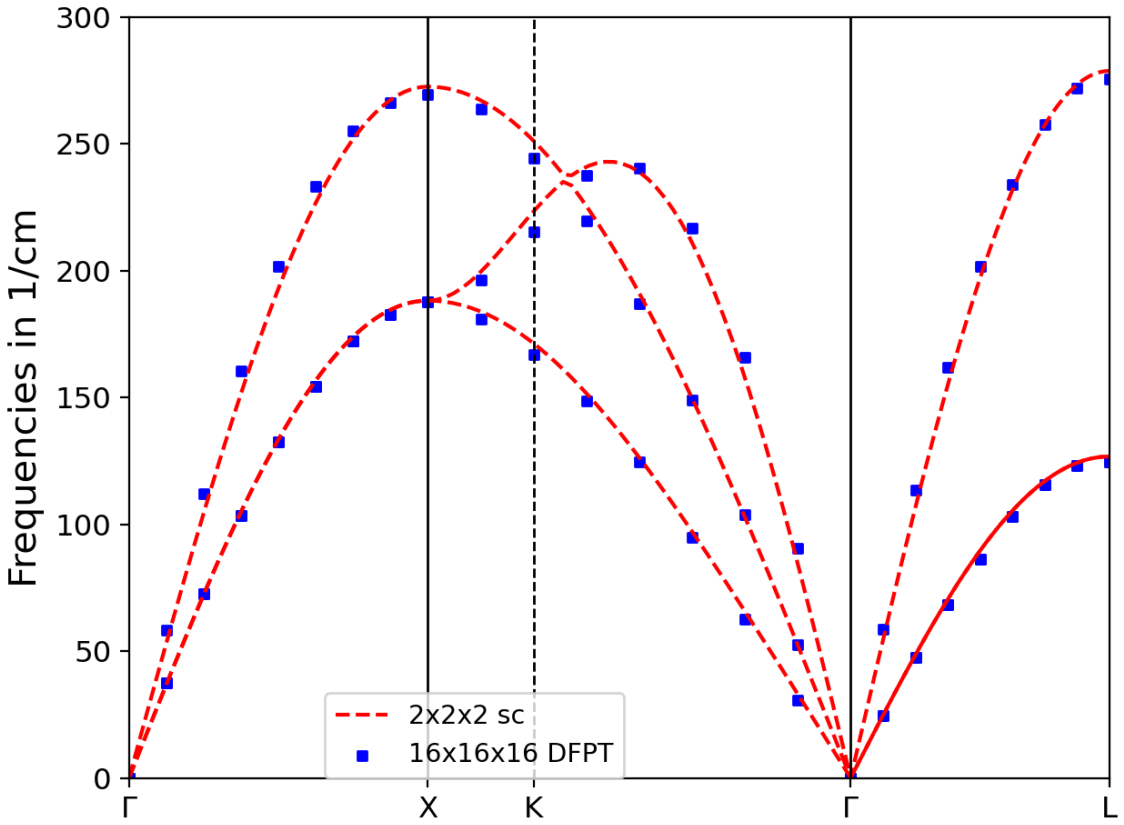



**Figure 6.2:** Phonon dispersion for fcc Cu. The red dashed curve shows the FD reference and the blue squares show the DFPT data.

noting that the maximum number of required density response SCF cycles was 13, which is only slightly more than for fcc Ne. We will use the good agreement in this realistic material as a baseline for further investigations at the end of the chapter and continue with the last candidate in the monatomic material group.

fcc Ni

fcc Ni constitutes the first (ferro-)magnetic material in our investigation. This means the calculation becomes spin polarized, which constitutes an added layer of complexity. The Sternheimer equation, like the Kohn–Sham equations for the ground-state run, are solved for each spin independently and increase the space of eigenstates by a factor of 2. Additionally, Ni is supplemented with LOs in FLEUR, although their impact is rather low when compared to an alkaline metal or other materials with nearly empty shells. Thus, we lift the additional restrictions (iii) and (v). As for the other materials, we first look at the collected input data in table 6.5.

**Table 6.5:** Overview of the specific calculational parameters of fcc Ni. More parameters in section 6.1.

| $N_{k_{x/y/z}}$ | $\ell_{\max}$ | $\ell_{\max,\text{nsph}}$ | $N_{\text{MT}}$ | $R_{\text{MT}}$ | dx | $a_{\text{latt}}$ |
|---|---|---|---|---|---|---|
| 16 | 10 | 8 | 701 | 2.12 $a_0$ | 0.017 | 6.472 $a_0$ |

The values are similar to those of fcc Cu, which is to be expected given it is directly adjacent to fcc Ni in the periodic table and chemically very similar. Its metallic character comes to mind, especially. The added complexity does affect the iteration number, though. For q-points close to $\mathbf{0}$, where we expect the convergence to be most tricky due to the diverging nature of the potential terms, we need up to 27 iteration steps, far exceeding the values for fcc Ne and Cu. Next, we look at the Goldstone modes in table 6.6.

**Table 6.6:** Overview of the acoustic $\Gamma$-point modes, $\omega$, in $\mathrm{cm}^{-1}$ for fcc Ni. No frequency exceeds an absolute value of $0.3\ \mathrm{cm}^{-1}$ (or $0.037$ meV | $0.009$ THz, respectively).

| | $\omega_1$ | $\omega_2$ | $\omega_3$ |
|---|---|---|---|
| FD | $5.64 \times 10^{-2}$ | $5.64 \times 10^{-2}$ | $5.64 \times 10^{-2}$ |
| DFPT | $-2.55 \times 10^{-1}$ | $-2.54 \times 10^{-1}$ | $-2.52 \times 10^{-1}$ |

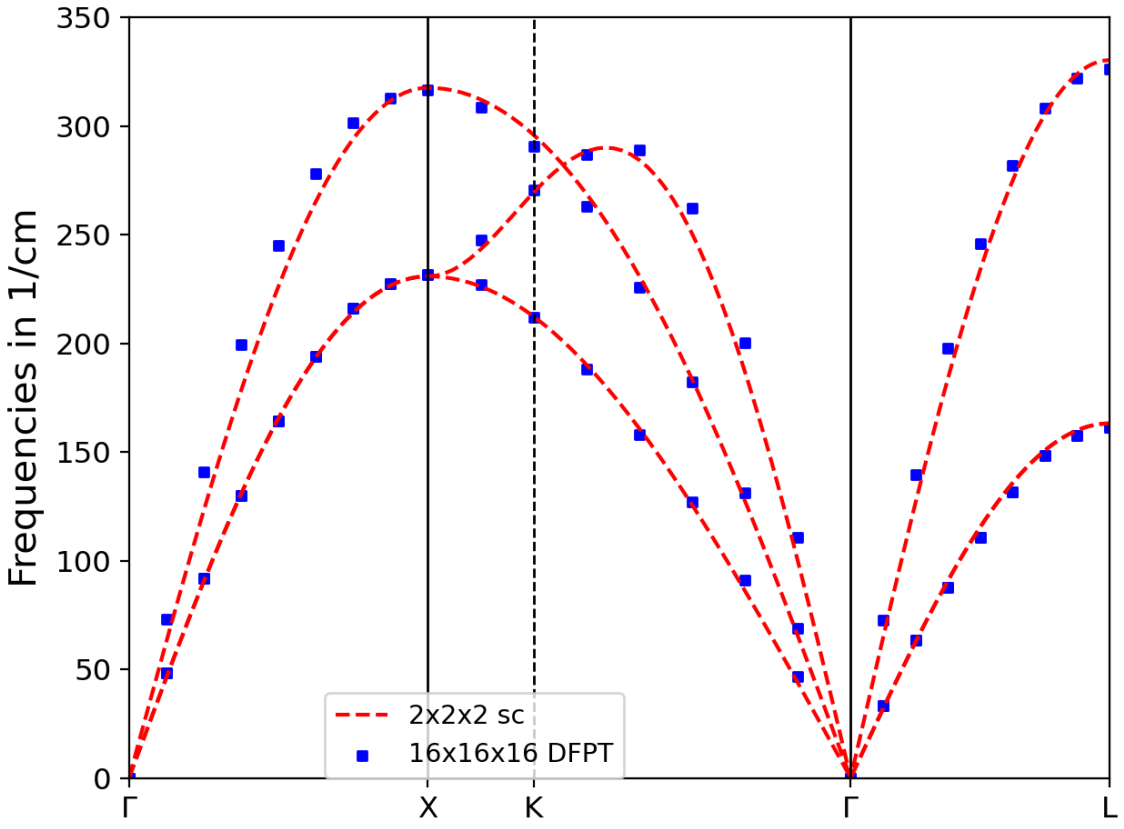



**Figure 6.3:** Phonon dispersion for fcc Ni. The red dashed curve shows the FD reference and the blue squares show the DFPT data.

They are once again very close to $0\ \mathrm{cm}^{-1}$, showing again the quality of both methods. We note, that the FD modes are once again of another order of magnitude as compared to the previous cases. There does not seem to be a discernible pattern that links the input parameters to the quality of the FD Goldstone mode. We will not investigate this matter further, as

the upper bound for the three test systems is less than $0.5$ cm$^{-1}$, but keep this threshold in mind when we look at more complicated materials. Figure 6.3 shows the resulting phonon dispersion. The curves have a similar extent to those of fcc Cu, which is as expected. There are once again no significant outliers (albeit a slight deviation for the longitudinal $\Gamma - X$ branch exists), validating the method for monatomic ferromagnets as well. So far, we restricted the investigation to fcc materials, which all have very similar dispersion with respect to their overall shape. Over the course of the DFPT implementation effort, there were also several tests with bcc crystals [94], that also showed overall good agreement with the FD benchmarks, but had some peculiarities that were not seen for the fcc case. Two of these materials will be discussed in the next chapter, where they serve as the object of convergence studies with respect to several parameters in the calculation. Together with the content of this section, these five materials serve as a reliable benchmark of the implementation and its quality. Checking even more monatomic materials is not instructive, which is why we continue with the discussion of several atoms per unit cell, where some of the restrictions we mentioned at the beginning of this section are lifted.

## 6.3 Polyatomic Materials

Relevant Terms for Polyatomic Materials

We started our discussion of monatomic materials with the requirement, that the Sternheimer equation has an analytical solution, that makes the dynamical matrix vanish at $\boldsymbol{q} = \mathbf{0}$. This went along with the physical argument, that the eigenenergy response has to vanish, as the atoms are not shifted against each other. Both these observations are no longer valid when more atoms come into play. To find a valid set of Goldstone modes, the dynamical matrix now has to show specific symmetries instead of straight up vanishing, which is more demanding on our algorithm. Moreover, in materials that are conductive, the existence of eigenenergy responses also makes the occupation number responses finite. To test the relevance of both terms separately, we choose a semiconductor and a metal as our next objects of investigation. We also look at an example of a semiconductor made up of different types of atoms.

Si

Si in a diamond structure is one of the most studied materials in density functional theory due to its relevance in modern technology and its relative accessibility. Its experimental lattice constant is closely matched by LDA functionals in both plane wave and FLAPW frameworks. Due to this, there is a lot of data to compare our results to, both on the theoretical and on the experimental side. We use Si as a test material to lift restriction (i). As there are, however, two identical atoms in the material, we do not gain additional parameters and can still summarize them in an equivalent table 6.7 as before.

**Table 6.7:** Overview of the specific calculational parameters of Si. More parameters in section 6.1.

| $N_{k_{x/y/z}}$ | $\ell_{\max}$ | $\ell_{\max,\mathrm{nsph}}$ | $N_{\mathrm{MT}}$ | $R_{\mathrm{MT}}$ | dx | $a_{\mathrm{latt}}$ |
|---|---|---|---|---|---|---|
| 16 | 9 | 7 | 677 | 2.05 $a_0$ | 0.017 | 10.207 $a_0$ |

Starting from these parameters, the FD and DFPT calculations were started in the same way as before. We note, that the DFPT run now takes quite a bit longer due to the increased extent of the dynamical matrix. It requires six Sternheimer SCF calculations instead of only three and the loop over both atoms also increases the runtime marginally at several points in the

internal workflow. Furthermore, the FD calculation becomes more involved. While a single displaced supercell calculation is still enough to calculate all relevant forces, a simple $2 \times 2 \times 2$ setup now already yields a 16 atom supercell. Tests have also shown, that the FD phonon dispersion that can be interpolated from this setup does not match the DFPT data nicely. We opted to analyze, whether this is a fault of the FD simulation. We found that the interpolated spectrum changes when we choose a $4 \times 4 \times 4$ supercell instead and the bigger cell leads to a significantly better agreement. This means we have to regard the supercell size as a convergence parameter of the FD calculation. In table 6.8 we show the resulting Goldstone modes from this setup.

**Table 6.8:** Overview of the acoustic $\Gamma$-point modes, $\omega$, in $\mathrm{cm}^{-1}$ for Si. No frequency exceeds an absolute value of $0.1$ $\mathrm{cm}^{-1}$ (or $0.012$ meV | $0.003$ THz, respectively).

| | $\omega_1$ | $\omega_2$ | $\omega_3$ |
|---|---|---|---|
| FD | $8.16 \times 10^{-2}$ | $8.16 \times 10^{-2}$ | $8.16 \times 10^{-2}$ |
| DFPT | $-7.20 \times 10^{-2}$ | $-3.54 \times 10^{-2}$ | $2.88 \times 10^{-2}$ |

As opposed to the previous cases, the DFPT modes are slightly closer to $0$ $\mathrm{cm}^{-1}$ than those from the FD run. This shows, that enforcing the acoustic sum rule in `phonopy` by subtracting the residual force is by no means an exact solution. Considering the number of iterations needed to converge the Sternheimer SCF runs, they go up to 15 at most. This is similar to the value for fcc Cu, indicating that the increased number in fcc Ni is due to either the spin polarization or the use of LOs.

Figure 6.4 shows the Si phonon dispersion. Aside from the internal consistency of FD and DFPT, for the often benchmarked Si we show experimental data as well. It was taken from three sources [186–188] that, when combined, give a sufficiently dense set of data along the high-symmetry lines. Additionally, we add a data point for a DFPT calculation at the second $\Gamma$-point, that neglects the emergence of eigenenergy responses (e1; *cf.* equation (5.39)), leading to a noticeable shift in the frequencies. While the FD frequencies are thrice degenerate at around $515.5$ $\mathrm{cm}^{-1}$, the DFPT run without the eigenenergy responses gives $526.5$ $\mathrm{cm}^{-1}$ and including them gives a better fit of $518.0$ $\mathrm{cm}^{-1}$, marking the importance of evaluating the terms. Finally, we refer to reference [189] for a comparison to calculations done with norm conserving pseudopotentials in the `ABINIT` code [57, 70, 179]. The calculations were converged to an accuracy of better than 1 $\mathrm{cm}^{-1}$ and were done with the Ceperley–Alder LDA functional [105]. The dispersion shows overall good agreement between the FD interpolation, the sampled DFPT values and the experimental data points. Especially in the acoustic modes towards the high-symmetry point $L$, the experimental and theoretical points form a continuous line that neatly overlays with the FD background. The agreement is slightly worse on the path that crosses $K$, being suppressed with respect to the experiment and differing between FD and DFPT in the degenerate transversal modes. The disagreement gets larger in the optical modes, where the theoretical predictions largely underestimate the experimental data and do not fully agree with each other as well. Considering the pseudopotential data [189], the match is also very good, in that we find a similar maximum frequency and dispersion shape. The overall scale of mismatch is tolerable and especially for the theoretical validation, increasing the cutoff parameters in both calculations and supercell size in the FD run might lead to

further convergence. A more in-depth analysis of the latter aspect will be shown in the next chapter.

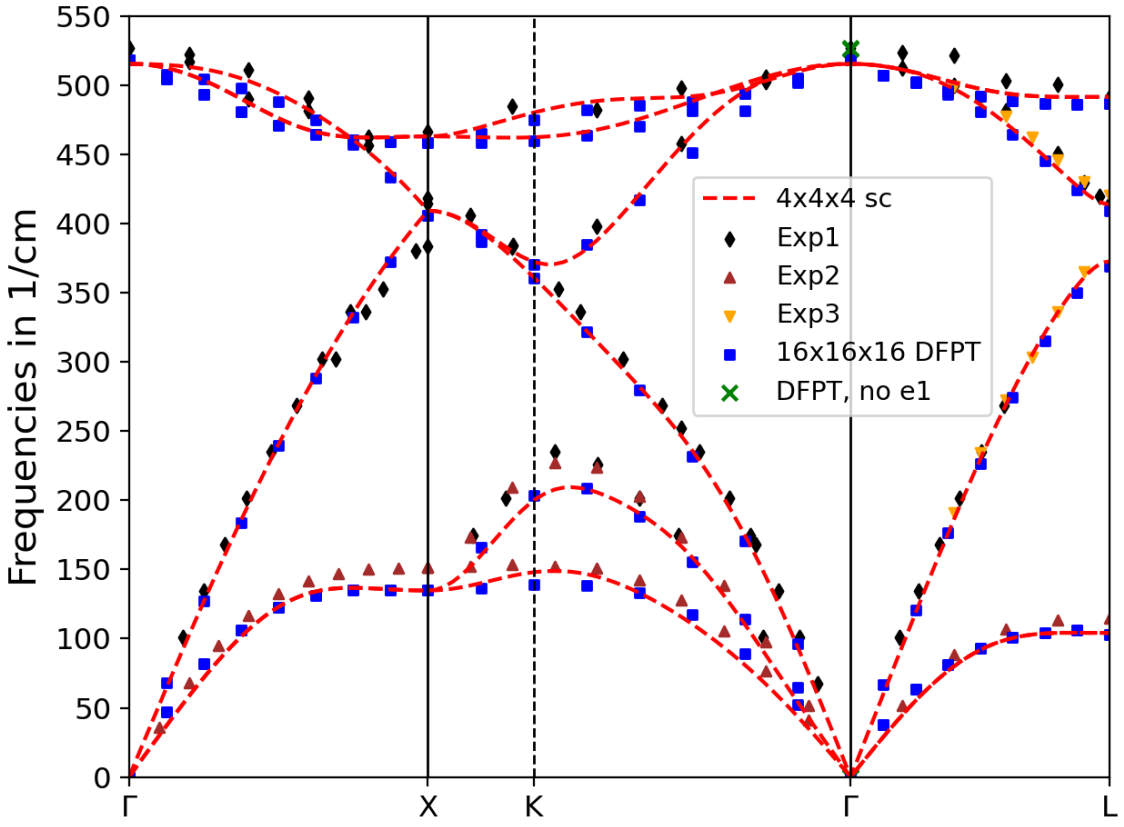



**Figure 6.4:** Phonon dispersion for Si. The red dashed curve shows the FD reference and the blue squares show the DFPT data. The green cross at the second $\Gamma$-point highlights the modified result in the absence of eigenenergy response terms. The black diamonds, brown upward triangles, and yellow downward triangles belong to experimental data from references [186], [187], and [188] respectively.

hcp Co

From the semiconducting Si, we move on to the ferromagnetic hcp Co. This not only serves as a test of the occupation number response (3.38), but also marks the first material in our test set, that does not crystallize in an fcc lattice (with a basis). Thus we implicitly test the validity of DFPT for different structures. In hcp lattices, the extent of the unit cell in one dimension is different from that of the hexagonal basis and enters as an additional parameter. The choice of parameters is summarized in table 6.9.

**Table 6.9:** Overview of the specific calculational parameters of hcp Co. More parameters in section 6.1.

| $N_{k_{x/y/z}}$ | $\ell_{\max}$ | $\ell_{\max,\text{nsph}}$ | $N_{\text{MT}}$ | $R_{\text{MT}}$ | dx | $a_{\text{latt}}$ | $c_{\text{latt}}$ |
|---|---|---|---|---|---|---|---|
| 24/24/16 | 10 | 8 | 717 | 2.17 $a_0$ | 0.017 | 4.606 $a_0$ | 7.356 $a_0$ |

Due to the non-cubic choice of lattice, it also becomes necessary to adapt the k-point density along each axis to reflect the difference between the in-plane and out-of-plane axes. We opted to increase the density in the former instead of reducing it in the latter to avoid a loss of accuracy in comparison to the other calculations. The other parameters were optimized/taken as the `FLEUR` default like before. As with Si, the $2 \times 2 \times 2$ supercell configuration proved insufficient to match the DFPT sample points and thus a $4 \times 4 \times 4$ supercell was used instead.

**Table 6.10:** Overview of the acoustic $\Gamma$-point modes, $\omega$, in $\mathrm{cm}^{-1}$ for hcp Co. No frequency exceeds an absolute value of $1.7\ \mathrm{cm}^{-1}$ (or $0.211$ meV | $0.051$ THz, respectively).

| | $\omega_1$ | $\omega_2$ | $\omega_3$ |
|---|---|---|---|
| FD | $-7.88 \times 10^{-6}$ | $1.28 \times 10^{-1}$ | $1.28 \times 10^{-1}$ |
| DFPT | $-6.46 \times 10^{-1}$ | $1.64 \times 10^{0}$ | $1.65 \times 10^{0}$ |

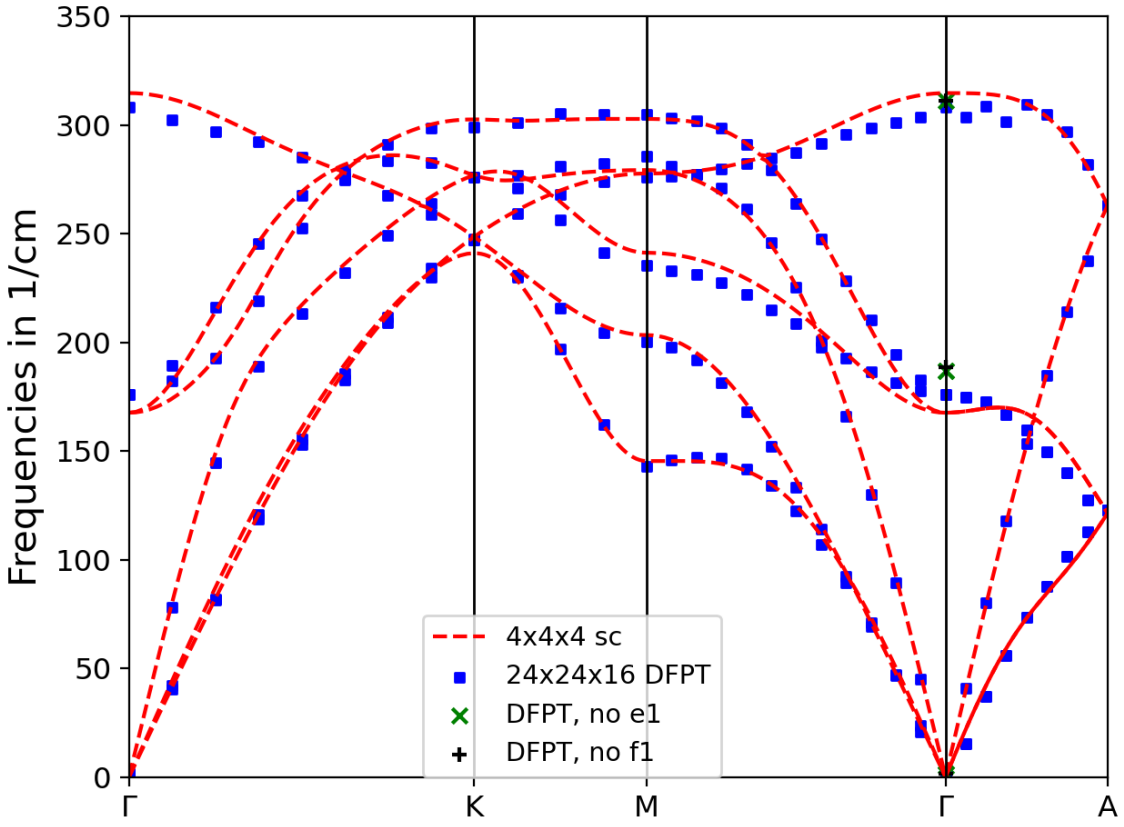



**Figure 6.5:** Phonon dispersion for hcp Co. The red dashed curve shows the FD reference and the blue squares show the DFPT data. The green cross at the second $\Gamma$-point highlights the modified result in the absence of eigenenergy response terms and the black plus neglects occupation number responses.

The resulting Goldstone modes are shown in table 6.10. There are several things to note. On the one hand, the degeneracy of the modes is lifted with one being clearly distinct from the other two. This one can be identified with the out-of-plane oscillation, *i.e.* a displacement of

the Co atoms in the z-direction. On the other hand, the DFPT modes are farther from zero than those in the FD case by at least an order of magnitude and all the values constitute the least clean Goldstone modes of all materials that were studied thus far. This is not surprising, as the dynamical matrix now takes on a more involved form and matching specific entries to cancel each other out in the eigenvalue calculation becomes numerically more difficult. The maximum iteration count reaches a new high of 39 cycles.

Figure 6.5 shows the resulting phonon dispersion. As was the case for Si, we explicitly show the data points that change, when the eigenenergy responses (e1, *cf.* equation (5.39)) and now additionally the occupation number responses (f1, equation (3.38)) are set to $0$, which affects both the first order density response through equation (3.33) and the dynamical matrix through (5.39). The overall agreement of the curve and the samples is once again good. As with Si, the optical branches are harder to match. At the $\Gamma$-point, the impact of the eigenenergy responses on the optical in-plane (middle) mode is visible, while that of the occupation number responses is negligible. Both terms are of lower impact in the out-of-plane (uppermost) mode. In numbers, the in-plane FD reference value lies at around $167.5$ cm$^{-1}$, the ones missing the e1/f1 terms lie at $189.0$ cm$^{-1}$ and $188.5$ cm$^{-1}$, respectively, and the full DFPT value gives $176.0$ cm$^{-1}$. The latter still does not fully match the FD value, but serves to continuously connect the dispersion sample values around $\Gamma$ on the path $M - \Gamma - A$, making it a valid correction.

SiC

The last material for this section serves to study the behavior of a polyatomic material in which the atoms are not all of the same element. To have a fluent transition from previous to new knowledge, we chose the semiconductor (3C) SiC in a zinc blende structure. This also means, that for each atomic parameter we now have two different values for the different atoms and the FD run needs two different displaced supercells and force calculations.

**Table 6.11:** Overview of the specific calculational parameters of SiC. For the atomic parameters, there are two values given each time representing the Si/C atom respectively. More parameters in section 6.1.

| $N_{k_{x/y/z}}$ | $\ell_{\max}$ | $\ell_{\max,\text{nsph}}$ | $N_{\text{MT}}$ | $R_{\text{MT}}$ | dx | $a_{\text{latt}}$ |
|---|---|---|---|---|---|---|
| 16 | 8/7 | 6/5 | 585/507 | 1.77/1.53 $a_0$ | 0.019/0.020 | 8.183 $a_0$ |

Once again, calculating clean Goldstone modes for the DFPT case proves difficult. The asymmetry of the lattice does not lend itself well to perfectly symmetric dynamical matrix elements and enforcing the acoustic sum rule in the FD case also becomes a little less precise. That said, the dispersion relation boasts the highest maximum values yet that are on a scale of over $900$ cm$^{-1}$, making a Goldstone mismatch of around $1$ cm$^{-1}$ still negligible. The modes are summarized in table 6.12.

**Table 6.12:** Overview of the acoustic $\Gamma$-point modes, $\omega$, in cm$^{-1}$ for SiC. No frequency exceeds an absolute value of $1.1$ cm$^{-1}$ (or $0.136$ meV | $0.033$ THz, respectively).

| | $\omega_1$ | $\omega_2$ | $\omega_3$ |
|---|---|---|---|
| FD | $1.36 \times 10^{-1}$ | $1.36 \times 10^{-1}$ | $1.36 \times 10^{-1}$ |
| DFPT | $-1.06 \times 10^{0}$ | $-9.75 \times 10^{-1}$ | $-9.49 \times 10^{-1}$ |

Unlike before, on the energy scale present in the SiC dispersion, neglecting the e1 terms in equation (5.39) do not make a significant difference. The FD value for the optical mode is a thrice degenerate $801.0\ \mathrm{cm}^{-1}$, while DFPT values give around $791.0\ \mathrm{cm}^{-1}$ and $795.0\ \mathrm{cm}^{-1}$ with and without the terms, respectively. The modes match quite closely, but a significant problem becomes appearent when we look at the full dispersion in figure 6.6.

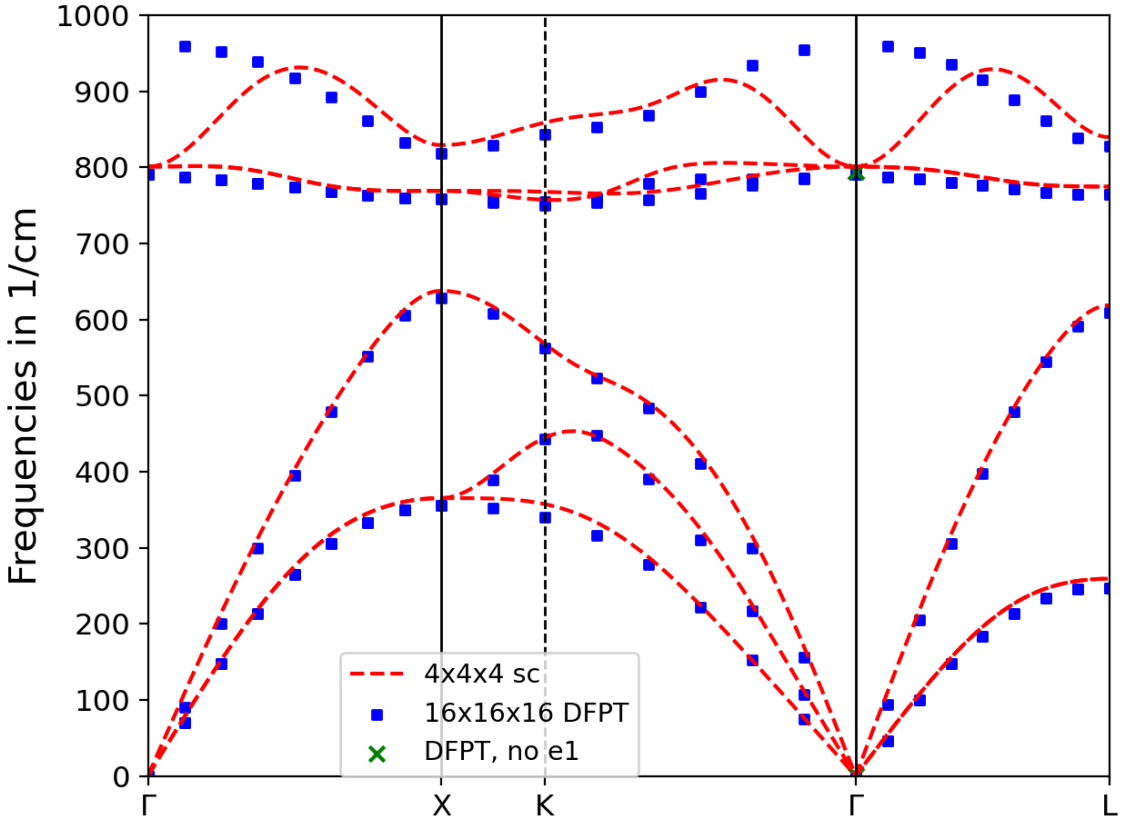



**Figure 6.6:** Phonon dispersion for SiC. The red dashed curve shows the FD reference and the blue squares show the DFPT data. The green cross at the second $\Gamma$-point highlights the modified result in the absence of eigenenergy response terms.

The maximum iteration count is 15. The FD calculations were done with a $4 \times 4 \times 4$ supercell as for the previous polyatomic cases. While the acoustic modes match excellently between the two methods, the optical modes paint a different picture. The transversal optical modes are of similar quality as in Si, but the longitudinal one shows a completely different behavior the closer it gets to $\Gamma$. This is due to the fact that SiC is polar *i.e.* it has an asymmetric charge distribution. This can induce dipole terms and cause the harmonic description of the force constant/dynamical matrix to no longer be sufficient. The need to take long-range effects into account arises [190]. These are usually taken into account by a non-analytical term correction (NAC) [191, 192], which can handily be evaluated in `phonopy` and lifts the degeneracy of the modes. For that, we need the so called Born effective charges and the static dielectric constant. Both of these quantities can either be calculated through Berry phase calculations [193], elaborate FD calculations with varying external electric fields [194], or similarly to the initial dynamical matrix from DFPT [176]. The correction is both needed to correct the DFPT result

at $\Gamma$ as well as that of the FD route in the vicinity of $\boldsymbol{q} \to \mathbf{0}$ [195], which is exactly what we see in the dispersion we calculated. As no method of calculating the necessary quantities is implemented in FLEUR at this point, we do not take the gap in the otherwise continuous dispersion as a gap in knowledge, but rather postpone the necessary implementation for this understood problem to a later point.

## 6.4 Using the q-point Interpolation

Beyond DFPT Data Points

The previous chapters served to highlight the current capabilities and limitations of the DFPT implementation by benchmarking calculations for specific q-points against FD results based on a well established force formalism and an external pre-/postprocessing tool. The more natural way in the context of a DFT ground-state calculation is sampling the Brillouin zone with a set of q-points and interpolating the phonon dispersion in the same way as it is done for the band structure with the underlying k-point set. This procedure becomes feasible with the symmetry considerations in section 3.2, that allow us to express the dynamical matrix at an unfolded q-point through one at an irreducible representative, the symmetry rotation matrix, and a phase factor, reducing the actual computational effort to an irreducible wedge of the BZ.

Calculation Setup

The setup for an interpolated phonon calculation is different from the single shot runs we described before. First of all, while the actual files for which the calculation is done still need to be without symmetry, we have to generate additional `.xml` files through the input generator, that do not have the `-nosym` option but instead an added prefix created by the parameter `-add_name fullsym`. In the actual `inp.xml` used for the phonon calculation, we add a parameter `qmode="1"` to the `juPhon` tag, that reads the k-point set from `fullsym_kpts.xml` (selected in the `fullsym_inp.xml` tag `kPointListSelection`) and uses it as a list of q-points instead of the one provided in `inp.xml`. Once the DM files for this list are written, we change the input file again. We add the parameters `l_scf="F"` and `l_band="T"` to `juPhon` and set the k-point list in the file to a path provided in `kpts.xml`. A file `JUDFT_WARN_ONLY` has to be created as well to bypass the warning, that the list of k-points for the band is not suitable for an SCF calculation. We then start the calculation again. FLEUR will read the DM files, unfold the symmetry onto each point of the full BZ, transform the set of DMs into real space (*i.e.* the space of lattice vectors, creating a force constant matrix several unit cells across), and finally transform it back for each q-point on the band path provided.

Testing with fcc Cu

To test the band interpolation, we once again turn to fcc Cu, that delivered favorable results before. We want to use the basic same input to (i) do single shot calculations and sample the phonon bandstructure with a density of $1/16$ in reciprocal space and (ii) interpolate the bandstructure from the IBZ of a set of $8 \times 8 \times 8$ q-points. If we overlay the interpolated curve with the sampled points, we can judge the quality of the interpolated curve. Figure 6.7 shows the resulting picture.

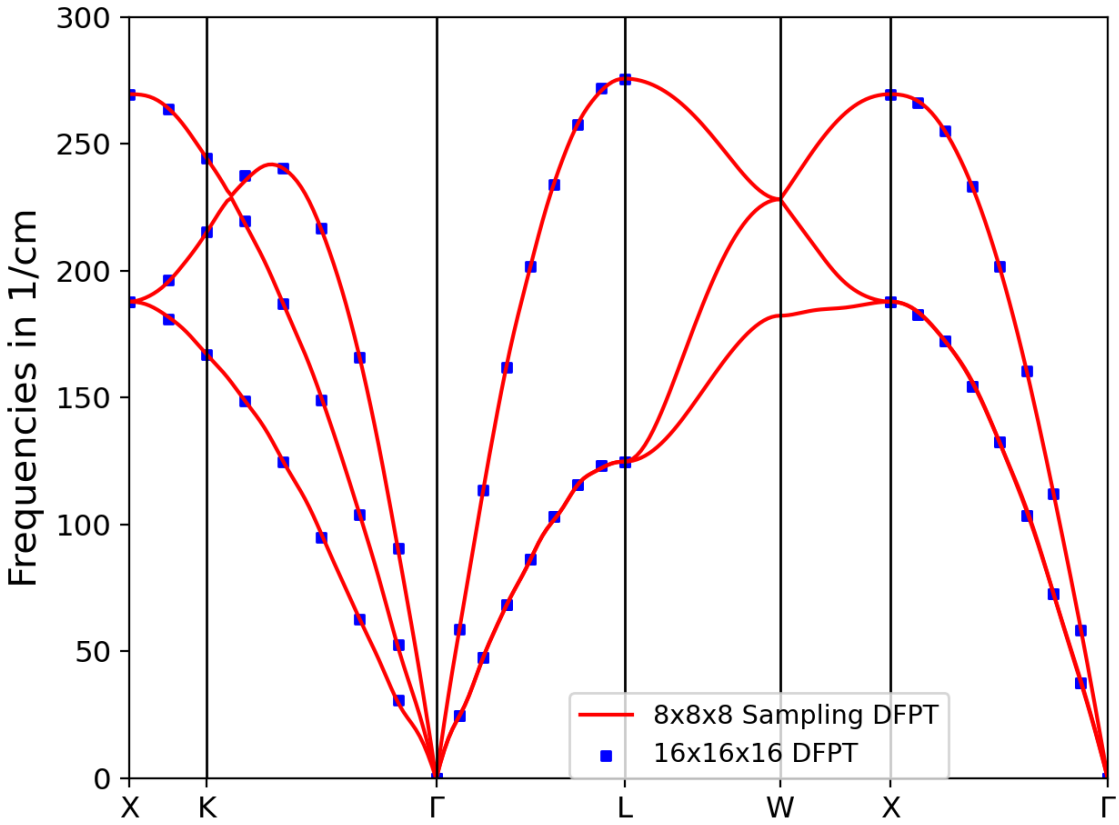



**Figure 6.7:** Phonon dispersion for fcc Cu. The red curve shows the interpolated $8 \times 8 \times 8$ reference and the blue squares show the DFPT data sampled from $16 \times 16 \times 16$.

The quality of the interpolation is basically perfect. While each second sample point is part of the interpolation set anyway and is thus well described by construction, the intermediary sixteenths are also very well matched by the interpolated curve. Near the $\Gamma$-point there is a slight waviness that we assume to be an artifact of the interpolation. This quality of interpolation also allows us to use it for a different purpose.

Phonon DOS

Having the possibility to calculate the full BZ of q-points at a fraction of the cost and being able to interpolate any other q-point from it consequently also allows us to interpolate a much denser grid of points than the one we started with. For example, from an $8 \times 8 \times 8$ IBZ sampling we can interpolate a full set of $16 \times 16 \times 16$ or even more points, making for a very dense q-point sampling. Such a dense sampling can be used to calculate the phonon density of states (DOS) without relying on large smearing parameters. Moreover, the tetrahedron method [196–198] can be used to gain a crisp curve that does not rely on a smearing at all.

Phonon DOS Calculation Setup

The FD `phonopy` part of the DOS calculation is very straight-forward based on the calculations we have already done. With the `FORCE_SETS` file created, all we have to do is invoke

```
phonopy -p mesh.conf --factor=5140.48767176083
```

from the console for a configuration file `mesh.conf` we prepared and the suitable factor to give the DOS in units of $\mathrm{cm}^{-1}$. For the comparisons we show later on, we provide the atom we

work on, the dimensions of the supercell, the number of mesh points on which to interpolate in each Cartesian direction, and the range and interval of energy values to write out. We use one file (with an additional smearing factor $\sigma$) for a smeared histogram approach to the DOS:

```
ATOM_NAME = Cu
DIM = 2 2 2
MP = 16 16 16
SIGMA = 5
DOS_RANGE = 0 300 0.1
```

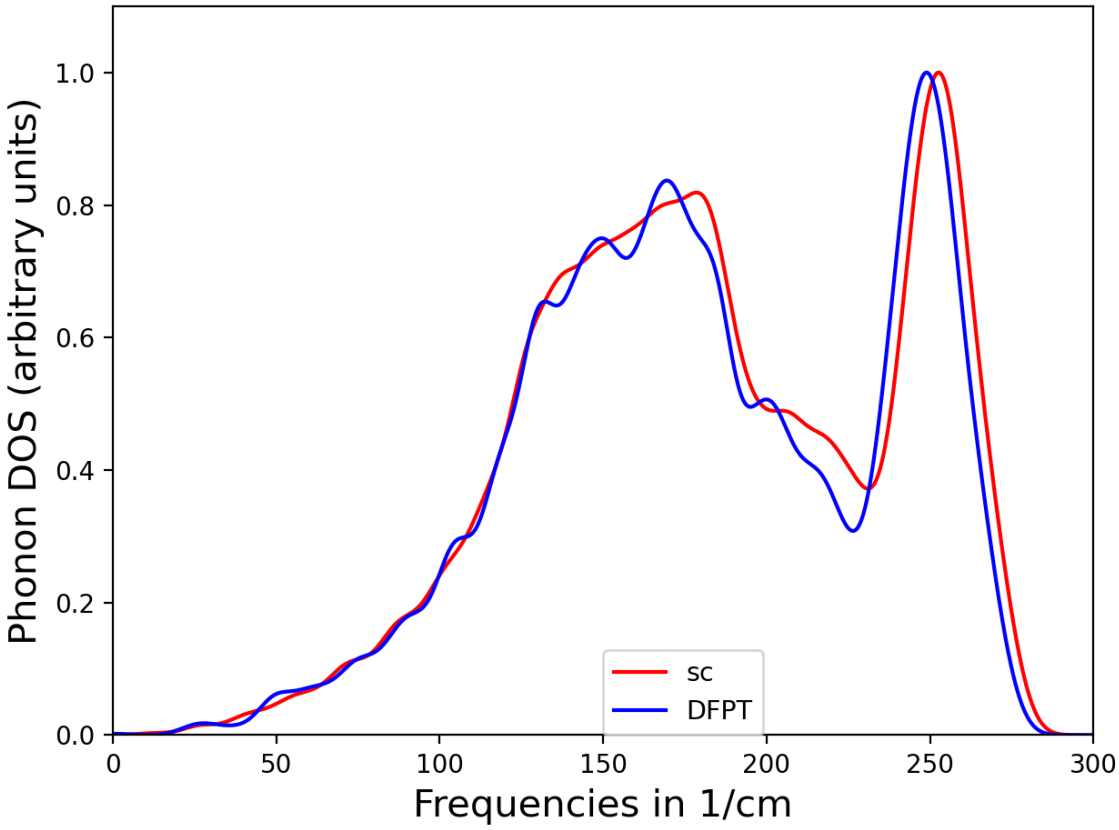



**Figure 6.8:** Phonon density of states for fcc Cu with the histogram method. The red curve shows the FD reference and the blue curve shows the DFPT data.

The energy values provided have to be given in the same units as the `--factor` argument calculates. For the DFPT side of the calculation, we start from the same interpolation set as before, but rather than setting `l_band="T"`, we set `l_intp="T"` and `l_dos="T"`. We work with a $16 \times 16 \times 16$ k-point list to interpolate the IBZ into. This set needs to be chosen in the `kPointListSelection` tag in `inp.xml`, while the sample set is set in the same way as for the bandstructure in `fullsym_inp.xml`. Additionally, we provide parameters for the DOS in the `bandDOS` tag: for the histogram method we choose `minEnergy="0"`, `maxEnergy="300"`, `sigma="5"`, and `numberPoints="3001"`. The energy limits and smearing are given in $\mathrm{cm}^{-1}$

These settings give a smooth dispersion with one broad growing plateau and a sharp peak at high energies, as shown in figure 6.8. This general structure is universal for the fcc crystal, just like the bandstructure was [185]. It is evident, that the DFPT calculation gives a neat match to the FD reference result, albeit with a slightly higher amount of fine structure, *i.e.* more local extrema. This can be due to the exact way in which the smearing factor is applied. It has a profound impact on the amount of oscillations in the curve. Too small smearing with a sparse k-point set can lead to many very sharp peaks that do not form a continuous curve. Too much smearing in contrast blurs out features of the curve. The smearing is thus a parameter that should be fine tuned. We chose to tune it for the FD phonon DOS and apply the same parameter for the DFPT calculation. The overall match of the curves extent is very good and the slight shift of the maximum directly relates to the phonon dispersion in figure 6.2, where the maximum values of the DFPT data fall ever so slightly below that from the FD case. The shape also gives a good fit to the general structure of fcc phonon DOS derived from the continued fraction method in [199].

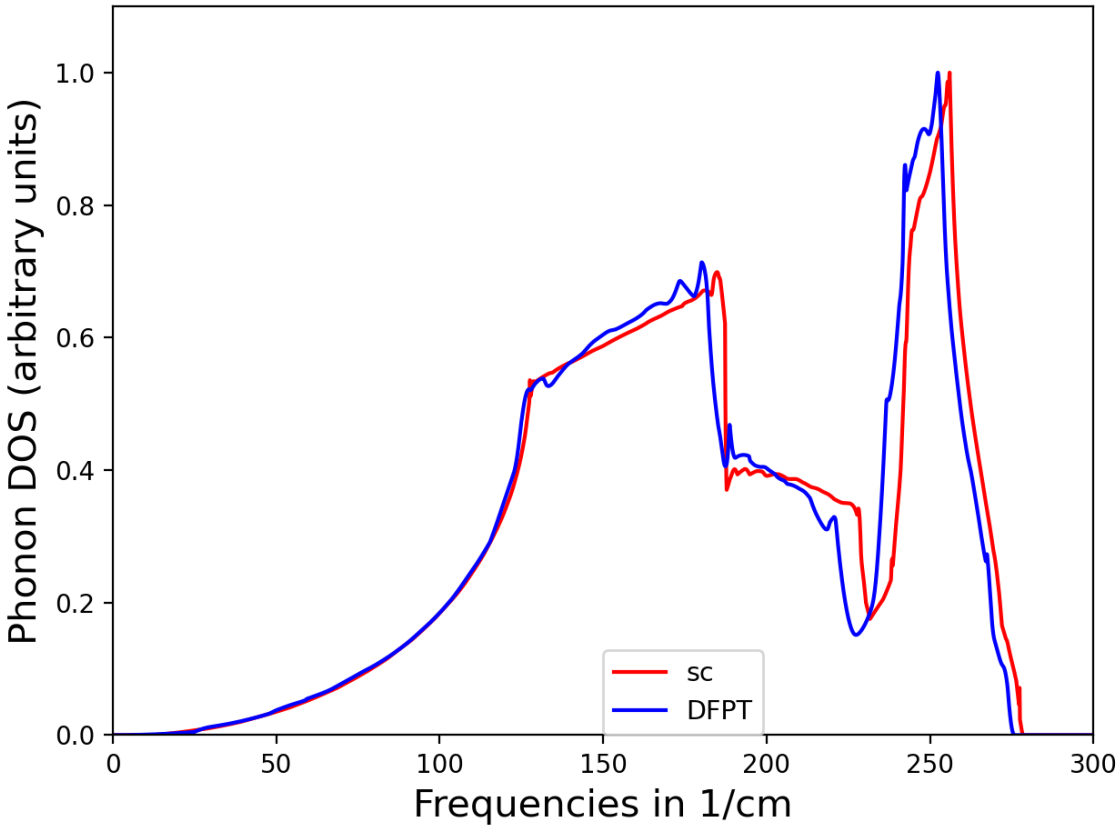



**Figure 6.9:** Phonon density of states for fcc Cu with the tetrahedron method. The red curve shows the FD reference and the blue curve shows the DFPT data.

For a calculation, whose comparability is not influenced by the smearing factor $\sigma$, we turn to the tetrahedron method of BZ integration. For this we need to remove the `SIGMA` tag from the FD configuration file, explicitly telling `phonopy` not to use the histogram method. In the `FLEUR` input, we reduce the smearing to a minuscule value and set `mode="tetra"` in the

`bzIntegration` tag. This is done, because `FLEUR` also allows a smearing parameter to be used in the tetrahedron method to smooth out the very crisp DOS and be able to compare to experimental results, which we do not want here.

The result is shown in figure 6.9. The good agreement between both methods becomes more nuanced here. In the low energy regime, where the DFPT data points neatly reproduced the FD dispersion curve in figure 6.2, the curves overlay excellently. Towards higher energies, the overall shape of the curve remains very similar, albeit shifted slightly downwards for the DFPT case. Both curves exhibit the same linearly building peak in the middle of the curve, drop and valley following it, and the same global maximum. We are very pleased with these results and count the phonon DOS capability of the `FLEUR` code as validated for future use.

## 6.5 Takeaways from the Validation

We presented a study of several test systems that represent different classes of materials and different problems that can arise in their DFPT treatment. An overall good agreement was obtained across all calculations, with some notes to be made. While for the monatomic crystals it sufficed to use fairly small $2 \times 2 \times 2$ supercells, the polyatomic materials required bigger ones to obtain the same level of agreement. The phonon dispersion relations for the polyatomic systems are more complex and this complexity is not necessarily covered well by a description with small supercells. We thus take the convergence of the FD phonon spectrum with respect to the supercell size as a requirement to produce accurate results. Aside from this agreement, we judge the quality of the DFPT calculation itself as excellent. In no case have the Goldstone modes, that are supposed to have exactly zero frequency, exceeded a relative value of 1% of the maximum value of the dispersion. Considering the iteration count, even for the smallest absolute q-points it took less than 30 iterations to converge the self-consistent Sternheimer equation below a tight threshold. We see a failure of the method in SiC, but this was to be expected considering existing knowledge about the phonon spectra of polar systems. Finally, the interpolation from a set of sample q-points to a continuous band structure on the relevant high-symmetry paths and the evaluation of the phonon density of states was successful. With these investigations finished, we turn to a more in-depth look at the parameters in the calculation to try and figure out, which have the most impact and which are of lesser importance.

Chapter 7

# Convergence Studies in bcc Metals


7.1 Supercell Convergence . . . . . 97
7.2 DFPT Convergence Parameters . . . . . 104
7.3 The Case of bcc Mo . . . . . 110


In the previous chapter, our main concern was to explore the extent to which the DFPT implementation can be applied to different classes of materials. There was always either a good agreement from the start or it could be achieved by increasing the size of the supercell used for the FD calculation. There are several valid questions, that arise in this context. First of all, are there materials that refuse to give accurate results with the current implementation and are not understood, as opposed to the case of SiC? How exactly does the FD phonon spectrum converge with respect to the size of the supercell? Which parameters are linked to the accuracy of the phonon dispersion and which have a lower impact? Especially the last question can be a guide to lowering the computational effort of the phonon calculation in FLEUR. For the convergence studies, we turn to another monatomic metal we have not tested yet: bcc Fe. It showed slight problems when it was last investigated [94] and we want to study it further to see, how these problems emerged.

## 7.1 Supercell Convergence

Initial Result

We begin with a procedure similar to the last chapter. We take the parameters determined for bcc Fe by the DFPT profile in FLEUR and optimize the lattice constant with a fit to the Birch-Murnaghan EOS. The resulting values are collected in table 7.2.

**Table 7.1:** Overview of the specific calculational parameters of bcc Fe. Parameters not contained in the table are kept at the FLEUR default or are explicitly mentioned in section 6.1.

| $N_{k_{x/y/z}}$ | $\ell_{\max}$ | $\ell_{\max,\mathrm{nsph}}$ | $N_{\mathrm{MT}}$ | $R_{\mathrm{MT}}$ | $dx$ | $a_{\mathrm{latt}}$ |
|---|---|---|---|---|---|---|
| 16 | 10 | 8 | 711 | 2.15 $a_0$ | 0.017 | 5.220 $a_0$ |

In addition to these parameters, the threshold for the modified coefficients from section 5.3 was increased to $10^{-5}$ Ha. The initial results are those for an FD reference with a $2 \times 2 \times 2$ supercell, which proved sufficient for the previous monatomic materials. Considering the level of complexity, bcc Fe falls into the same category as fcc Ni. Hence, in principle, we expect a similarly good quality for the calculation. This is confirmed, when we look at the Goldstone modes in table 7.2.

**Table 7.2:** Overview of the acoustic Γ-point modes, $\omega$, in $\mathrm{cm}^{-1}$ for bcc Fe. No frequency exceeds an absolute value of $0.2$ $\mathrm{cm}^{-1}$ (or $0.025$ meV | $0.006$ THz, respectively).

| | $\omega_1$ | $\omega_2$ | $\omega_3$ |
|---|---|---|---|
| FD | $-5.81 \times 10^{-6}$ | $-4.61 \times 10^{-6}$ | $-3.26 \times 10^{-6}$ |
| DFPT | $1.28 \times 10^{-1}$ | $1.29 \times 10^{-1}$ | $1.31 \times 10^{-1}$ |

As was the case for all previous calculations, the Goldstone frequencies are of negligible magnitude, assuming the dispersion is once again in the regime of a few hundred $\mathrm{cm}^{-1}$. To verify this, we opted to use the q-point interpolation to gain access to a full phonon dispersion and density of states. We can then directly compare the full breadth of phonon information between the FD and DFPT case, to find areas of good and bad agreement. The special points on the path are the high-symmetry points $H = (-1/2, 1/2, 1/2)^T$ and $N = (0, 0, 1/2)^T$ in internal coordinates and the intermediary point $P = (1/4, 1/4, 1/4)^T$.

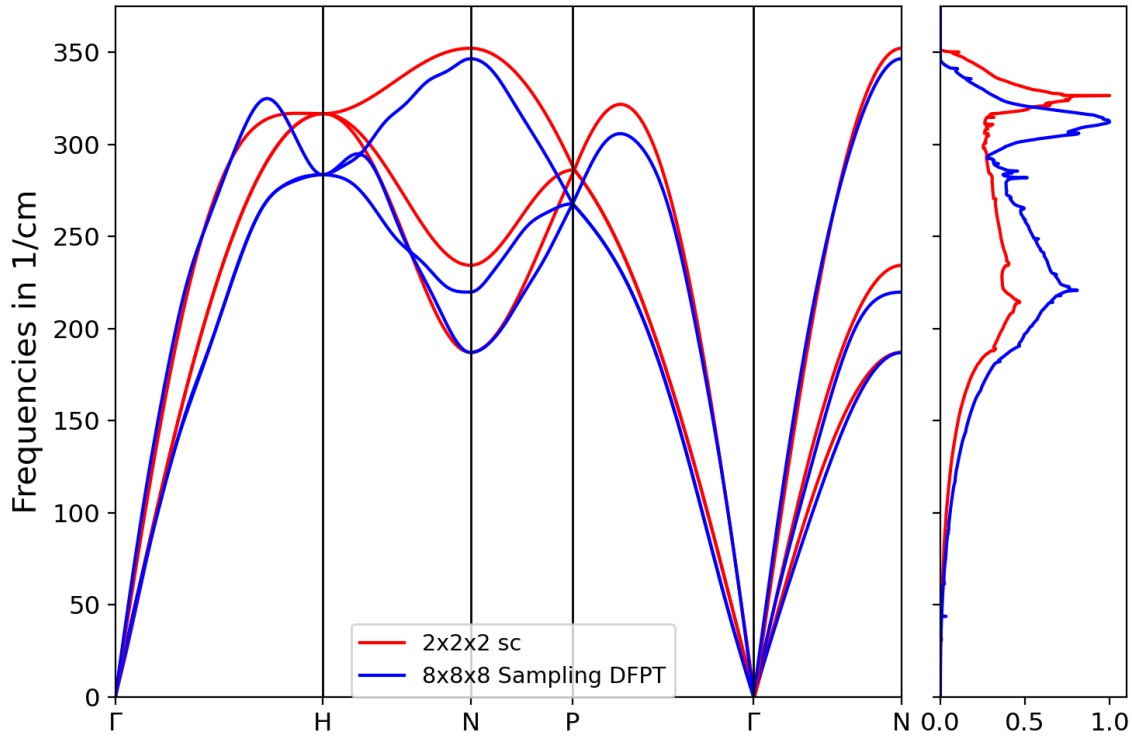



**Figure 7.1:** Phonon dispersion and DOS for bcc Fe. The red curves show the FD reference and the blue curves show the DFPT data.

For the same DOS parameter set as in section 6.4 (and using the tetrahedron method), this results in figure 7.1, where the DOS is plotted next to the phonon bands in a standard electronic structure fashion. The comparison of the data shows, that the match between both calculations highly depends on the high-symmetry path and mode we look at. For example, there is an excellent agreement for the lowermost acoustic branch at and around $N$ and the path from $\Gamma$ to $N$ manifests very similarly regardless of the calculation (with a slight deviation of the uppermost acoustic mode). The other special points, however, take on completely different values and especially the behavior around $H$ is fundamentally different. Where the FD calculation finds a flat maximum for the longitudinal mode, the DFPT curve has a peak to the left of the high-symmetry point and instead forms a valley. As opposed to fcc materials [185], the curve shape in bcc crystals is directly influenced by both the nearest and next-nearest neighbor force constants. Their ratio determines *e.g.* whether such a peak exists and how pronounced it is. The mismatch indicates, that the ratio of the next-nearest to nearest neighbor force constants is larger in the DFPT result. The differences of course also translate to the DOS, where the high energy FD peak is sharper than for DFPT and the lower energy broad peak is higher in the latter case. This can be either due to a bad description of the dispersion by FD not being able to capture a structure with many peaks through interpolation or a bad result from the DFPT run.

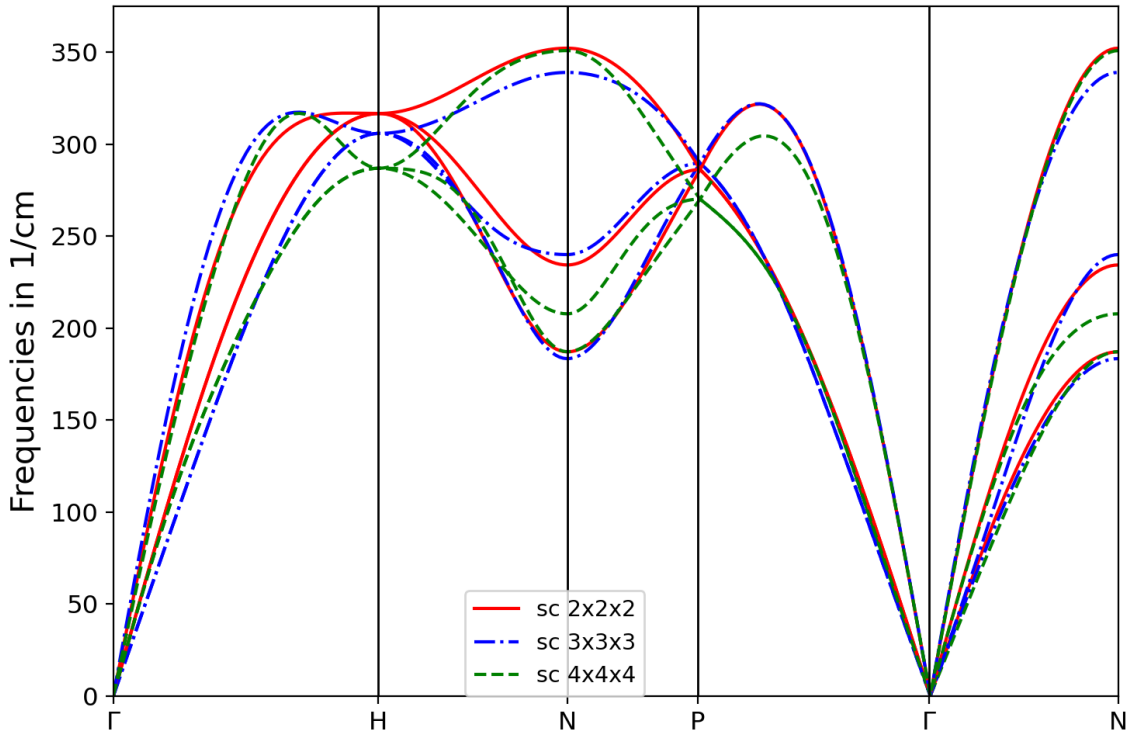



**Figure 7.2:** FD Phonon dispersions for bcc Fe and different supercell configurations. The red solid curve shows the $2 \times 2 \times 2$ supercell result, while the blue dash-dotted curve represents $3 \times 3 \times 3$ and the fully dashed green one $4 \times 4 \times 4$.

Convergence Behavior

Both arguments are equally valid, but since we already observed a difference in the dispersions for different supercell sizes (*cf.* [94] and section 6.3), we first want to investigate such

trends more systematically and see, whether the match to the DFPT results becomes better or the results converge to a completely different curve. Specifically, we do so by looking at the phonon dispersions of the same bcc Fe system, but for supercells of sizes $N \times N \times N$ for $N \in \{2, 3, 4, 5, 6, 7, 8\}$. These calculations become costly very fast, because they inflate the monatomic unit cell to a supercell with $N^3$ atoms, respectively. This means if a good convergence does not emerge for some of the smaller supercells, even a badly optimized DFPT calculation quickly becomes more efficient than the FD approach. We first look at the smaller supercells from 2 to 4 copies in each direction (figure 7.2). It is immediately visible, that while some parts of the dispersion remain practically the same in all three cases (lowest branch from $\Gamma$ to $N$), there is some improvement towards the DFPT results. The valley at $H$ emerges, consequently making the peak on the path from $\Gamma$ to $H$ visible. The band crossing at $P$ is shifted downward, to a value similar to the one the DFPT results showed (a concrete overlay will be shown later). Interestingly, the uppermost mode at $N$ differs between the $N = 2$ and $N = 3$ cases, but returns to its original value for $N = 4$. Since it is a high-symmetry point and therefore is associated to a phonon with a two cell periodicity, it stands to reason that such a frequency can be best described when the supercell size is also a multiple of two. This line of reasoning would also explain the improvement of the value at $P$, as it represents a four cell periodic phonon. To clarify such notions, we look at the next set of supercell sizes in figure 7.3.

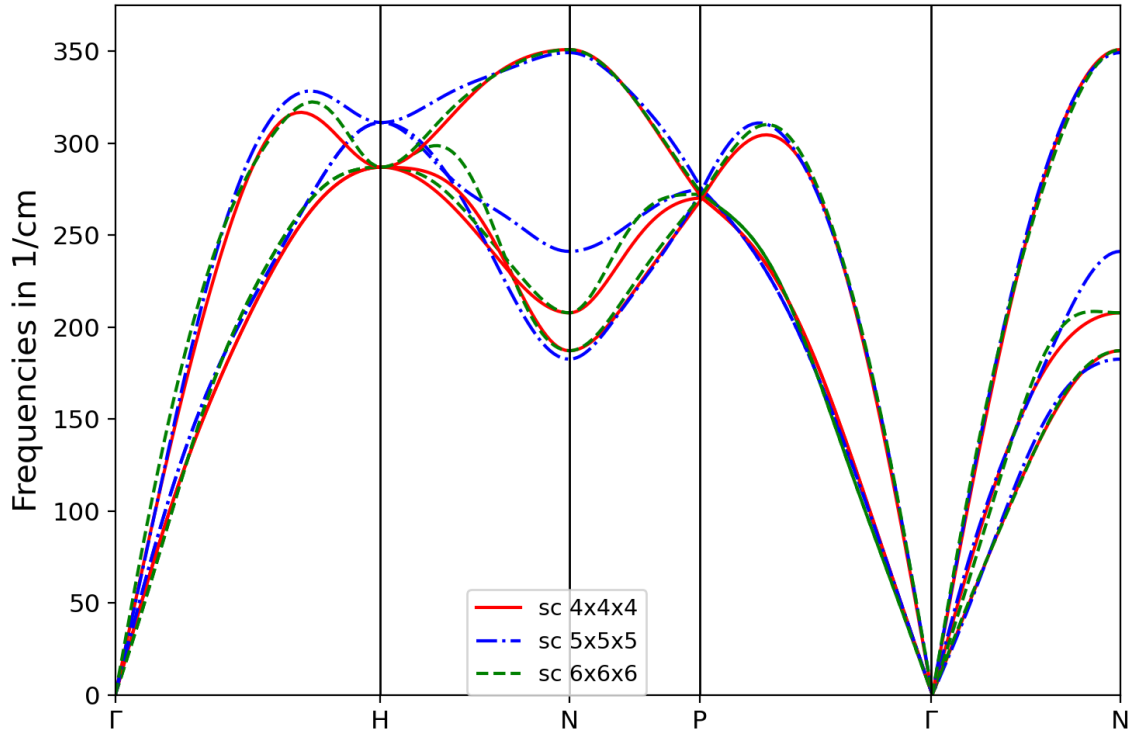



**Figure 7.3:** FD Phonon dispersions for bcc Fe and different supercell configurations. The red solid curve shows the $4 \times 4 \times 4$ supercell result, while the blue dash-dotted curve represents $5 \times 5 \times 5$ and the fully dashed green one $6 \times 6 \times 6$.

The results are not quite what we would have expected. The special point $P$ and the maximum at $N$ remain very stable throughout all three sizes, dispelling the notion that the phonon wave has to "fit" neatly into the supercell to describe it best. At $H$ on the other hand, the $5 \times 5 \times 5$ supercell jumps back to a higher value, reducing the extent of the peak before it. Such a jump can also be seen at $N$ and on the path from $H$ to $N$ in the middle mode. So overall, it seems we can at least quantify the supercell convergence as being better for even numbered supercells, with the odd numbered supercells deviating from the trend that was set. As our interpolations for the DFPT calculation is done on a reduced set of q-vectors representing an $8 \times 8 \times 8$ grid, we assume that the same quality of interpolation should be achievable with a supercell of the same size, which constitutes a ground-state and force calculation for 512 atoms. This is completely disproportional to the monatomic system for which we want to calculate the dispersion and is not practicable for repeated calculations. For the sake of completeness and being thorough, we still present results for the next two supercell sizes and compare them to $6 \times 6 \times 6$ in figure 7.4.

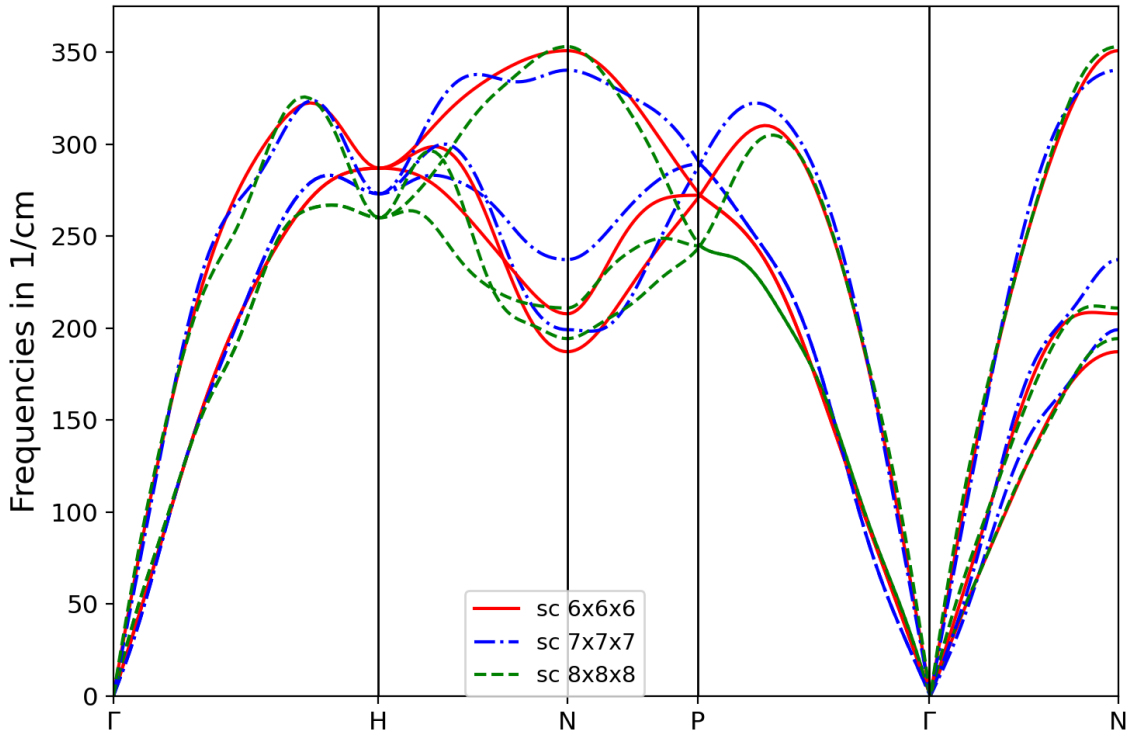



**Figure 7.4:** FD Phonon dispersions for bcc Fe and different supercell configurations. The red solid curve shows the $6 \times 6 \times 6$ supercell result, while the blue dash-dotted curve represents $7 \times 7 \times 7$ and the fully dashed green one $8 \times 8 \times 8$.

For the odd supercell with 7 repetitions in each direction, we find a similar behavior to the previous ones. It deviates from the high-symmetry points that were already properly captured by small, even-numbered supercells. It does notably keep a very similar peak shape left of $H$, which can be understood in terms of divisions of the Brillouin zone. For even supercells, all high-symmetry points should get at least a moderately good description, because they represent supercells with a cell periodicity of 2. For odd supercells, this is not the case and

they instead should give the best description of the curve in fractions that correspond to their extent. That means, if we understand the points $\Gamma$ and $H$ as 0 and 1/2, the odd supercell can give a good description of the curve at *e.g.* 3/7, which lies in close vicinity to the peak. We look at the biggest supercell size next. Disappointingly, it does not stick to the trend of the previous even supercells in keeping the high-symmetry points stable and refining the curve shape in between. Rather, it deviates at the highlighted points, but keeps the peak stable as did the $7 \times 7 \times 7$ calculation (3/8 is close to the peak as well). We have no concrete explanation for this phenomenon, but there are some ideas that can come into play. First, the large supercell might make the single small displacement that we chose so insignificant for distant atoms, that the resulting forces become indistinguishable from numerical noise. In fact, analyzing the force file reveals that the biggest contributions of several mHa/$a_0$ occur only on the displaced atom, with some in the range of $10^{-4}$ Ha/$a_0$ and $10^{-5}$ Ha/$a_0$. This already constitutes the limit of this calculation, as the force convergence threshold was set to the latter value. It stands to reason, that setting a lower threshold and thus allowing for more accuracy can change the resulting picture, but this would only make the calculation even more costly and even less feasible for repeated usage. It is also not guaranteed, that the convergence down towards higher force accuracy is smooth and easily achieved. For this specific case, we checked that further force convergence ($10^{-8}$ Ha/$a_0$) does not yield a visible difference. Another factor that might come into play is the sampling of the Brillouin zone of the calculation itself. With growing supercell size, the number of k-points used is reduced subsequently according to the default choices of the `FLEUR` code, as it is reasonable to choose a sparser sampling when the unit cell itself and thus the number of wave functions is already large. For $6 \times 6 \times 6$, this results in a set of 8 k-points, that notably still contain the high-symmetry points. At $8 \times 8 \times 8$, the cell has become so large, that only the $\Gamma$-point is found anymore. While we cannot directly infer a link between the lack of high-symmetry points in the k-point set and them being lackluster in the phonon dispersion, this is at least something worth mentioning and the reduction of the BZ onto only $\Gamma$ might not be entirely enough to correctly describe the electronic structure of the extensive cell. Testing this hypothesis would once again necessitate an even more involved calculation. Since the main time consumption of the calculation in such large systems happens in the diagonalization, increasing the k-point count by a factor of 8 (or rather by 4 due to symmetry) nearly translates to a factor 4 onto the runtime. Considering that this is just a hypothesis, the 512 atom system is much to big to experiment with for something we can much more easily achieve with a DFPT calculation - however unoptimized it may still be with respect to runtime. To avoid wasting computational resources, we instead focus on other means of improving the match between the dispersions.

Improved Supercells

The supercells with the best convergence, namely $4 \times 4 \times 4$ and $6 \times 6 \times 6$, have already become quite large and the biggest ones defy the notion of convergence altogether, instead deviating from previously established trends. It stands to reason that there should be a better way of converging out with respect to their size. One way `phonopy` offers is the optional `--pm` argument for the command line, when the supercell is constructed. When the set of possible displaced supercells is found and reduced to its utmost minimum, normally displacements that are directly opposed to each other (like $\pm x$ in one direction) are reduced to a single displacement. We can prohibit this automatic reduction and see, whether this has an impact on the accuracy of the dispersion for this specific case. Instead of increasing the number of atoms and the size of the supercell by a factor of 8, this instead only doubles the calculational effort and remains quite affordable. The results are shown in figure 7.5.

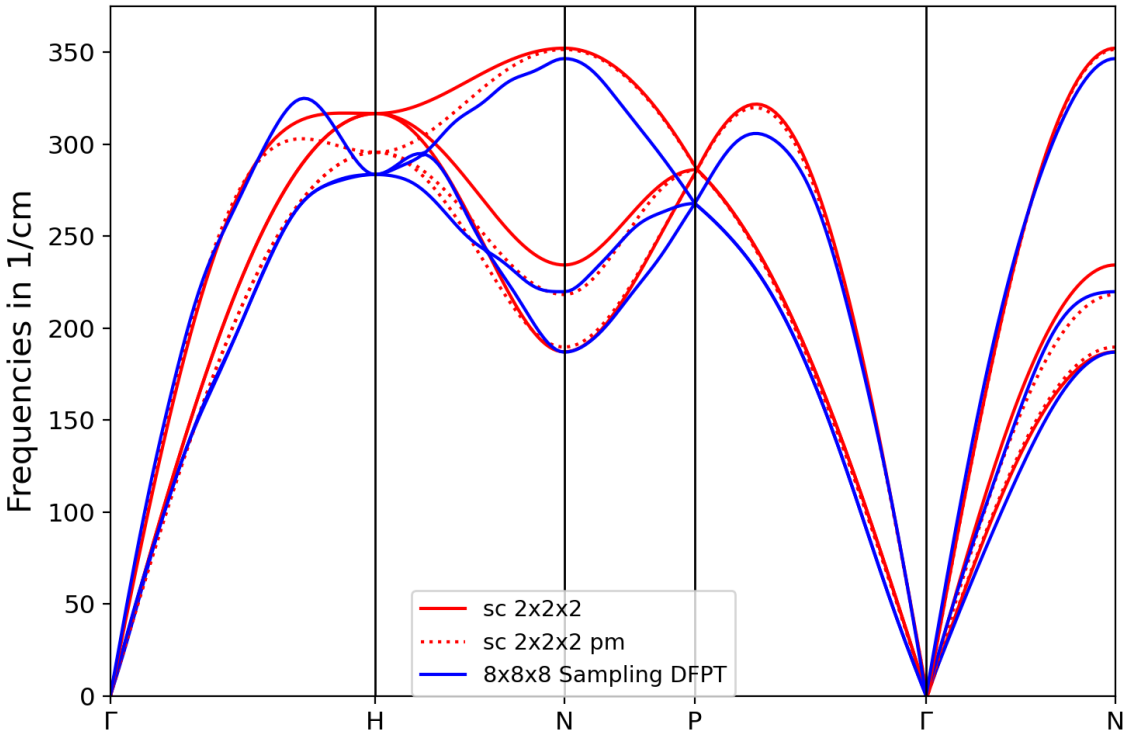



**Figure 7.5:** Phonon dispersions for bcc Fe at different FD supercell configurations and for DFPT. The red solid curve shows the $2 \times 2 \times 2$ supercell result, the red dotted result has the $\pm\, 2 \times 2 \times 2$ supercell and the blue solid curve shows DFPT data.

Considering we created only slightly more computational effort by calculating two displaced $2 \times 2 \times 2$ cells instead of one, the results already look vastly better. The notion of a peak and valley for $H$ can be seen and the middle branch at $N$ gives a way better fit than before. In general, the values for this high-symmetry point now match very nicely to the DFPT result for the lower two branches. There is, however, no change with respect to $P$, which apparently still necessitates a bigger supercell. From previous experience, we directly turned to the $4 \times 4 \times 4$ case for this and compare all of our top level results against each other. Unfortunately, the new results do nothing to improve upon the standard $4 \times 4\times$ supercell for the DFPT comparison. We collect the most accurate results in figure 7.6.

The biggest reasonable supercell $6 \times 6 \times 6$ shows a tight fit to the DFPT result for the full $\Gamma$-$H$ and $\Gamma$-$P$ paths. There is a slight deviation for the upper mode at $N$ and a slightly larger one for the middle mode. Consequently, the path $H$-$N$-$P$ gives a slight mismatch between the two methods. The two FD calculations, however, match closely in the aforementioned region, so it stands to reason that this result is reasonably well converged. Curiously, this mismatch is opposite to the case of the $\pm\, 2 \times 2 \times 2$ supercell, where the middle $N$ branch was very well matched and $P$ instead disagreed. It is quite possible, that this is an artifact of the interpolation from the force constant matrix, but currently we do not know of a straight-forward way to verify this notion or remedy the problem.

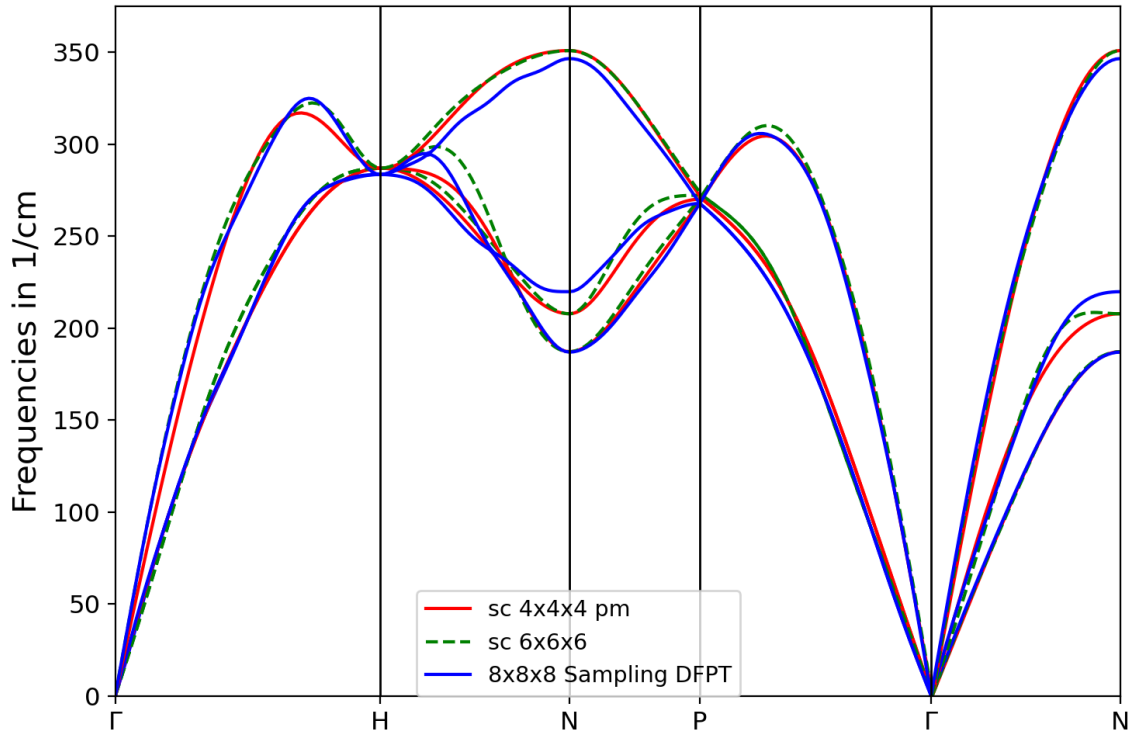



**Figure 7.6:** Phonon dispersions for bcc Fe at different FD supercell configurations and for DFPT. The red solid curve shows the $\pm\ 4 \times 4 \times 4$ supercell result, the green dashed result has the $6 \times 6 \times 6$ supercell and the blue solid curve shows DFPT data.

Furthermore, as the main focus of this work is not the investigation of FD results, where they only serve as a benchmark for the DFPT results, we conclude this section. We take the $4 \times 4 \times 4$ supercell to be a good middle ground between the convergence of the FD results and the necessity to have accessible benchmarks whose computational effort does not vastly outweigh their usefulness.

## 7.2 DFPT Convergence Parameters

We showed, that the FD simulations require large supercells to give a good match to the DFPT data. In a sense, that makes DFPT calculations a lot cheaper for a desired accuracy threshold. This difference in computational cost will only become more prominent for a better optimized DFPT process, where time is saved as opposed to the current implementation. We leave the further optimization of the procedure as a future task and look at the problem in a different way. We have set several parameters in the calculation, like the plane wave cutoff, to quite high values to ensure the quality of the dispersion results. In this section we want to evaluate for some parameters, whether we could settle for less and still get a decent result with less time-consuming calculations. We stick with bcc Fe as our test material, as its wavy dispersion structure already gave a good challenge for the supercell investigation.

### 7.2.1 Distance Threshold Convergence

The standard convergence threshold in the FLEUR code is $\varepsilon_{\text{SCF}} = 1 \times 10^{-5}\ a_0^{-3}$ (and consequently $\varepsilon_{\text{SCF}} = 1 \times 10^{-5}\ a_0^{-4}$ for DFPT). For all previous calculations, we have kept this threshold fixed, leading to the iteration counts noted for each material. We investigated, how this parameter influences the dispersion curve. For this we fine tuned the threshold from $1 \times 10^{0}\ a_0^{-4}$ to $1 \times 10^{-8}\ a_0^{-4}$ in a logarithmic fashion, *i.e.* reducing the cutoff by a factor of $10$ each step (with $0.5 \times 10^{-x}\ a_0^{-4}$ in between each time). The resulting data points do not directly correspond to a calculation that has exactly the convergence threshold as its final distance, but rather to one with a distance below it. Since the density response can converge with bigger steps than are captured by our grid, this can lead to several data points with the same value back to back. Additionally, a smaller absolute q-vector results in much bigger values for the potential and consequently much larger initial and overall distances. This naturally means a lot more iterations happen for such a q-point and the point, at which actual convergence is achieved in relation to the distances, can be reached faster. The results are plotted in figure 7.7.

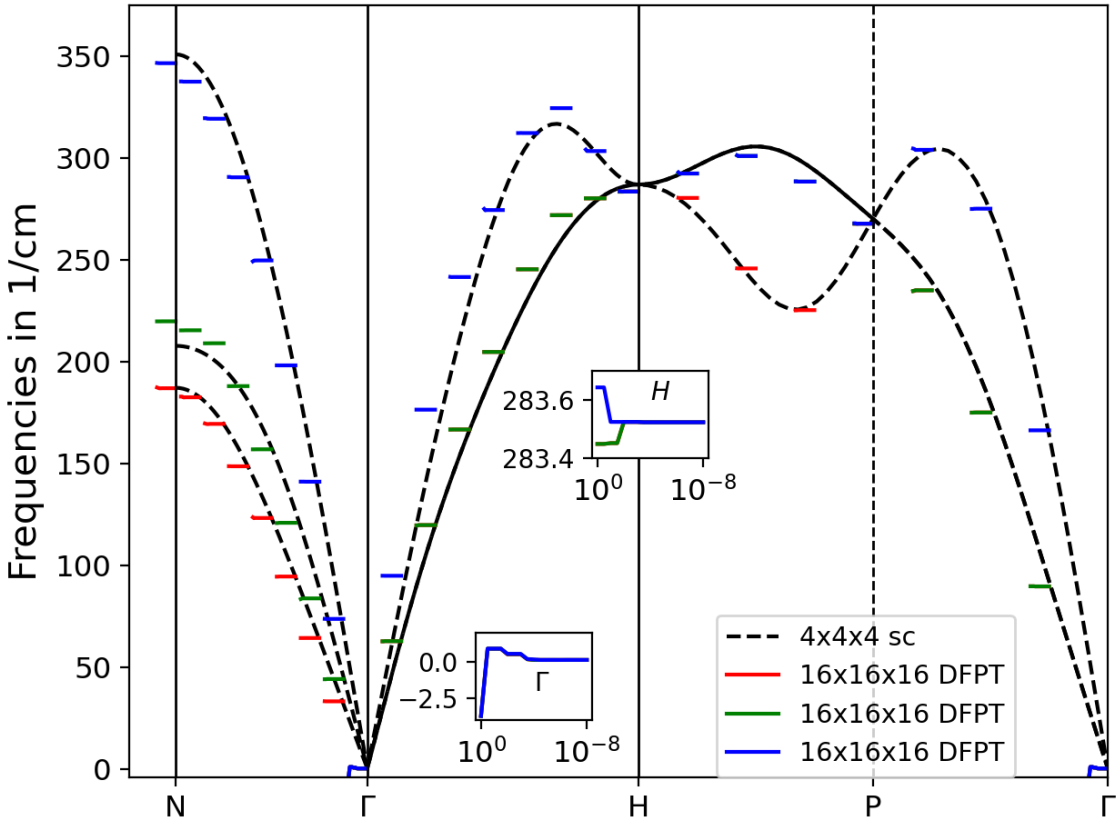



**Figure 7.7:** Phonon dispersions for bcc Fe at different DFPT convergence thresholds. The black dashed curve shows the $4 \times 4 \times 4$ supercell result, while the red, green, and blue lines show the three phonon modes for specific q-points with respect to the thresholds.

The different convergence thresholds are shown as a small graph at each of the q-points sampled for the curve. On the scale of the full dispersion, these graphs appear flat aside from some small deviations at the starting point for certain modes. In line with the reasoning, that

the same distance for a smaller q-point means an already better convergence, the deviations are only visible to the naked eye for the larger q-vectors and $\Gamma$. For the latter, the convergence behavior can be best associated with that of the ground-state run, as there is no component of the potential that acquires large values due to a small wave vector. The small inlets in the plot zoom in on the convergence behavior of the high-symmetry points $\Gamma$ and $H$. At $\Gamma$, we see the largest deviations from our reference values, where there is an uncertainty of up to 3 $\mathrm{cm}^{-1}$ when the density response is not fully converged. On the other hand, the values at $H$ are converged to an accuracy of less than a tenth of that for even the largest thresholds. Carefully checking all the data points shows, that none of them (except for the ones at $\Gamma$) have a convergence margin of more than 1 $\mathrm{cm}^{-1}$, meaning that if we take such an uncertainty (less than $0.3\%$) as accurate enough, we can save several iterations for each q-point and drastically reduce the computation time.

We can set up a similar but inverse parameter test by looking at the phonon dispersion for a fixed maximum number of iterations. The result is plotted in figure 7.8.

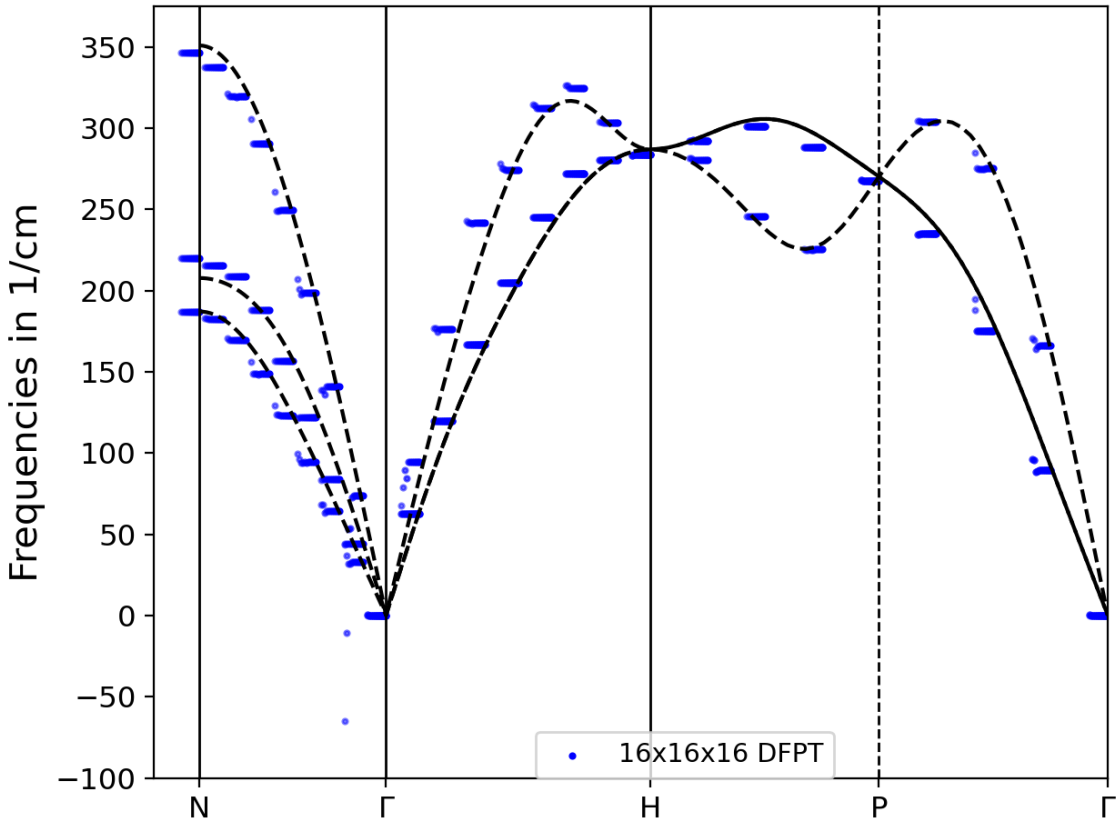



**Figure 7.8:** Phonon dispersions for bcc Fe for different maximum numbers of iteration in the Sternheimer SCF cycle. The black dashed curve shows the $4 \times 4 \times 4$ supercell result, while the blue dotted lines show the three phonon modes for specific q-points with respect to the iterations.

The convergence plot for each mode and q-point is visualized as a dotted line. The range goes from 5 iterations to 15, yielding 11 data points each. For smaller iteration counts, the

results diverge to wildly to show a coherent plot. While for higher modes, corresponding mostly to larger absolute q-points, the dotted curves form continuous lines, the single points are clearly distinct for small ones. This means the small q-point need some more iterations to converge. This is a somewhat complementary statement to the one from the previous plot, where the same convergence threshold means a different amount of iterations for different sizes of the q-point. We want to quantify this notion by plotting the first iteration distance of the Sternheimer cycles for each Cartesian direction $j$ against the corresponding component $q_j$ of the q-point in figure 7.9.

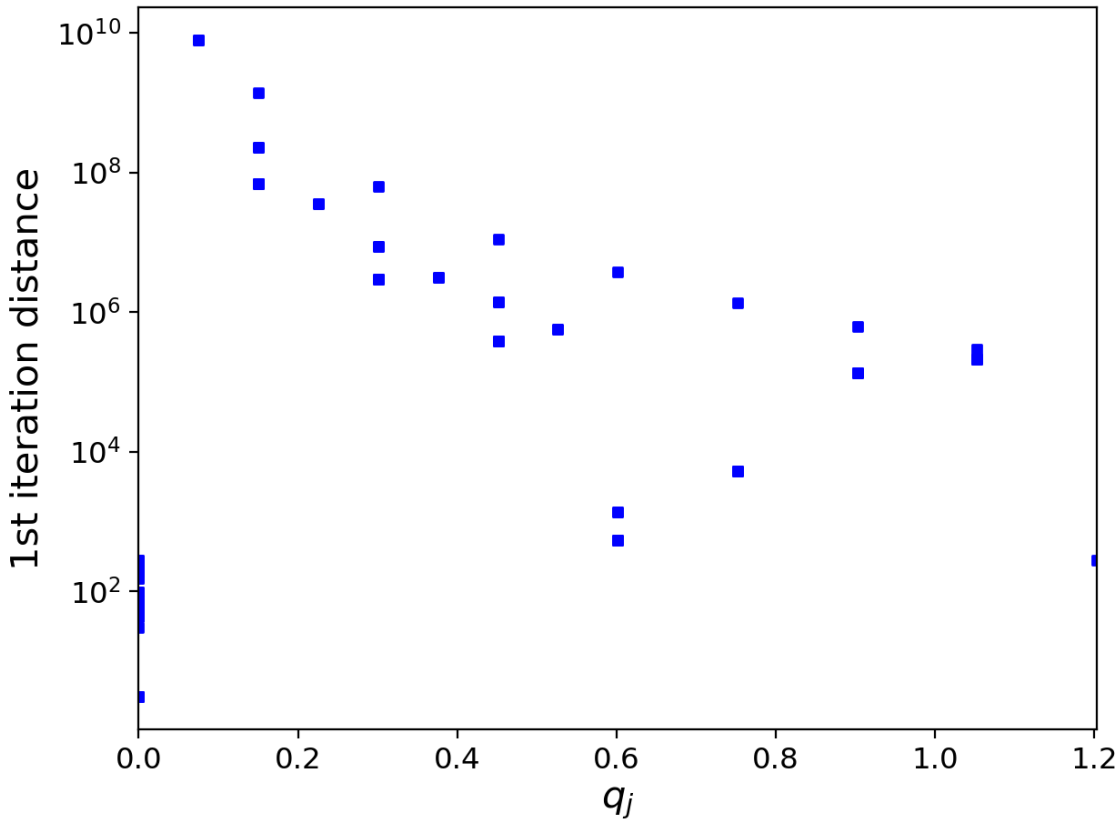



**Figure 7.9:** First iteration distances of the Sternheimer SCF-loop for bcc Fe plotted against the Cartesian q-point component parallel to the displacement. The y-axis is given on a logarithmic scale.

Aside from a few outliers, there is a clear trend towards smaller distances for larger q-components. The lowest values at $q_j = 0$ belong to the $\Gamma$-point. The higher values at $q_j \approx 0.6$ belong to the intermediary point $P$ and the lower ones to the high-symmetry point $N$. The values at $q_j \approx 1.2$ stem from $H$. So the most obvious outliers are related to special points in the BZ, while the rest shows a rather clear downwards trend. We can summarize the insights from the threshold/iteration convergence by relating them to the requirement, that the second order energy response has to be variational. We see clearly, that only a few iterations (or conversely a large threshold) suffice to achieve well-converged results for the dispersion, in spite of very large first iteration distances at small q-points. *I.e.* a badly converged set of

wave functions yields a sufficient end result. This observation can be carried over to other parameters.

### 7.2.2 Basis-Set Cutoff Convergence

The next parameter whose influence we want to investigate is the plane wave cutoff $K_{\text{max}}$. It is of central importance in any DFT calculation, as it determines the set of reciprocal lattice vectors $\boldsymbol{G}$ that are constructed for each k-point, thereby determining the size of the basis set and their maximum kinetic energy. In the LAPW framework, this also influences the MT spheres indirectly through the sets of matching coefficients. As a rule of thumb, it is usually wise to choose $\ell^{\gamma}_{\text{max}} \approx K_{\text{max}} R^{\gamma}_{\text{MT}}$ [133]. Here, we deviate from this rationale and vary the plane wave cutoff from $3.5\ a_0^{-1}$ to the reference result of $4.5\ a_0^{-1}$ in steps of $0.1\ a_0^{-1}$, all the while keeping the angular cutoff and MT radius fixed at the values in table 7.1. Otherwise we would have to establish which of these we would have to change by how much. Keeping them fixed can also have an influence on the lattice constant, which we choose to ignore to avoid additional EOS runs for every $K_{\text{max}}$ chosen. The results are shown in figure 7.10.

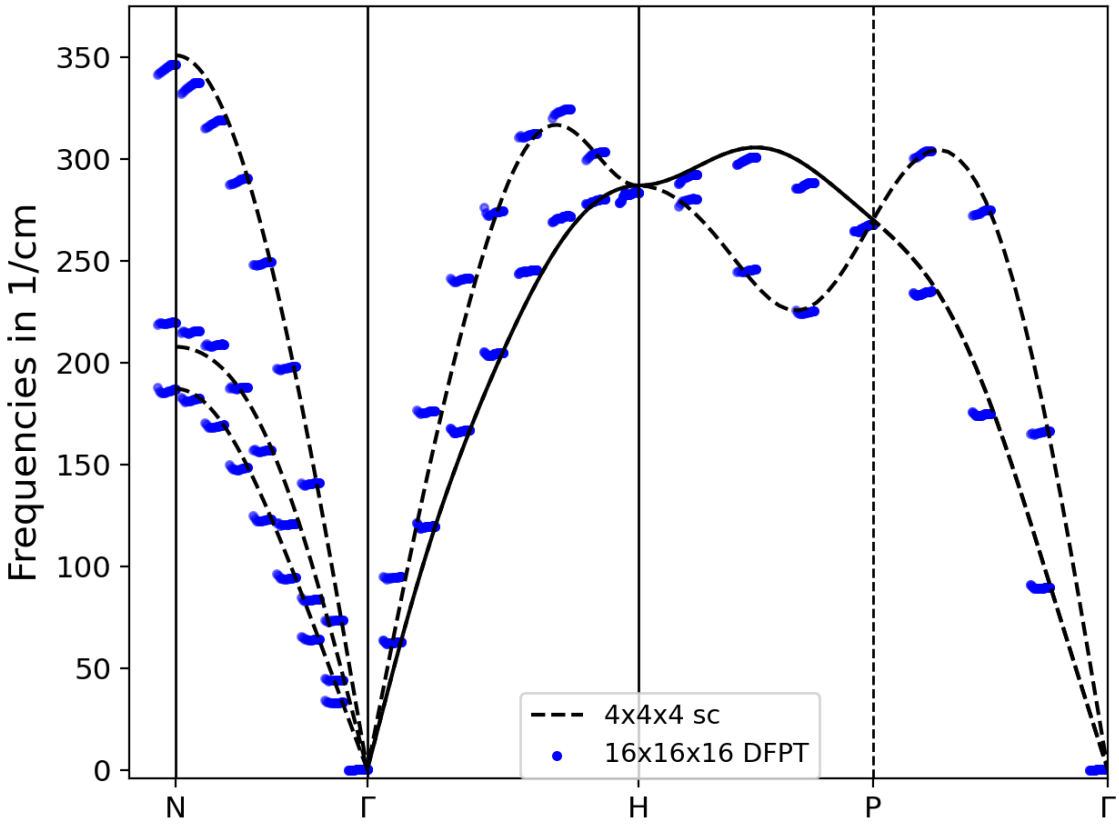



**Figure 7.10:** Phonon dispersions for bcc Fe at different plane wave cutoffs. The black dashed curve shows the $4 \times 4 \times 4$ supercell result, while the blue dotted lines show the phonon frequencies for specific q-points with respect to the cutoffs.

The LAPW basis cutoff has a more significant impact than the convergence threshold had. To the naked eye, there is a visible curve shape for the data points, which converge towards the value of the original cutoff. The largest ranges of values are found for the largest frequency values, where a convergence span of up to 5 $cm^{-1}$ can be observed. For the specified range of cutoff parameters, this is still somewhat small and can likely be attributed to the fact, that we would technically have to reoptimize the system for each of them. This reinforces the notion, that the formalism is variational, as the basis cutoff also influences the quality of the wave functions and thus their convergence. We therefore keep in mind that choosing a lower value of $K_{\text{max}}$ can be a valid way to cut down on the calculation time, as it significantly reduces the time spent on diagonalizing the Hamiltonian for each k-point (*cf.* the scaling aspect in section 5.6).

### 7.2.3 k-point Set Convergence

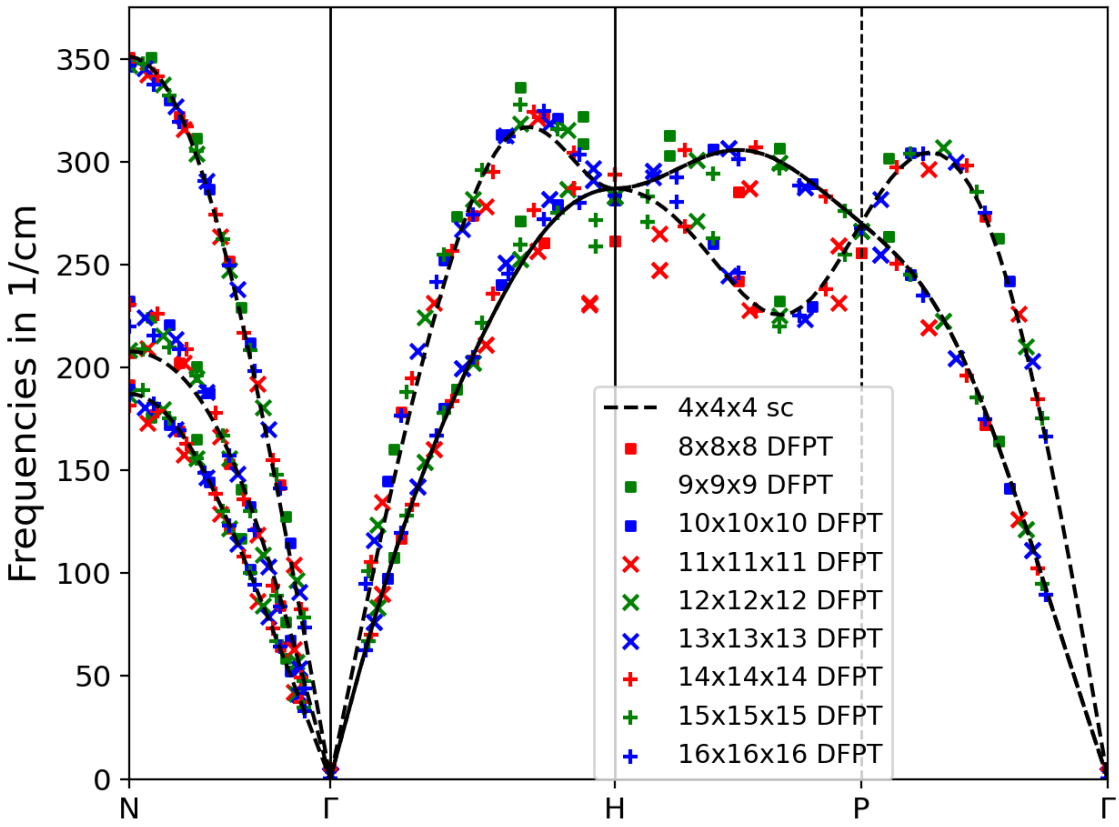



**Figure 7.11:** Phonon dispersions for bcc Fe at different k-point meshes. The black dashed curve shows the $4 \times 4 \times 4$ supercell result, various data points show the phonon frequencies for specific q-points with respect to the sets.

We established in section 6.4, that it is most instructive to calculate the dynamical matrices for a set of q-points that cover the IBZ of the crystal lattice, *e.g.* we showed that the fcc Cu dispersion interpolated on the 29 points needed for an $8 \times 8 \times 8$ q-point grid suffice to

reproduce the sampled q-points of the $16 \times 16 \times 16$ grid. In general, in a calculation with an $N_x \times N_y \times N_z$ k-point grid, all q-points $\{l/N_x, m/N_y, n/N_z\}_{(l,m,n)\in\mathbb{Z}^3}$ can be calculated directly without an interpolation. This means, that we can sample the phonon dispersion with a high density of q-points for different k-point grids to see, how the data points converge with respect to the density of the BZ sampling and its parity (odd/even).

This was done in the debugging phase of the project for a reciprocal energy cutoff (*cf.* section 6.4) of $10^{-7}$ Ha, yielding the data shown in figure 7.11. There are several things to note about this plot. First and foremost, there are several sections and modes of the dispersion, where the data from all k-point sets shows excellent agreement with the FD reference. These branches, like the $\Gamma$-$P$ path and the uppermost and lowermost modes of $\Gamma$-$N$, are therefore very stable with respect to changing the k-point set and easily converged at quite a sparse mesh of $8 \times 8 \times 8$. The same cannot be said for the middle branch and everything around the high-symmetry point $H$. There, two key points are of note. The denser sets tend to converge better towards the reference (note for example the $8 \times 8 \times 8$ marker at $H$ as compared to that of $16 \times 16 \times 16$), but there are some notable outliers. The odd numbered markers closest to $H$ vary wildly in quality with no clear trend of convergence with higher grid densities. This can be due to the fact, that the energies close to it can be near-degenerate to those of $\boldsymbol{q} = \mathbf{0}$, which means a higher cutoff on them might be in order. As we do not plan on using these types of k-point sets for the other calculations in this work, such a study is beyond its scope. We now try to apply the knowledge we gained from this section to another bcc test system.

## 7.3 The Case of bcc Mo

Experiences with bcc Metals

As we already mentioned, in the group of monatomic materials there was not as good an agreement between DFPT and FD calculations for the bcc as for the fcc case [94]. This could, however, be remedied by turning to bigger supercell sizes and the convergence behavior was explicitly highlighted for the case of bcc Fe in section 7.1. But there was one material that consistently resisted an acceptable degree of agreement, in that certain features of the DFPT data could by no means be reproduced in the FD approach.

bcc Mo

The material in question is bcc Mo. It is a transition metal that is usually supplemented with local orbitals in FLEUR and in this case, the supplementation is more important than for fcc Ni or bcc Fe, as there are relevant semicore states with high lying energies, that are not well described as confined to the core. Aside from this, it does not exemplify a new class of materials and should be treatable in the same way the other test materials have. We begin, as always, by giving the parameter set and optimized structure for the system in table 7.3.

**Table 7.3:** Overview of the specific calculational parameters of bcc Mo. Parameters not contained in the table are kept at the FLEUR default or are explicitly mentioned in section 6.1.

| $N_{k_{x/y/z}}$ | $\ell_{\max}$ | $\ell_{\max,\text{nsph}}$ | $N_{\text{MT}}$ | $R_{\text{MT}}$ | $dx$ | $a_{\text{latt}}$ |
|---|---|---|---|---|---|---|
| 16 | 11 | 8 | 793 | 2.15 $a_0$ | 0.016 | 5.884 $a_0$ |

Initial testing of this system done in [93] revealed problems with the imaginary parts of the eigenvectors, that needed to be projected onto the real axis to ensure the inversion symmetry of the system. Further testing in the scope of this work showed, that these problems are

related to the fact that there is a discrepancy between the numerical gradient of the effective potential and the analytical form that is constructed in the DFPT workflow, specifically in the Coulomb part. The gradient of the density shows significant noise near the nucleus and the standard integrator (6-point Simpson scheme) used in the Poisson solver of FLEUR propagates this towards the edge of the MT. A similar problem was observed in [200], where the Poisson solver had trouble with the divergence of the magnetic field, that was used as its input density. Such fringe cases required the implementation of a 4-point spline integrator [201, 202], that is able to smooth over such noise. Without the spline the dispersion showed inflated values on some branches and a lot of soft modes of similar extent. Using the spline integration scheme was sufficient to fix the most auspicious problems the DFPT data had. The resulting Goldstone modes are summarized in table 7.4.

**Table 7.4:** Overview of the acoustic Γ-point modes, $\omega$, in $\mathrm{cm}^{-1}$ for bcc Mo. No frequency exceeds an absolute value of $0.07$ $\mathrm{cm}^{-1}$ (or $0.009$ meV | $0.002$ THz, respectively).

| | $\omega_1$ | $\omega_2$ | $\omega_3$ |
|---|---|---|---|
| FD | $6.93 \times 10^{-6}$ | $7.11 \times 10^{-6}$ | $7.55 \times 10^{-6}$ |
| DFPT | $-6.50 \times 10^{-2}$ | $-6.01 \times 10^{-2}$ | $-4.31 \times 10^{-2}$ |

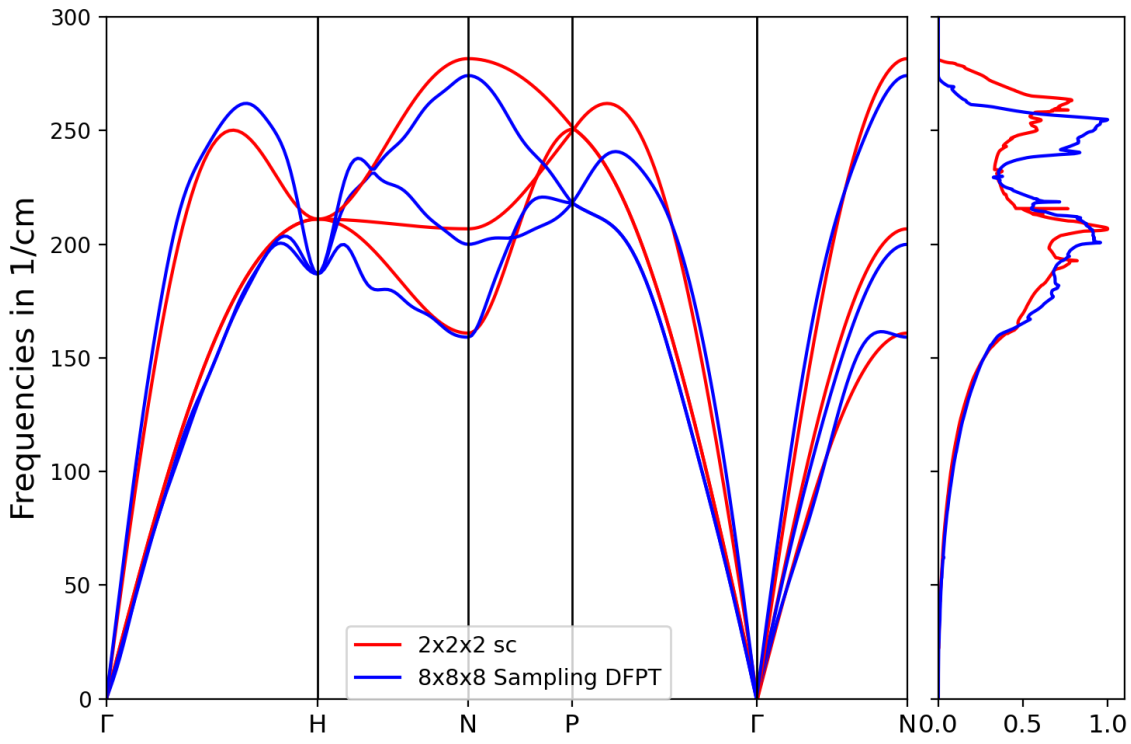



**Figure 7.12:** Phonon dispersion and DOS for bcc Mo. The red curves show the FD reference and the blue curves show the DFPT data.

The frequencies are once again very close to $0$ and fall within the range we specified in the conclusion of the previous chapter. The maximum iteration count was $16$. The curiosities of bcc Mo arise when we look at other high-symmetry points. For the initial results of the full

dispersion, we show once again the interpolated DFPT curve and the FD results for a $2 \times 2 \times 2$ (plus/minus displacement) supercell alongside the phonon DOS in figure 7.12. The areas of agreement and disagreement are quite similar to the previous case of bcc Fe. While some lines neatly align, in FD there is a distinct lack of features close to the high-symmetry points, like the small bump on the lowermost branch close to $N$ on $\Gamma$-$N$, that converge toward the same value. Especially the points $H$ and $P$ are also heavily mismatched. While the band crossing in $P$ can be seen in both curves, the FD reference shows a significantly higher value. At $H$, the DFPT data falls steeply into a minimum for all branches, while the FD calculation makes it look more like a saddle point - the upper mode goes into a minimum and the degenerate lower modes into a maximum. The value is also shifted upwards. These mismatches directly translate to the phonon DOS. Both calculations give two distinct broad peaks, but in the FD case the valley between them is more than double the size of the DFPT one.

Convergence and Stability

Due to the stark mismatch of the two calculations, we have made various attempts to tune the results by adjusting parameters and workflows in both cases. On the FD side, there was a significant influence on the curve when a $4 \times 4 \times 4$ supercell was used instead. Calculating this same supercell with two separate opposing displacements did not yield any noteworthy change anymore, just as it was the case for bcc Fe. We use this as the new reference curve.

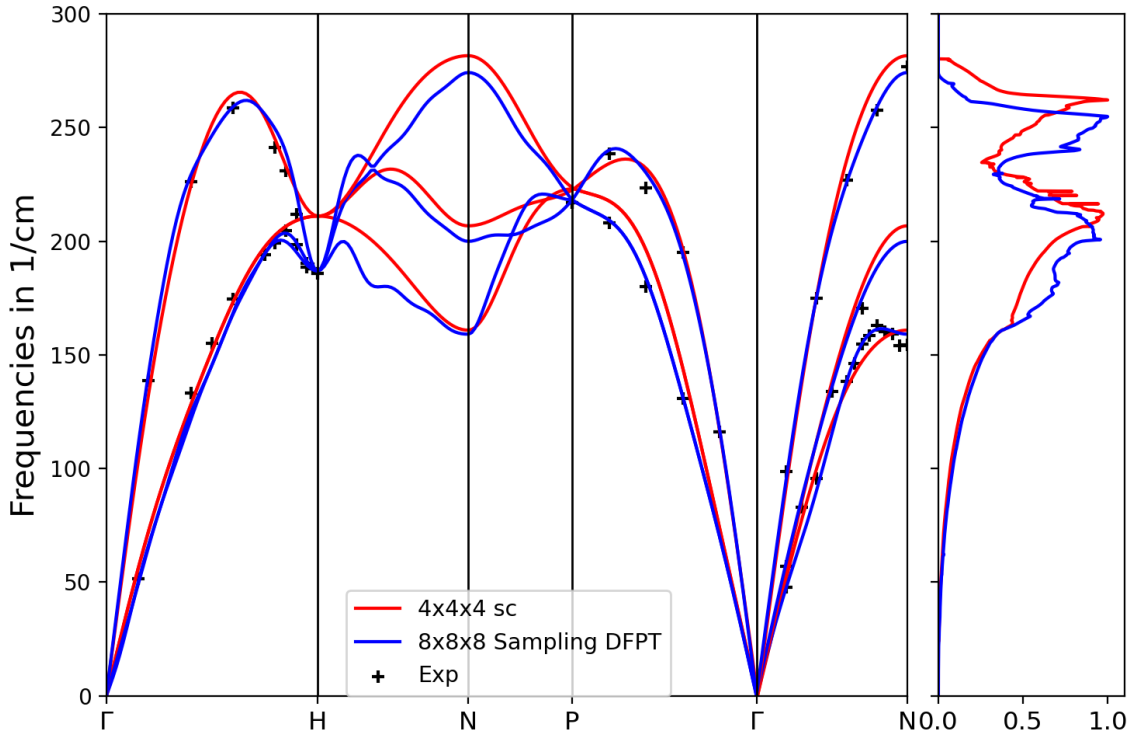



**Figure 7.13:** Phonon dispersion and DOS for bcc Mo. The red curves show the FD reference and the blue curves show the DFPT data. The black pluses show experimental data from [203].

For DFPT, on the other hand, we tried to further converge the calculation by drastically increasing some cutoff parameters. The plane wave cutoff $K_{\text{max}}$ did not have a significant

impact when increased above values of $4.5$, which is already moderately big. The same goes for the density cutoff $G_{\text{max}}$. Finally, we checked the influence of the k-point set by drastically increasing the number of points in each Cartesian direction from 16 to 40 for the $\Gamma$-$N$ branch. Doing so did not make the bump in the lowest branch disappear, but rather showed it in smooth way with higher resolution. So, in summary, the DFPT curve was very stable against the parameter changes we made. Thus, we consider it converged. The question is: if both curves are converged to their final form and still disagree - which calculation type yields the more accurate results. Since the ground-state calculation gives us an optimized system with a lattice constant very close to the experimental one ($3.114$ vs $3.142$ [204]) despite using LDA, it stands to reason that our results should be able to replicate experimental data for the phonon dispersion very well.

To verify this, we used the data from [203]. The results of the $4 \times 4 \times 4$ supercell and the $16 \times 16 \times 16$ k-point DFPT calculation are shown alongside the measurements in figure 7.13. Comparing both curves to each other and to the experimental data gives the clear impression, that DFPT delivers a better match. Both the minimum at $H$ and the slight buckle before $N$ are visible in the data points, cementing our view that the DFPT calculation has reproduced features, that the FD approach is not able to capture easily. This is in equal parts confusing and easily explainable. Considering the mismatch of features close to high-symmetry points, they represent phonons that only become commensurate with a supercell when we look at many wavelengths. In contrast, a high-symmetry point is commensurate with the $2 \times 2 \times 2$ supercell already. This is also neatly confirmed by the fact, that $P$ is well described with the $4 \times 4 \times 4$ supercell. The one thing that is hard to explain is the mismatch at $H$. We would expect a good agreement of the point itself and then some deviations around it with respect to the peak structure. But that is not the case - the point itself is mismatched and does not dramatically improve with the supercell size.

We still attribute the good fit of the DFPT curve to a matter of convergence in the interpolation: The direct calculation of the IBZ interpolation points is done with a high-accuracy k-point grid and the interpolation is done on $8 \times 8 \times 8$ q-points. Again, it stands to reason that this is twice as accurate as the present supercell approach and an $8 \times 8 \times 8$ supercell would fare better. This, however, constitutes a ground-state and force calculation for a system of 512 atoms, which is utterly wasteful for the calculation of such an inherently small (monatomic) system. Additionally, it turns out that such a large supercell calculation does not come without its flaws either, as we already observed for bcc Fe in section 7.1 and is shown again in figure 7.14 for bcc Mo.

The resulting curve for the big supercell only locally improves upon the smaller one and has a noticeable drop in quality in other branches. On the upside, the upper mode of $N$ now gives a tight fit to the DFPT curve. The drop towards a local minimum in $H$ also finally emerges. The problems lie mostly in the lower branches. The lower $N$ mode shrinks so significantly, that it drastically alters the dispersion on the $\Gamma$-$N$ and $H$-$N$-$P$ paths. There is also a distinct waviness to the curve, that is likely an artifact of the large cell. After all, more repetitions in each direction allow more freedom in the Fourier interpolation, which does not necessarily translate to a strict improvement. The convergence behavior of bcc Mo with respect to supercell size thus proves rather erratic. Furthermore, as stated before, calculations on this scale are anything but worth it and the DFPT approach is validated as a less cost intensive, more accurate solution to calculate the phonon dispersion. This holds true for this specific material and is backed

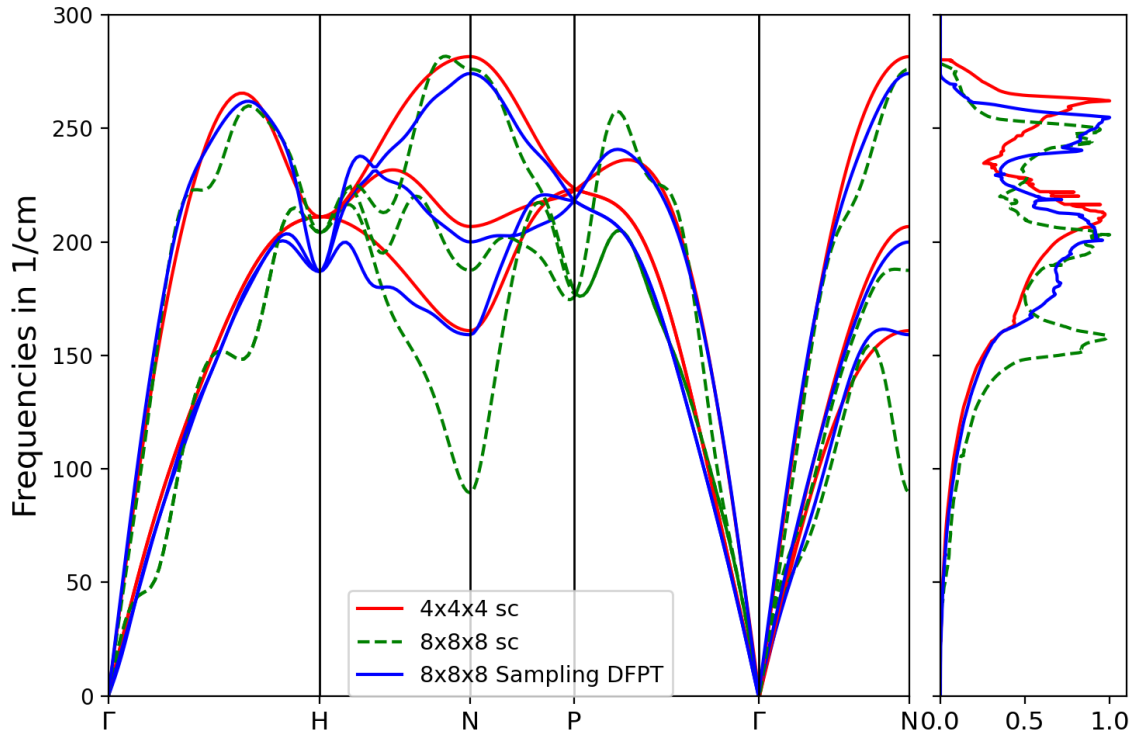



**Figure 7.14:** Phonon dispersion and DOS for bcc Mo. The red curves show the FD $4 \times 4 \times 4$ supercell, the dashed green line $8 \times 8 \times 8$, and the blue curves show the DFPT data.

up by the previous knowledge from the bcc Fe calculations, but is to be taken with a grain of salt when we move to polyatomic crystals of interest, where the DFPT calculation time grows quickly.

Chapter 8

# Phonons in Magnetic Materials

8.1 Phonon Dispersions of Elemental Magnets . . . . . 115
8.2 Interplay of Magnetism and Phonons in Magnetic Lanthanides . . . . . 125

In the zoo of DFT codes, each one has its advantages and disadvantages. Due to the relative simplicity of the basis, big parts of the plane wave formalism are less complicated than the LAPW basis, at the cost of losing access to information about properties near the core like the electric field gradients. This is due to the replacement of the Coulomb singularity and inner-shell electrons by a smooth pseudopotential. The main drawback is, that these pseudopotentials are not universal and new ones can become necessary for specific elements and specific properties under consideration. In the FLAPW formalism, where no such replacement is made, the basis formalism is a lot more involved, but the all-electron nature is fully contained and there is in principle no restriction as to what elements can be described well. At its core, the identity of the FLEUR code is that of a high-precision property calculator for 2D and 3D materials that contain complex magnetism. Electrons for both spins are explicitly treated in the KS equations for any collinear calculation and advanced features like non-collinear magnetism, spin-orbit interaction, and spin spirals [205] are available to properly describe a multitude of different magnetic configurations. As the adaptation of these more involved capabilities to the DFPT formalism is beyond the scope of this work, the investigations in this chapter are limited to collinear ferro- (FM) and antiferromagnets (AFM).

## 8.1 Phonon Dispersions of Elemental Magnets

In section 6.3 and chapter 7, we investigated the phonon dispersions of the elemental FM hcp Co and bcc Fe with both the FD and the DFPT implementation. The results showed good agreement between both methods, but there was no further investigation into the ramifications of the magnetic structure for the phononic one. *I.e.*, there was no investigation as to what influence the FM nature has on the dispersion and whether an AFM setup, which is optimized to a different lattice constant, shows significant differences. For this we first did an EOS run for the bcc Fe and hcp Co systems with an AFM setup to find the corresponding ground-state

configuration. The parameters were directly adopted from tables 7.1 and 6.9, aside from the lattice constant that we want to find a new value for. All reciprocal energy cutoffs for the DFPT runs (*cf.* section 5.3) are set to $10^{-5}$ Ha.

bcc Fe

To set up a bcc Fe system that can become AFM, it is advantageous to set it up as a simple cubic crystal with a two atom basis. This results in a mapping of the bcc q-vectors onto those of the simple cubic cell, where the six resulting frequencies are either degenerate or represent the modes of two different bcc q-points mapped onto the same simple cubic one. To find the necessary set of sample points, we derived

$$\boldsymbol{q}_{\text{sc}} \overset{!}{=} \boldsymbol{q}_{\text{bcc}} \tag{8.1}$$

$$\Leftrightarrow \boldsymbol{q}_{\text{sc,int}}^T \cdot \underline{B}_{\text{sc}} = \boldsymbol{q}_{\text{bcc,int}}^T \cdot \underline{B}_{\text{bcc}} \tag{8.2}$$

$$\Leftrightarrow \boldsymbol{q}_{\text{sc,int}}^T = \boldsymbol{q}_{\text{bcc,int}}^T \cdot \underline{B}_{\text{bcc}} \underline{B}_{\text{sc}}^{-1} = \boldsymbol{q}_{\text{bcc,int}}^T \cdot \begin{pmatrix} 0 & 1 & 1 \\ 1 & 0 & 1 \\ 1 & 1 & 0 \end{pmatrix}. \tag{8.3}$$

The EOS run shows that bcc Fe is not stable in an AFM configuration with the chosen LDA functional and rather converges to a ground state with no magnetization. Thus, the first comparison we can make is between the FM and nonmagnetic (NM) state. The resulting lattice constant is roughly $5.099\ a_0$, so about $97.7\%$ that of the FM case with a magnetic moment of $2.055\ \mu_B$ per MT sphere. The resulting phonon dispersions are shown in figure 8.1.

The data points from the different cases differ greatly. While the FM shows a fully stable dispersion, several branches of the NM calculation have significantly negative values, *i.e.* imaginary frequencies and thus instabilities. This means the associated phonon eigenvectors do not represent the direction of an atomic oscillation, but rather a direction into which the lattice wants to relax to form a new structure. Looking at the path from $N$ to $\Gamma$ specifically, the values nearly match the positive extent of the dispersion in the FM case. A point to note here, is that the halfway point on this path was very hard to converge in the DFPT run and to make it feasible, the convergence parameter was turned up to $5 \times 10^{-4}\ a_0^{-4}$, which it still took many iterations to fall below. At $N$, the eigenvectors of the soft modes reveal that there are two energetically more preferable structure relaxations, that are degenerate to each other. It amounts to shifting the atoms at $(0, 0, 0)$ and $(1/2, 1/2, 1/2)$ into the direction $\hat{\boldsymbol{e}} = (-\hat{\boldsymbol{e}}_x + \hat{\boldsymbol{e}}_y)/\sqrt{2}$ and $\hat{\boldsymbol{e}} = (+\hat{\boldsymbol{e}}_x - \hat{\boldsymbol{e}}_y)/\sqrt{2}$ respectively with a periodicity of two unit cells. This is tantamount to shifting the $(110)$ planes of the lattice against each other, moving the system towards a close packed structure. This is very nice in a sense, because it is common knowledge that LDA predicts NM fcc Fe to be the ground state of elemental iron [206]. This shortcoming is neatly reproduced by the soft modes in our dispersion.

As we added a second atom to properly describe the different magnetic configurations, the phonon dispersion is modified from the pure bcc lattice in that it shows optical modes from a backfolding of branches or rather more than one bcc q-point that maps to the same one in the simple cubic cell. This is especially visible on the fully symmetric $\Gamma$-$H$ and $H$-$P$ paths. To validate the new setup against the one from chapter 7, we map select paths from figure 7.1 onto the new dispersion, which results in figure 8.2.

The overall agreement of the dotted line and the new samples of DFPT data is very good. A noticeable shortcoming, however is the deviation of the optical mode at the high symmetry

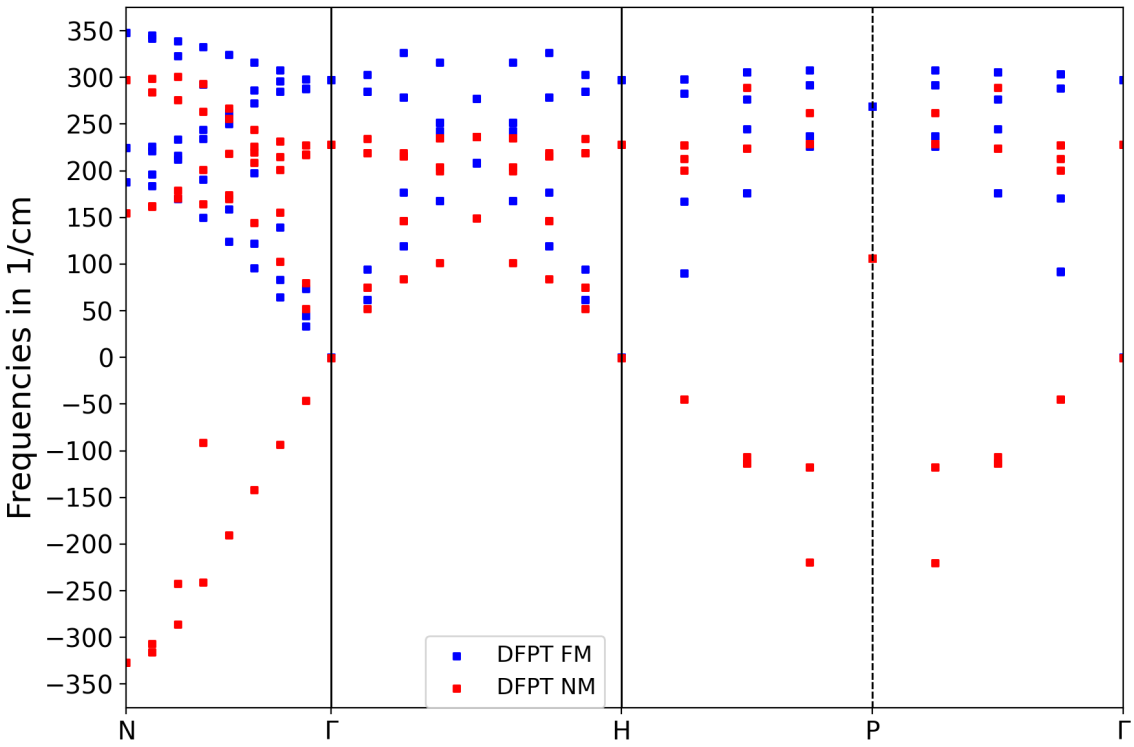



**Figure 8.1:** DFPT phonon dispersions for bcc Fe expressed as a simple cubic system with a two atom basis. The blue data points belong to the FM system and the red points are those of the NM configuration.

point $H$. It is equivalent to the $\Gamma$-point for this setup and thus subject to special terms that only apply there. A similar bump can be seen when looking closely at the $\Gamma$-point of Si in figure 6.4 and emerges again for more materials later on. This indicates a problem with the eigenenergy responses that was previously undetected and is subject to future investigations. Due to the enormous difference between the FM and NM dispersion, we also want to take a look at the resulting phonon DOS shown in figure 8.3. It was again calculated with the tetrahedron method.

As it can be expected from the dispersion, the two curves are drastically different. Instead of showing a two peak structure with a broad one at lower and a sharper one at higher frequencies, the positive energy regime has only one sharp peak, that is embedded in a plateau limited by two smaller sub peaks. The sharp peak neatly corresponds to the maximum of the broad peak from the FM case, while the sharp FM peak is completely missing. The corresponding modes instead move downwards in energy (partially to the negative regime). This means an excitation of the system in the corresponding broad energy range would make it relax into a different state rather than oscillate, which is, again, something that is known for NM bcc iron. We conclude this small discussion and move on to the next elemental ferromagnet, hcp Co.

hcp Co

The AFM hcp Co setup needs no modification from the FM case, as there are already two atoms in the unit cell. We only need to initialize the calculation with inverted state occupations for one of the atoms to generate two magnetic moments that are opposed to each other. As was

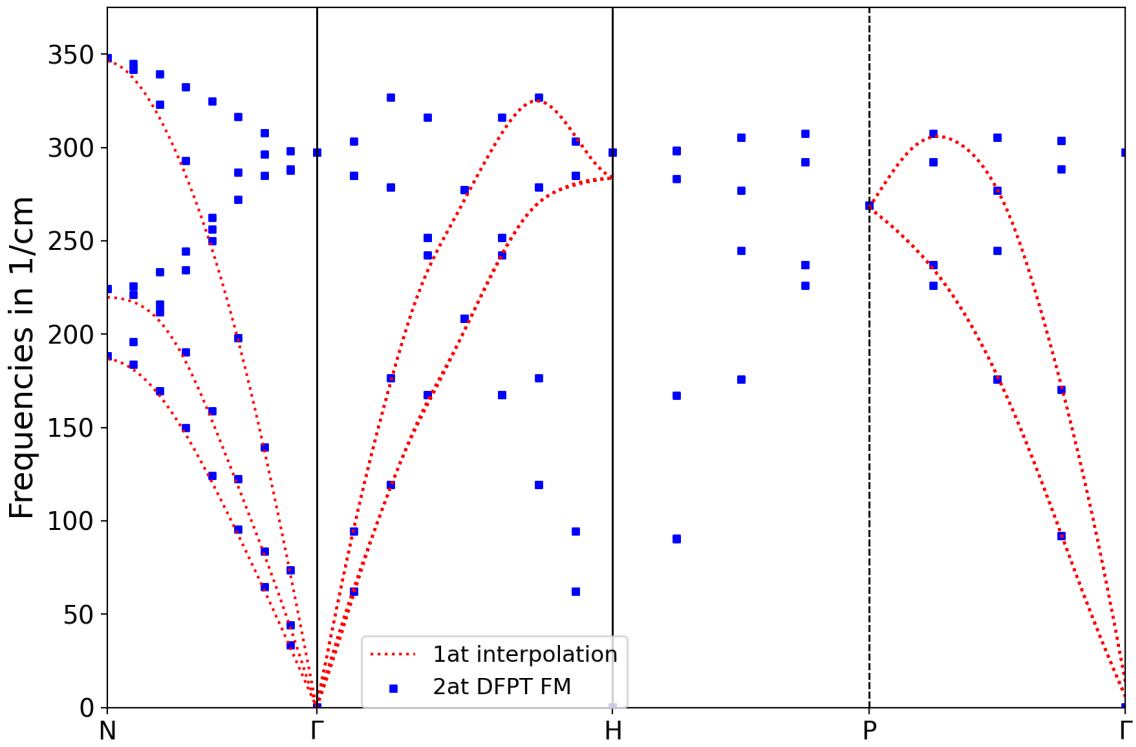



**Figure 8.2:** DFPT phonon dispersions for bcc Fe. The blue data points belongs to the FM system expressed as a simple cubic system with a two atom basis and the red dotted lines correspond to the original bcc crystal with a single atom.

the case for bcc Fe, this setup with the VWN LDA functional yields a nonmagnetic state, which we compare to the FM one again. The lattice constant shrinks to about $98.8\%$ from the FM setup with a magnetic moment of $1.553\ \mu_B$ per MT sphere. Figure 8.4 shows the resulting comparison.

In contrast to bcc Fe, the nonmagnetic state does not exhibit soft modes. Both the FM and NM structure show a stable dispersion with a very similar overall form. The NM data points, however, are generally shifted upwards. There is also a slight change in the form of the lowermost acoustic mode on $M$-$\Gamma$, where the dip towards the high-symmetry point vanishes for the NM setup. As it was the case for two atomic bcc Fe, we initially found an outlier for the $\Gamma$-point, consolidating the notion that there is still something unclear about the eigenenergy response in polyatomic materials. This outlier could be fixed by turning of the correction for occupied-occupied band combinations as described in section 5.3 (more specifically equation (5.24) in the final iteration and equation (5.28)), but this change made no difference for any other material in this chapter.

Regarding the impact of the magnetic structure on the phonon dispersion, we want to further clarify the way in which this is expressed. For this we turn to modified structures in the next section.

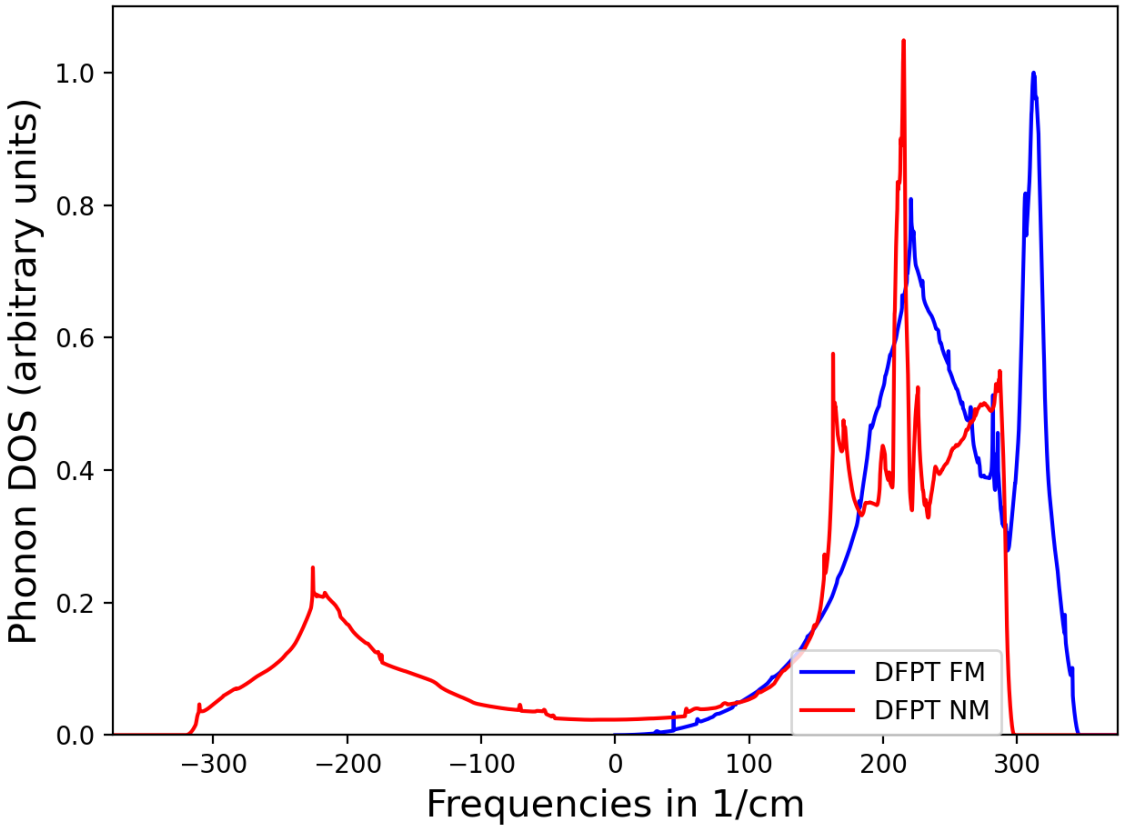



**Figure 8.3:** DFPT phonon DOS for bcc Fe. The blue curve belongs to the FM system and the red one is that of the NM state.

### 8.1.1 Exchanging the Magnetic Textures

Swapping the Magnetic Setups

The previous calculations showed, that bcc Fe and hcp Co both tend to a nonmagnetic state when they are initialized with an AFM electron density. The calculated lattice constants are also different by a slight margin. Considering the differences we noted for the phonon dispersions of the FM and NM cases, the question arises whether they are due to the difference in the magnetic structure or the difference of the crystal lattice itself. The latter seems likely for hcp Co in figure 8.4, where the FM spectrum is overall suppressed in comparison to the NM one. To investigate these relations, we set up another set of cells, where the lattice parameters of the FM and AFM setup are interchanged.

bcc Fe

We compare the spectrum of FM bcc Fe for the lattice constants optimized in an FM and AFM (nonmagnetic) setup. The result is shown in figure 8.5.

Both spectra are stable and very similar. They show the same overall trends and curve shapes, but the FM in the optimized lattice for the nonmagnetic state is generally drawn towards higher frequencies as opposed to the base FM. This is a direct effect of the smaller predicted structure. With the same form of magnetism, a smaller lattice constant directly corresponds to more repulsion of the atoms and thus higher energies and higher oscillation frequencies when they shift against one another. To draw further conclusions, we look at the opposite

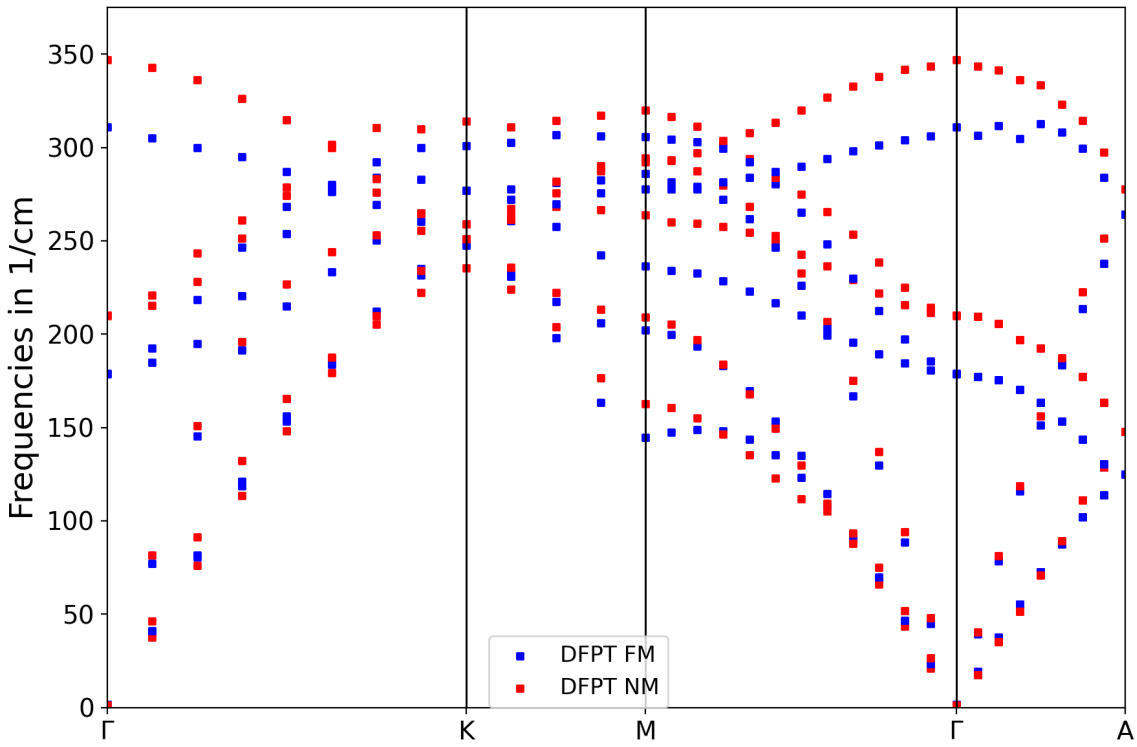



**Figure 8.4:** DFPT phonon dispersions for hcp Co. The blue data points belong to the FM system and the red points are those of the AFM setup that loses its magnetization in the SCF loop.

case of the NM one in the structure of the FM, which results in figure 8.6. The lattice constant in this case is big enough to support an actual AFM ground state, where the magnetization is not lost, so we added the AFM data points as well.

The different NM states shown in the figure are related in the same way as those for the FM were. The spectrum with the smaller lattice constant (NM) tends to have higher absolute frequencies both on the positive and negative side. The general structure, especially with respect to the pronounced soft modes close to $N$, is very similar in both lattices, hinting at preferred structures that are not bcc. The AFM in the FM structure shows the same general curve shape, but as for the original NM, it had convergence problems. In this case not only at a singular q-point but for the full curve aside from the high-symmetry points. The convergence threshold was thus made bigger again. The point $\boldsymbol{q} = (1/4, 1/4, 0)$ (in internal coordinates) itself was not able to converge even with this increased threshold and is thus missing in some branches (*e.g.* the soft mode). The convergence problems are likely due to the fact, that the optimized NM lattice constant lies right in the regime, where the phase change from AFM to NM happens. The EOS run already proved tricky, which translates to the DFPT calculation. The NM configuration with the FM lattice constant did not show this problem, but rather converged nicely (with the same increased cutoff) - the point that is missing in the AFM curve is present here.

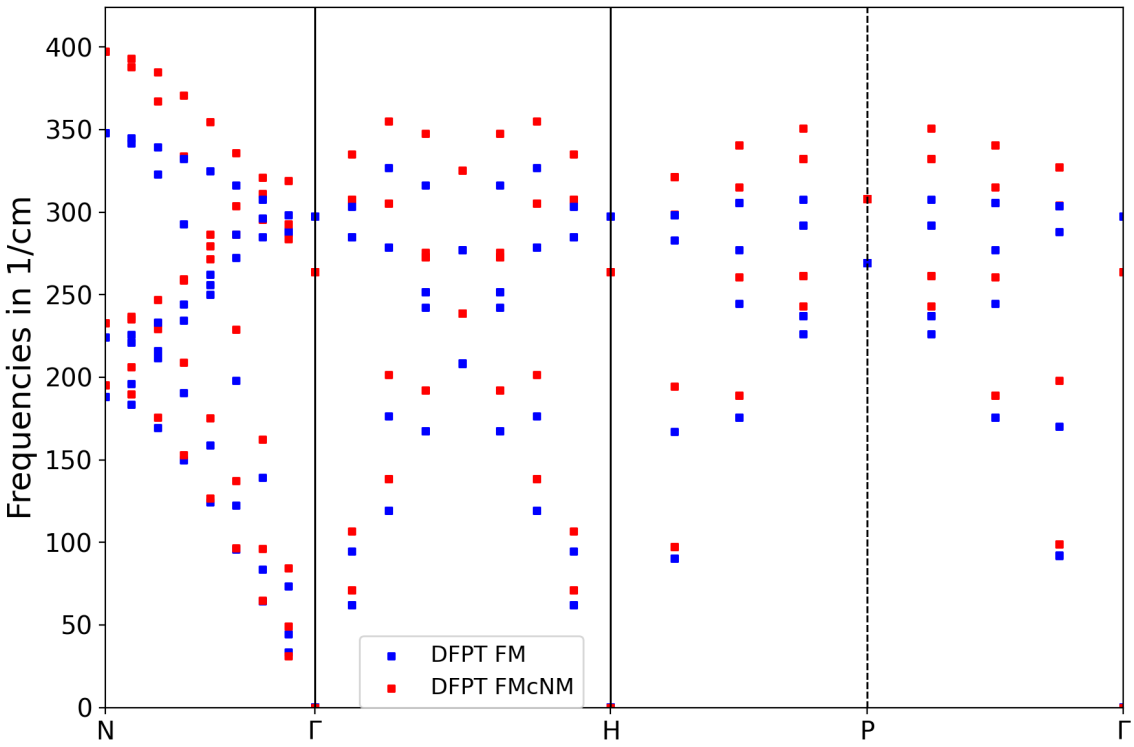



**Figure 8.5:** DFPT phonon dispersions for bcc Fe expressed as a simple cubic system with a two atom basis. The blue data points belong to the FM system with the lattice constant $a = 5.220\ a_0$ and the red points are those of the AFM setup ($a = 5.099\ a_0$) with an FM ground-state density. FMcAFM is a shorthand notation for the FM system in an AFM lattice constant.

Combining the insights from both plots leads us to the following conclusion: While the lattice constant and thus the distances between the atoms have a significant impact on the energy and frequency range, the qualitative behavior is dictated largely by the magnetic configuration.

hcp Co

We look next at the FM and NM hcp Co systems. Figure 8.7 shows the interchanged systems both in an FM ground-state configuration. We observe the same behavior as for the bcc Fe FM. Both dispersions are stable and the FM in the NM structure is scaled upwards as expected with respect to its smaller lattice constant. The relative scaling between the curves is about five to seven percent. The finer features, like the oscillations on the uppermost mode on $\Gamma$-$A$ and the flattening of the lowermost band near the high-symmetry point $M$ on $M$-$\Gamma$, are also identical between the two systems. These features are distinctly different for the NM in figure 8.8.

Again, the curve shapes are virtually identical safe for a scaling factor. The highlighted features from the FM case are not present. On the path that previously showed an oscillation, there is now a rather smoothly decreasing curve and near $M$ the flattening makes way for a more parabolic curve shape. The different magnetic structures in the same lattice, while showing different features, have a very similar extent, in that the maxima of the curves land at roughly 310 $\text{cm}^{-1}$ for the smaller and 345 $\text{cm}^{-1}$ for the larger lattice constant respectively. This reinforces our previous statement, that the main effect of the lattice size is on the overall

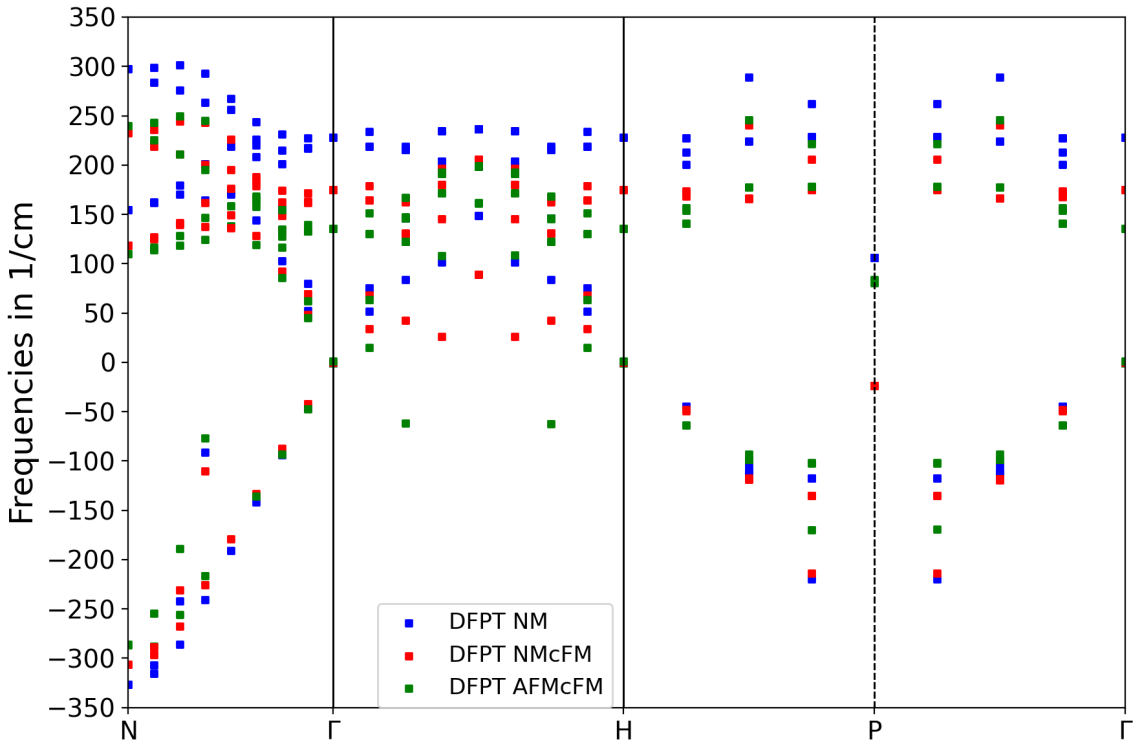



**Figure 8.6:** DFPT phonon dispersions for bcc Fe expressed as a simple cubic system with a two atom basis. The blue data points belong to the NM system with the respective lattice constant ($a = 5.099\ a_0$) and the red points are those of the FM setup ($a = 5.220\ a_0$) with an NM ground-state density. The green data points additionally show the AFM configuration at the FM lattice constant.

scaling of the dispersion, while its exact features are beholden to its magnetic structure. After further belaying this notion, we want to check it for more demanding magnetic materials.

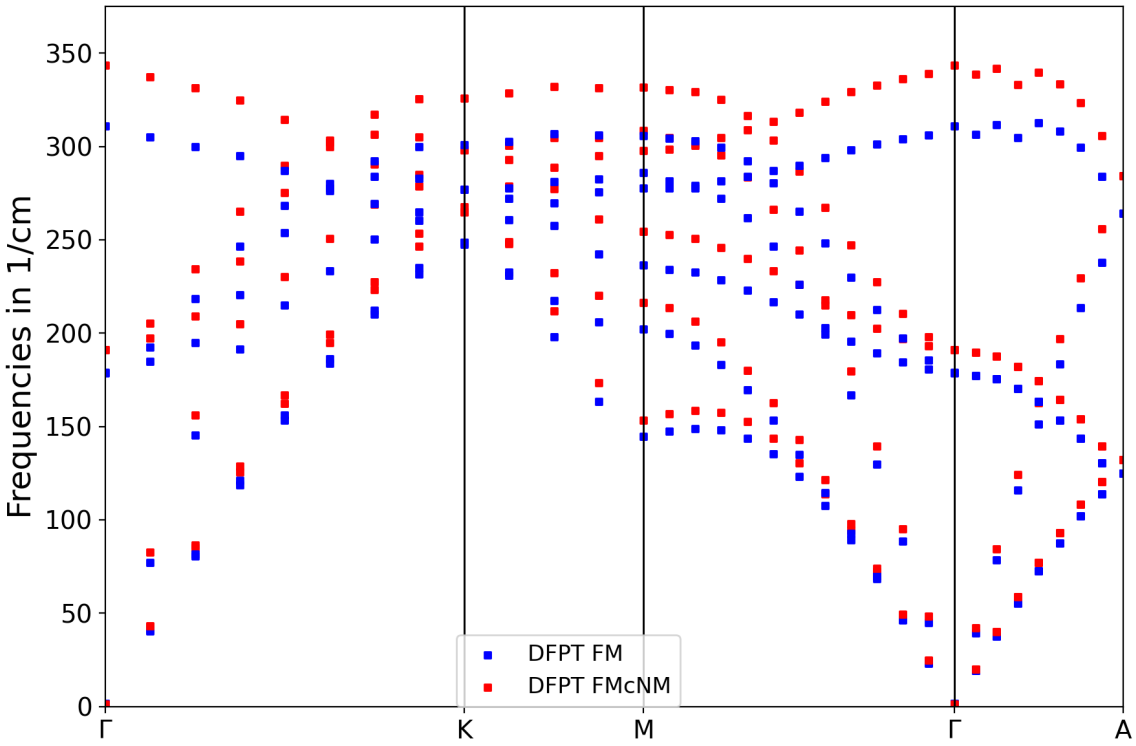



**Figure 8.7:** DFPT phonon dispersions for hcp Co. The blue data points belong to the FM ($a = 4.606\ a_0, c = 7.356\ a_0$) and the red points are those of the NM setup ($a = 4.550\ a_0, c = 7.266\ a_0$) with an FM ground-state density.

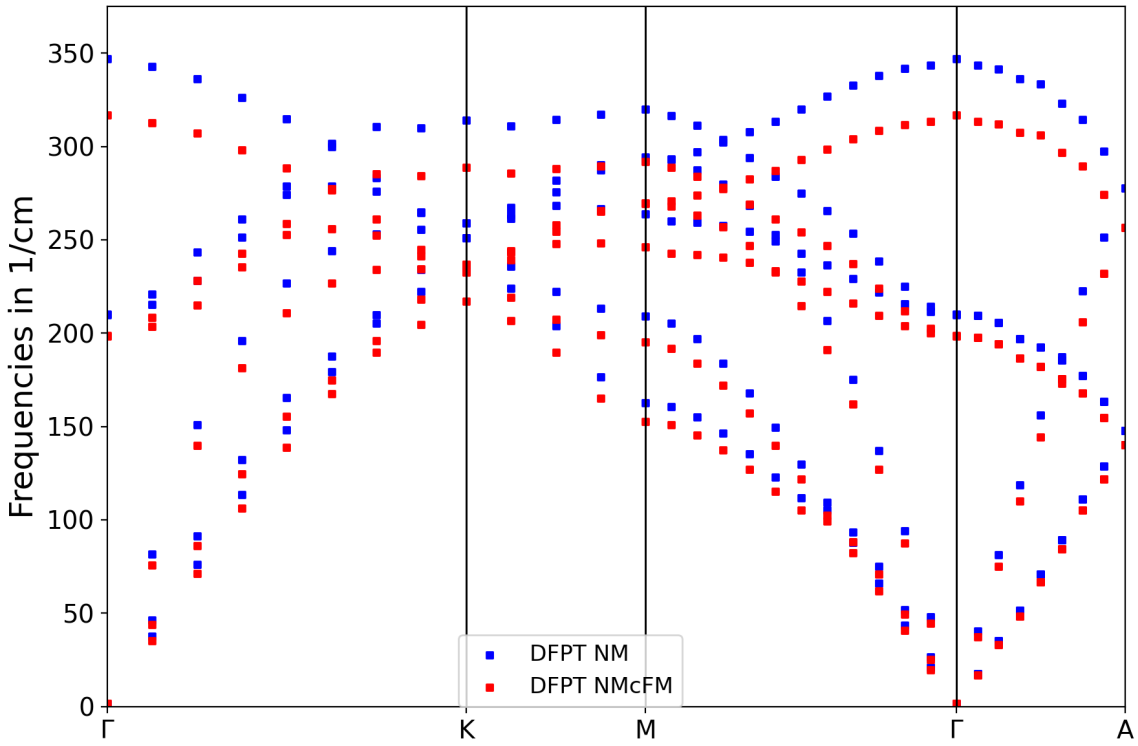



**Figure 8.8:** DFPT phonon dispersions for hcp Co. The blue data points belong to the NM ($a = 4.550\ a_0, c = 7.266\ a_0$) and the red points are those of the FM setup ($a = 4.606\ a_0, c = 7.356\ a_0$) with a NM ground-state density.

## 8.2 Interplay of Magnetism and Phonons in Magnetic Lanthanides

In the introduction to this chapter, we explicitly highlighted the advantages of FLEUR as a tool to cover materials that are difficult to access in pseudopotential calculations. One such class of materials is the lanthanide group. The high-energy $4f$-electrons are hard to describe in such a framework, while high-precision FLAPW codes agree nicely on the resulting structures. This is especially evident in [75], where the WIEN2k [207] code and FLEUR give close to identical results, while plane wave codes that are benchmarked against their average either diverge massively with respect to the calculated structure and EOS or give no data at all, because the required pseudopotentials are not applied. We take this as an opportunity to investigate the phonon dispersions in two of the magnetic lanthanides, for which the amount of resources and previous studies is very sparse. We select two 4f elements with zero orbital moments, Eu and Gd, to avoid the problems of treating the intraatomic Coulomb energy interaction correctly to obtain the proper orbital moments. Eu crystallizes in the bcc structure and GD in the hcp structure. This means we can draw comparisons to the two magnetic materials we already discussed and start with the latter this time.

### 8.2.1 The Phonon Dispersion of hcp Gd

Gd crystallizes in an hcp structure. It has seven $4f$ electrons, which constitutes a half-filled shell. They are characterized by a very localized nature. In past investigations of hcp Gd with FLEUR [208] it was noted, that the LDA overestimates the itinerancy of the $4f$ electrons. Their description as valence electrons leads to a bad description of the band structure with low-lying, near dispersionless minority $4f$ bands and additionally leads to the wrong magnetic ground state, where the AFM configuration is energetically preffered over the FM one. This does not constitute the correct ground-state for hcp Gd. Both problems can be remedied by treating the $4f$ states as fully polarized core electrons as well as a treatment of the system with DFT+U, explicitly taking the highly correlated nature of the system into account. We opt to use the first of these two methods, as DFPT+U is as of yet not implemented in the DFPT branch of FLEUR, and investigate the phonon dispersions of both FM and AFM hcp Gd. Additionally, we benchmark the results against FD curves as we did in several previous calculations. We start with the ferromagnetic structure.

(A)FM Structure and Comparison

For the setup of the hcp Gd system, we stick as closely as possible to the parameter choices provided in [208], given that the FLEUR code has gone through many iterations and changes since then. The most significant differences were the replacement of a second energy window for the $5s$ and $5p$ electrons by local orbitals (which the code does by default at the moment) and the setting of both angular momentum cutoffs to the same value, as none is provided for $\ell_{\text{nonsph}}$ and we set it to a slightly higher value to contain odd number contributions to *e.g.* the density gradient. The parameters are summarized in table 8.1 for an FM structure with a magnetization of $6.473\ \mu_B$ and an AFM structure with $\pm 6.261\ \mu_B$.

The FD results were calculated for a $4 \times 4 \times 4$ supercell, as (just like in the case of hcp Co) the smaller $2 \times 2 \times 2$ one did not yield a sufficiently satisfying fit between the FD and DFPT approach. We begin the discussion of the FM results analogously to those in the previous chapters 6 and 7 and look at the Goldstone modes of hcp Gd. They are summarized in table 8.2.

**Table 8.1:** Overview of the specific calculational parameters of (A)FM hcp Gd. Where the parameters differ for the FM and AFM structure, there are two values given. More parameters in section 6.1.

| $N_{k_{x/y/z}}$ | $\ell_{\max}$ | $\ell_{\max,\text{nsph}}$ | $N_{\text{MT}}$ | $R_{\text{MT}}$ | dx | $a_{\text{latt}}$ | $c_{\text{latt}}$ |
|---|---|---|---|---|---|---|---|
| 24/24/16 | 9 | 9 | 981 | 2.8 $a_0$ | 0.014 | 6.749/6.734 $a_0$ | 10.779/10.754 $a_0$ |

**Table 8.2:** Overview of the acoustic Γ-point modes, $\omega$, in $\text{cm}^{-1}$ for FM hcp Gd. No frequency exceeds an absolute value of $1.4$ $\text{cm}^{-1}$ (or $0.174$ meV | $0.042$ THz, respectively).

| | $\omega_1$ | $\omega_2$ | $\omega_3$ |
|---|---|---|---|
| FD | $-7.15 \times 10^{-2}$ | $-7.15 \times 10^{-2}$ | $-5.45 \times 10^{-2}$ |
| DFPT | $1.14 \times 10^{0}$ | $1.38 \times 10^{0}$ | $1.39 \times 10^{0}$ |

The modes show the largest values in this thesis so far for the DFPT case. The dispersion takes on frequencies up to around 120 $\text{cm}^{-1}$, which makes the deviation of the Goldstone modes a percentile error. While this is worse than the previous materials, it is still sufficiently small for a good comparison to the FD benchmark. It is also way below some of the uncertainties in the only set of experimental Gd phonon dispersion data that we found [209]. We show the FD and DFPT results as well as the experimental data in figure 8.9.

The overall shape of the curve is very reminiscent of that in the case of hcp Co. This is not surprising, as we also had very similar dispersion across all fcc materials we studied and the lattice structure has the most significant impact on the ways the atoms can oscillate. The match between FD and DFPT is good, broadly speaking. The main differences occur at the high-symmetry points, for example the values at $K$ do not align optimally. Furthermore, there is a significant deviation of the DFPT data at $\Gamma$ both with respect to the FD benchmark and the trend that is indicated by the other DFPT samples in its vicinity. We explicitly pointed out a similar deviation for bcc Fe in a two atom lattice. This points to a leftover problem with the code or missing correction terms for the $\Gamma$ point explicitly. As was mentioned before, similar outliers appeared in hcp Co but could be fixed in that case (*cf.* section 8.1). The same fix does not work here, unfortunately. Comparing both the FD and DFPT results to the experimental data obtained from [209], we do not get all too good of an agreement. The general shape of our curves towards $M$ matches that of the experimental data points, but the values are significantly too large. This can be attributed to the fact, that the optimized lattice constant for our setup is around $98.4\%$ of the experimental one, which is given in the literature as $6.858$ $a_0$ [210] (close to the result of $98.6\%$ provided in [208]). Better results can be expected, when the restrictions to the ground state calculation are lifted and a setup that can accurately reproduce the experimental lattice constant is used. It is a little bit bigger than the provided LDA setup predicts, which would thus shift the whole spectrum slightly downwards and thus right towards the experimental data points we show. As a second point of reference we found an hcp Gd dispersion in[211], which was produced from atomic spin dynamics simulations. The curve shape and general frequency magnitude (when converted to THz) are similar, but the degeneracies at the high-symmetry points differ and further similarities are not really given. For now we postpone further investigations and turn to an analogous study of the AFM

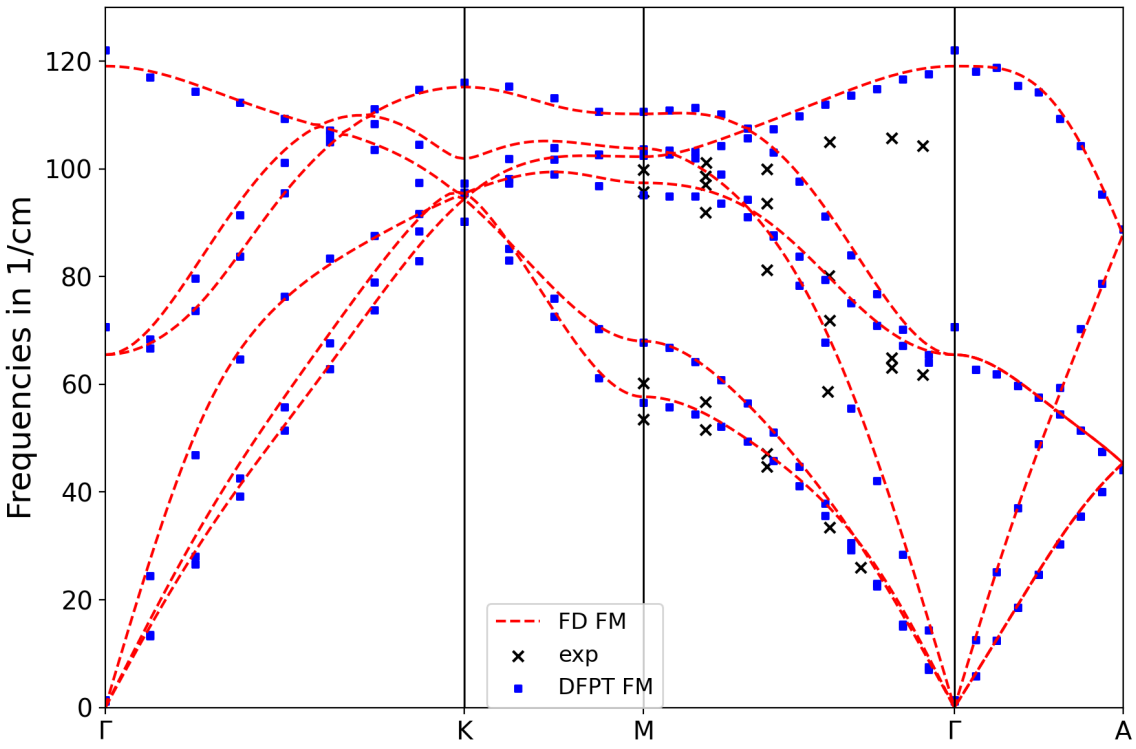



**Figure 8.9:** Phonon dispersions for FM hcp Gd. The blue data points belong to the DFPT data and the red dashed lines represent the FD benchmark. The black crosses are from a set of experimental data in [209].

hcp Gd setup to highlight possible differences. The Goldstone mode data is summarized in table 8.3.

**Table 8.3:** Overview of the acoustic Γ-point modes, $\omega$, in $\mathrm{cm}^{-1}$ for AFM hcp Gd. No frequency exceeds an absolute value of $2.0\ \mathrm{cm}^{-1}$ (or $0.248$ meV | $0.060$ THz, respectively).

| | $\omega_1$ | $\omega_2$ | $\omega_3$ |
|---|---|---|---|
| FD | $-3.20 \times 10^{-6}$ | $8.31 \times 10^{-2}$ | $8.31 \times 10^{-2}$ |
| DFPT | $-1.90 \times 10^{0}$ | $-1.90 \times 10^{0}$ | $1.21 \times 10^{0}$ |

The values are of the same magnitude as in the FM case. Once again, we find the FD frequencies orders of magnitude smaller. This is in line with the previously compared materials. We also find the same 2+1 degeneracy as in hcp Co and the FM hcp Gd, *e.g.* the minuscule first frequency for the FD case, that is four orders of magnitude smaller than the other two. Such effects are numerical artifacts produced by the FD formalism and are not found to be consistent. The full dispersion is shown in figure 8.10.

Both the strengths and shortcomings of the dispersion closely match those of the FM case. We note the same general quality and the pronounced outliers at $\Gamma$. Curiously, the values at $K$ match more closely, but conversely there is a decrease in quality for the lower optical modes near $\Gamma$, even aside from the outlier. We want to study the similarities and differences in the

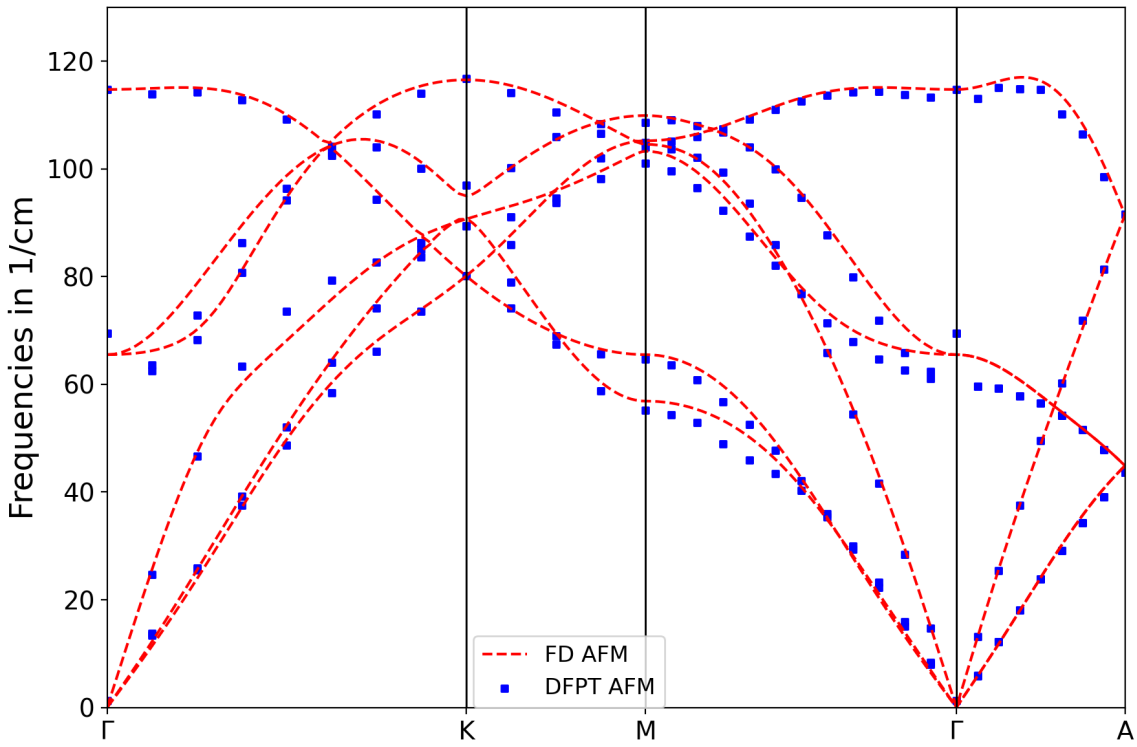



**Figure 8.10:** Phonon dispersions for AFM hcp Gd. The blue data points belong to the DFPT data and the red dashed lines represent the FD benchmark.

spectra more in-depth by directly plotting the DFPT data of both magnetic configurations against one another in figure 8.11.

The aforementioned points of comparison are clearly visible in the plot. It is not directly obvious, how the differences come to pass, considering the slightly different lattice constants and different magnetism. Previously, we linked the curves extent to the first and the fine structure to the second effect.

Swapping the Structures

By again swapping the optimized structure from the FD case with that of the AFM and vice versa while retaining the respective form of magnetism, we can quantify such considerations. This is actually easier here than for the simpler magnets bcc Fe and hcp Co, sunce in this case both magnetic structures are stable at both optimized lattice constants. For the resulting FM setups, the dispersion curves are shown in figure 8.12.

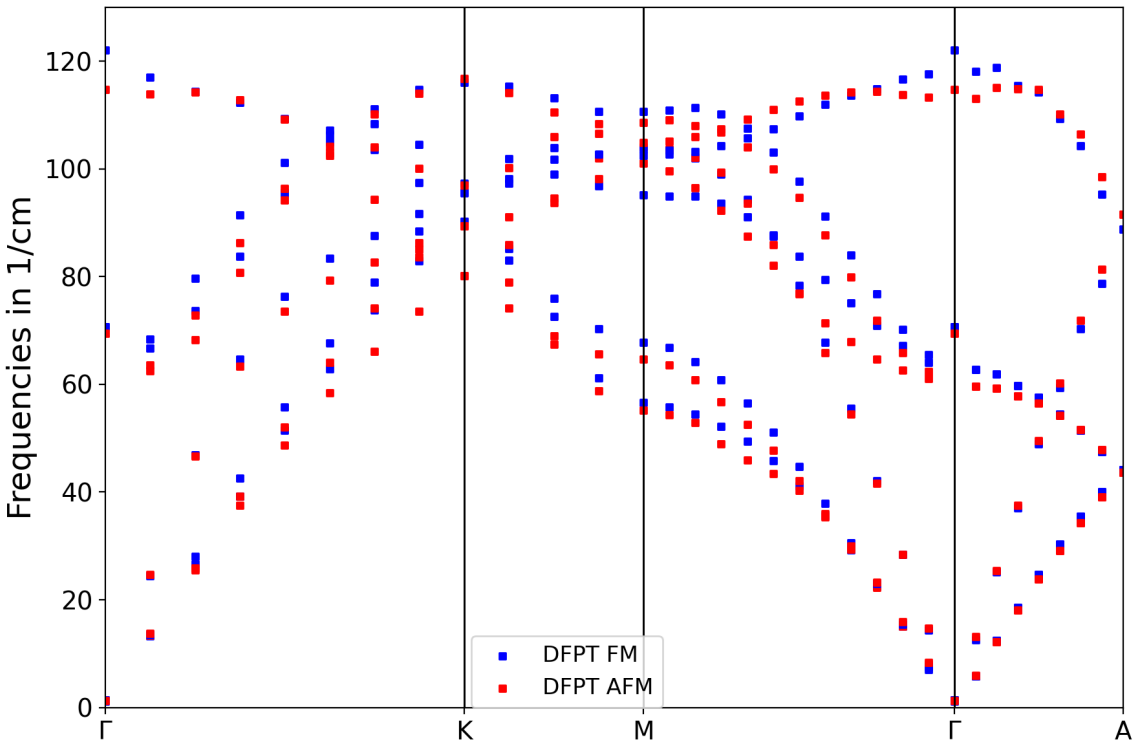



**Figure 8.11:** DFPT phonon dispersions for hcp Gd. The blue data points belong to the FM and the red points are those of the AFM.

The resulting dispersion curves are practically identical up to a small scaling factor. As expected from the previous structures, the slightly larger structure (FM) gives slightly smaller frequencies on the full range of q-points. There is no point at which the fine structures diverge, which we want to validate for the AFM structures as well in figure 8.13.

The same observations from the previous plot hold for this one as well. In conclusion, the marginal difference between the FM and AFM lattice constant does not produce a significant impact on the phonon dispersion, while the difference in magnetic coupling does lead to visible differences in the curve shape on several of the high-symmetry paths. This is likely due to the large magnetic moments that are either aligned or directly opposite to each other.

In this case, the effects can be separated cleanly, which motivates further investigations of the interplay between the magnetic structure and phonon physics in the future. In the case of hcp Gd, such studies should be postponed to a point, when more powerful functional classes like the GGA have been adapted to the FLEUR DFPT framework or, even more optimally, DFPT+U is implemented. Once this is the case, studies of thin Gd films and surfaces [212], compounds [213], and alloys [214] should also be under consideration. In the latter two cases, an implementation of the non-analytical term correction can prove necessary as well. For now, we want to concern ourselves with another material from the lanthanide line, that is right next to hcp Gd in the periodic table.

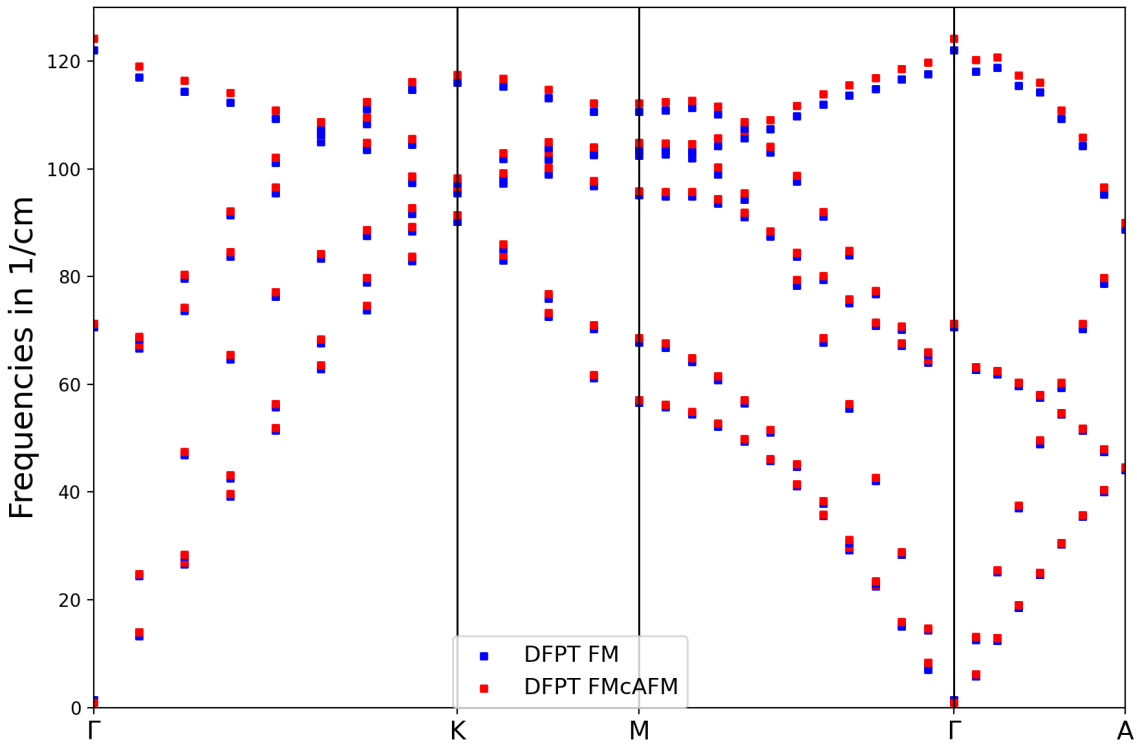



**Figure 8.12:** DFPT phonon dispersions for hcp Gd. The blue data points belong to the FM and the red points are those of the AFM setup with an FM ground-state density.

### 8.2.2 The Phonon Dispersion of Collinear bcc Eu

(A)FM Structure and Comparison

Bcc Eu is another rare-earth metal with a half-filled $4f$ shell. It's electron configuration ($[\mathrm{Xe}]4f^7 6s^2$) is distinct from that in hcp Gd ($[\mathrm{Xe}]4f^7 5d^1 6s^2$)in that it does not have the single $5d$ electron. Its equilibrium lattice constant at room temperature is around $8.659\ a_0$ [215] and it forms a spin-spiral ground-state instead of a simple collinear FM or AFM. In the scope of this work, we nonetheless treat it as such. As opposed to hcp Gd, we do not manipulate the default electronic structure by putting the $4f$ electrons into the core and instead take the system as is. The parameters are taken from a set of preliminary considerations done for a publication by Turek *et al.* [216]. The optimized FM structure exhibits a magnetization of $6.773\ \mu_B$ at about $89.7\%$ of the experimental lattice constant and the AFM $\pm 6.710\ \mu_B$ at $89.9\%$. So in this case, the FM is bound more strongly than the AFM and both results agree well with what is noted in reference [216]. The parameters used are found in table 8.4.

**Table 8.4:** Overview of the specific calculational parameters of (A)FM bcc Eu. Where the parameters differ for the FM and AFM structure, there are two values given. More parameters in section 6.1.

| $N_{k_{x/y/z}}$ | $\ell_{\max}$ | $\ell_{\max,\mathrm{nsph}}$ | $N_{\mathrm{MT}}$ | $R_{\mathrm{MT}}$ | dx | $a_{\mathrm{latt}}$ |
|---|---|---|---|---|---|---|
| 16/16/16 | 11 | 8 | 827 | 2.5 $a_0$ | 0.016 | 7.770/7.789 $a_0$ |

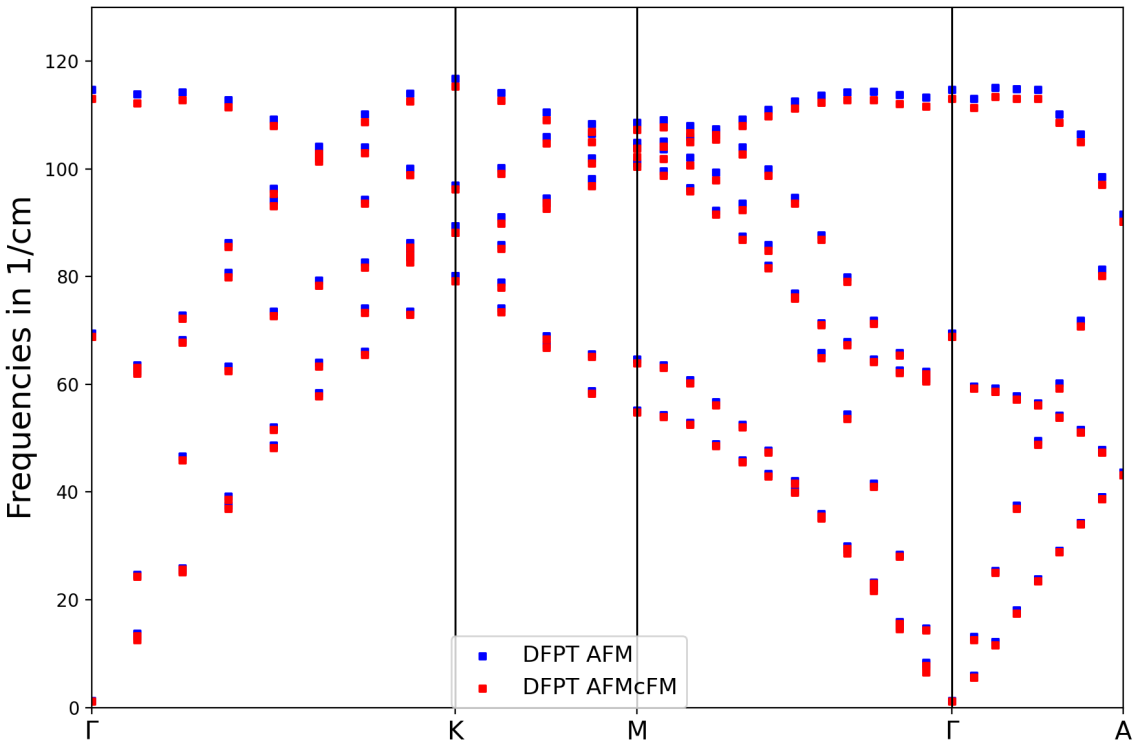



**Figure 8.13:** DFPT phonon dispersions for hcp Gd. The blue data points belong to the AFM and the red points are those of the FM setup with an AFM ground-state density.

For these optimized structures of bcc Eu, the FM is energetically slightly preferable with an energy difference of $-3.69$ meV. We want to validate the insights about the magnetic effects in the phonon dispersion from the previous materials and thus provide a comparison of the FM and AFM results in figure 8.14. We forego the FD benchmark and, since Eu is a very efficient neutron absorber (atomic mass of $151.97\ u$ vs $157.25\ u$ in hcp Gd) that prohibits neutron scattering measurements, also did not find any experimental data to show.

Considering the frequency range and curve shape, the dispersion is about what we would expect. Due to the larger in-plane lattice constant than in hcp Gd, the modes are overall softer. Additionally, the shape is reminiscent of bcc Fe due to the same type of lattice. The differences of the FM and AFM dispersion emerge in specific sections of the curve, for example in the transversal acoustic modes of the $N$-$\Gamma$ path and $H$-$\Gamma$. Other parts only show marginal differences that are likely linked to the lattice constant once more.

Swapping the Structures

By now we have a standard procedure to validate such claims. So we once again swap the structures of both magnets and look at a purely FM and AFM comparison respectively. The former is found in figure 8.15.

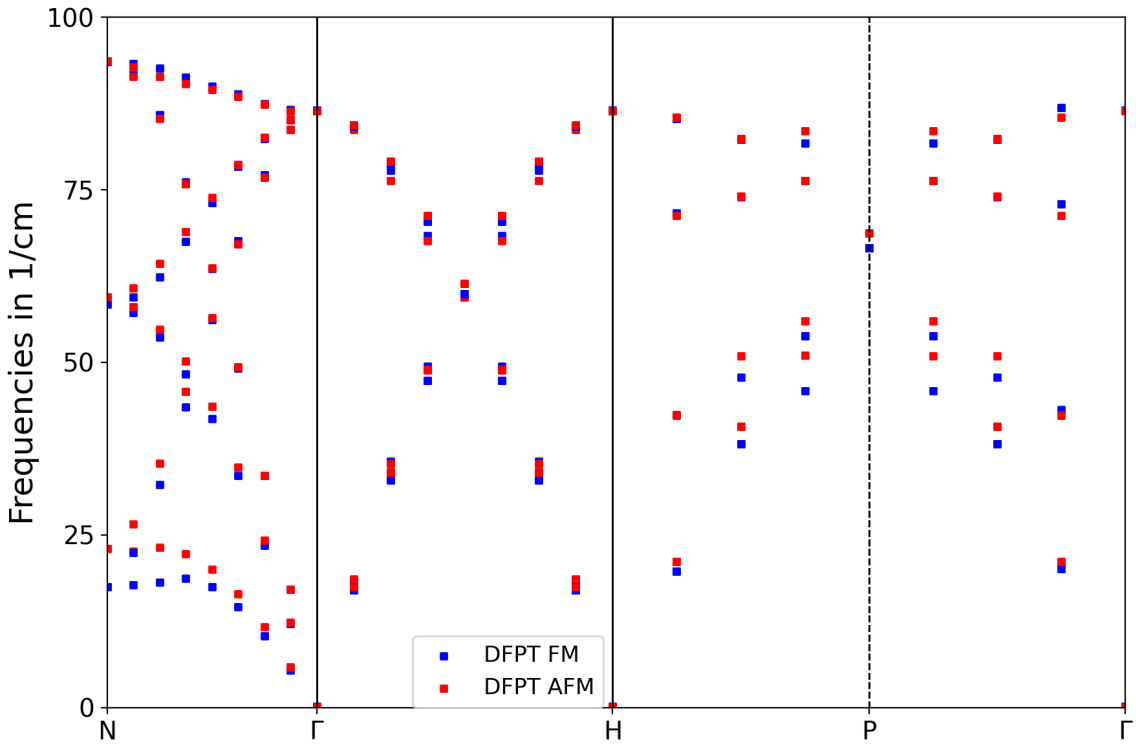



**Figure 8.14:** DFPT phonon dispersions for bcc Eu expressed as a simple cubic system with a two atom basis. The blue data points belong to the FM and the red points are those of the AFM.

The curves for both lattice constants are nearly indistinguishable. There are no divergent paths and only minuscule deviations at specific points, which can be due to minimally different convergence results at the low frequencies the spectrum exhibits. There is nothing more of note to say, so we move on to the AFM in figure 8.16.

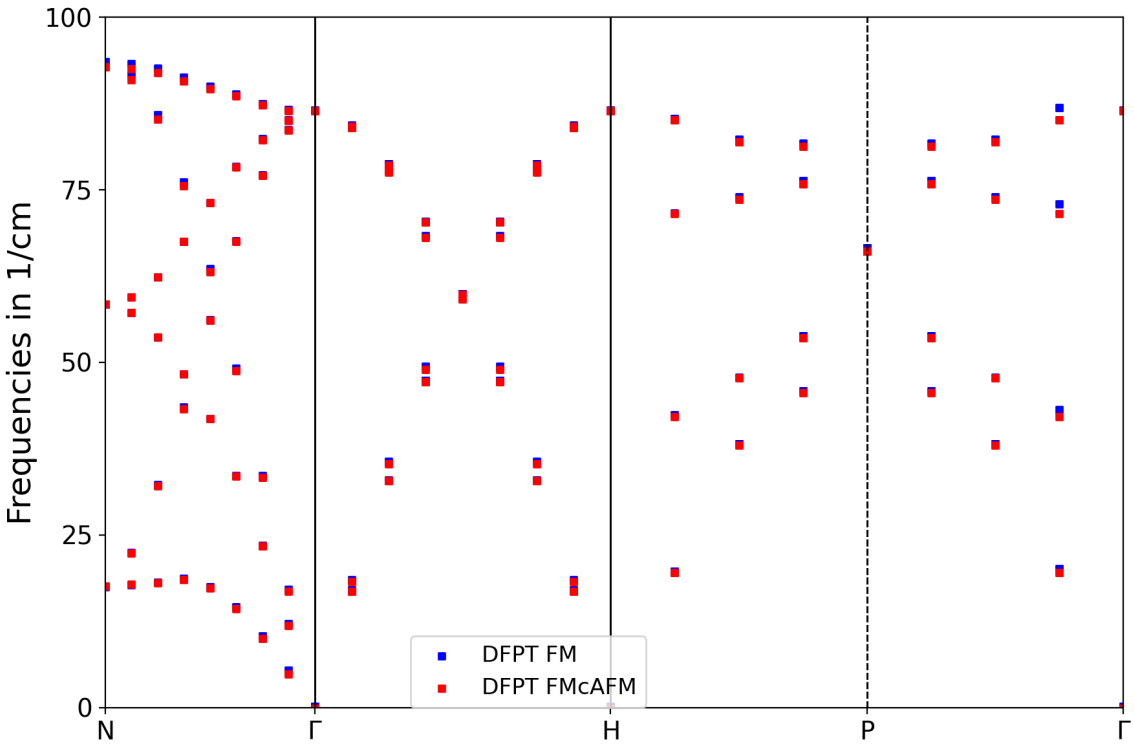



**Figure 8.15:** DFPT phonon dispersions for bcc Eu expressed as a simple cubic system with a two atom basis. The blue data points belong to the FM and the red points are those of the AFM setup with an FM ground-state density.

Here, the near perfect match between both curves is even more evident. One thing to note about all curves of bcc Eu, is that the outlier on the $\Gamma$ point that was present for the other magnetic metals can also be seen here, where the optical mode would match continuously to the branches to its left and right for a slightly smaller value.

Outlook

This concludes our discussion of bcc Eu as well as that of the magnetic materials overall. In hcp Gd, we noted that it will be worthwhile to revisit the material once more powerful xc functionals for DFPT or DFPT+U are available in FLEUR. In this specific material, it will be even more instructive to return once the implementations of spin-spirals and DFPT have been adapted to one another to study the actual ground state that bcc Eu assumes. Moving away from the elemental structure, there have been investigations into EuO [217], that exhibits strong electron-phonon coupling and will thus be of interest once the NAC is implemented. As a summary to this chapter, we were able to both show and distinguish the impact that the lattice constant and the magnetic configuration have on the phonon dispersion of both two standard elemental magnets and two rare-earth ones. Though this was done on a crude level of comparing FM and AFM, this motivates further research into the nature of spin-phonon and phonon-magnon coupling as the method is developed further.

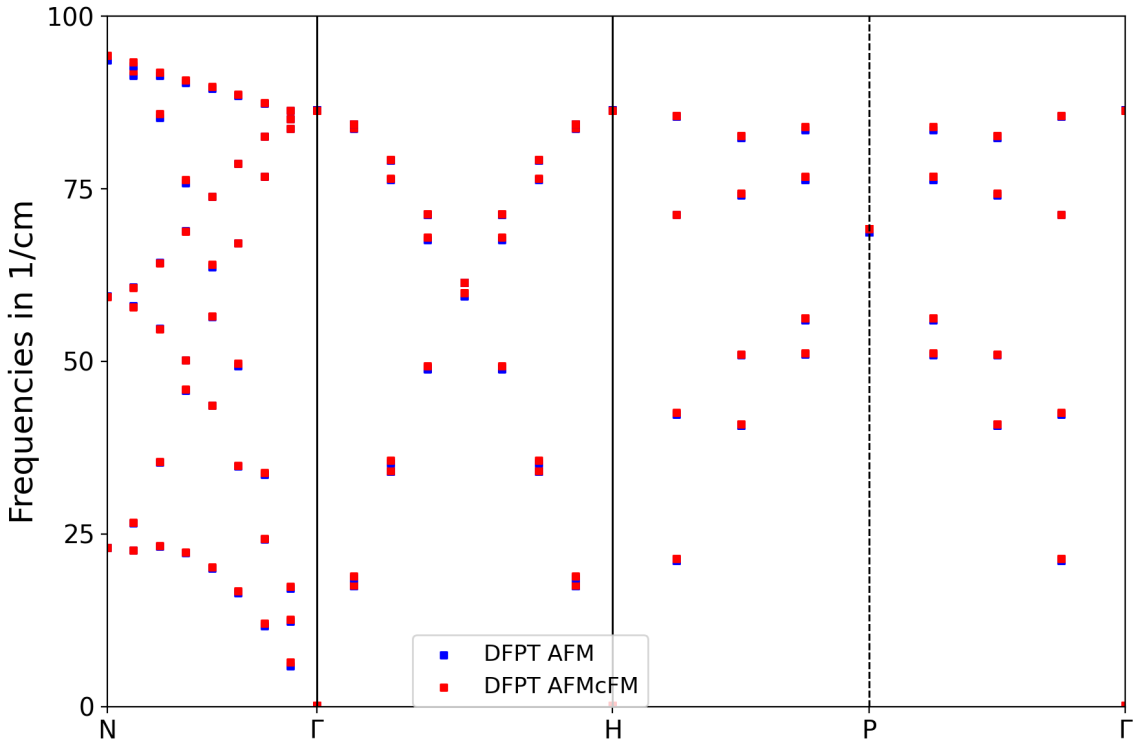



**Figure 8.16:** DFPT phonon dispersions for bcc Eu expressed as a simple cubic system with a two atom basis. The blue data points belong to the AFM and the red points are those of the FM setup with an AFM ground-state density.

Chapter 9

# Phonons in 2D Materials

9.1 Pseudo 2D Systems . . . . . 136
9.2 2D Film DFPT in the FLAPW Method . . . . . 140

As we already highlighted in the introduction, the phononic properties of 2D materials, like unsupported monolayers or multilayered systems, have been of particular interest in recent years. One of the most relevant subclasses in this context are van-der-Waals (vdW) materials, that are bound in a layered structure by in-plane covalent effects and short-range interlayer vdW forces. The description of such materials in DFT is usually done by bulk calculations employing an electronic structure code with periodic boundary conditions and the supercell concept, also known as the repeated slab model. For monolayer systems, this amounts to setups with large lattice spacings in the out-of-plane direction. For layered systems, there exist implementations of different types of vdW interactions, which are also partially extended to the DFPT formalism [218, 219]. While the base implementation is available in the FLEUR code, the DFPT terms are not yet available. The first part of this chapter shows first results for two selected materials in this repeated slab approach.

Film Systems

Aside from the bulk approach, the FLEUR code offers an alternative approach to treat monolayers or thin film systems. It goes back to the film mode of the LAPW method [220], in which a 2D slab of periodic atoms is perfectly embedded in semi-infinite vacua. Running the code in this mode changes the LAPW basis from one periodic in 3 dimensions to one, where only the in-plane directions are described by the periodic plane waves and the out-of-plane direction (usually denoted by $z$) takes on a different, non-periodic form with a slab (similar to the interstitial region of the bulk) embedded into a vacuum above and below that are treated in real space similar to the functions in the muffin-tin spheres. The film mode is of renewed importance due to the surge of interest in 2D materials, particularly graphene and related materials like silicene and transition metal dichalcogenides (TMDCs). In contrast to a setup that embeds a 2D film into a bulk by a supercell with large interlayer distances, the 2D setup is computationally less demanding, as the large 3D unit cell mandates a large number of reciprocal lattice vectors and therefore a large number of basis functions. An extension of the DFPT formalism to this film mode is currently in development and initial results as well as ongoing problems are highlighted in the second part of this chapter.

## 9.1 Pseudo 2D Systems

$VSe_2$ $VSe_2$ is a transition metal dichalcogenide, that crystallizes in a layered 1T structure (a nice visualization of which can be found in reference [221]) with 3 atoms in the unit cell. It was shown to have metallic behavior with a charge density wave ground-state at low temperatures [222–224]. It also exhibits strong ferromagnetism as a monolayer on van der Waals substrate materials [225] at room temperature. This is the magnetic configuration we choose for our studies in this section. Since the 1T-structure poses the most challenging setup for our DFPT implementation yet, it gives us a good opportunity to examine its accuracy for a new upper threshold. The calculation is set up with a hexagonal unit cell with an angle of $120\,\mathrm{deg}$ between the in-plane unit vectors. The V atom sits at the origin and the Se atoms at positions $(1/3, -1/3, z_{Se})$ and $(-1/3, 1/3, -z_{Se})$ with respect to the lattice vectors. The z-position of the inversion symmetric Se atoms is a free parameter of the system that needs to be optimized alongside the lattice constants of the crystal. For this we did a simple force relaxation. The optimization was done in the following order: First, the in-plane lattice constant was optimized, then the interlayer distance and lastly the Se position. The remaining calculation parameters of interest are captured in table 9.1, aside from those that are the same as in all the calculations in chapter 6.

**Table 9.1:** Overview of the specific calculational parameters of $VSe_2$. For the atomic parameters, there are two values given representing the V/Se atoms respectively where they differ. More parameters in section 6.1.

| $N_{k_{x/y/z}}$ | $\ell_{\max}$ | $\ell_{\max,\mathrm{nsph}}$ | $N_{\mathrm{MT}}$ | $R_{\mathrm{MT}}$ | dx | $a_{\mathrm{latt}}$ | $c_{\mathrm{latt}}$ |
|---|---|---|---|---|---|---|---|
| 24/24/16 | 10 | 8 | 661 | 2.19 $a_0$ | 0.018/0.019 | 6.328 $a_0$ | 11.595 $a_0$ |

We find a parameter of $z_{Se} = 0.25657$. With this parameter and the optimized lattice constants in hand, we can once again perform FD and DFPT runs in the same fashion as we did in chapter 6. The FD calculation was set up with a set of three $2 \times 2 \times 2$ supercells. This is the minimum amount required to interpolate the phonon dispersion of the three atom system and mandates three calculations of 24 atom lattices. For the DFPT results, we sampled the same high-symmetry paths as for hcp Co and hcp Gd, whereby we did not use an interpolation, as it would require a large amount of q-points, while the k-point density set specified by the grid already provides us with 32 sample points for evaluation.

We begin the discussion of the results with the Goldstone modes shown in table 9.2.

**Table 9.2:** Overview of the acoustic $\Gamma$-point modes, $\omega$, in $\mathrm{cm}^{-1}$ for $VSe_2$. No frequency exceeds an absolute value of $3.9\ \mathrm{cm}^{-1}$ (or $0.484$ meV | $0.117$ THz, respectively).

| | $\omega_1$ | $\omega_2$ | $\omega_3$ |
|---|---|---|---|
| FD | $-3.38 \times 10^{-2}$ | $-3.38 \times 10^{-2}$ | $-3.16 \times 10^{-2}$ |
| DFPT | $-8.90 \times 10^{-1}$ | $3.85 \times 10^{0}$ | $3.85 \times 10^{0}$ |

While the residual frequencies of the DFPT $\Gamma$-point acoustic modes mark the highest values we have encountered yet (likely due to the increased complexity of the unit cell), they are still on the scale of $1\ \mathrm{cm}^{-1}$, making for only percentile deviations in a dispersion with values two

orders of magnitude larger. A more pressing matter are the optical modes at the same q-point, summarized in table 9.3.

**Table 9.3:** Overview of the optical Γ-point modes, $\omega$, in $cm^{-1}$ for $VSe_2$.

| | $\omega_4$ | $\omega_5$ | $\omega_6$ | $\omega_7$ | $\omega_8$ | $\omega_9$ |
|---|---|---|---|---|---|---|
| FD | 143.91 | 143.91 | 193.24 | 193.24 | 214.01 | 338.29 |
| DFPT | 139.79 | 139.79 | 185.61 | 185.61 | 557.87 | 331.68 |

The overall agreement between both approaches is acceptable, but there is a significant discrepancy for the $\omega_8$ mode. The DFPT result is more than twice as high compared to the FD case and far exceeds the other values. Such a single deviation is unlike anything we have encountered before, *e.g.* in SiC where the LO-TO splitting cannot be reproduced at the $\Gamma$-point due to the missing correction terms from the electric field responses. We turn to the full dispersion curve in figure 9.1 to see, whether we deal with an isolated problem or a deficiency of a full band.

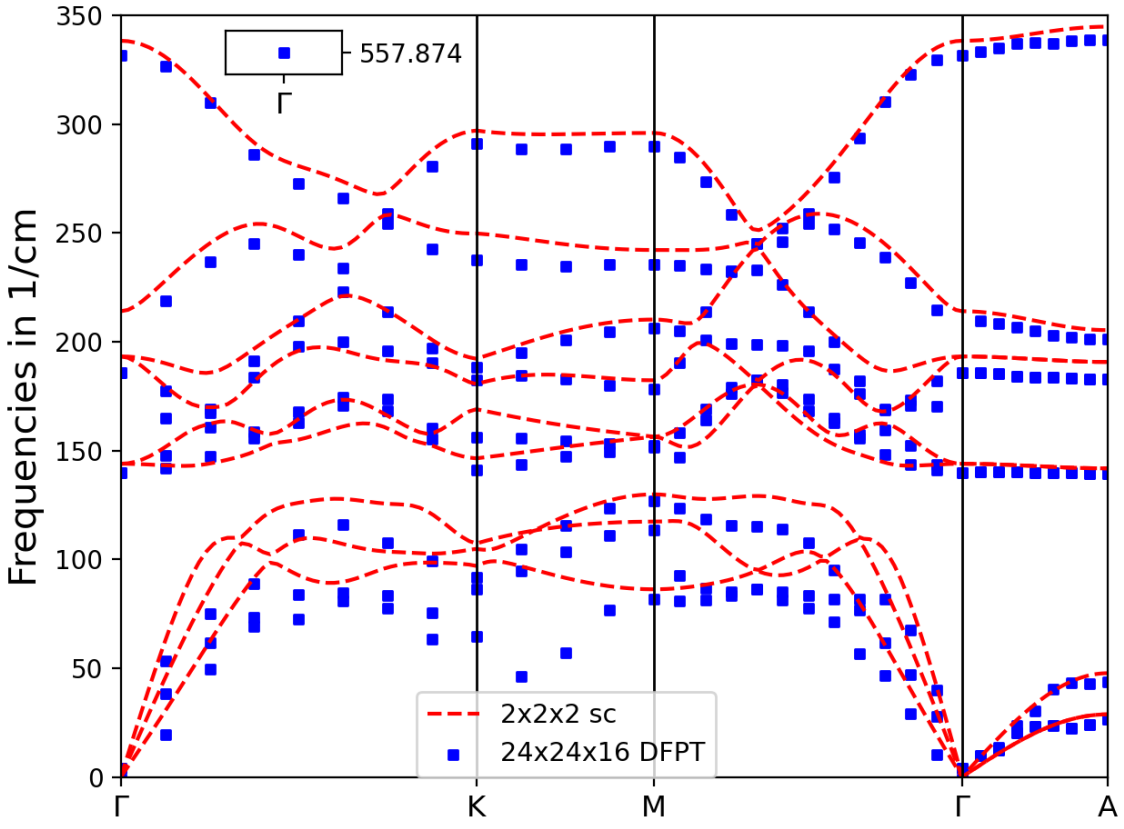



**Figure 9.1:** Phonon dispersion for $VSe_2$. The red curve shows the FD $2 \times 2 \times 2$ supercell and the blue dots show the DFPT data. A specific $\Gamma$-point outlier far outside the range of the other values is visualized as an inlay.

The plot shows that the discrepancy is an outlier that only affects the $\Gamma$-point. Otherwise, the curves continue on smoothly and agree well enough with the small supercell FD result for the optical branches. The acoustic branches do not agree that well and it stands to reason, that the calculation needs more refinement with respect to its parameters to improve the fit. But the problem of the isolated stray mode is more blatant. Since $VSe_2$ is a metal and the FD curve shows proper splitting of the optical modes, the missed mode cannot be chalked up to the same mechanisms as in SiC. Instead it stands to reason, that there is a problem with the calculation of $\boldsymbol{q} = \mathbf{0}$-specific terms like the eigenenergy or occupation number responses, that has not yet become as prevalent. After all, less pronounced bumps on an otherwise smooth curve could also be seen for the materials in chapter 8. We want to isolate the possibility of both options, a discrepancy in either the energies or occupations, by investigating a similar material without metallic character.

$MoSe_2$

Replacing the 1T unit cell structure by the related 1H [221], that forms trigonal prisms of Se around the transition metal instead of octahedrons, switching the V atom out for one of Mo, and looking at an unsupported monolayer in a large supercell repeated in z-direction gives us $MoSe_2$. The new material is a semiconductor and sees increasing interest in the wake of 2D material research driven by the established discoveries *e.g.* in graphene. It is studied alongside other TMD monolayers for a wide range of applications [50] especially due to the broad spectrum of band gaps that can be found in this material class, whereas graphene is a conductor. For our purposes $MoSe_2$ marks a suitable test case, as it is distinguished from $VSe_2$ by exactly this property. This means in terms of $\boldsymbol{q} = \mathbf{0}$ corrections, there is no longer any occupation number response term, but still one for the eigenenergies. This term only contributes directly to the dynamical matrix and thus has no influence on the convergence of the Sternheimer equation. We restrict our analysis to the phonon frequencies at $\Gamma$ and compare the DFPT results to a FD calculation with a $2 \times 2 \times 1$ supercell, which is warranted due to a large cell extent in the z-direction. The DFPT calculation is set up for a k-point grid of $24 \times 24 \times 1$ points in the BZ. Table 9.4 summarizes the parameters of the setup.

**Table 9.4:** Overview of the specific calculational parameters of $MoSe_2$. More parameters in section 6.1.

| $N_{k_{x/y/z}}$ | $\ell_{\max}$ | $\ell_{\max,\mathrm{nsph}}$ | $N_{\mathrm{MT}}$ | $R_{\mathrm{MT}}$ | dx | $a_{\mathrm{latt}}$ | $c_{\mathrm{latt}}$ |
|---|---|---|---|---|---|---|---|
| 24/24/1 | 10 | 8 | 661 | 2.23 $a_0$ | 0.019 | 6.305 $a_0$ | 33.909 $a_0$ |

The Mo atom once again sits at the origin of the unit cell, while the Se atoms sit at $(1/3, -1/3, z_{Se})$ and $(1/3, -1/3, -z_{Se})$ with an optimized $z_{Se} = 0.09425$ or around $3.196\ a_0$ in absolute coordinates. This represents a tight film that is not symmetric under inversion, but under reflection with respect to the xy-plane. To check the overall quality of the calculation, we first evaluate the Goldstone modes as we are used to do.

**Table 9.5:** Overview of the acoustic $\Gamma$-point modes, $\omega$, in $\mathrm{cm}^{-1}$ for $MoSe_2$. No frequency exceeds an absolute value of $2.0\ \mathrm{cm}^{-1}$ (or $0.248$ meV | $0.060$ THz, respectively).

| | $\omega_1$ | $\omega_2$ | $\omega_3$ |
|---|---|---|---|
| FD | $2.35 \times 10^{-2}$ | $3.26 \times 10^{-2}$ | $3.26 \times 10^{-2}$ |
| DFPT | $-1.98 \times 10^{0}$ | $-1.95 \times 10^{0}$ | $-3.36 \times 10^{-1}$ |

The values are in a similar range to those in $VSe_2$, leading to a sufficient quality of the frequency convergence. Thus, we can look at the optical frequencies, that are our main point of interest. They are summarized in table 9.6 for calculations both with and without the energy response contribution to the DM.

**Table 9.6:** Overview of the optical Γ-point modes, $\omega$, in $cm^{-1}$ for $MoSe_2$. The first row belongs to the supercell calculation, the second one to the DFPT run, and the third to a DFPT run, where the eigenenergy response is neglected.

| | $\omega_4$ | $\omega_5$ | $\omega_6$ | $\omega_7$ | $\omega_8$ | $\omega_9$ |
|---|---|---|---|---|---|---|
| FD | 165.543 | 165.543 | 240.022 | 280.634 | 280.634 | 355.68 |
| DFPT | 165.863 | 165.863 | 383.844 | 280.334 | 280.360 | 357.308 |
| no e1 | 165.863 | 165.863 | 492.240 | 279.264 | 279.316 | 357.308 |

There are three things of note here. First, the DFPT and FD values agree nicely for all optical phonon frequencies except one, which is exactly the same pattern as it was for $VSe_2$. Second, the calculated frequencies agree nicely with results that can be found in the literature [49, 226]. Third, the deactivation of the eigenenergy response term has a profound impact on exactly this frequency, while the other modes remain largely unchanged. This makes the initial proposition, that the problem is linked to the $\Gamma$-specific terms all the more likely. This observation is currently one of the active points of investigation and no remedy has been found yet. There are however some things to be noted that came up during the investigation.

Analyzing the Problem

The dynamical matrix for the TMD systems at $\Gamma$ takes on a specific form that exhibits some distinct symmetries, as can be read from the output of the FD simulation. Each of the 9 $3 \times 3$ submatrices of a single atom combination $(\beta, \alpha)$ is diagonal, the main diagonal of the full matrix contains only positive values, and the matrix is of course Hermitian. Both DFPT results share the symmetries that are proposed by the FD reference and many values are very similar. But there are two distinct values that are nearly twice as large as they are supposed to, namely the Se atom combinations of the z-direction. The outlier frequency is directly linked to these matrix elements. This prompted a small stepped analysis of several quantities of the Sternheimer loop for the z-displacement of the Se atoms. While it is hard to say with certainty, when the involved quantities behave right or wrong, one result that is of note is related to the first density perturbation created for these displacements. It turns out that the basis correction part makes the unit cell integral of the perturbation non-vanishing, hence creating a finite change of the charge in the system. This does not happen for the other displacement atoms and directions and is thus possibly linked to the current problem. Another quick test we did was to vary the distance of the layer repetition to see whether there is a convergence effect of the outlier frequency. No such effect was found, but rather a linear looking decrease of the frequency in question, while the other ones stayed basically stable. Considering the different contributions to the dynamical matrix, this could be directly linked to the Hellmann–Feynman terms, that involve derivatives of the external potential. Further investigation of this particular calculation is warranted. In this specific case, however, there might be still more at play. In recent studies of 2D materials, that included TMDCs, it was shwon that the LO-TO splitting breaks down near the $\Gamma$-point when no dipole-dipole interaction is taken into account [227–229]. This is once again related to the missing NAC, that we need to apply for polar materials. Moreover, out-of-plane acoustic (ZA) (also known

as flexural phonons) oftentimes required more rigorous study [230] to overcome numerical difficulties. We keep the latter part in mind when we discuss the implementation of true film DFPT in FLEUR.

## 9.2 2D Film DFPT in the FLAPW Method

### 9.2.1 The FLAPW Method for Thin Films

Cell Setup and Basic Formalism

The formalism that is explained in this chapter largely follows the ideas of Krakauer, Posternak, Freeman, Wimmer, and Weinert, that were established on paper and subsequently implemented in their FLAPW code in the late 1970s and early 1980s [73, 170, 173, 220]. The FLEUR code is a descendant of the original framework that they developed. The method starts from a modified unit cell setup, that replaces the periodic repetition in one of the Cartesian directions (we choose the z-axis to be out-of-plane) on both sides of the atoms and the interstitial region by a vacuum. This transition happens at the points $z = \pm D/2$, where $D$ is the film thickness that we specify. We refer to this as the slab. There is a slightly larger second parameter $\tilde{D}$, that specifies the extent of a pseudo unit cell that could also be repeated into the z-direction and is used as the reference to construct the IR plane waves.

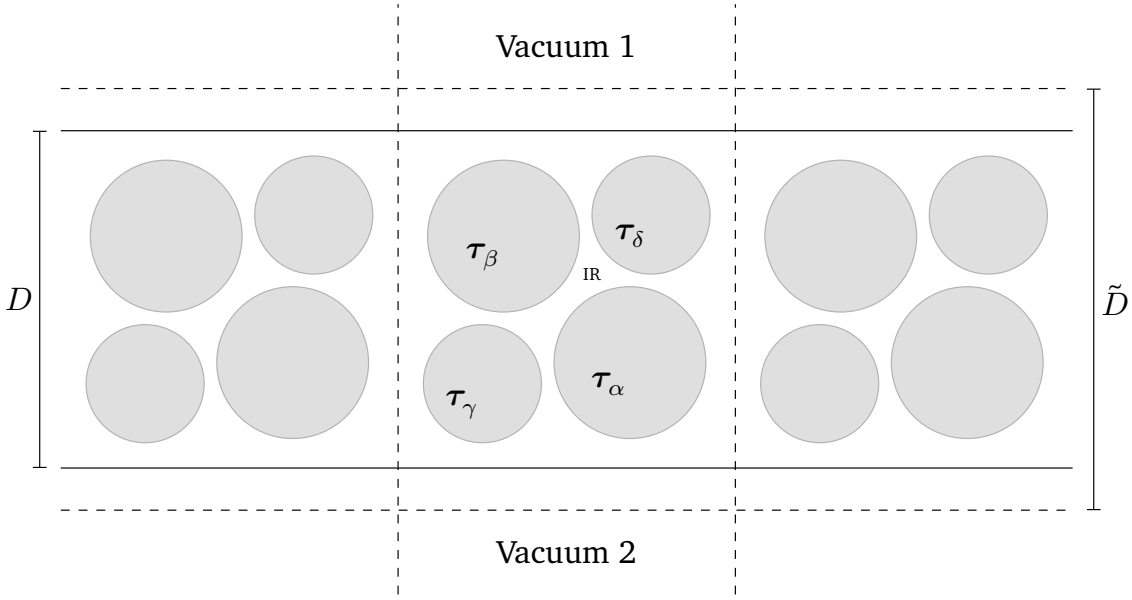



**Figure 9.2:** Sketch of the unit cell setup in the film LAPW method, based on the bulk equivalent in figure 4.1. The unit cell used to construct the plane wave basis of the IR is highlighted with dashed lines while the IR-Vacuum transition is marked by the full lines.

Due to the nature of this setup, the z-components of the reciprocal lattice vectors are distinguished from the in-plane part and the k-point set used to sample the BZ is reduced to a set of

2D vectors (or 3D vectors with only vanishing z-component respectively):

$$\begin{aligned} \boldsymbol{G} &= \boldsymbol{G}_{||} + \boldsymbol{G}_{\perp} && (9.1)\\ &= G_{||}\hat{\boldsymbol{e}}_{||} + G_{\perp}\hat{\boldsymbol{e}}_z, && (9.2)\\ \boldsymbol{k} &= k_{||}\hat{\boldsymbol{e}}_{||} = (k_x, k_y)^T. && (9.3) \end{aligned}$$

The vectors $\boldsymbol{G}$ for the basis and density/potential expansion are selected in the same way as they were in the bulk case by the plane wave cutoffs $K_{\max}$ and $G_{\max}$. While the basis set (and subsequently the representation of the density and potential) remains the same in the MT region and IR slab, the vacuum region is now represented by a set of functions

$$X^{\text{vac}}(\boldsymbol{r}) = \sum_{\boldsymbol{G}_{||}} X_{\text{vac}}(\boldsymbol{G}_{||}, z)\mathrm{e}^{\mathrm{i}\boldsymbol{G}_{||}\cdot\boldsymbol{r}_{||}}, \tag{9.4}$$

that are the product of z-dependent terms with no premandated shape and plane waves that are now projected onto the slab plane.

Here, the vacuum super-/subscript is to be understood both as an indicator and as an index, because there are two vacuum regions we need to account for, which are not necessarily perfectly symmetric. Naturally, in the FLEUR code the representations of the density and potential are additionally brought into a symmetrized form, that is similar to the star representation of the interstitial, only with z-dependent coefficients and the set of $N_{\text{op,2D}}$ 2D-symmetries. The 2D stars with indices $s2D$ are defined as

$$f_{s2D}(\boldsymbol{r}) = \frac{1}{N_{\text{op,2D}}} \sum_{\text{op,2D}} \mathrm{e}^{\mathrm{i}(\underline{R}_{\text{2D}}\boldsymbol{G}_{||,s2D})(\boldsymbol{r}_{||}-\boldsymbol{t}_{\text{2D}})}, \tag{9.5}$$

which leads to the density and potential representation

$$X^{\text{vac}}(\boldsymbol{r}) = \sum_{s2D} X_{\text{vac}}(z, s2D) f_{s2D}(\boldsymbol{r}). \tag{9.6}$$

The Vacuum Basis Set

While the general representation of the vacuum quantities looks very similar to that of the IR, the actual construction of the basis functions is more reminiscent of the MT region and uses a lot of the same ideas, that were used to embed the spheres into the plane wave background. Specifically, the vacuum basis is constructed from z-dependent functions very reminiscent of the radial functions in the MT, that are the solution to the KS equation for the $\boldsymbol{G}_{||} = \boldsymbol{0}$ part of the vacuum effective potential and their respective energy derivatives, leading to a linearized form that can easily be matched against the plane waves at the vacuum border. The functions are determined by

$$\mathcal{H}^{\text{vac}} u^{\text{vac}}_{\boldsymbol{G}_{||},\boldsymbol{k}}(z) = \left(-\frac{1}{2}\partial_z^2 + \frac{1}{2}(\boldsymbol{G}_{||}+\boldsymbol{k})^2 + V^{\text{vac}}_{\text{eff}}(\boldsymbol{G}_{||}=\boldsymbol{0}, z)\right) u^{\text{vac}}_{\boldsymbol{G}_{||},\boldsymbol{k}}(z) = E^{\text{vac}} u^{\text{vac}}_{\boldsymbol{G}_{||},\boldsymbol{k}}(z) \tag{9.7}$$

and for the given energy parameter $E^{\text{vac}}$ are normalized according to

$$1 = \langle u^{\text{vac}}_{\boldsymbol{G}_{||},\boldsymbol{k}} | u^{\text{vac}}_{\boldsymbol{G}_{||},\boldsymbol{k}} \rangle_{\text{vac}} = \int_{\text{vac}} u^{\text{vac}}_{\boldsymbol{G}_{||},\boldsymbol{k}}(z) u^{\text{vac}}_{\boldsymbol{G}_{||},\boldsymbol{k}}(z)\mathrm{d}z. \tag{9.8}$$

The corresponding energy derivatives are found by differentiating equation (9.7) and yield

$$\mathcal{H}^{\text{vac}} \dot{u}^{\text{vac}}_{\boldsymbol{G}_{||},\boldsymbol{k}}(z) = u^{\text{vac}}_{\boldsymbol{G}_{||},\boldsymbol{k}}(z) + E^{\text{vac}} \dot{u}^{\text{vac}}_{\boldsymbol{G}_{||},\boldsymbol{k}}(z). \tag{9.9}$$

As for their MT equivalents, the energy derivatives are orthogonal to the initial functions and are not normalized. From these functions we construct the vacuum part of the LAPW basis functions as

$$\phi^{\text{vac}}_{\boldsymbol{k}\boldsymbol{G}}(\boldsymbol{r}) = \frac{1}{\sqrt{A}} \left( a^{\text{vac}}_{\boldsymbol{k},\boldsymbol{G}} u^{\text{vac}}_{\boldsymbol{G}_\parallel,\boldsymbol{k}}(z) + b^{\text{vac}}_{\boldsymbol{k},\boldsymbol{G}} \dot{u}^{\text{vac}}_{\boldsymbol{G}_\parallel,\boldsymbol{k}}(z) \right) \mathrm{e}^{\mathrm{i}(\boldsymbol{k}+\boldsymbol{G}_\parallel)\cdot\boldsymbol{r}_\parallel}, \tag{9.10}$$

with a normalization factor that contains the area $A$ of the vacuum boundary. The matching coefficients are found, as was the case for the MT basis, by requiring the basis to be continuous to 1st order at the boundaries. This leads to a linear system of equations, that is solved by

$$\begin{pmatrix} a^{\text{vac}}_{\boldsymbol{k},\boldsymbol{G}} \\ b^{\text{vac}}_{\boldsymbol{k},\boldsymbol{G}} \end{pmatrix} = \sqrt{\frac{A}{\tilde{\Omega}}} \mathrm{e}^{\mathrm{i}G_\perp z_{\text{vac}}} \underline{U}^{\text{vac},-1}_{\boldsymbol{k},\boldsymbol{G}_\parallel} \cdot \begin{pmatrix} 1 \\ \mathrm{i}G_\perp \end{pmatrix}. \tag{9.11}$$

It is important to note, that the plane waves are normalized by the volume of the extended slab of size $\tilde{D}$. The value of $z_{\text{vac}}$ is $\pm D/2$ for the upper and lower vacuum, respectively. The matrix of boundary values and its inverse are identical in form to those of the MT case and contain the z-dependent functions, their energy derivatives, and the corresponding derivatives with respect to $z$:

$$\underline{U}^{\text{vac}}_{\boldsymbol{k},\boldsymbol{G}_\parallel} = \begin{pmatrix} u^{\text{vac}}_{\boldsymbol{G}_\parallel,\boldsymbol{k}}(z_{\text{vac}}) & \dot{u}^{\text{vac}}_{\boldsymbol{G}_\parallel,\boldsymbol{k}}(z_{\text{vac}}) \\ u^{\text{vac}'}_{\boldsymbol{G}_\parallel,\boldsymbol{k}}(z_{\text{vac}}) & \dot{u}^{\text{vac}'}_{\boldsymbol{G}_\parallel,\boldsymbol{k}}(z_{\text{vac}}) \end{pmatrix}, \tag{9.12}$$

$$\underline{U}^{\text{vac},-1}_{\boldsymbol{k},\boldsymbol{G}_\parallel} = \frac{1}{W^{\text{vac}}_{\boldsymbol{k},\boldsymbol{G}_\parallel}} \begin{pmatrix} \dot{u}^{\text{vac}'}_{\boldsymbol{G}_\parallel,\boldsymbol{k}}(z_{\text{vac}}) & -u^{\text{vac}'}_{\boldsymbol{G}_\parallel,\boldsymbol{k}}(z_{\text{vac}}) \\ -u^{\text{vac}'}_{\boldsymbol{G}_\parallel,\boldsymbol{k}}(z_{\text{vac}}) & u^{\text{vac}}_{\boldsymbol{G}_\parallel,\boldsymbol{k}}(z_{\text{vac}}) \end{pmatrix}. \tag{9.13}$$

The Wronskian of the matrix is constructed from the same functions as their equivalents in the MT case, but takes on a different value than before due to the different nature of this boundary. Some manipulation of the equations shows

$$W^{\text{vac}}_{\boldsymbol{k},\boldsymbol{G}_\parallel} = u^{\text{vac}}_{\boldsymbol{G}_\parallel,\boldsymbol{k}}(z_{\text{vac}}) \dot{u}^{\text{vac}'}_{\boldsymbol{G}_\parallel,\boldsymbol{k}}(z_{\text{vac}}) - \dot{u}^{\text{vac}}_{\boldsymbol{G}_\parallel,\boldsymbol{k}}(z_{\text{vac}}) u^{\text{vac}'}_{\boldsymbol{G}_\parallel,\boldsymbol{k}}(z_{\text{vac}}) = 2 \neq 0. \tag{9.14}$$

The Wronskian is therefore once again finite and there can be no asymptote problem, meaning that the matching of the vacuum basis to that of the IR is always possible. In the same vein as for the MT matching coefficients, we can handily contract them with the expansion coefficients to create new matching coefficients

$$\begin{pmatrix} A^{\text{vac}}_{\boldsymbol{k}\nu,\boldsymbol{G}_\parallel} \\ B^{\text{vac}}_{\boldsymbol{k}\nu,\boldsymbol{G}_\parallel} \end{pmatrix} = \sum_{G_\perp} z_{\boldsymbol{k}\boldsymbol{G}\nu} \begin{pmatrix} a^{\text{vac}}_{\boldsymbol{k},\boldsymbol{G}} \\ b^{\text{vac}}_{\boldsymbol{k},\boldsymbol{G}} \end{pmatrix} \tag{9.15}$$

that are smaller and thus computationally more convenient. Considering the construction of the Hamiltonian and overlap elements for the vacuum, they are constructed in a way very reminiscent of the spherical and non-spherical distinction of the MT. The overlap reads

$$S^{\text{vac}}_{\boldsymbol{G}',\boldsymbol{G}}(\boldsymbol{k}) = \delta_{\boldsymbol{G}'_\parallel,\boldsymbol{G}_\parallel} \left( a^{\text{vac}*}_{\boldsymbol{k},\boldsymbol{G}'} a^{\text{vac}}_{\boldsymbol{k},\boldsymbol{G}} + b^{\text{vac}*}_{\boldsymbol{k},\boldsymbol{G}'} b^{\text{vac}}_{\boldsymbol{k},\boldsymbol{G}} \langle \dot{u}^{\text{vac}}_{\boldsymbol{G}_\parallel,\boldsymbol{k}} | \dot{u}^{\text{vac}}_{\boldsymbol{G}_\parallel,\boldsymbol{k}} \rangle_{\text{vac}} \right) \tag{9.16}$$

and is thus reminiscent of the spherical MT part, while the Hamiltonian forms a contraction of the matching coefficients with a matrix $\underline{t}$ in each of the functions:

$$H^{\text{vac}}_{\boldsymbol{G}',\boldsymbol{G}}(\boldsymbol{k}) = \sum_{(\cdot)'(\cdot)} a^{\text{vac}*}_{\boldsymbol{k},\boldsymbol{G}'(\cdot)'} t^{(\cdot)'(\cdot)}_{\boldsymbol{G}'_\parallel,\boldsymbol{G}_\parallel} a^{\text{vac}}_{\boldsymbol{k},\boldsymbol{G}(\cdot)}. \tag{9.17}$$

The matching coefficients $a, b$ are written here as simply $a$ with an index $(\cdot)$ that indicates whether they belong to the z-dependent functions or their energy derivatives. The matrix elements are comprised of the evaluated potential for the non-vanishing in-plane reciprocal vectors and by the evaluated Hamiltonian that defined the z-dependent functions in the first case for $\boldsymbol{G}'_{||} = \boldsymbol{G}_{||}$. This leads to

$$t^{(\cdot)'(\cdot)}_{\boldsymbol{G}'_{||},\boldsymbol{G}_{||}} := (1 - \delta_{\boldsymbol{G}'_{||},\boldsymbol{G}_{||}}) \langle {}^{(\cdot)'\text{vac}}u_{\boldsymbol{G}'_{||},\boldsymbol{k}} | V^{\text{vac}}_{\text{eff}}(\boldsymbol{G}'_{||} - \boldsymbol{G}_{||}, z) | {}^{(\cdot)\text{vac}}u_{\boldsymbol{G}_{||},\boldsymbol{k}} \rangle_{\text{vac}} + \delta_{\boldsymbol{G}'_{||},\boldsymbol{G}_{||}} c^{(\cdot)'(\cdot)}_{\boldsymbol{G}_{||},\boldsymbol{k}}. \tag{9.18}$$

The factors that correspond to the MT spherical case (in the already symmetrized form) are

$$c^{(\cdot)'(\cdot)}_{\boldsymbol{G}_{||},\boldsymbol{k}} = \begin{cases} E^{\text{vac}}, & (\cdot)'(\cdot) = u, u \\ 1/2, & (\cdot)'(\cdot) = u, \dot{u} \text{ or } \dot{u}, u \\ E^{\text{vac}} \left\langle \dot{u}^{\text{vac}}_{\boldsymbol{G}_{||},\boldsymbol{k}} | \dot{u}^{\text{vac}}_{\boldsymbol{G}_{||},\boldsymbol{k}} \right\rangle_{\text{vac}}, & (\cdot)'(\cdot) = \dot{u}, \dot{u}. \end{cases} \tag{9.19}$$

Finally, we can write down the wave functions for the vacuum region in terms of the contracted matching coefficients and the z-dependent functions to find

$$\psi^{\text{vac}}_{\boldsymbol{k}\nu}(\boldsymbol{r}) = \sum_{\boldsymbol{G}} z_{\boldsymbol{k}\boldsymbol{G}\nu} \phi^{\text{vac}}_{\boldsymbol{k}\boldsymbol{G}}(\boldsymbol{r}) = \sum_{\boldsymbol{G}_{||}} \left( A^{\text{vac}}_{\boldsymbol{k}\nu,\boldsymbol{G}_{||}} u^{\text{vac}}_{\boldsymbol{G}_{||},\boldsymbol{k}}(z) + B^{\text{vac}}_{\boldsymbol{k}\nu,\boldsymbol{G}_{||}} \dot{u}^{\text{vac}}_{\boldsymbol{G}_{||},\boldsymbol{k}}(z) \right) \mathrm{e}^{\mathrm{i}(\boldsymbol{k}+\boldsymbol{G}_{||})\cdot\boldsymbol{r}_{||}}. \tag{9.20}$$

The Density Generation

As the spatial dependence of the density and potential in the vacuum is determined by a 2D plane wave, the coefficients that carry relevant information about these quantities are the z-dependent functions. They can be found for the vacuum in the same way the radial density coefficients were found by contracting the matching coefficients over all indices but the angular quantum numbers $\ell(')$ and the k-point, and subsequently multiplying the result with the solutions to the spherical KS. The angular quantum numbers are replaced by the in-plane reciprocal lattice vectors and the radial solutions by the z-dependent ones. This leads to

$$n_{\text{vac}}(\boldsymbol{G}''_{||}, z) = \sum_{\boldsymbol{k}\nu} \tilde{f}_{\boldsymbol{k}\nu} \sum_{\substack{\boldsymbol{G}'^{(\cdot)'}_{||} \\ \boldsymbol{G}^{(\cdot)}_{||}}} A^{\text{vac}*}_{\boldsymbol{k}\nu,\boldsymbol{G}'^{(\cdot)'}_{||}} {}^{(\cdot)'\text{vac}}u_{\boldsymbol{G}'_{||},\boldsymbol{k}}(z) A^{\text{vac}}_{\boldsymbol{k}\nu,\boldsymbol{G}^{(\cdot)}_{||}} {}^{(\cdot)\text{vac}}u_{\boldsymbol{G}_{||},\boldsymbol{k}}(z) \delta_{\boldsymbol{G}''_{||},\boldsymbol{G}_{||}-\boldsymbol{G}'_{||}}, \tag{9.21}$$

$$= \sum_{\boldsymbol{k}} \sum_{\substack{\boldsymbol{G}'^{(\cdot)'}_{||} \\ \boldsymbol{G}^{(\cdot)}_{||}}} d^{\boldsymbol{k}\text{vac}}_{\boldsymbol{G}'_{||}\boldsymbol{G}_{||}\boldsymbol{G}''^{(\cdot)'(\cdot)}_{||}} {}^{(\cdot)'\text{vac}}u_{\boldsymbol{G}'_{||},\boldsymbol{k}}(z) u^{\text{vac}}_{\boldsymbol{G}_{||},\boldsymbol{k}}(z). \tag{9.22}$$

For the sake of completeness, we mention that on top of this valence electron contribution, there is also one for the core electrons, that is modeled as an exponential tail from the vacuum boundary outwards.

The Potential Generation

For the potential generation, we need a scheme that correctly takes into account all three distinct regions - the MT, the IR and the vacuum - and their respective (pseudo-)densities into account. This is trivial for the xc potential, where we only need to correctly transform the vacuum density into real space and then do the same operations we would do for the real space MT and IR density in a bulk run. The Coulomb potential calculation is more involved. As the MT part is fully analogous to a bulk calculation, our main task is to provide a consistent solution for the vacuum and the IR. For this we look at the defining Poisson equation (4.34),

where we cancel the 2D plane waves out. This leads to a 1D screened Poisson equation for the potential coefficients:

$$\left[\partial_z^2 - G_{||}^2\right] V_C(\boldsymbol{G}_{||}, z) = -4\pi n(\boldsymbol{G}_{||}, z). \tag{9.23}$$

This equation holds for both the vacuum and the interstitial region. There are two distinct cases to be considered in solving this equation. We first turn to the arguably easier one of those.

$\boldsymbol{G}_{||} = \boldsymbol{0}$

In the case of $\boldsymbol{G}_{||} = \boldsymbol{0}$, the screening term is dropped from the Poisson equation, which significantly reduces its complexity. We define

$$n_0(z) := \begin{cases} n^{\text{vac}}(\boldsymbol{G}_{||} = \boldsymbol{0}, z), & \boldsymbol{r} \in \text{vac}, \\ \sum_{G_\perp} n_{\text{ps}}(\boldsymbol{G} = \boldsymbol{G}_\perp) \mathrm{e}^{\mathrm{i}G_\perp z}, & \boldsymbol{r} \in \text{IR} \end{cases} \tag{9.24}$$

and

$$V_0(z) := \begin{cases} V_{\text{C}}^{\text{vac}}(\boldsymbol{G}_{||} = \boldsymbol{0}, z), & \boldsymbol{r} \in \text{vac}, \\ \sum_{G_\perp} V_{\text{C,IR}}(\boldsymbol{G}) \mathrm{e}^{\mathrm{i}G_\perp z}, & \boldsymbol{r} \in \text{IR} \end{cases} \tag{9.25}$$

as a shorthand notation for the density and potential in this case. It is important to note, that the density in the vacuum part corresponds to the true electron density in this region, while the IR part is the pseudodensity of the electrons and ions. It is constructed in the same way as it was for the bulk, with the important distinction that an extra step is taken to ensure charge neutrality. The pseudodensity and vacuum density are integrated and in case the result does not vanish, a correction term is added to the $n_{\text{ps}}(\boldsymbol{G} = \boldsymbol{0})$ component of the pseudodensity. From this, we solve the simplified Poisson equation by direct integration:

$$\partial_z^2 V_0(z) = -4\pi n_0(z) \tag{9.26}$$

$$\Leftrightarrow V_0(z) = -4\pi \int_z^\infty \int_{z'}^\infty n_0(z'') dz'' dz'. \tag{9.27}$$

Here, we implicitly took the boundary conditions $V_0(\infty) = 0$ and $V_0'(\infty) = 0$ into account. Due to the downwards integration from $\infty$ to $z$, the result depends on the region that $z$ is in. If it is in the upper vacuum ($z \geq D/2$), we can define the integrated charge

$$\sigma_0^+(z) := \int_z^\infty n_0(z') dz' \tag{9.28}$$

and use it to find

$$V^0(z) = -4\pi \int_z^\infty \sigma_0^+(z') dz' =: V_0^+(z) \tag{9.29}$$

for the potential. By construction, this potential term does not depend on the density in any region but the upper vacuum itself. This is no longer the case for the potential in the interstitial region ($|z| \leq D/2$). Here, both the integrated charge up to the upper vacuum boundary and the potential at this point enter into the calculation. We define the averaged charge in the slab $\bar{n}$ by

$$\bar{n} := -\frac{1}{D} \int_{-D/2}^{D/2} n_0(z) dz = -\left[ n_{\text{ps}}(\boldsymbol{0}) + \sum_{G_\perp \neq 0} n_{\text{ps}}(\boldsymbol{G} = \boldsymbol{G}_\perp) j_0(G_\perp D/2) \right] \tag{9.30}$$

and use it to write

$$V_0(z) = V_0^+(D/2) - 4\pi(D/2 - z)\left(\sigma_0^+(D/2) - \bar{n}/2(D/2 - z)\right) \tag{9.31}$$
$$+4\pi \sum_{G_\perp \neq 0} n_{\text{ps}}(\boldsymbol{G} = \boldsymbol{G}_\perp)\left\{\left[e^{iG_\perp z} - e^{iG_\perp D/2}\right]/G_\perp^2\right. \tag{9.32}$$
$$+\mathrm{i}\cos\left(G_\perp D/2\right)(D/2 - z)/G_\perp \tag{9.33}$$
$$\left.+j_0(G_\perp D/2)(z^2 - D^2/4)/2\right\} \tag{9.34}$$

for the interstitial region. Going yet further down into the lower vacuum ($z \leq -D/2$), both the upper vacuum and the IR contribute to the potential. We define the lower vacuum equivalent of the integrated charge (9.28) as

$$\sigma_0^-(z) := \int_z^{-D/2} n_0(z')dz' \tag{9.35}$$

and the fully summed interstitial terms as

$$\Sigma_{\text{IR}} := -4\pi i \sum_{G_\perp \neq \mathbf{0}} n_{\text{ps}}(\boldsymbol{G} = \boldsymbol{G}_\perp) j_1(G_\perp D/2) D^2/2 \tag{9.36}$$

we can write the lower vacuum potential as

$$V^0(z) = V_0^+(D/2) - 4\pi\left(D\sigma_0^+(D/2) - \bar{n}D^2/2\right) + \Sigma_{\text{IR}} \tag{9.37}$$
$$-4\pi \int_z^{-D/2} \sigma_0^-(z') - D\bar{n} + \sigma_0^+(D/2)dz'. \tag{9.38}$$

This form is still relatively simple and straight-forward to implement.

The case of non-vanishing reciprocal lattice vectors is both a lot more relevant in the scope of this thesis and a lot more complicated. We begin by once again defining shorthand notations $\boldsymbol{G}_{||} \neq \mathbf{0}$

$$n_{\boldsymbol{G}_{||}}(z) := \begin{cases} n^{\text{vac}}(\boldsymbol{G}_{||}, z) & \boldsymbol{r} \in \text{vac} \\ \sum_{G_\perp} n_{\text{ps}}(\boldsymbol{G}_{||} + \boldsymbol{G}_\perp)\mathrm{e}^{\mathrm{i}G_\perp z} & \boldsymbol{r} \in \text{IR} \end{cases} \tag{9.39}$$

for the density and

$$V_{\boldsymbol{G}_{||}}(z) := \begin{cases} V_{\text{C}}^{\text{vac}}(\boldsymbol{G}_{||}, z) & \boldsymbol{r} \in \text{vac} \\ \sum_{G_\perp} V_{\text{C,IR}}(\boldsymbol{G}_{||} + \boldsymbol{G}_\perp)\mathrm{e}^{\mathrm{i}G_\perp z} & \boldsymbol{r} \in \text{IR} \end{cases} \tag{9.40}$$

for the potential. Now, we have to solve the full form of the screened Poisson equation, which is done with the help of a Green's function:

$$\left[\partial_z^2 - G_{||}^2\right] V_{\boldsymbol{G}_{||}}(z) = -4\pi n_{\boldsymbol{G}_{||}}(z) \tag{9.41}$$
$$\Leftrightarrow V_{\boldsymbol{G}_{||}}(z) = \int_{-\infty}^{\infty} G(z - z')n_{\boldsymbol{G}_{||}}(z')dz'. \tag{9.42}$$

This Green's function is coupled to the same operations on the left hand side of the equation but results in a $\delta$-distribution instead:

$$\left[\partial_z^2 - G_{||}^2\right] G(z - z') = -4\pi\delta(z - z'). \tag{9.43}$$

It also obeys the same boundary condition of vanishing at $\pm\infty$ as the potential does. With this knowledge, we can solve for

$$G(z-z') = \frac{2\pi}{|\boldsymbol{G}_{||}|}\mathrm{e}^{-|\boldsymbol{G}_{||}||z-z'|}. \tag{9.44}$$

Evaluating the Green's function integral for any of the regions gives contributions from each one, respectively. Explicitly evaluating the analytic form for the IR contributions, for $z \geq D/2$ we find

$$\begin{aligned}
V_{\boldsymbol{G}_{||}}(z) = \quad & \frac{2\pi}{|\boldsymbol{G}_{||}|}\Bigg[e^{-|\boldsymbol{G}_{||}|z}\int_{-\infty}^{-D/2} n_{\boldsymbol{G}_{||}}(z')e^{|\boldsymbol{G}_{||}|z'}dz' && (9.45)\\
+ \quad & e^{-|\boldsymbol{G}_{||}|z}\int_{D/2}^{z} n_{\boldsymbol{G}_{||}}(z')e^{|\boldsymbol{G}_{||}|z'}dz' && (9.46)\\
+ \quad & e^{|\boldsymbol{G}_{||}|z}\int_{z}^{\infty} n_{\boldsymbol{G}_{||}}(z')e^{-|\boldsymbol{G}_{||}|z'}dz' && (9.47)\\
& + e^{-|\boldsymbol{G}_{||}|z}\sum_{G_\perp} 2n_{\mathrm{ps}}(\boldsymbol{G})\frac{\sinh\left((|\boldsymbol{G}_{||}|+iG_\perp)\frac{D}{2}\right)}{(|\boldsymbol{G}_{||}|+iG_\perp)}\Bigg], && (9.48)
\end{aligned}$$

the $|z| \leq D/2$ part is

$$\begin{aligned}
V_{\boldsymbol{G}_{||}}(z) = \quad & \frac{2\pi}{\boldsymbol{G}_{||}}\Bigg[e^{-|\boldsymbol{G}_{||}|z}\int_{-\infty}^{-D/2} e^{|\boldsymbol{G}_{||}|z'}n_{\boldsymbol{G}_{||}}(z')dz' && (9.49)\\
+ \quad & e^{|\boldsymbol{G}_{||}|z}\int_{D/2}^{\infty} e^{-|\boldsymbol{G}_{||}|z'}n_{\boldsymbol{G}_{||}}(z')dz' && (9.50)\\
+ \quad & \sum_{G_\perp}\frac{2|\boldsymbol{G}_{||}|n_{\mathrm{ps}}(\boldsymbol{G})}{|\boldsymbol{G}_{||}|^2+G_\perp^2}e^{iG_\perp z} && (9.51)\\
& - \sum_{G_\perp}\frac{n_{\mathrm{ps}}(\boldsymbol{G})}{|\boldsymbol{G}_{||}|^2+G_\perp^2}\Bigg\{e^{-|\boldsymbol{G}_{||}|z}e^{-(|\boldsymbol{G}_{||}|+iG_\perp)\frac{D}{2}}(|\boldsymbol{G}_{||}|-iG_\perp) && (9.52)\\
& + e^{|\boldsymbol{G}_{||}|z}e^{-(|\boldsymbol{G}_{||}|-iG_\perp)\frac{D}{2}}(|\boldsymbol{G}_{||}|+iG_\perp)\Bigg\}\Bigg], && (9.53)
\end{aligned}$$

and finally, $z \leq -D/2$ gives

$$\begin{aligned}
V_{\boldsymbol{G}_{||}}(z) = \quad & \frac{2\pi}{|\boldsymbol{G}_{||}|}\Bigg[e^{-|\boldsymbol{G}_{||}|z}\int_{-\infty}^{z} n_{\boldsymbol{G}_{||}}(z')e^{|\boldsymbol{G}_{||}|z'}dz' && (9.54)\\
+ \quad & e^{|\boldsymbol{G}_{||}|z}\int_{z}^{-D/2} n_{\boldsymbol{G}_{||}}(z')e^{-|\boldsymbol{G}_{||}|z'}dz' && (9.55)\\
+ \quad & e^{|\boldsymbol{G}_{||}|z}\int_{D/2}^{\infty} n_{\boldsymbol{G}_{||}}(z')e^{-|\boldsymbol{G}_{||}|z'}dz' && (9.56)\\
& + e^{|\boldsymbol{G}_{||}|z}\sum_{G_\perp} 2n_{\mathrm{ps}}(\boldsymbol{G})\frac{\sinh\left((|\boldsymbol{G}_{||}|-iG_\perp)\frac{D}{2}\right)}{(|\boldsymbol{G}_{||}|-iG_\perp)}\Bigg]. && (9.57)
\end{aligned}$$

For both $\boldsymbol{G}_{||} = \boldsymbol{0}$ and $\boldsymbol{G}_{||} \neq \boldsymbol{0}$, the plane wave coefficients of the IR potential are found by a 1D Fourier transform of the real space potential we calculated. It is done in the z-direction only and defined in terms of the unit cell instead of the slab. Hence, we need to take the

part of the vacuum region between $\pm D$ and $\pm\tilde{D}$ into account in the Fourier transform. As mentioned before, the propagation of the resulting coefficients into the MT boundary problem is unchanged from the bulk case. This concludes the discussion of the vacuum potential generation.

Total Energy Calculations

The last aspect that is modified by the film setup is the calculation of the total energy or, more generally, of integrals over the unit cell. While previous integrations *e.g.* in equation (2.13) were performed over the unit cell $\Omega$, we now need to take the vacuum into account as well and integrate over the full stretch from $z = -\infty$ to $z = \infty$ in the 2D unit cell $\Omega_{2D}$. This leads to two consequences. First, the step function in equation (4.9) needs to be slightly modified to not only filter out the MT, but also the vacuum region through

$$\hat{\Theta}(\boldsymbol{G}) \longrightarrow \hat{\Theta}(\boldsymbol{G}) + \delta_{\boldsymbol{G},\mathbf{0}}(DA/\tilde{\Omega} - 1) + \sum_{G_\perp \neq 0} (DA/\tilde{\Omega}) \sin(\mathrm{i}G_\perp D/2)/(G_\perp D/2), \quad (9.58)$$

where we introduced the area $A$ of the vacuum boundary of the unit cell and the unit cell volume $\tilde{\Omega}$ that is defined with respect to $\tilde{D}$. A second aspect is, that every integral over the full 2D unit cell will contain a vacuum contribution constructed from the density and potential 2D star coefficients. It can be expressed analogously to the MT and IR terms in section 4.1 by

$$\int_{\text{vac}} X_{\text{vac}}(\boldsymbol{r}) Y_{\text{vac}}(\boldsymbol{r}) \mathrm{d}\boldsymbol{r} = \mathrm{A} \sum_{s2D} \int_{\text{vac}} X^*_{\text{IR}}(z, s2D) Y_{\text{IR}}(z, s2D) \mathrm{d}z \quad (9.59)$$

and subsequently enters the density mixing procedure as well. All these aspects have long been a part of the FLEUR code and an extension of the DFPT formalism to this framework is both desirable and a matter of completeness.

### 9.2.2 Changes to the DFPT Formalism

Advantages of the Thin Film Treatment

To begin the discussion of the thin film FLAPW DFPT formalism, we first recall the specific form of the k-points, as it translates to the phonon wave vectors we have to calculate and interpolate between as well. They have no component in the out-of-plane direction, which in theory makes the system scale a lot better. Doubling the number of k-points in each direction, for example, now increases the total count by a factor of $4$ instead of $8$. The q-points consequently also read

$$\boldsymbol{q} = q_{||}\hat{\boldsymbol{e}}_{||} = (q_x, q_y)^T. \quad (9.60)$$

Additionally, the film approach replaces the method of simulating a slab by putting periodic images of a single layer far away from each other, which constitutes a very large unit cell and a proportionally large set of out-of-plane reciprocal lattice vectors $G_\perp$. A thin film can instead be used, whose unit cell (defined by $\tilde{D}$) does not need to be exceptionally large, once again making the calculation a lot cheaper. We systematically go through the adaptions that need to be done to the DFPT formalism to incorporate the thin film implementation.

Total Energy Response

Our investigation of the necessary changes to FLEUR DFPT starts at the total energy. We recall, that for a method with no dependence of the basis on the atomic positions, the second order response of the total energy is solely determined by the density (response) and quantities

related to the external potential (equation (3.29)). Neglecting for a moment the correction terms necessary in the LAPW basis, we can write the corresponding form for the film as

$$E_{\text{tot}}^{(2)\beta j-\alpha i+} = \int_{\Omega_{2D}} \left[ n^{(1)\beta j-}(\boldsymbol{r}) V_{\text{ext}}^{(1)\alpha i+}(\boldsymbol{r}) + n(\boldsymbol{r}) V_{\text{ext}}^{(2)\beta j-\alpha i+}(\boldsymbol{r}) \right] \mathrm{d}\boldsymbol{r} + E_{\text{ii}}^{(2)\beta j-\alpha i+}. \tag{9.61}$$

The integration domain $\Omega_{2D}$ signifies the volume of the 2D unit cell, *i.e.* the slab and the two vacuum regions going to $z = \pm\infty$. Due to the position dependent nature of the basis set, the actual equation we need to solve for the response is a lot more involved, due to basis set correction terms in the MT and surface integrals along the MT boundaries. As the position of the vacuum boundary is in no way dependent on the atomic positions, the only additional contribution to equation (4.87) comes from the vacuum integral terms in the HF part. Aside from this the construction of $E_{\text{ii}}^{(2)\beta j-\alpha i+}$ will change due to a different workflow of the potential generation. This means we need the external potential to first and second order in the vacuum for the first integral and the ion-ion interaction, respectively. If we additionally transform the integral of the second order external potential like in equation (5.56), we also end up with two surface terms at the upper and lower vacuum boundaries:

$$\int_{\Omega_{2D}} n(\boldsymbol{r}) V_{\text{ext}}^{(2)\beta j-\alpha i+}(\boldsymbol{r}) \mathrm{d}\boldsymbol{r} = \int_{\Omega_{2D}} (\nabla_j n(\boldsymbol{r})) \delta_{\beta\alpha} V_{\text{ext}}^{(1)\alpha i\boldsymbol{0}}(\boldsymbol{r}) \mathrm{d}\boldsymbol{r} \tag{9.62}$$

$$- \sum_{\gamma} \oint_{\partial\gamma} \left[ n(\boldsymbol{r}) V_{\text{ext}}^{(1)\alpha i\boldsymbol{0}}(\boldsymbol{r}) \right]_{\text{SF}} \hat{\boldsymbol{e}}_{r,j} \mathrm{d}S \tag{9.63}$$

$$- \delta_{j,z} \sum_{\text{vac}} \oint_{\partial\text{vac}} \left[ n(\boldsymbol{r}) V_{\text{ext}}^{(1)\alpha i\boldsymbol{0}}(\boldsymbol{r}) \right]_{\text{SF}} \mathrm{d}S. \tag{9.64}$$

This is in principle quite compact and only requires the additional calculation of the numerical density gradient in the vacuum. For the in-plane directions, this is very akin to the IR case, as the derivative only produces a prefactor, while for the z-derivative, we need to actually use a numerical differentiation routine. Both cases pose no big problems. But additional care needs to be taken with respect to the sign of the surface terms. Since the normal vector of each respective region points outwards, the upper vacuum term and the lower interstitial term get a $(-)$ sign, while the lower vacuum term and the upper interstitial term are positive.

Density Response

The density response in the vacuum case translates directly to an analogous form from the response of the MT density and the original density of the vacuum. It is constructed from the z-dependent functions for $\boldsymbol{k}$ and $\boldsymbol{k}+\boldsymbol{q}$ as

$$n_{\text{vac}}^{(1)\beta j+}(\boldsymbol{G}''_{\parallel} + \boldsymbol{q}, z) = \sum_{\boldsymbol{k}} \sum_{\substack{\boldsymbol{G}'^{(\cdot)'}_{\parallel} \\ \boldsymbol{G}^{(\cdot)}_{\parallel}}} d^{\boldsymbol{k}\text{vac},(1)\beta j+}_{\boldsymbol{G}'_{\parallel}\boldsymbol{G}_{\parallel}\boldsymbol{G}''^{(\cdot)'(\cdot)}_{\parallel}} u^{(\cdot)'\text{vac}}_{\boldsymbol{G}'_{\parallel},\boldsymbol{k}}(z) u^{\text{vac}}_{\boldsymbol{G}_{\parallel},\boldsymbol{k}+\boldsymbol{q}}(z) \tag{9.65}$$

with a new density coefficient

$$d^{\boldsymbol{k}\text{vac},(1)\beta j+}_{\boldsymbol{G}'_{\parallel}\boldsymbol{G}_{\parallel}\boldsymbol{G}''^{(\cdot)'(\cdot)}_{\parallel}} = \sum_{\nu} \tilde{f}_{\boldsymbol{k}\nu} A^{\text{vac}*}_{\boldsymbol{k}\nu,\boldsymbol{G}'^{(\cdot)'}_{\parallel}} A^{\text{vac},(1)\beta j+}_{\boldsymbol{k}\nu,\boldsymbol{G}^{(\cdot)}_{\parallel}} \delta_{\boldsymbol{G}''_{\parallel},\boldsymbol{G}_{\parallel}-\boldsymbol{G}'_{\parallel}} \tag{9.66}$$

$$+ \sum_{\nu} \tilde{f}^{(1)\beta j+}_{\boldsymbol{k}\nu} A^{\text{vac}*}_{\boldsymbol{k}\nu,\boldsymbol{G}'^{(\cdot)'}_{\parallel}} A^{\text{vac}}_{\boldsymbol{k}\nu,\boldsymbol{G}^{(\cdot)}_{\parallel}} \delta_{\boldsymbol{G}''_{\parallel},\boldsymbol{G}_{\parallel}-\boldsymbol{G}'_{\parallel}}. \tag{9.67}$$

The modified contracted matching coefficient that appears is defined as

$$A^{\text{vac},(1)\beta j+}_{\boldsymbol{k}\nu,\boldsymbol{G}^{(\cdot)}_{\parallel}} = \sum_{G_{\perp}} 2 z^{(1)\beta j+}_{\boldsymbol{k}\boldsymbol{G}\boldsymbol{q}\nu} a^{\text{vac}}_{\boldsymbol{k}+\boldsymbol{q},\boldsymbol{G}^{(\cdot)}}. \tag{9.68}$$

Note, that no basis correction terms like imaginary number prefactors and gradient terms appear. Since the resulting density variables are only a very slight modification from the base case, they are easily implemented and we can move on to the next small aspect.

Hamiltonian and Overlap Response

As the vacuum basis does not depend on the atomic positions, there are no matrix response terms related to a basis correction. Furthermore, the Hamiltonian itself does not give a response term except for that of the effective potential. This means the only additional matrix element we need to calculate is

$$H^{(1)\beta j+,\text{vac}}_{\boldsymbol{G}',\boldsymbol{G}} = \langle \phi_{\boldsymbol{k}\boldsymbol{G}'\boldsymbol{q}} | V^{(1)\beta j+}_{\text{eff}} | \phi_{\boldsymbol{k}\boldsymbol{G}} \rangle_{\text{vac}}. \tag{9.69}$$

Just like the basic Hamiltonian matrix elements, its constituents can be expressed as the evaluation of a matrix $\underline{t}$ with respect to the matching coefficients, though this time evaluated for $\boldsymbol{k}+\boldsymbol{q}$ on the left side:

$$H^{(1)\beta j+,\text{vac}}_{\boldsymbol{G}',\boldsymbol{G}}(\boldsymbol{k}+\boldsymbol{q},\boldsymbol{k}) = \sum_{(\cdot)'(\cdot)} a^{\text{vac}*}_{\boldsymbol{k}+\boldsymbol{q},\boldsymbol{G}'(\cdot)'} t^{(1)\beta j+,(\cdot)'(\cdot)}_{\boldsymbol{G}'_{||}+\boldsymbol{q},\boldsymbol{G}_{||}} a^{\text{vac}}_{\boldsymbol{k},\boldsymbol{G}(\cdot)}. \tag{9.70}$$

The $\underline{t}$-matrix elements are also evaluated partially with the coefficients at $\boldsymbol{k}+\boldsymbol{q}$, but have no distinction between the vanishing and non-vanishing reciprocal vector difference, as well as no energy terms. They read

$$t^{(1)\beta j+,(\cdot)'(\cdot)}_{\boldsymbol{G}'_{||}+\boldsymbol{q},\boldsymbol{G}_{||}} = \langle {}^{(\cdot)'\text{vac}}u_{\boldsymbol{G}'_{||},\boldsymbol{k}+\boldsymbol{q}} | V^{(1)\beta j+,\text{vac}}_{\text{eff}}(\boldsymbol{G}'_{||}+\boldsymbol{q}-\boldsymbol{G}_{||},z) | {}^{(\cdot)\text{vac}}u_{\boldsymbol{G}_{||},\boldsymbol{k}} \rangle_{\text{vac}}. \tag{9.71}$$

This concludes the next small set of terms to implement.

Potential Response

The last set of terms, that we need to look at, is the potential response formalism for the thin film - particularly the Coulomb part. Aside from being provided with the response pseudodensity in the same way as the bulk and subsequently using the same formalism as for the ground-state film calculation, there is one main point to keep in mind. While there was a clear distinction between the $\boldsymbol{G}_{||}=\boldsymbol{0}$ and $\boldsymbol{G}_{||}\neq\boldsymbol{0}$ before, the screened Poisson equation now reads

$$\left[\partial_z^2 - |\boldsymbol{G}_{||}+\boldsymbol{q}|^2\right] V_C^{(1)\beta j+}(\boldsymbol{G}_{||}+\boldsymbol{q},z) = -4\pi n^{(1)\beta j+}(\boldsymbol{G}_{||}+\boldsymbol{q},z). \tag{9.72}$$

Since for $\boldsymbol{q}\neq\boldsymbol{0}$, the term $\boldsymbol{G}_{||}+\boldsymbol{q}$ cannot become zero (except for with q-vectors that we would not even want to calculate the DM for), each reciprocal lattice vector is treated with the Green's function formalism. Only for $\boldsymbol{G}_{||}=\boldsymbol{q}=\boldsymbol{0}$ the direct integration must be applied.

Results for the in-Plane Mode

Now that the extension of the FLAPW method to the 2D DFPT case is established, we want to highlight some first promising results that could be obtained from the formalism. For this we look at graphene, the material that single-handedly sparked a renewal of interest in 2D materials [50] that is as of yet unbroken. We want to compare a 3D setup, where the hexagonal monolayer of C atoms is described by periodically repeating layers with a big interlayer distance of $18\ a_0$, which constitutes a pseudo film calculation, to a true 2D film with the new implementation. The film thickness for the latter is chosen as $D = 10\ a_0$, whereas the extent of the plane wave defining unit cell is $\tilde{D} = 12.5\ a_0$. The remaining parameters are habitually given in table 9.7

Aside from this, the reciprocal energy cutoff was set to $10^{-5}$ Ha, as for a cutoff of $10^{-7}$ Ha the film curve dipped slightly towards $M$. With these parameters, we run three calculations. First,

**Table 9.7:** Overview of the specific calculational parameters for graphene. More parameters in section 6.1.

| $N_{k_{x/y/z}}$ | $\ell_{\text{max}}$ | $\ell_{\text{max,nsph}}$ | $N_{\text{MT}}$ | $R_{\text{MT}}$ | dx | $a_{\text{latt}}$ |
|---|---|---|---|---|---|---|
| 24/24/1 | 12 | 10 | 981 | 1.18 $a_0$ | 0.010 | 4.644 $a_0$ |

we want an FD benchmark, for which we do a supercell calculation with an $8 \times 8 \times 1$ supercell. Smaller cells tended to show soft modes that we do not expect in graphene, so we converged the result with respect to the supercell size. Second is the pseudo film calculation in DFPT. Optimally, it matches neatly against the FD benchmark to provide a doubly verified benchmark for the third calculation, which is the 2D run with the newly implemented formalism. Before we look at the full dispersion, we summarize the Goldstone modes of the FD benchmark and the film calculation in table 9.8.

**Table 9.8:** Overview of the acoustic $\Gamma$-point modes, $\omega$, in $\text{cm}^{-1}$ for the 2D graphene film calculation.

| | $\omega_1$ | $\omega_2$ | $\omega_3$ |
|---|---|---|---|
| FD bulk | $-3.46 \times 10^{-2}$ | $-3.46 \times 10^{-2}$ | $-9.46 \times 10^{-6}$ |
| DFPT bulk | $-2.58 \times 10^{0}$ | $-3.57 \times 10^{0}$ | $-2.45 \times 10^{0}$ |
| DFPT film | $-1.58 \times 10^{2}$ | $-2.45 \times 10^{0}$ | $-2.45 \times 10^{0}$ |

As opposed to all previous cases, there is now one significant soft mode for the DFPT film case, while the pseudo film bulk and the FD reference take on sufficiently small values as always. The same holds for the dispersion curve, where we get a soft mode in the true film where the bulk results are stable. We first show only the in-plane modes of the DFPT calculations, they are shown in figure 9.3.

The data from both DFPT calculations agrees nicely. Most points lie nearly perfectly atop each other and there is only one significant discrepancy to discuss. At $K$, there is a significant outlier below the acoustic modes, that instead belongs to the optical regime in the bulk case. Such a deviation at a high-symmetry point is similar to what we have seen for the $\Gamma$-point in several polyatomic materials in this thesis, but it only appears for the film calculation, which suggests the effect does not stem from the same problem. At $\Gamma$ there is in fact a splitting of the optical modes that should actually be a degenerate pair [231], but it is exactly the same in the bulk and film cases. This means aside from the inconsistency at $K$, the true film implementation reproduces the results from the bulk case.

We have yet to closely investigate the deviation at $K$ closely, but there is at least the notion, that in can be connected to the handling of degenerate states in solving the Sternheimer equation. This idea arises from the fact, that the reciprocal energy cutoff needed to be increased for the film as opposed to the bulk setup, which reveals that the eigenenergy spectrum is overall more sensitive to the DFPT procedure. Effects connected to the states, especially for the high-symmetry points where $\boldsymbol{k}$ and $\boldsymbol{k} + \boldsymbol{q}$ form many degenerate pairs of energies, are therefore a plausible cause of the deviation.

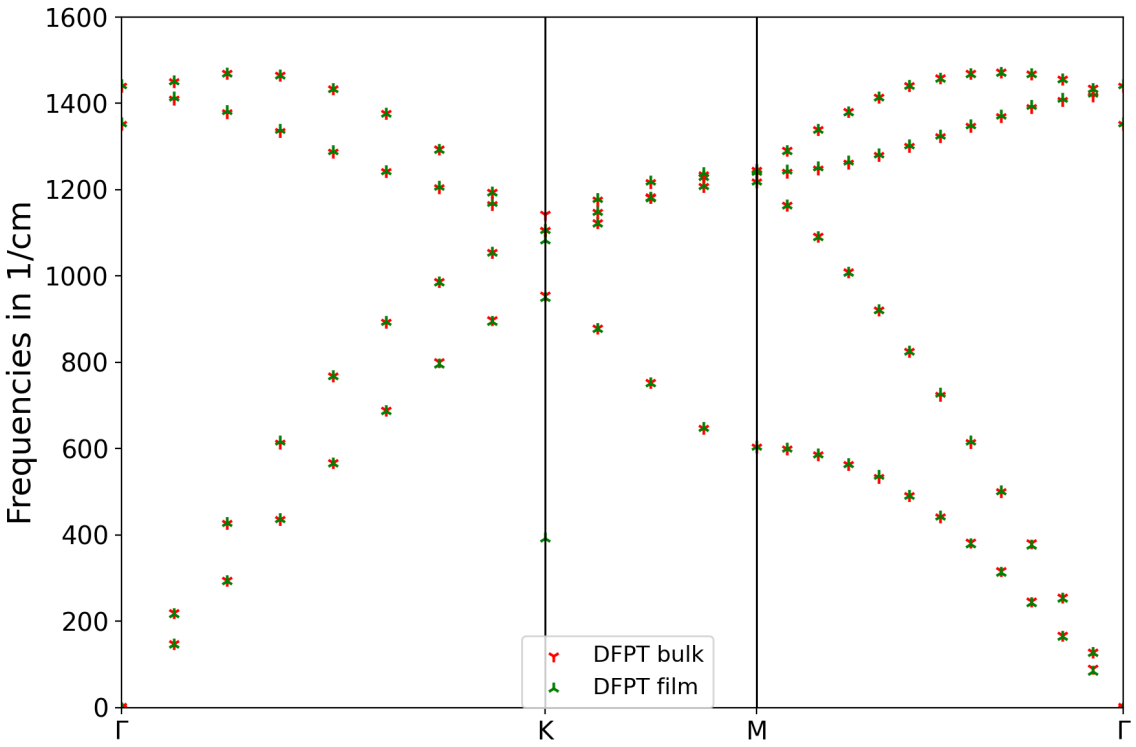



**Figure 9.3:** Phonon dispersions for the in-plane modes of graphene. The red data points belong to the DFPT data of a bulk calculation with far apart layers. The green data points belong to a true film FLAPW calculation.

This concludes the discussion of the in-plane modes in graphene. The investigation into the origin of the soft ZA mode and a mismatch in the corresponding out-of-plane optical mode (ZO) is still ongoing and therefore not in the main part of this thesis. The current situation is instead shown in appendix D.

Chapter 10

# Conclusion

I have implemented in the electronic structure code FLEUR [90, 91], a state-of-the-art realization of the density-functional perturbation theory (DFPT) approach to phonon calculations for the full-potential linearized augmented plane-wave (FLAPW) method [71–73]. It was based on the juPhon plugin, a standalone program developed in the institute PGI-1 of Forschungszentrum Jülich [93]. I have extended this milestone version to a competitive and practical version by (i) replacing the $X\alpha$ method [95] for exchange by the local density approximation (LDA) [105, 106, 108, 109] to the exchange-correlation energy functional, (ii) enabling the treatment of multiple atoms per unit cell (up to 3 atoms per unit cell have been explored), (iii) implementing spin-polarized density-functional perturbation theory to treat materials exhibiting collinear magnetism, (iv) introducing correction terms to the response of the wave function's expansion coefficients that remedied problems present for specific materials like fcc Ne, and (v) implementing new property calculators such as the full phonon bandstructure by q-point interpolation and, based on this, the phonon density of states. All the while, the standalone plugin was reintroduced to the FLEUR code to reduce code redundancy and increase its maintainability. Beyond that, the development of the DFPT for truly two-dimensional slabs embedded in semi-infinite vacua has been initiated, put through a first set of tests, and is currently in progress. This feature will be a valuable tool in the research of 2D quantum materials [30, 49, 50] - especially magnetic ones, as the FLAPW is an appropriate method for this purpose.

I validated the current implementation for a diverse set of materials. The basic monatomic materials improved from the juPhon version included an insulator (fcc Ne) and a metal (fcc Cu). The extension to spin-polarized DFPT allowed a satisfactory validation of a ferromagnetic (FM) metal (fcc Ni) as well. The introduction of an atomic basis for the unit cell led to the successful validation of semiconductors (Si in diamond and SiC in zinc blende structure) and a polyatomic magnetic metal (hcp Co). It was shown that the method provides the same, if not even a higher, quality of results than that of reference calculations performed with the finite displacement (FD) method in conjunction with the phonopy package. For the exemplary material of FM bcc Fe, I demonstrated the robustness of the DFPT method with respect to several parameters such as the convergence threshold for the density response, the LAPW basis cutoff, and the density of the k-point sampling of the Brillouin zone. I showed, that the

convergence of the DFPT results in terms of these cutoff parameters and thresholds is much less costly than the large supercell sizes that must be chosen for the convergence of FD results, and that the latter is neither guaranteed nor smooth. This was explicitly the case for bcc Fe and the transition metal bcc Mo, where I benchmarked the results against experimental data [203] and could easily reproduce it with the DFPT method, while the FD supercells failed to converge to the experimental results. However, it should be noted that at the current state of implementation the FD calculations for small supercells (*e.g.* $2 \times 2 \times 2$ cells) are still a lot faster than their DFPT equivalents. This is due to the maximum possible exploitation of crystal symmetry provided by `phonopy` and `FLEUR`, that is not yet present for the DFPT implementation.

I used the improved implementation to study the behavior of phonons in magnetic materials. For the elemental FM bcc Fe I showed, that a nonmagnetic setup yields a profoundly different phonon dispersion with extremely soft modes that mandate a structural phase transition. This is well in line with the observation, that the local density approximation (LDA) a nonmagnetic structure to be the true ground state for fcc Fe. For both bcc Fe and hcp Co, I analyzed the effect of the lattice constant on the phonon dispersion against that of the magnetic configuration. The key takeaway message is that the shape of the dispersion curve is mainly dictated by the magnetic configuration, while the lattice constants that vary between the two ground states significantly impact the overall magnitude of the curve. The same could be seen more clearly for the rare-earth magnets hcp Gd and bcc Eu. As the lattice constants differ only slightly between their FM and AFM ground states, the impact of the magnetic configuration on the curve shape is a lot more pronounced than the scaling effect. This motivates more future research into the interplay of phonons and magnetism as well as the phonon physics of rare-earth metals in general. The latter group of materials is a field of study, that is mostly reserved to FLAPW due to its all-electron nature and thus FLAPW-DFPT is the optimal tool to further this research.

By implementing the DFPT in the FLAPW method, I advanced a methodology that was barely studied internationally and at our institute [94]. It is natural that on the way to implementation, we encountered a number of numerical difficulties. I was able to solve the problem of outliers in fcc Ne using the reciprocal energy correction, to tame the bcc Mo dispersion that was previously erratic by switching to a different radial integration scheme, to improve the match between the FD and DFPT results for Si, Co, and SiC by moving to bigger supercells in the FD calculations and to impressively show, that DFPT gives an extraordinarily good fit to experimental data for bcc Mo, while the FD approach breaks down for too large supercells. Some other problems that I want to draw attention to here have already been investigated, but not yet solved to our complete satisfaction. Particularly, I want to highlight the deviations from the otherwise smooth dispersion curve at the $\Gamma$-point when there is more than one atom per unit cell involved. The extent of these deviations ranged from negligible (hcp Co, Si), to small (bcc Fe, bcc Eu), to significant (hcp Gd), and finally to large (TMDCs). These deviations were linked to phenomena that play out on the state-dependent level, but whether the problem lies in the eigenenergy responses, the occupation number responses that are formed from them, in the correction terms for near-degenerate energies, or a combination of the three factors is yet to be determined. The second issue of note is the current state of the DFPT thin film implementation. While the in-plane modes overlap nicely with a reference bulk calculation, there are deviations at the high-symmetry points even aside from $\Gamma$. Moreover, the out-of-plane modes deviate in both the acoustic and optical regime. This was linked to an

overlap of both a constant shift (*i.e.* a deviation of the out-of-plane Goldstone mode) and a q-dependent problem at small wave vectors. Both problems are still under active investigation. Another drawback of the current implementation is the runtime. In terms of parallelization, the implementation makes use of everything that is also available for the ground state, like the MPI parallelization over the k-points and the various OMP loops strewn throughout the code. This can be done due to adapting existing routines in contrast to rewriting new ones for each part of the calculation. But the main bottlenecks are the evaluation of the expansion coefficients for the wave function response, that involves all states, and the overall number of necessary Sternheimer self-consistency loops. Both the option to reduce the number of states considered and the reduction of necessary loops by symmetry are currently under consideration.

This concludes the discussion of the current state of development for the FLEUR DFPT implementation. The next steps of advancements may be adapting the various other capabilities of the code. They range from more powerful functional classes like the generalized gradient approximation (GGA) [110–113], to tools for more complex magnetism like the spin-orbit coupling [133, 134] and the possibility of non-collinear magnetism [131, 132] and spin-spirals [205], to explicitly taking strong Coulomb interactions into account through Hubbard $U$, $J$, and $V$ parameters (DFT+U) [135]. This will make the feature just as versatile as the ground-state code is. As a property calculator, it is then crucial to make more results available, such as the electron-phonon coupling [65] *e.g.* to gain insight about superconducting properties of a material [14] and to investigate the relations between complex magnetism and phonon physics (spin-phonon and phonon-magnon interaction) [24, 26, 31, 213, 217]. Another way in which to continue the work is making more thermodynamical quantities available by postprocessing the phonon density of states. DFPT is a general method to calculate second order derivatives to the total energy. Thus, different interactions can be treated. This will necessitate the extension of the formalism to different perturbations than vibrational ones. One example is the response of the system to electric fields [46, 232]. It is currently in development and also gives us access to the Born effective charges and static dielectric tensor needed to augment the phonon dispersions of polar materials with the non-analytical term correction [176, 192].

In summary, the framework presented and validated in this thesis marks a significant step forward for the field of FLAPW-DFPT and the physics of phonons in structurally, chemically, magnetically, and electronically complex materials.

Appendix A

# Further Exploitation of Symmetry

In the late stages of this thesis, we did some additional work with respect to the usage of symmetry to reduce the computational effort of the DFPT procedure. This is the most basic requirement to make it more efficient than the FD reference calculations, which already contain a symmetry reduction and can sometimes be sufficient even with small supercells. The details on the theory and algorithm are pushed to this appendix, as the implementation was not used in any of the results present in the thesis, albeit already being implemented and showing promise.

We start from equation (3.13) and look at a symmetry operation, that leaves the q-point $\boldsymbol{q} = \underline{S} \cdot \boldsymbol{q}$ unchanged and maps the atoms $(\beta', \alpha')$ onto $(\beta, \alpha)$. We additionally shift one of the rotation matrices to the left hand side to find

$$\underline{D}_{\beta',\alpha'}(\boldsymbol{q}) = \mathrm{e}^{\mathrm{i}\boldsymbol{q}\cdot(\boldsymbol{\tau}_{\alpha'}-\boldsymbol{\tau}_{\beta'})}\mathrm{e}^{-\mathrm{i}\boldsymbol{q}\cdot(\boldsymbol{\tau}_{\alpha}-\boldsymbol{\tau}_{\beta})}\underline{S}\,\underline{D}_{\beta,\alpha}(\boldsymbol{q})\,\underline{S}^T \tag{A.1}$$

$$\Leftrightarrow \underline{S}^T\,\underline{D}_{\beta',\alpha'}(\boldsymbol{q}) = \mathrm{e}^{\mathrm{i}\boldsymbol{q}\cdot(\boldsymbol{\tau}_{\alpha'}-\boldsymbol{\tau}_{\beta'})}\mathrm{e}^{-\mathrm{i}\boldsymbol{q}\cdot(\boldsymbol{\tau}_{\alpha}-\boldsymbol{\tau}_{\beta})}\underline{D}_{\beta,\alpha}(\boldsymbol{q})\,\underline{S}^T \tag{A.2}$$

We multiply both sides of this equation from the left with $\hat{\boldsymbol{e}}_j^T$ and write the dynamical matrices component wise, to find

$$\sum_{j'i'} S_{j'j} D^{j',i'}_{\beta',\alpha'}(\boldsymbol{q})\hat{\boldsymbol{e}}^T_{i'} = \mathrm{e}^{\mathrm{i}\boldsymbol{q}\cdot(\boldsymbol{\tau}_{\alpha'}-\boldsymbol{\tau}_{\beta'})}\mathrm{e}^{-\mathrm{i}\boldsymbol{q}\cdot(\boldsymbol{\tau}_{\alpha}-\boldsymbol{\tau}_{\beta})}\sum_k\left[\sum_i D^{j,i}_{\beta,\alpha}(\boldsymbol{q})S_{ki}\right]\hat{\boldsymbol{e}}^T_k. \tag{A.3}$$

This essentially constitutes a linear equation with three (possibly unknown) rows of the dynamical matrix on the left hand side and one known but rotated one on the right hand side. This is a solvable equation, provided we have at most one unknown row on the left hand side that has a non-vanishing prefactor. So there are three things that need to be added to the calculation. First we need to find the reduced group of symmetries that does not affect $\boldsymbol{q}$. Second for each calculated row of the dynamical matrix and each symmetry the rotated right hand side needs to be saved. Third, and most crucially, we need a routine that is called for each new displacement calculation but the first row, where equation (A.3) in checked for a solution. Should such a solution exist, the Sternheimer self consistency loop for this displacement row can be skipped completely by using the one gained by symmetry instead. The workflow of the current implementation is shown in algorithm 2.

**Algorithm 2:** Calculating new DM rows from existing ones.

**Input:** $\beta' j', \{\underline{S}\}, \{\underline{S} \cdot \boldsymbol{D}^{j}_{\beta,\alpha}\}_{\forall\alpha}, \{\boldsymbol{D}^{j}_{\beta,\alpha}\}_{\forall\alpha}$
**Output:** $\{\boldsymbol{D}^{j'}_{\beta',\alpha'}\}_{\forall\alpha'}$
**for** $\alpha$ **do**
  **for** $\beta$ **do**
    **for** $\underline{S}$ **do**
      **if** $\boldsymbol{\tau}_\beta \neq \underline{S}\boldsymbol{\tau}_{\beta'}$ *or* $\boldsymbol{\tau}_\alpha \neq \underline{S}\boldsymbol{\tau}_{\alpha'}$ **then**
        cycle $\underline{S}$
      **end if**
      **for** *available* $j$ **do**
        rhsvec ←$\mathrm{e}^{\mathrm{i}\boldsymbol{q}\cdot(\boldsymbol{\tau}_{\alpha'}-\boldsymbol{\tau}_{\beta'})}\underline{S} \cdot \boldsymbol{D}^{j}_{\beta,\alpha}$;
        i_done ←0;
        i_need ←3;
        **for** $k'$ **do**
          **if** $\boldsymbol{D}^{k'}_{\beta',\alpha'}$ *is available* **then**
            l_done[$k'$] ←true;
            i_done ←i_done + 1;
            l_need[$k'$] ←false;
            i_need ←i_need - 1;
            rhsvec ←rhsvec - $S_{k',j}\boldsymbol{D}^{k'}_{\beta',\alpha'}$;
            cycle $k'$;
          **else**
            **if** $S_{k',j} = 0$ **then**
              l_need[$k'$] ←false;
              i_need ←i_need - 1;
              rhsvec ←rhsvec - $S_{k',j}\boldsymbol{D}^{k'}_{\beta',\alpha'}$;
              cycle $k'$;
            **end if**
          **end if**
          k_need ←$k'$
        **end for**
        **if** $i_{done} = 0/3$ *or* $i_{need} \neq 1$ *or* $|rhsvec|=0$ **then**
          cycle $j$
        **end if**
        **if** $S_{k_{need},j} \neq 0$ **then**
          $\boldsymbol{D}^{k_{\mathrm{need}}}_{\beta',\alpha'}$ ←rhsvec
        **end if**
        cycle $\alpha'$
      **end for**
    **end for**
  **end for**
**end for**

The input quantities are the indices of the new DM row, the set of symmetry operations that leave the q-point unchanged, and the transformed and untransformed rows of the DM, that are already known. The output is the full new row of the DM, in case it is solvable. Currently, this reduction is implemented but not yet used to skip parts of the calculation. Rather, we output the solution by symmetry and compare it to that calculated directly from the Sternheimer cycle. We tested this for the $MoSe_2$ system from chapter 9 to possibly reduce the amount of necessary Sternheimer cycles at each q-point from nine to something lower. For $\boldsymbol{q} \neq \mathbf{0}$ the results agree nicely, with correctly reproduced values across the full sampled dispersion curve. The algorithm manages to shirk four out of nine calculations, foregoing the y-displacement of each of the atoms and the z-displacement of the second Se atom. This is nearly a reduction by half, but we are convinced that the x-displacement of the second Se atom should also be skippable. Furthermore, at $\boldsymbol{q} = \mathbf{0}$ we find mostly correct absolute values up to a negative prefactor on some elements of the matrix, but the results are a lot less accurate than for the finite q-points. Further dissection of the results is warranted.

Appendix B

# Installing and Using FLEUR with DFPT

To use the features that are described in this work, we need to first install a version of FLEUR in which they are all implemented. The presented state-of-the-art can be obtained by cloning the git repository from https://iffgit.fz-juelich.de/fleur/fleur and using the command line git checkout MaX-R7.1 to access the correct version. From there it is the task of the user to correctly compile the code into a working executable as described in the tutorial on flapw.de [90]. There are two additional compile options, that are usually not mandatory but required in the context of DFPT. First, the code must be compiled while linking a version of Hierarchical Data Format library HDF5 [233]. This is because the density responses are written out in this format with no other fallback options. The second mandatory option is compiling with the libxc [171] library of xc functionals, that enables the usage of functionals and their derivatives without hard-coding them into FLEUR itself. As the implementation of functional derivatives to second order (as they are needed by DFPT) for all possible xc functionals would be an excruciating task, there are no plans to lift this requirement.

As mentioned in section 6.1, the input file for our FD calculations needs to take on a specific form. Below we provide an example input file for the $MoSe_2$ calculation in section 9.1, as it is the most complex material analyzed in this work and serves to highlight the parameters that can be set in the basic input file.

```
4_2 MoSe2

&input film=f /

3.327     -3.327      0.0000000000 ! a1
3.327      3.327      0.0000000000 ! a2
0.000      0.000     17.8927192846 ! a3
1.89515158089
0.5 -0.75 1.0

3 ! num atoms
42.1 0.0 0.0 0.0
34.1 1.0 -1.0  0.0942542746
34.1 1.0 -1.0 -0.0942542746
```

```
&factor 3.0 3.0 1.0 /

&atom element="Mo" id=42.1 rmt=2.23 jri=661 dx=0.019 lmax=10
   lnonsph=8 /
&atom element="Se" id=34.1 rmt=2.23 jri=661 dx=0.019 lmax=10
   lnonsph=8 /

&kpt div1=24 div2=24 div3=1 tkb=0.001 /
&exco xctyp='vwn' /
```

The lattice vectors a1-3 are provided in Å, which transform to $a_0$ by a conversion factor of around $1.8897$. The factor provided in the input file is slightly different, as it is multiplied by the factor obtained from the Birch-Murnaghan fit. The interlayer distance in a3 and the z-position of the Se atoms were also optimized, which leads to the long numbers provided in the file. The negative scaling factor of $-0.75$ is read as a factor of $\sqrt{3/4} = \sqrt{3}/2$ by the FLEUR input generator and gives us the correct in-plane hexagonal lattice vectors of $(a/2, \mp\sqrt{3}a/2)^T$. From this input the FD and DFPT calculations can be run according to the workflows described in section 6.1.

Appendix C

# Second Order Coordinate Transformation

Section 5.1 introduced the matrix $\underline{\zeta}$, that relates the Cartesian to the natural coordinates associated to the angular momentum $\ell = 1$. For the analytical second order response terms described in section 5.5, an analogous transformation is needed that takes two directional indices instead of one and belongs to $\ell = 2$ instead. So instead of a $3 \times 3$ matrix, we find a $3 \times 3 \times 5$ object with elements $\chi_{j,i,m}$. The non-vanishing ones are

i) $\chi_{1,1,\pm 2} = \sqrt{4\pi/5}\sqrt{3/2}$,

ii) $\chi_{2,2,\pm 2} = -\sqrt{4\pi/5}\sqrt{3/2}$,

iii) $\chi_{1,2,\pm 2} = \chi_{2,1,\pm 2} = \mp\sqrt{4\pi/5}\sqrt{3/2}\mathrm{i}$,

iv) $\chi_{1,3,\pm 1} = \chi_{3,1,\pm 1} = \mp\sqrt{4\pi/5}\sqrt{3/2}$,

v) $\chi_{2,3,\pm 1} = \chi_{3,2,\pm 1} = \sqrt{4\pi/5}\sqrt{3/2}\mathrm{i}$,

vi) $\chi_{1,1,0} = \chi_{2,2,0} = -\chi_{3,3,0}/2 = -\sqrt{4\pi/5}$,

and the rest of them are zero. With this transformation, the multipole elements can be constructed and inserted into the pseudodenstiy in the same way they were for the first order response.

Appendix D

# Out-of-Plane Modes of the Film DFPT Implementation

We tested the implementation described in section 9.2 for graphene, a hexagonal film of C atoms with a two atom unit cell that forms a honeybomb structure. In this setup, we can once again postulate certain results that are to be expected. Specifically, we expect three acoustic modes starting at $0$ cm$^{-1}$ at the $\Gamma$-point. Furthermore, if we set up the same system as a 3D repeated slab with big spacing between the layers, we expect a very similar phonon dispersion to arise from it. We have managed to fulfill these predictions for the in-plane modes, where we achieved a tight fight between its DFPT run and the 2D DFPT data after increasing the reciprocal eigenenergy cutoff for the corrections to the Sternheimer equation (5.24) to $10^{-5}$ Ha to remedy a kink along the otherwise smooth branches. Something that did not match at all, however, was the out-of-plane mode. It is quite natural, that if a specific part of the calculation causes trouble, it would be this one, as the atomic motion is parallel to the axis perpendicular to the film and should thus prove more numerically challenging. Even in basic DFT self-consistency calculations, shifting the positions of all atoms by the same amount in the $z$-direction can influence the result for the total energy, which is not the case for bulk setups, where translational invariance is guaranteed in each direction. Though some progress in solving this problem was made, it is not yet fully solved. The following appendix serves too highlight our train of thought and approaches to remedy the soft out-of-plane modes.

## D.1 Changes to the Formalism

We investigated this problem very closely and, to start very early into the calculation, analyzed the first order response of the external potential. As our test system is inversion symmetric, the components of the upper and lower vacuum should be identical up to a prefactor. We also expect the $\boldsymbol{G}_{||} = \mathbf{0}$ component to vanish in this region, as it is determined from a density that is $0$ in the vacuum, which is the case for quantities related to the external potential. Due to the construction from the upper vacuum downwards, this was not fulfilled in the case of the potential gradient with respect to $z$ or the response to an atomic displacement in this same direction. The result was a constant vacuum term to first and a linear one to second

order. We have tried several methods to remedy this discrepancy. The initial approach was to forcefully set the lower vacuum component of the gradient and response to $0$ and, for the sake of a continuous result, correct the interstitial part by a linear part with an offset. This improved the situation for the first order quantities, but did not work very well for the second order external potential, which is needed for the ion-ion interaction terms.

As the first method was not very well motivated from a theoretical point of view, but rather served to forcefully correct the anomaly, we came up with a somewhat heuristic motivation that can give us a similar correction. If we start from the defining Poisson equation of the $\boldsymbol{G}_{||} = \mathbf{0}$ potential component and differentiate with respect to $z$, the (pseudo-)density is differentiated as well:

$$\partial_z^2 V_0(z) = -4\pi n_0(z) \tag{D.1}$$
$$\Leftrightarrow \partial_z^2 V_0'(z) = -4\pi n_0'(z) \tag{D.2}$$
$$\Leftrightarrow \partial_z^2 V_0''(z) = -4\pi n_0''(z). \tag{D.3}$$

Taking into account, that the density term is finite only inside the slab, it is discontinuous at the vacuum boundaries. This translates, by differentiation, into two $\delta$-peaks for the derivative density and $\delta'$-terms to second order. Taking these into account gives a linear correction term again and allows for a discontinuity between the vacua and the slab that depends on the pseudodensity of the external potential Poisson equation instead of that for the response. This method served to gain better results for the out-of-plane dispersion, but we could clearly see a discontinuity introduced between the $\boldsymbol{q} = \mathbf{0}$ and $\boldsymbol{q} \neq \mathbf{0}$ contributions to the DM that resulted from Hellmann–Feynman terms, *i.e.* exactly those related to the external potential and its responses. We attribute this to the fact, that we only apply a correction to the $\boldsymbol{G}_{||} = \boldsymbol{q} = \mathbf{0}$ term and no correction whatsoever to the $\boldsymbol{q} \neq \mathbf{0}$ part. Such a correction cannot be inferred from the original potential, as it is strictly defined for $\boldsymbol{q} = \mathbf{0}$. Additionally, constructing only the external potential from the vacuum Poisson solver is sort of problematic, as it wants to normalize the integrated charge of the slab and vacua to $0$, but it should be set to the sum of the ionic charges instead for the external potential. Lastly, saving and carrying the boundary values of the external potential pseudodensity through the code results in additional complexity and optional parameter passing, which is very inelegant.

Hence, we tried a different approach to motivate the correction, that does not rely on extra quantities that would not be present in the potential generation and is also valid for the $\boldsymbol{G}_{||} + \boldsymbol{q} \neq \mathbf{0}$ components. We start from the general defining Poisson equation of the 2D problem and integrate both sides in an $\varepsilon$-perimeter of the boundaries:

$$\left[\partial_z^2 - G_{||}^2\right] V_{\boldsymbol{G}_{||}}(z) = -4\pi n_{\boldsymbol{G}_{||}}(z) \tag{D.4}$$
$$\Leftrightarrow [\partial_z V_{\boldsymbol{G}_{||}}(z)]_{\pm D/2} - G_{||}^2 [\int \mathrm{d}z V_{\boldsymbol{G}_{||}}(z)]_{\pm D/2} = -4\pi [\int \mathrm{d}z\, n_{\boldsymbol{G}_{||}}(z)]_{\pm D/2}. \tag{D.5}$$

If we assume that whatever potential we calculate is discontinuous at most, hence not containing any $\delta$-peaks and the like, the middle term will vanish and we are left with an equation, that relates the jump condition of the potential derivative to the jump of the indefinite integral of the pseudodensity. Since we know the analytic form of this density both in the slab and in the vacua (where it is $0$), we can also express this jump analytically. Defining $\Delta_{\pm}(\boldsymbol{G}_{||})$ as the

jump of a particular component at the upper (+) and lower (−) boundary, we can write

$$\Delta_{\pm}(\boldsymbol{G}_{||}) = -n_{\text{ps}}(\boldsymbol{G} = \boldsymbol{G}_{||})D/2 \pm \sum_{G_{\perp}\neq 0} \mathrm{i} n_{\text{ps}}(\boldsymbol{G}) \frac{\mathrm{e}^{\pm \mathrm{i} G_{\perp} D/2}}{G_{\perp}}. \tag{D.6}$$

We explicitly capture this discontinuity as a $\delta$-contribution to the pseudodensity, meaning it will give explicit contributions to the potential when integrated:

$$n_{\boldsymbol{G}_{||}}(z) \longrightarrow n_{\boldsymbol{G}_{||}}(z) + \delta(z - D/2)\Delta_{+}(\boldsymbol{G}_{||}) + \delta(z + D/2)\Delta_{-}(\boldsymbol{G}_{||}). \tag{D.7}$$

By direct integration, this leads to linear corrections of the external potential in the $\boldsymbol{G}_{||} = \boldsymbol{0}$ case

$$V_0(z) \longrightarrow V_0(z) - 4\pi[(D/2 - z)(1 - \Theta(z - D/2))\Delta_{+}(0) \tag{D.8}$$

$$+(-D/2 - z)(1 - \Theta(z + D/2))\Delta_{-}(0)] \tag{D.9}$$

and contributes a set of Green's function terms for the $\boldsymbol{G}_{||} \neq \boldsymbol{0}$ case

$$V_{\boldsymbol{G}_{||}}(z) \longrightarrow V_{\boldsymbol{G}_{||}}(z) + G(z - D/2)\Delta_{+}(\boldsymbol{G}_{||}) + G(z + D/2)\Delta_{-}(\boldsymbol{G}_{||}). \tag{D.10}$$

The latter of course also directly translates to a possible correction for $\boldsymbol{G}_{||} + \boldsymbol{q} \neq \boldsymbol{0}$. A quick check of this correction for $\boldsymbol{G}_{||} = \boldsymbol{0}$ reveals, that it does not have the desired result. The constant term that exists in the lower vacuum *e.g.* for $\partial_z V_{\text{ext}}$ is given only by $\Sigma_{\text{IR}}$ due to the symmetry of the system. The new correction can be analytically checked to exactly cancel the cosine part in this term. The sine term would require a correction that is of second order, giving a reciprocal term proportional to $G_{\perp}^2$. We thus look at the second order jump condition

$$[V_{\boldsymbol{G}_{||}}(z)]_{\pm D/2} = -4\pi[\int \mathrm{d}z \int \mathrm{d}z\, n_{\boldsymbol{G}_{||}}(z)]_{\pm D/2} \tag{D.11}$$

as well. It can be expressed in terms of discontinuities as

$$\Delta^{(2)}_{\pm}(\boldsymbol{G}_{||}) = \mp n_{\text{ps}}(\boldsymbol{G} = \boldsymbol{G}_{||})D^2/4 \pm \sum_{G_{\perp}\neq 0} n_{\text{ps}}(\boldsymbol{G}) \frac{\mathrm{e}^{\pm \mathrm{i} G_{\perp} D/2}}{G_{\perp}^2} \tag{D.12}$$

and produces corrections

$$V_0(z) \longrightarrow V_0(z) + 4\pi[(1 - \Theta(z - D/2))\Delta^{(2)}_{+}(0) \tag{D.13}$$

$$+(1 - \Theta(z + D/2))\Delta^{(2)}_{-}(0)] \tag{D.14}$$

for $\boldsymbol{G}_{||} = \boldsymbol{0}$ and

$$V_{\boldsymbol{G}_{||}}(z) \longrightarrow V_{\boldsymbol{G}_{||}}(z) + G'(z - D/2)\Delta^{(2)}_{+}(\boldsymbol{G}_{||}) + G'(z + D/2)\Delta^{(2)}_{-}(\boldsymbol{G}_{||}). \tag{D.15}$$

for the $\boldsymbol{G}_{||} \neq \boldsymbol{0}$ components respectively. For the external potential gradient, it can be shown that this form exactly cancels out $\Sigma_{\text{IR}}$ and thus guarantees a vanishing first order. The second order was also checked to vanish.

Introducing these new correction terms yields a similar improvement to the previous approach, but without introducing a discontinuity. This is more favorable, but the results produced with this correction still yield discrepancies between the FD reference and the DFPT data for small

q-vectors. The $\boldsymbol{G}_{||} \neq \mathbf{0}$ does not behave properly when implemented and it stands to reason that there is either a flaw in the derivation or in the current implementation.

Convergence in $G_\perp$

Both attempts at implementing a discontinuity correction raised the question, why such terms become necessary in the first place. *I.e.* why does the pseudodensity become highly discontinuous at the vacuum boundary? The density that goes into the potential generation consists of two parts. Firstly, there is the true plane wave expansion of the electron density (or in this case its response) in the interstitial. This quantity and its vacuum counterpart are constructed from the plane wave and vacuum basis, that are matched against each other to ensure continuity and differentiability. The discontinuities of the density can hence not stem from this contribution. The second contribution is the true "pseudo-" part that expands the MT electronic charge and ionic $\delta$-charges as a smooth plane wave density in the slab and has no contribution in the vacuum. Since this density is tied to step functions for each MT, it is hard to converge with respect to the set of reciprocal lattice vectors $\boldsymbol{G}$. This convergence is tied to a proper localization of the pseudodensity within the MTs and too low cutoffs will make it finite outside this region. This goes especially for the vacuum boundaries as well, which is directly tied to the convergence in the out-of-plane reciprocal lattice vectors. The argument, that the discontinuities arise from an insufficient localization of the pseudodensity is underpinned by the fact that we noted much larger discontinuities for the external potential terms, that are only tied to the ionic charges, as opposed to the Coulomb ones, where the electronic charges contribute as well. In the second case the charges partially compensate each other, which leads to smaller resulting multipole moments. This does nothing to improve the localization of the step function itself, but smaller coefficients of course constitute a smaller overall pseudodensity in real space and thus a smaller discontinuity at the vacuum boundary. So to validate the importance of the plane wave cutoff, we ran test calculations for an increased $G_{\text{max}}$ parameter and an increased film thickness, both of which increase the amount of $\boldsymbol{G}$ chosen especially for the z-direction. This turned out to be beneficial and made the correction negligible, at the cost of increasing the calculation time vastly. We therefore thought of two ways to make this increase in accuracy less costly.

Modifying the Cutoff Behavior

The first option was to look only at the problematic quantities and increase the plane wave cutoff locally for the generation of the external potential responses. This has the benefit of only increasing the runtime at select parts of the run instead of in every calculation of the potential or density. The downside is that this affects the amount of reciprocal lattice vectors for each of the three Cartesian direction, while we explicitly found the out-of-plane convergence to be the relevant one. This means an increase of computational cost that is largely wasteful. The more sophisticated approach we agreed on is the introduction of a new global cutoff parameter $G_{\text{max,z}}$, that governs the selection of the out-of-plane lattice vectors. In practice, the new cutoff changes the selection criterion for the vectors and instead of $|\boldsymbol{G}| < G_{\text{max}}$ we instead use

$$|\boldsymbol{G}_{||}| < G_{\text{max}}, |G_\perp| < G_{\text{max,z}}. \tag{D.16}$$

This way, the vectors are no longer bounded by a sphere in reciprocal space, but rather by an in-plane circle that forms a tube in the out-of-plane direction. The new cutoff parameter can stretch this tube without increasing its in-plane extent, which keeps the amount of $\boldsymbol{G}_{||}$ constant while increasing the accuracy of the z-dependent representation. At cutoffs that we set to same values as the increased ones from the local approach, the results were of the same quality at a fraction of the runtime increase, which promises to be of future use.

## D.2 State-of-the-Art for the out-of-Plane Modes

To conclude this section, we discuss the results that were missing from figure 9.3, *i.e.* the out-of-plane modes and the FD benchmark. Aside from that, we show an additional data set, where the out-of-plane modes were corrected by the offset at $\Gamma$ according to the acoustic sum rule. This results in figure D.1.

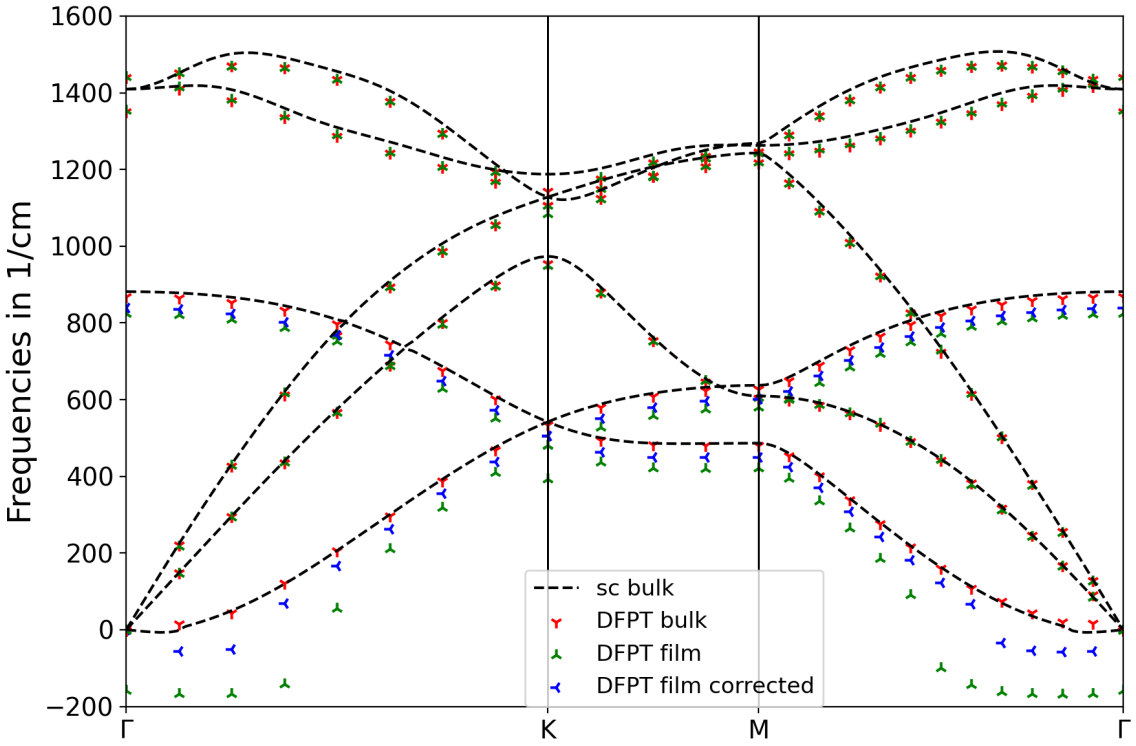



**Figure D.1:** Phonon dispersions for graphene. The red data points belong to the DFPT data and the black dashed lines represent the FD benchmark of a bulk calculation (both with far apart layers). The green and blue data points belong to a true film FLAPW calculation, where the latter have been corrected by the offset of the $\Gamma$-point.

For the benchmark curves, the DFPT bulk data agrees nicely with the FD reference aside from the $\Gamma$-point. This is likely due to the same reason as in the metallic systems in chapter 8 and the materials in the previous section 9.1, where only $\Gamma$ showed modes that deviated from the trend given by the sample points in its vicinity. The need for further investigations into this problem has already been noted. Moving on to the film, while the direct result of the 2D calculation shows a significant soft mode across the full sampled path through the BZ and an offset in the out-of-plane optical mode, enforcing the acoustic sum rule is very beneficial for it. The correction shifts the mismatched optical mode slightly upwards and moves the soft mode closer to the oscillatory regime. The resulting data points (shown in blue for these particular branches) do, however, not remedy the underlying problem. The ZO mode is not matched and the ZA mode still gives imaginary frequencies close to $\Gamma$. So there is more at hand than a simple offset problem. This can be made even more evident by applying a different correction. The film ZO mode seems to be shifted from the bulk one somewhat constantly, so if we shift

the out-of-plane film modes by the offset of the ZO mode at $\Gamma$ instead of enforcing the acoustic sum rule, we arrive at a different result, shown in figure D.2.

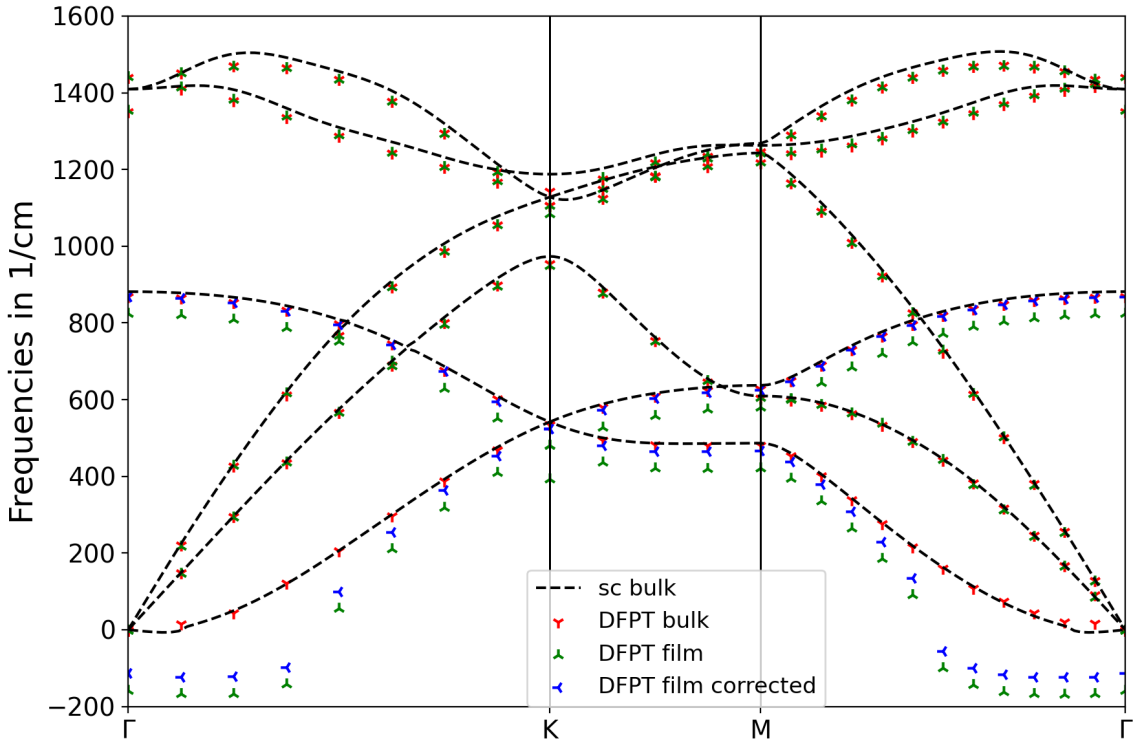



**Figure D.2:** Phonon dispersions for graphene. The red data points belong to the DFPT data and the black dashed lines represent the FD benchmark of a bulk calculation (both with far apart layers). The green and blue data points belong to a true film FLAPW calculation, where the latter have been corrected by the ZO offset of the $\Gamma$-point.

The applied correction serves to improve the ZO mode vastly. Far away from $\Gamma$, the ZA mode is also improved, which leads us to the conclusion that there are two superposed problems at hand. On the one hand there is a small constant shift in the out-of-plane modes, on the other hand there is a deviation that becomes increasingly large for smaller q-points. This is in line with the fact, that the correction terms for $\boldsymbol{G}_{||} + \boldsymbol{q} \neq \boldsymbol{0}$ we derived did not yield an improvement for the calculation and are thus not applied at the moment.

Outlook

The present implementation of the thin film DFPT formalism serves as a starting point for future development. Specifically we are interested in the modification of the phonon dispersion due to the application of external electric or magnetic fields. Considering the former, they inherently break the 3D periodicity of the bulk system by contributing a potential term that depends on the position vector $\boldsymbol{r}$, but in a film setup a linear potential term in with respect to $z$, *i.e.* an electric field that is parallel to the out-of-plane axis does not pose a problem. So even if it turns out that the 2D formalism cannot be used to achieve a speed-up for film calculations, it would still be valuable to study the phonon physics under an external influence, likely once the NAC has been implemented to properly describe polar materials at all q-points.

# Bibliography


[1] Max Born and Kun Huang. *Dynamical Theory of Crystal Lattices*. Oxford University Press, London, 1954.

[2] N. W. Ashcroft and N. D. Mermin. *Solid State Physics*. Holt-Saunders, 1976.

[3] G. Venkataraman, L. Feldkamp, and V.C. Sahni. *Dynamics of Perfect Crystals*. MIT Press, 1975.

[4] G.P. Srivastava. *The Physics of Phonons*. 1st ed. Taylor and Francis, 1990. DOI: 10.1201/9780203736241.

[5] P. Y. Yu and M. Cardona. *Fundamentals of Semiconductors. Physics and Materials Properties*. 4th ed. Springer Berlin, 2010. DOI: 10.1007/978-3-642-00710-1.

[6] B. N. Brockhouse and A. T. Stewart. "Scattering of Neutrons by Phonons in an Aluminum Single Crystal." In: *Phys. Rev.* 100 (2 Oct. 1955), pp. 756–757. DOI: 10.1103/PhysRev.100.756.

[7] B. N. Brockhouse et al. "Crystal Dynamics of Lead. I. Dispersion Curves at 100°K." In: *Phys. Rev.* 128 (3 Nov. 1962), pp. 1099–1111. DOI: 10.1103/PhysRev.128.1099.

[8] Bertram N. Brockhouse. "Slow neutron spectroscopy and the grand atlas of the physical world." In: *Rev. Mod. Phys.* 67 (4 Oct. 1995), pp. 735–751. DOI: 10.1103/RevModPhys.67.735.

[9] B. Dorner et al. "First measurement of a phonon dispersion curve by inelastic X-ray scattering." In: *Zeitschrift für Physik B Condensed Matter* 69.2 (June 1987), pp. 179–183. ISSN: 1431-584X. DOI: 10.1007/BF01307274. URL: https://doi.org/10.1007/BF01307274.

[10] R. Colella and B. W. Batterman. "X-Ray Determination of Phonon Dispersion in Vanadium." In: *Phys. Rev. B* 1 (10 May 1970), pp. 3913–3921. DOI: 10.1103/PhysRevB.1.3913.

[11] M. Mohr et al. "Phonon dispersion of graphite by inelastic x-ray scattering." In: *Phys. Rev. B* 76 (3 July 2007), p. 035439. DOI: 10.1103/PhysRevB.76.035439.

[12] J T Gourley and W A Runciman. "Multiphonon infrared absorption spectra of MgO and CaO." In: *Journal of Physics C: Solid State Physics* 6.3 (Feb. 1973), p. 583. DOI: 10.1088/0022-3719/6/3/021. URL: https://dx.doi.org/10.1088/0022-3719/6/3/021.

[13] R. Saito et al. "Probing Phonon Dispersion Relations of Graphite by Double Resonance Raman Scattering." In: *Phys. Rev. Lett.* 88 (2 Dec. 2001), p. 027401. DOI: 10.1103/PhysRevLett.88.027401.

[14] J. Bardeen, L. N. Cooper, and J. R. Schrieffer. “Microscopic Theory of Superconductivity.” In: *Phys. Rev.* 106 (1 Apr. 1957), pp. 162–164. DOI: 10.1103/PhysRev.106.162.

[15] Gerald D. Mahan. *Many-Particle Physics*. Springer US, 2000. DOI: 10.1007/978-1-4757-5714-9.

[16] R H Olsson III and I El-Kady. “Microfabricated phononic crystal devices and applications.” In: *Measurement Science and Technology* 20.1 (Nov. 2008), p. 012002. DOI: 10.1088/0957-0233/20/1/012002.

[17] Xiang Li et al. “Designing phononic crystal with anticipated band gap through a deep learning based data-driven method.” In: *Computer Methods in Applied Mechanics and Engineering* 361 (2020), p. 112737. DOI: 10.1016/j.cma.2019.112737.

[18] Xuetao Zhu et al. “Classification of charge density waves based on their nature.” In: *Proceedings of the National Academy of Sciences* 112.8 (2015), pp. 2367–2371. DOI: 10.1073/pnas.1424791112.

[19] Woochul Kim. “Strategies for engineering phonon transport in thermoelectrics.” In: *J. Mater. Chem. C* 3 (40 2015), pp. 10336–10348. DOI: 10.1039/C5TC01670C.

[20] Jino Im, Choong H. Kim, and Hosub Jin. “Ferroelectricity-Driven Phonon Berry Curvature and Nonlinear Phonon Hall Transports.” In: *Nano Letters* 22.20 (Oct. 2022), pp. 8281–8286. ISSN: 1530-6984. DOI: 10.1021/acs.nanolett.2c03095.

[21] D. Abergel et al. “Properties of Graphene: A Theoretical Perspective.” In: *Adv. Phys.* 59 (Mar. 2010). DOI: 10.1080/00018732.2010.487978.

[22] Xiaokun Gu and Ronggui Yang. “Phonon transport and thermal conductivity in two-dimensional materials.” In: *Annual Review of Heat Transfer* 19.1 (2016), pp. 1–65. DOI: 10.1615/annualrevheattransfer.2016015491.

[23] Jialin Gong et al. “Dirac phonons in two-dimensional materials.” In: *Physical Review B* 106.21 (Dec. 2022). DOI: 10.1103/physrevb.106.214317.

[24] Mingqiang Gu et al. “Spin–phonon dispersion in magnetic materials.” In: *Journal of Physics: Condensed Matter* 34.37 (July 2022), p. 375802. DOI: 10.1088/1361-648X/ac7f17.

[25] Alessandro Lunghi. “Toward exact predictions of spin-phonon relaxation times: An ab initio implementation of open quantum systems theory.” In: *Science Advances* 8.31 (2022), eabn7880. DOI: 10.1126/sciadv.abn7880.

[26] Simon Streib et al. “Magnon-phonon interactions in magnetic insulators.” In: *Phys. Rev. B* 99 (18 May 2019), p. 184442. DOI: 10.1103/PhysRevB.99.184442.

[27] Sebastian F. Maehrlein et al. “Dissecting spin-phonon equilibration in ferrimagnetic insulators by ultrafast lattice excitation.” In: *Science Advances* 4.7 (2018). DOI: 10.1126/sciadv.aar5164.

[28] A. Stupakiewicz et al. “Ultrafast phononic switching of magnetization.” In: *Nature Physics* 17.4 (Jan. 2021), pp. 489–492. DOI: 10.1038/s41567-020-01124-9.

[29] C. S. Davies et al. *Phononic Switching of Magnetization by the Ultrafast Barnett Effect*. 2023.

[30] Hanyu Zhu et al. “Observation of chiral phonons.” en. In: *Science* 359.6375 (Feb. 2018), pp. 579–582.

[31] C. H. Sohn et al. “Strong Spin-Phonon Coupling Mediated by Single Ion Anisotropy in the All-In–All-Out Pyrochlore Magnet $Cd_2Os_2O_7$.” In: *Phys. Rev. Lett.* 118 (11 Mar. 2017), p. 117201. DOI: 10.1103/PhysRevLett.118.117201.

[32] Dongwook Go et al. “Orbitronics: Orbital currents in solids.” In: *EPL (Europhysics Letters)* 135.3 (Aug. 2021), p. 37001. DOI: 10.1209/0295-5075/ac2653.

[33] Xiaoou Zhang et al. “Thermal Hall Effect Induced by Magnon-Phonon Interactions.” In: *Phys. Rev. Lett.* 123.16 (Oct. 2019), p. 167202. DOI: 10.1103/PhysRevLett.123.167202.

[34] P. Hohenberg and W. Kohn. “Inhomogeneous Electron Gas.” In: *Phys. Rev.* 136 (3B Nov. 1964), B864–B871. DOI: 10.1103/PhysRev.136.B864.

[35] W. Kohn and L. J. Sham. “Self-Consistent Equations Including Exchange and Correlation Effects.” In: *Phys. Rev.* 140 (4A Nov. 1965), A1133–A1138. DOI: 10.1103/PhysRev.140.A1133.

[36] W. Kohn. “Nobel Lecture: Electronic structure of matter—wave functions and density functionals.” In: *Rev. Mod. Phys.* 71 (5 Oct. 1999), pp. 1253–1266. DOI: 10.1103/RevModPhys.71.1253.

[37] Axel D. Becke. “Perspective: Fifty years of density-functional theory in chemical physics.” In: *J. Chem. Phys.* 140.18A301 (2014). DOI: 10.1063/1.4869598.

[38] R. O. Jones. “Density functional theory: Its origins, rise to prominence, and future.” In: *Rev. Mod. Phys.* 87.3 (Aug. 2015), pp. 897–923. DOI: 10.1103/RevModPhys.87.897.

[39] S. L. Chaplot, Mittal R., and N. Choudhury. *Thermodynamic Properties of Solids: Experiment and Modeling*. WILEY-VCH Verlag GmbH and Co. KGaA, 2010.

[40] K. Kunc and R. M. Martin. “Ab Initio Force Constants of Germanium.” In: *J. Phys. Colloques* 42.C6 (1981), pp. 649–651. DOI: 10.1051/jphyscol:19816189.

[41] K. Kunc and Richard M. Martin. “Ab Initio Force Constants of GaAs: A New Approach to Calculation of Phonons and Dielectric Properties.” In: *Phys. Rev. Lett.* 48.6 (Feb. 1982), pp. 406–409. DOI: 10.1103/PhysRevLett.48.406.

[42] Siqing Wei and M. Y. Chou. “Ab initio calculation of force constants and full phonon dispersions.” In: *Phys. Rev. Lett.* 69.19 (Nov. 1992), pp. 2799–2802. DOI: 10.1103/PhysRevLett.69.2799.

[43] N. E. Zein. “Density Functional Calculations of Elastic Moduli and Phonon Spectra of Crystals.” In: *Fiz. Tverd. Tela* 26 (1984), p. 3024. English Translation in Sov. Phys. Solid State 26.10 (1984), pp. 1825-1828.

[44] Stefano Baroni, Paolo Giannozzi, and Andrea Testa. “Green’s-function approach to linear response in solids.” In: *Phys. Rev. Lett.* 58.18 (May 1987), pp. 1861–1864. DOI: 10.1103/PhysRevLett.58.1861.

[45] X. Gonze and J.-P. Vigneron. “Density-functional approach to nonlinear-response coefficients of solids.” In: *Phys. Rev. B* 39.18 (June 1989), pp. 13120–13128. DOI: 10.1103/PhysRevB.39.13120.

[46] Xavier Gonze. “First-principles responses of solids to atomic displacements and homogeneous electric fields: Implementation of a conjugate-gradient algorithm.” In: *Phys. Rev. B* 55.16 (Apr. 1997), pp. 10337–10354. DOI: 10.1103/PhysRevB.55.10337.

[47] Stefano Baroni et al. “Phonons and related crystal properties from density-functional perturbation theory.” In: *Rev. Mod. Phys.* 73.2 (July 2001), pp. 515–562. DOI: 10.1103/RevModPhys.73.515.

[48] F. Kuroda, T. Fukushima, and T. Oguchi. “First-principles study of magnetism and phase stabilities of V2 based antiferromagnetic Heusler alloys.” In: *Journal of Applied Physics* 127.19 (May 2020). 193904. ISSN: 0021-8979. DOI: 10.1063/1.5143826.

[49] Ali Kandemir et al. “Thermal transport properties of MoS2 and MoSe2 monolayers.” In: *Nanotechnology* 27.5 (Jan. 2016), p. 055703. DOI: 10.1088/0957-4484/27/5/055703.

[50] Wonbong Choi et al. “Recent development of two-dimensional transition metal dichalcogenides and their applications.” In: *Materials Today* 20.3 (2017), pp. 116–130. ISSN: 1369-7021. DOI: https://doi.org/10.1016/j.mattod.2016.10.002.

[51] F.J. Di Salvo J.A. Wilson and S. Mahajan. “Charge-density waves and superlattices in the metallic layered transition metal dichalcogenides.” In: *Advances in Physics* 24.2 (1975), pp. 117–201. DOI: 10.1080/00018737500101391.

[52] Nicholas A. Pike et al. “Vibrational and dielectric properties of the bulk transition metal dichalcogenides.” In: *Phys. Rev. Mater.* 2 (6 June 2018), p. 063608. DOI: 10.1103/PhysRevMaterials.2.063608.

[53] D. R. Hamann, M. Schlüter, and C. Chiang. “Norm-Conserving Pseudopotentials.” In: *Phys. Rev. Lett.* 43 (20 Nov. 1979), pp. 1494–1497. DOI: 10.1103/PhysRevLett.43.1494.

[54] D. R. Hamann. “Semiconductor Charge Densities with Hard-Core and Soft-Core Pseudopotentials.” In: *Phys. Rev. Lett.* 42 (10 Mar. 1979), pp. 662–665. DOI: 10.1103/PhysRevLett.42.662.

[55] Leonard Kleinman and D. M. Bylander. “Efficacious Form for Model Pseudopotentials.” In: *Phys. Rev. Lett.* 48 (20 May 1982), pp. 1425–1428. DOI: 10.1103/PhysRevLett.48.1425.

[56] N. Troullier and José Luriaas Martins. “Efficient pseudopotentials for plane-wave calculations.” In: *Phys. Rev. B* 43 (3 Jan. 1991), pp. 1993–2006. DOI: 10.1103/PhysRevB.43.1993.

[57] X. Gonze et al. “First-principles computation of material properties: the ABINIT software project.” In: *Computational Materials Science* 25.3 (2002), pp. 478–492. DOI: 10.1016/S0927-0256(02)00325-7.

[58] M D Segall et al. “First-principles simulation: ideas, illustrations and the CASTEP code.” In: *Journal of Physics: Condensed Matter* 14.11 (Mar. 2002), p. 2717. DOI: 10.1088/0953-8984/14/11/301.

[59] Matthieu J. Verstraete et al. “Density functional perturbation theory with spin-orbit coupling: Phonon band structure of lead.” In: *Phys. Rev. B* 78 (4 July 2008), p. 045119. DOI: 10.1103/PhysRevB.78.045119.

[60] Xavier Andrade et al. “Time-dependent density-functional theory in massively parallel computer architectures: the octopus project.” In: *Journal of Physics: Condensed Matter* 24.23 (May 2012), p. 233202. DOI: 10.1088/0953-8984/24/23/233202.

[61] Andrea Dal Corso. "Density-functional perturbation theory with ultrasoft pseudopotentials." In: *Phys. Rev. B* 64 (23 Nov. 2001), p. 235118. DOI: 10.1103/PhysRevB.64.235118.

[62] Andrea Dal Corso and Adriano Mosca Conte. "Spin-orbit coupling with ultrasoft pseudopotentials: Application to Au and Pt." In: *Phys. Rev. B* 71 (11 Mar. 2005), p. 115106. DOI: 10.1103/PhysRevB.71.115106.

[63] Andrea Dal Corso. "Density functional perturbation theory for lattice dynamics with fully relativistic ultrasoft pseudopotentials: Application to fcc-Pt and fcc-Au." In: *Phys. Rev. B* 76 (5 Aug. 2007), p. 054308. DOI: 10.1103/PhysRevB.76.054308.

[64] Andrea Dal Corso. "Density functional perturbation theory within the projector augmented wave method." In: *Phys. Rev. B* 81 (7 Feb. 2010), p. 075123. DOI: 10.1103/PhysRevB.81.075123.

[65] Matthieu J Verstraete. "Ab initio calculation of spin-dependent electron–phonon coupling in iron and cobalt." In: *Journal of Physics: Condensed Matter* 25.13 (Mar. 2013), p. 136001. DOI: 10.1088/0953-8984/25/13/136001.

[66] Andrea Dal Corso and Stefano de Gironcoli. "Ab initio phonon dispersions of Fe and Ni." In: *Phys. Rev. B* 62 (1 July 2000), pp. 273–277. DOI: 10.1103/PhysRevB.62.273.

[67] Andrea Dal Corso. "Projector augmented-wave method: Application to relativistic spin-density functional theory." In: *Phys. Rev. B* 82 (7 Aug. 2010), p. 075116. DOI: 10.1103/PhysRevB.82.075116.

[68] Andrea Urru and Andrea Dal Corso. "Density functional perturbation theory for lattice dynamics with fully relativistic ultrasoft pseudopotentials: The magnetic case." In: *Phys. Rev. B* 100 (4 July 2019), p. 045115. DOI: 10.1103/PhysRevB.100.045115.

[69] Fabio Ricci et al. "Density functional perturbation theory within noncollinear magnetism." In: *Phys. Rev. B* 99 (18 May 2019), p. 184404. DOI: 10.1103/PhysRevB.99.184404.

[70] Xavier Gonze et al. "The Abinit project: Impact, environment and recent developments." In: *Computer Physics Communications* 248 (2020), p. 107042. DOI: 10.1016/j.cpc.2019.107042.

[71] O. Krogh Andersen. "Linear methods in band theory." In: *Phys. Rev. B* 12 (8 Oct. 1975), pp. 3060–3083. DOI: 10.1103/PhysRevB.12.3060.

[72] D D Koelling and G O Arbman. "Use of energy derivative of the radial solution in an augmented plane wave method: application to copper." In: *Journal of Physics F: Metal Physics* 5.11 (Nov. 1975), p. 2041. DOI: 10.1088/0305-4608/5/11/016.

[73] E. Wimmer et al. "Full-potential self-consistent linearized-augmented-plane-wave method for calculating the electronic structure of molecules and surfaces: $O_2$ molecule." In: *Phys. Rev. B* 24.2 (July 1981), pp. 864–875. DOI: 10.1103/PhysRevB.24.864.

[74] Kurt Lejaeghere et al. "Reproducibility in density functional theory calculations of solids." In: *Science* 351.6280 (2016), aad3000. DOI: 10.1126/science.aad3000.

[75] Emanuele Bosoni et al. "How to verify the precision of density-functional-theory implementations via reproducible and universal workflows." In: *Nature Reviews Physics* 6.1 (Jan. 2024), pp. 45–58. ISSN: 2522-5820. DOI: 10.1038/s42254-023-00655-3.

[76] Uliana Alekseeva et al. “Hybrid Parallelization and Performance Optimization of the FLEUR Code: New Possibilities for All-Electron Density Functional Theory.” In: *Euro-Par 2018: Parallel Processing*. Ed. by Marco Aldinucci, Luca Padovani, and Massimo Torquati. Cham: Springer International Publishing, 2018, pp. 735–748. ISBN: 978-3-319-96983-1.

[77] Volker Eyert. “The Plane-Wave Based Full-Potential ASW Method.” In: *The Augmented Spherical Wave Method: A Comprehensive Treatment*. Lecture Notes in Physics. Berlin, Heidelberg: Springer Berlin Heidelberg, 2013, pp. 113–172. ISBN: 978-3-642-25864-0. DOI: 10.1007/978-3-642-25864-0_4.

[78] Dimitar Pashov et al. “Questaal: A package of electronic structure methods based on the linear muffin-tin orbital technique.” In: *Computer Physics Communications* 249 (2020), p. 107065. ISSN: 0010-4655. DOI: https://doi.org/10.1016/j.cpc.2019.107065.

[79] N Papanikolaou, R Zeller, and P H Dederichs. “Conceptual improvements of the KKR method.” In: *Journal of Physics: Condensed Matter* 14.11 (Mar. 2002), pp. 2799–2823. DOI: 10.1088/0953-8984/14/11/304.

[80] Rici Yu, D. Singh, and H. Krakauer. “All-electron and pseudopotential force calculations using the linearized-augmented-plane-wave method.” In: *Phys. Rev. B* 43.8 (Mar. 1991), pp. 6411–6422. DOI: 10.1103/PhysRevB.43.6411.

[81] Daniel A. Klüppelberg, Markus Betzinger, and Stefan Blügel. “Atomic force calculations within the all-electron FLAPW method: Treatment of core states and discontinuities at the muffin-tin sphere boundary.” In: *Phys. Rev. B* 91 (3 Jan. 2015), p. 035105. DOI: 10.1103/PhysRevB.91.035105.

[82] Rici Yu and H. Krakauer. “Linear-response calculations within the linearized augmented plane-wave method.” In: *Phys. Rev. B* 49.7 (Feb. 1994), pp. 4467–4477. DOI: 10.1103/PhysRevB.49.4467.

[83] S. Y. Savrasov. “Linear-response theory and lattice dynamics: A muffin-tin-orbital approach.” In: *Phys. Rev. B* 54.23 (Dec. 1996), pp. 16470–16486. DOI: 10.1103/PhysRevB.54.16470.

[84] Henry Krakauer, Rici Yu, and Cheng-Zhang Wang. “Ab initio linear response calculations of lattice dynamics using an LAPW basis.” In: *International Journal of Quantum Chemistry* 56.S29 (1995), pp. 131–136. DOI: https://doi.org/10.1002/qua.560560813.

[85] Cheng-Zhang Wang, Rici Yu, and Henry Krakauer. “First-principles calculations of phonon dispersion and lattice dynamics in $La_2CuO_4$.” In: *Phys. Rev. B* 59 (14 Apr. 1999), pp. 9278–9284. DOI: 10.1103/PhysRevB.59.9278.

[86] R. Kouba et al. “Phonons and electron-phonon interaction by linear-response theory within the LAPW method.” In: *Phys. Rev. B* 64.18 (Aug. 2001), p. 184306. DOI: 10.1103/PhysRevB.64.184306.

[87] J. H. Lee. “First-principles Linear Response All-Electron FLAPW Study of Lattice Dynamics/phonons and the Effect of Magnetism.” PhD thesis. Northwesterns University, 2005.

[88] Joo-Hyoung Lee, Young-Chung Hsue, and Arthur J. Freeman. “Magnetically induced variations in phonon frequencies.” In: *Phys. Rev. B* 73 (17 May 2006), p. 172405. DOI: 10.1103/PhysRevB.73.172405.

[89] J.-H. Lee and A.J. Freeman. “Spin-induced variations of phonon frequencies in ferromagnetic metals.” In: *Journal of Magnetism and Magnetic Materials* 310.2, Part 2 (2007). Proceedings of the 17th International Conference on Magnetism, pp. 1084–1086. ISSN: 0304-8853. DOI: https://doi.org/10.1016/j.jmmm.2006.10.728.

[90] *The FLEUR project*. https://www.flapw.de/.

[91] Daniel Wortmann et al. *FLEUR*. Version MaX-R6.2. May 2023. DOI: 10.5281/zenodo.7891361. URL: https://doi.org/10.5281/zenodo.7891361.

[92] Daniel Aaron Klüppelberg. “First-principle investigation of displacive response in complex solids.” Dissertation, RWTH Aachen University, 2015. Dissertation. Jülich: RWTH Aachen, 2016, XI, 177 S. ISBN: 978-3-95806-123-1. URL: http://hdl.handle.net/2128/10020.

[93] Christian-Roman Gerhorst. “Density-Functional Perturbation Theory within the All-Electron Full-Potential Linearized Augmented Plane-Wave Method: Application to Phonons.” Dissertation, RWTH Aachen University, 2022. Dissertation. Jülich: RWTH Aachen University, 2022, pp. xvi, 317. ISBN: 978-3-95806-649-6. URL: http://hdl.handle.net/2128/31894.

[94] Christian-Roman Gerhorst et al. “Phonons from density-functional perturbation theory using the all-electron full-potential linearized augmented plane-wave method FLEUR*.” In: *Electronic Structure* 6.1 (Jan. 2024), p. 017001. DOI: 10.1088/2516-1075/ad1614.

[95] J. C. Slater. “A Simplification of the Hartree-Fock Method.” In: *Phys. Rev.* 81 (3 Feb. 1951), pp. 385–390. DOI: 10.1103/PhysRev.81.385.

[96] Paul Adrien Maurice Dirac and Ralph Howard Fowler. “Quantum mechanics of many-electron systems.” In: *Proceedings of the Royal Society of London. Series A, Containing Papers of a Mathematical and Physical Character* 123.792 (1929), pp. 714–733. DOI: 10.1098/rspa.1929.0094. eprint: https://royalsocietypublishing.org/doi/pdf/10.1098/rspa.1929.0094. URL: https://royalsocietypublishing.org/doi/abs/10.1098/rspa.1929.0094.

[97] M. Born and R. Oppenheimer. “Zur Quantentheorie der Molekeln.” In: *Annalen der Physik* 389.20 (1927), pp. 457–484. DOI: https://doi.org/10.1002/andp.19273892002. eprint: https://onlinelibrary.wiley.com/doi/pdf/10.1002/andp.19273892002. URL: https://onlinelibrary.wiley.com/doi/abs/10.1002/andp.19273892002.

[98] V. Fock. “Näherungsmethode zur Lösung des quantenmechanischen Mehrkörperproblems.” In: *Zeitschrift für Physik* 61.1 (Jan. 1930), pp. 126–148. ISSN: 0044-3328. DOI: 10.1007/BF01340294. URL: https://doi.org/10.1007/BF01340294.

[99] W. Pauli. “Über den Zusammenhang des Abschlusses der Elektronengruppen im Atom mit der Komplexstruktur der Spektren.” In: *Zeitschrift für Physik* 31.1 (Feb. 1925), pp. 765–783. ISSN: 0044-3328. DOI: 10.1007/BF02980631. URL: https://doi.org/10.1007/BF02980631.

[100] Chr. Møller and M. S. Plesset. “Note on an Approximation Treatment for Many-Electron Systems.” In: *Phys. Rev.* 46 (7 Oct. 1934), pp. 618–622. DOI: 10.1103/PhysRev.46.618.

[101] Jiří Čížek. “On the Correlation Problem in Atomic and Molecular Systems. Calculation of Wavefunction Components in Ursell-Type Expansion Using Quantum-Field Theoretical Methods.” In: *The Journal of Chemical Physics* 45.11 (Dec. 1966), pp. 4256–4266. ISSN: 0021-9606. DOI: 10.1063/1.1727484.

[102] C. David Sherrill and Henry F. Schaefer. “The Configuration Interaction Method: Advances in Highly Correlated Approaches.” In: ed. by Per-Olov Löwdin et al. Vol. 34. Advances in Quantum Chemistry. Academic Press, 1999, pp. 143–269. DOI: https://doi.org/10.1016/S0065-3276(08)60532-8.

[103] P. A. M. Dirac. “Note on Exchange Phenomena in the Thomas Atom.” In: *Mathematical Proceedings of the Cambridge Philosophical Society* 26.3 (1930), pp. 376–385. DOI: 10.1017/S0305004100016108.

[104] R.G. Parr and Y. Weitao. *Density-Functional Theory of Atoms and Molecules*. International Series of Monographs on Chemistry. Oxford University Press, 1989. ISBN: 9780199878727.

[105] D. M. Ceperley and B. J. Alder. “Ground State of the Electron Gas by a Stochastic Method.” In: *Phys. Rev. Lett.* 45 (7 Aug. 1980), pp. 566–569. DOI: 10.1103/PhysRevLett.45.566.

[106] U. von Barth and L. Hedin. “A local exchange-correlation potential for the spin polarized case. i.” In: *Journal of Physics C: Solid State Physics* 5.13 (July 1972), p. 1629. DOI: 10.1088/0022-3719/5/13/012.

[107] J. P. Perdew and Alex Zunger. “Self-interaction correction to density-functional approximations for many-electron systems.” In: *Phys. Rev. B* 23 (10 May 1981), pp. 5048–5079. DOI: 10.1103/PhysRevB.23.5048.

[108] John P. Perdew and Yue Wang. “Accurate and simple analytic representation of the electron-gas correlation energy.” In: *Phys. Rev. B* 45 (23 June 1992), pp. 13244–13249. DOI: 10.1103/PhysRevB.45.13244.

[109] S. H. Vosko, L. Wilk, and M. Nusair. “Accurate spin-dependent electron liquid correlation energies for local spin density calculations: a critical analysis.” In: *Canadian Journal of Physics* 58.8 (1980), pp. 1200–1211. DOI: 10.1139/p80-159.

[110] David C. Langreth and M. J. Mehl. “Beyond the local-density approximation in calculations of ground-state electronic properties.” In: *Phys. Rev. B* 28 (4 Aug. 1983), pp. 1809–1834. DOI: 10.1103/PhysRevB.28.1809.

[111] A. D. Becke. “Density-functional exchange-energy approximation with correct asymptotic behavior.” In: *Phys. Rev. A* 38 (6 Sept. 1988), pp. 3098–3100. DOI: 10.1103/PhysRevA.38.3098.

[112] John P. Perdew et al. “Atoms, molecules, solids, and surfaces: Applications of the generalized gradient approximation for exchange and correlation.” In: *Phys. Rev. B* 46 (11 Sept. 1992), pp. 6671–6687. DOI: 10.1103/PhysRevB.46.6671.

[113] John P. Perdew, Kieron Burke, and Matthias Ernzerhof. “Generalized Gradient Approximation Made Simple.” In: *Phys. Rev. Lett.* 77 (18 Oct. 1996), pp. 3865–3868. DOI: 10.1103/PhysRevLett.77.3865.

[114] E. I. Proynov, S. Sirois, and D. R. Salahub. “Extension of the LAP functional to include parallel spin correlation.” In: *International Journal of Quantum Chemistry* 64.4 (1997), pp. 427–446. DOI: https://doi.org/10.1002/(SICI)1097-461X(1997)64:4<427::AID-QUA5>3.0.CO;2-Y. eprint: https://onlinelibrary.wiley.com/doi/pdf/10.1002/%28SICI%291097-461X%281997%2964%3A4%3C427%3A%3AAID-QUA5%3E3.0.CO%3B2-Y. URL: https://onlinelibrary.wiley.com/doi/abs/10.1002/%28SICI%291097-461X%281997%2964%3A4%3C427%3A%3AAID-QUA5%3E3.0.CO%3B2-Y.

[115] Troy Van Voorhis and Gustavo E. Scuseria. “A novel form for the exchange-correlation energy functional.” In: *The Journal of Chemical Physics* 109.2 (July 1998), pp. 400–410. ISSN: 0021-9606. DOI: 10.1063/1.476577. eprint: https://pubs.aip.org/aip/jcp/article-pdf/109/2/400/8106958/400_1_online.pdf.

[116] John P. Perdew et al. “Accurate Density Functional with Correct Formal Properties: A Step Beyond the Generalized Gradient Approximation.” In: *Phys. Rev. Lett.* 82 (12 Mar. 1999), pp. 2544–2547. DOI: 10.1103/PhysRevLett.82.2544.

[117] Joseph B. Krieger et al. “Construction of An Accurate Self-interaction-corrected Correlation Energy Functional Based on An Electron Gas with A Gap.” In: *Electron Correlations and Materials Properties*. Ed. by A. Gonis, N. Kioussis, and M. Ciftan. Boston, MA: Springer US, 1999, pp. 463–477. ISBN: 978-1-4615-4715-0. DOI: 10.1007/978-1-4615-4715-0_28. URL: https://doi.org/10.1007/978-1-4615-4715-0_28.

[118] Stefan Kurth, John P. Perdew, and Peter Blaha. “Molecular and solid-state tests of density functional approximations: LSD, GGAs, and meta-GGAs.” In: *International Journal of Quantum Chemistry* 75.4-5 (1999), pp. 889–909. DOI: https://doi.org/10.1002/(SICI)1097-461X(1999)75:4/5<889::AID-QUA54>3.0.CO;2-8. eprint: https://onlinelibrary.wiley.com/doi/pdf/10.1002/%28SICI%291097-461X%281999%2975%3A4/5%3C889%3A%3AAID-QUA54%3E3.0.CO%3B2-8. URL: https://onlinelibrary.wiley.com/doi/abs/10.1002/%28SICI%291097-461X%281999%2975%3A4/5%3C889%3A%3AAID-QUA54%3E3.0.CO%3B2-8.

[119] Matthias Ernzerhof. “Construction of the adiabatic connection.” In: *Chemical Physics Letters* 263.3 (1996), pp. 499–506. ISSN: 0009-2614. DOI: https://doi.org/10.1016/S0009-2614(96)01225-0. URL: https://www.sciencedirect.com/science/article/pii/S0009261496012250.

[120] John P. Perdew, Matthias Ernzerhof, and Kieron Burke. “Rationale for mixing exact exchange with density functional approximations.” In: *The Journal of Chemical Physics* 105.22 (Dec. 1996), pp. 9982–9985. ISSN: 0021-9606. DOI: 10.1063/1.472933. eprint: https://pubs.aip.org/aip/jcp/article-pdf/105/22/9982/9439202/9982_1_online.pdf.

[121] Kieron Burke, Matthias Ernzerhof, and John P. Perdew. “The adiabatic connection method: a non-empirical hybrid.” In: *Chemical Physics Letters* 265.1 (1997), pp. 115–120. ISSN: 0009-2614. DOI: https://doi.org/10.1016/S0009-2614(96)01373-5. URL: https://www.sciencedirect.com/science/article/pii/S0009261496013735.

[122] Matthias Ernzerhof and Gustavo E. Scuseria. “Assessment of the Perdew–Burke–Ernzerhof exchange-correlation functional.” In: *The Journal of Chemical Physics* 110.11 (Mar. 1999), pp. 5029–5036. ISSN: 0021-9606. DOI: 10.1063/1.478401. eprint: https://pubs.aip.org/aip/jcp/article-pdf/110/11/5029/10797375/5029_1_online.pdf.

[123] Carlo Adamo and Vincenzo Barone. “Toward reliable density functional methods without adjustable parameters: The PBE0 model.” In: *The Journal of Chemical Physics* 110.13 (Apr. 1999), pp. 6158–6170. ISSN: 0021-9606. DOI: 10.1063/1.478522. eprint: https://pubs.aip.org/aip/jcp/article-pdf/110/13/6158/10797469/6158_1_online.pdf.

[124] John P. Perdew and Karla Schmidt. “Jacob’s ladder of density functional approximations for the exchange-correlation energy.” In: *AIP Conference Proceedings* 577.1 (July 2001), pp. 1–20. ISSN: 0094-243X. DOI: 10.1063/1.1390175. eprint: https://pubs.aip.org/aip/acp/article-pdf/577/1/1/12108089/1_1_online.pdf.

[125] M. Weinert and J. W. Davenport. “Fractional occupations and density-functional energies and forces.” In: *Phys. Rev. B* 45 (23 June 1992), pp. 13709–13712. DOI: 10.1103/PhysRevB.45.13709.

[126] S. Blügel et al. *Computational Condensed Matter Physics : lecture manuscripts of the 37th Spring School of the Institute of Solid State Research ; this Spring School was organized by the Institute of Solid State Research in the Forschungszentrum Jülich on March 6 - 17 ...* Vol. 32. Schriften des Forschungszentrums Jülich . Reihe Materie und Material / Matter and Materials. Record converted from VDB: 12.11.2012. Jülich: Forschungszentrum, Zentralbibliothek, 2006. ISBN: 3-89336-430-7. URL: http://hdl.handle.net/2128/2396.

[127] C. G. Broyden. “A Class of Methods for Solving Nonlinear Simultaneous Equations.” In: *Mathematics of Computation* 19.92 (1965), pp. 577–593. ISSN: 00255718, 10886842. URL: http://www.jstor.org/stable/2003941 (visited on 10/28/2023).

[128] C. G. Broyden. “Quasi-Newton methods and their application to function minimisation.” In: *Mathematics of Computation* 21 (1967), pp. 368–381. URL: https://api.semanticscholar.org/CorpusID:10793035.

[129] Donald G. Anderson. “Iterative Procedures for Nonlinear Integral Equations.” In: *J. ACM* 12.4 (Oct. 1965), pp. 547–560. ISSN: 0004-5411. DOI: 10.1145/321296.321305.

[130] Stefan Blügel. *First principles calculations of the electronic structure of magnetic overlayers on transition metal surfaces*. Tech. rep. Juel-2197. Jülich, 1988, 125 p. URL: http://hdl.handle.net/2128/18476.

[131] Ph. Kurz et al. “Ab initio treatment of noncollinear magnets with the full-potential linearized augmented plane wave method.” In: *Phys. Rev. B* 69 (2 Jan. 2004), p. 024415. DOI: 10.1103/PhysRevB.69.024415.

[132] J Kubler et al. “Density functional theory of non-collinear magnetism.” In: *Journal of Physics F: Metal Physics* 18.3 (Mar. 1988), p. 469. DOI: 10.1088/0305-4608/18/3/018. URL: https://dx.doi.org/10.1088/0305-4608/18/3/018.

[133] D. J. Singh and L. Nordström. *Planewaves, Pseudopotentials, and the LAPW Method*. 2nd ed. Springer New York, 2006. DOI: 10.1007/978-0-387-29684-5.

[134] Gustav Bihlmayer. “Computing Solids: Models, ab-initio methods and supercomputing.” In: ed. by Stefan Blügel et al. Vol. 74. Schriften des Forschungszentrums Jülich. Reihe Schlüsseltechnologien / Key Technologies. The Spring School was organized by the Institute for Advanced Simulationand the Peter Grünberg Institute of the Forschungszentrum Jülich. Jülich: Forschungszentrum Jülich GmbH Zentralbibliothek, Verlag, Mar. 10, 2014. Chap. A10, getr. Zählung. ISBN: 978-3-89336-912-6. URL: http://hdl.handle.net/2128/8540.

[135] Vladimir I Anisimov, F Aryasetiawan, and A I Lichtenstein. “First-principles calculations of the electronic structure and spectra of strongly correlated systems: the LDA+ U method.” In: *Journal of Physics: Condensed Matter* 9.4 (Jan. 1997), p. 767. DOI: 10.1088/0953-8984/9/4/002. URL: https://dx.doi.org/10.1088/0953-8984/9/4/002.

[136] “Electron correlations in narrow energy bands.” In: *Proceedings of the Royal Society of London. Series A. Mathematical and Physical Sciences* 276.1365 (Nov. 1963), pp. 238–257. DOI: 10.1098/rspa.1963.0204.

[137] L. N. Oliveira, E. K. U. Gross, and W. Kohn. “Density-Functional Theory for Superconductors.” In: *Phys. Rev. Lett.* 60 (23 June 1988), pp. 2430–2433. DOI: 10.1103/PhysRevLett.60.2430.

[138] M. Lüders et al. “Ab initio theory of superconductivity. I. Density functional formalism and approximate functionals.” In: *Phys. Rev. B* 72 (2 July 2005), p. 024545. DOI: 10.1103/PhysRevB.72.024545.

[139] M. A. L. Marques et al. “Ab initio theory of superconductivity. II. Application to elemental metals.” In: *Phys. Rev. B* 72 (2 July 2005), p. 024546. DOI: 10.1103/PhysRevB.72.024546.

[140] Antonio Sanna. “The Physics of Correlated Insulators, Metals, and Superconductors.” In: ed. by Eva Pavarini et al. Vol. 7. Schriften des Forschungszentrums Jülich. Reihe Modeling and Simulation. Jülich: Forschungszentrum Jülich GmbH Zentralbibliothek, Verlag, Sept. 25, 2017. Chap. 16, 450 S. ISBN: 978-3-95806-224-5. URL: http://hdl.handle.net/2128/15283.

[141] T. L. Gilbert. “Hohenberg-Kohn theorem for nonlocal external potentials.” In: *Phys. Rev. B* 12 (6 Sept. 1975), pp. 2111–2120. DOI: 10.1103/PhysRevB.12.2111.

[142] G. Vignale. “Current Density Functional Theory.” In: *Time-Dependent Density Functional Theory*. Ed. by Miguel A.L. Marques et al. Berlin, Heidelberg: Springer Berlin Heidelberg, 2006, pp. 75–91. ISBN: 978-3-540-35426-0. DOI: 10.1007/3-540-35426-3_5. URL: https://doi.org/10.1007/3-540-35426-3_5.

[143] P. H. Dederichs et al. “Ground States of Constrained Systems: Application to Cerium Impurities.” In: *Phys. Rev. Lett.* 53 (26 Dec. 1984), pp. 2512–2515. DOI: 10.1103/PhysRevLett.53.2512.

[144] Erich Runge and E. K. U. Gross. “Density-Functional Theory for Time-Dependent Systems.” In: *Phys. Rev. Lett.* 52 (12 Mar. 1984), pp. 997–1000. DOI: 10.1103/PhysRevLett.52.997.

[145] Felix Bloch. “Über die Quantenmechanik der Elektronen in Kristallgittern.” In: *Zeitschrift für Physik* 52.7-8 (July 1929), pp. 555–600. DOI: 10.1007/bf01339455.

[146] G. Kresse, J. Furthmüller, and J. Hafner. “Ab initio Force Constant Approach to Phonon Dispersion Relations of Diamond and Graphite.” In: *Europhysics Letters* 32.9 (Dec. 1995), p. 729. DOI: 10.1209/0295-5075/32/9/005. URL: https://dx.doi.org/10.1209/0295-5075/32/9/005.

[147] A. A. Maradudin and S. H. Vosko. “Symmetry Properties of the Normal Vibrations of a Crystal.” In: *Rev. Mod. Phys.* 40 (1 Jan. 1968), pp. 1–37. DOI: 10.1103/RevModPhys.40.1.

[148] A. Togo and I. Tanaka. “First principles phonon calculations in materials science.” In: *Scr. Mater.* 108 (Nov. 2015), pp. 1–5.

[149] Atsushi Togo et al. “Implementation strategies in phonopy and phono3py.” In: *J. Phys. Condens. Matter* 35.35 (2023), p. 353001. DOI: 10.1088/1361-648X/acd831.

[150] Atsushi Togo. “First-principles Phonon Calculations with Phonopy and Phono3py.” In: *J. Phys. Soc. Jpn.* 92.1 (2023), p. 012001. DOI: 10.7566/JPSJ.92.012001.

[151] R. M. Sternheimer. “Electronic Polarizabilities of Ions from the Hartree-Fock Wave Functions.” In: *Phys. Rev.* 96.4 (Nov. 1954), pp. 951–968. DOI: 10.1103/PhysRev.96.951.

[152] Xavier Gonze. “Adiabatic density-functional perturbation theory.” In: *Phys. Rev. A* 52 (2 Aug. 1995), pp. 1096–1114. DOI: 10.1103/PhysRevA.52.1096.

[153] Xavier Gonze. “Perturbation expansion of variational principles at arbitrary order.” In: *Phys. Rev. A* 52 (2 Aug. 1995), pp. 1086–1095. DOI: 10.1103/PhysRevA.52.1086.

[154] Xavier Gonze. “Erratum: Adiabatic density-functional perturbation theory.” In: *Phys. Rev. A* 54 (5 Nov. 1996), pp. 4591–4591. DOI: 10.1103/PhysRevA.54.4591.

[155] Daniel Wortmann. “Computing Solids: Models, ab-initio methods and supercomputing.” In: ed. by Stefan Blügel et al. Vol. 74. Schriften des Forschungszentrums Jülich. Reihe Schlüsseltechnologien / Key Technologies. The Spring School was organized by the Institute for Advanced Simulationand the Peter Grünberg Institute of the Forschungszentrum Jülich. Jülich: Forschungszentrum Jülich GmbH Zentralbibliothek, Verlag, Mar. 10, 2014. Chap. D4, getr. Zählung. ISBN: 978-3-89336-912-6. URL: http://hdl.handle.net/2128/8540.

[156] James R Chelikowsky. “The pseudopotential-density functional method applied to nanostructures.” In: *Journal of Physics D: Applied Physics* 33.8 (Apr. 2000), R33. DOI: 10.1088/0022-3727/33/8/201. URL: https://dx.doi.org/10.1088/0022-3727/33/8/201.

[157] David Vanderbilt. “Soft self-consistent pseudopotentials in a generalized eigenvalue formalism.” In: *Phys. Rev. B* 41 (11 Apr. 1990), pp. 7892–7895. DOI: 10.1103/PhysRevB.41.7892.

[158] J. C. Slater. “Wave Functions in a Periodic Potential.” In: *Phys. Rev.* 51 (10 May 1937), pp. 846–851. DOI: 10.1103/PhysRev.51.846.

[159] J.C. Slater. “Energy Band Calculations by the Augmented Plane Wave Method**The research reported in this paper has been assisted by the National Science Foundation and the Office of Naval Research, as well as by the Army, Navy, and Air Force.” In: ed. by Per-Olov Löwdin. Vol. 1. Advances in Quantum Chemistry. Academic Press, 1964, pp. 35–58. DOI: https://doi.org/10.1016/S0065-3276(08)60374-3. URL: https://www.sciencedirect.com/science/article/pii/S0065327608603743.

[160] Stefan Blügel and Gustav Bihlmayer. “The Full-Potential Linearized Augmented Plane Wave Method.” In: *Computational Nanoscience: Do It Yourself!* Lecture Notes of the Winter School 2006. Ed. by Johannes Grotendorst, Stefan Blügel, and Dominik Marx. Vol. 31. Publication Series of the John von Neumann Institute for Computing (NIC). NIC-Directors, 2006. ISBN: 3-00-017350-1.

[161] Paul M. Marcus. “Variational methods in the computation of energy bands.” In: *International Journal of Quantum Chemistry* 1.S1 (1967), pp. 567–588. DOI: https://doi.org/10.1002/qua.560010659.

[162] S. L. Altmann and A. P. Cracknell. “Lattice Harmonics I. Cubic Groups.” In: *Rev. Mod. Phys.* 37 (1 Jan. 1965), pp. 19–32. DOI: 10.1103/RevModPhys.37.19.

[163] Hiroshi Yamagami. “Fully relativistic noncollinear magnetism in spin-density-functional theory: Application to USb by means of the fully relativistic spin-polarized LAPW method.” In: *Phys. Rev. B* 61 (9 Mar. 2000), pp. 6246–6256. DOI: 10.1103/PhysRevB.61.6246.

[164] D D Koelling and B N Harmon. “A technique for relativistic spin-polarised calculations.” In: *Journal of Physics C: Solid State Physics* 10.16 (Aug. 1977), p. 3107. DOI: 10.1088/0022-3719/10/16/019. URL: https://dx.doi.org/10.1088/0022-3719/10/16/019.

[165] David Singh. “Ground-state properties of lanthanum: Treatment of extended-core states.” In: *Phys. Rev. B* 43 (8 Mar. 1991), pp. 6388–6392. DOI: 10.1103/PhysRevB.43.6388.

[166] E Sjöstedt, L Nordström, and D.J Singh. “An alternative way of linearizing the augmented plane-wave method.” In: *Solid State Communications* 114.1 (2000), pp. 15–20. ISSN: 0038-1098. DOI: https://doi.org/10.1016/S0038-1098(99)00577-3.

[167] Christoph Friedrich et al. “Elimination of the linearization error in GW calculations based on the linearized augmented-plane-wave method.” In: *Phys. Rev. B* 74 (4 July 2006), p. 045104. DOI: 10.1103/PhysRevB.74.045104.

[168] Gregor Michalicek et al. “Elimination of the linearization error and improved basis-set convergence within the FLAPW method.” In: *Computer Physics Communications* 184.12 (2013), pp. 2670–2679. ISSN: 0010-4655. DOI: 10.1016/j.cpc.2013.07.002.

[169] Markus Betzinger et al. “Local exact exchange potentials within the all-electron FLAPW method and a comparison with pseudopotential results.” In: *Phys. Rev. B* 83 (4 Jan. 2011), p. 045105. DOI: 10.1103/PhysRevB.83.045105.

[170] M. Weinert. “Solution of Poisson’s equation: Beyond Ewald-type methods.” In: *J. Math. Phys.* 22.11 (1981), pp. 2433–2439. DOI: 10.1063/1.524800.

[171] Susi Lehtola et al. “Recent developments in libxc — A comprehensive library of functionals for density functional theory.” In: *SoftwareX* 7 (2018), pp. 1–5. DOI: 10.1016/j.softx.2017.11.002.

[172] Su-Huai Wei, Henry Krakauer, and M. Weinert. “Linearized augmented-plane-wave calculation of the electronic structure and total energy of tungsten.” In: *Phys. Rev. B* 32 (12 Dec. 1985), pp. 7792–7797. DOI: 10.1103/PhysRevB.32.7792.

[173] M. Weinert, E. Wimmer, and A. J. Freeman. “Total-energy all-electron density functional method for bulk solids and surfaces.” In: *Phys. Rev. B* 26.8 (Oct. 1982), pp. 4571–4578. DOI: 10.1103/PhysRevB.26.4571.

[174] P. Pulay. “Ab initio calculation of force constants and equilibrium geometries in polyatomic molecules.” In: *Molecular Physics* 17.2 (1969), pp. 197–204. DOI: 10.1080/00268976900100941.

[175] Markus Betzinger et al. “Precise response functions in all-electron methods: Application to the optimized-effective-potential approach.” In: *Phys. Rev. B* 85.24 (June 2012), p. 245124. DOI: 10.1103/PhysRevB.85.245124.

[176] Xavier Gonze and Changyol Lee. “Dynamical matrices, Born effective charges, dielectric permittivity tensors, and interatomic force constants from density-functional perturbation theory.” In: *Phys. Rev. B* 55 (16 Apr. 1997), pp. 10355–10368. DOI: 10.1103/PhysRevB.55.10355.

[177] Andrea Dal Corso. “Density functional perturbation theory within the projector augmented wave method.” In: *Phys. Rev. B* 81 (7 Feb. 2010), p. 075123. DOI: 10.1103/PhysRevB.81.075123.

[178] P. P. Ewald. “Die Berechnung optischer und elektrostatischer Gitterpotentiale.” In: *Annalen der Physik* 369.3 (1921), pp. 253–287. DOI: https://doi.org/10.1002/andp.19213690304. eprint: https://onlinelibrary.wiley.com/doi/pdf/10.1002/andp.19213690304. URL: https://onlinelibrary.wiley.com/doi/abs/10.1002/andp.19213690304.

[179] Aldo H. Romero et al. “ABINIT: Overview and focus on selected capabilities.” In: *The Journal of Chemical Physics* 152.12 (2020), p. 124102. DOI: 10.1063/1.5144261.

[180] Volker Strassen. “Gaussian elimination is not optimal.” In: *Numerische Mathematik* 13.4 (Aug. 1969), pp. 354–356. ISSN: 0945-3245. DOI: 10.1007/BF02165411.

[181] Don Coppersmith and Shmuel Winograd. “Matrix multiplication via arithmetic progressions.” In: *Journal of Symbolic Computation* 9.3 (1990). Computational algebraic complexity editorial, pp. 251–280. ISSN: 0747-7171. DOI: https://doi.org/10.1016/S0747-7171(08)80013-2.

[182] Francis Birch. “Finite Elastic Strain of Cubic Crystals.” In: *Phys. Rev.* 71 (11 June 1947), pp. 809–824. DOI: 10.1103/PhysRev.71.809.

[183] H. Leutwyler. “Nonrelativistic effective Lagrangians.” In: *Physical Review D* 49.6 (Mar. 1994), pp. 3033–3043. DOI: 10.1103/physrevd.49.3033.

[184] K. F. Niebel, J. A. Venables, and Charles Alfred Coulson. “An explanation of the crystal structure of the rare gas solids.” In: *Proceedings of the Royal Society of London. A. Mathematical and Physical Sciences* 336.1606 (1974), pp. 365–377. DOI: 10.1098/rspa.1974.0024.

[185] Martin T. Dove. *Introduction to Lattice Dynamics*. Cambridge Topics in Mineral Physics and Chemistry. Cambridge University Press, 1993.

[186] Jiří Kulda et al. "Inelastic-neutron-scattering study of phonon eigenvectors and frequencies in Si." In: *Phys. Rev. B* 50 (18 Nov. 1994), pp. 13347–13354. DOI: 10.1103/PhysRevB.50.13347.

[187] G. Nilsson and G. Nelin. "Study of the Homology between Silicon and Germanium by Thermal-Neutron Spectrometry." In: *Phys. Rev. B* 6 (10 Nov. 1972), pp. 3777–3786. DOI: 10.1103/PhysRevB.6.3777.

[188] D. Strauch, A. P. Mayer, and B. Dorner. "Phonon eigenvectors in Si determined by inelastic neutron scattering." In: *Zeitschrift für Physik B Condensed Matter* 78.3 (Oct. 1990), pp. 405–410. ISSN: 1431-584X. DOI: 10.1007/BF01313321.

[189] M. Aouissi et al. "Phonon spectra of diamond, Si, Ge, and $\alpha-\mathrm{Sn}$: Calculations with real-space interatomic force constants." In: *Phys. Rev. B* 74 (5 Aug. 2006), p. 054302. DOI: 10.1103/PhysRevB.74.054302.

[190] Robert M. Pick, Morrel H. Cohen, and Richard M. Martin. "Microscopic Theory of Force Constants in the Adiabatic Approximation." In: *Phys. Rev. B* 1 (2 Jan. 1970), pp. 910–920. DOI: 10.1103/PhysRevB.1.910.

[191] Paolo Giannozzi et al. "Ab initio calculation of phonon dispersions in semiconductors." In: *Phys. Rev. B* 43 (9 Mar. 1991), pp. 7231–7242. DOI: 10.1103/PhysRevB.43.7231.

[192] X. Gonze et al. "Interatomic force constants from first principles: The case of $\alpha$-quartz." In: *Phys. Rev. B* 50 (17 Nov. 1994), pp. 13035–13038. DOI: 10.1103/PhysRevB.50.13035.

[193] Philippe Ghosez and Xavier Gonze. "Band-by-band decompositions of the Born effective charges." In: *Journal of Physics: Condensed Matter* 12.43 (Oct. 2000), p. 9179. DOI: 10.1088/0953-8984/12/43/308.

[194] Xinjie Wang and David Vanderbilt. "First-principles perturbative computation of dielectric and Born charge tensors in finite electric fields." In: *Phys. Rev. B* 75 (11 Mar. 2007), p. 115116. DOI: 10.1103/PhysRevB.75.115116.

[195] Y Wang et al. "A mixed-space approach to first-principles calculations of phonon frequencies for polar materials." In: *Journal of Physics: Condensed Matter* 22.20 (Apr. 2010), p. 202201. DOI: 10.1088/0953-8984/22/20/202201.

[196] O. Jepson and O.K. Anderson. "The electronic structure of h.c.p. Ytterbium." In: *Solid State Communications* 9.20 (1971), pp. 1763–1767. ISSN: 0038-1098. DOI: https://doi.org/10.1016/0038-1098(71)90313-9.

[197] G. Lehmann and M. Taut. "On the Numerical Calculation of the Density of States and Related Properties." In: *physica status solidi (b)* 54.2 (1972), pp. 469–477. DOI: https://doi.org/10.1002/pssb.2220540211.

[198] Peter E. Blöchl, O. Jepsen, and O. K. Andersen. "Improved tetrahedron method for Brillouin-zone integrations." In: *Phys. Rev. B* 49 (23 June 1994), pp. 16223–16233. DOI: 10.1103/PhysRevB.49.16223.

[199] Treglia, G. and Desjonquères, M.-C. “Bulk and surface vibrational and thermodynamical properties of fcc transition and noble metals : a systematic study by the continued fraction technique.” In: *J. Phys. France* 46.6 (1985), pp. 987–1000. DOI: 10.1051/jphys:01985004606098700.

[200] Alexander Neukirchen. “Source-Free Exchange-Correlation Magnetic Fields in the FLAPW Method.” Masterarbeit, RWTH Aachen, 2020. Masterarbeit. RWTH Aachen, 2020, 90 p. DOI: 10.34734/FZJ-2023-03226.

[201] I. J. Schoenberg. “Contributions to the problem of approximation of equidistant data by analytic functions. Part A. On the problem of smoothing or graduation. A first class of analytic approximation formulae.” In: *Quarterly of Applied Mathematics* 4.1 (1946), pp. 45–99. ISSN: 1552-4485. DOI: 10.1090/qam/15914.

[202] I. J. Schoenberg. “Contributions to the problem of approximation of equidistant data by analytic functions. Part B. On the problem of osculatory interpolation. A second class of analytic approximation formulae.” In: *Quarterly of Applied Mathematics* 4.2 (1946), pp. 112–141. ISSN: 1552-4485. DOI: 10.1090/qam/16705.

[203] J. Zarestky et al. “Temperature dependence of the vibrational modes of molybdenum.” In: *Phys. Rev. B* 28 (2 July 1983), pp. 697–701. DOI: 10.1103/PhysRevB.28.697.

[204] Wheeler P. Davey. “Precision Measurements of the Lattice Constants of Twelve Common Metals.” In: *Phys. Rev.* 25 (6 June 1925), pp. 753–761. DOI: 10.1103/PhysRev.25.753.

[205] M. Heide, G. Bihlmayer, and S. Blügel. “Describing Dzyaloshinskii–Moriya spirals from first principles.” In: *Physica B: Condensed Matter* 404.18 (2009), pp. 2678–2683. ISSN: 0921-4526. DOI: https://doi.org/10.1016/j.physb.2009.06.070.

[206] C. S. Wang, B. M. Klein, and H. Krakauer. “Theory of Magnetic and Structural Ordering in Iron.” In: *Phys. Rev. Lett.* 54 (16 Apr. 1985), pp. 1852–1855. DOI: 10.1103/PhysRevLett.54.1852.

[207] Peter Blaha et al. “WIEN2k: An APW+lo program for calculating the properties of solids.” In: *The Journal of Chemical Physics* 152.7 (Feb. 2020), p. 074101. ISSN: 0021-9606. DOI: 10.1063/1.5143061.

[208] Ph Kurz, G Bihlmayer, and S Blügel. “Magnetism and electronic structure of hcp Gd and the Gd(0001) surface.” In: *Journal of Physics: Condensed Matter* 14.25 (June 2002), p. 6353. DOI: 10.1088/0953-8984/14/25/305.

[209] *Phonon dispersion in Lanthanides: Gd (and Sm, Eu, Dy)*. http://ftp.esrf.eu/pub/UserReports/33665_A.pdf. Accessed: 2024-03-15.

[210] J. R. Banister, S. Legvold, and F. H. Spedding. “Structure of Gd, Dy, and Er at Low Temperatures.” In: *Phys. Rev.* 94 (5 June 1954), pp. 1140–1142. DOI: 10.1103/PhysRev.94.1140.

[211] Lokanath Patra and Bolin Liao. “Indirect Exchange Interaction Leads to Large Lattice Contribution to Magnetocaloric Entropy Change.” In: *Phys. Rev. Lett.* 131 (6 Aug. 2023), p. 066703. DOI: 10.1103/PhysRevLett.131.066703.

[212] Muhammad Sultan et al. “Electron- and phonon-mediated ultrafast magnetization dynamics of Gd(0001).” In: *Phys. Rev. B* 85 (18 May 2012), p. 184407. DOI: 10.1103/PhysRevB.85.184407.

[213] Sudipta Mahana et al. “Local inversion symmetry breaking and spin-phonon coupling in the perovskite $GdCrO_3$.” In: *Phys. Rev. B* 96 (10 Sept. 2017), p. 104106. DOI: 10.1103/PhysRevB.96.104106.

[214] Rui Wang et al. “First-principles calculations of phonon and thermodynamic properties of AlRE (RE=Y, Gd, Pr, Yb) intermetallic compounds.” In: *Physica Scripta* 85.3 (Feb. 2012), p. 035705. DOI: 10.1088/0031-8949/85/03/035705.

[215] N. G. Nereson, C. E. Olsen, and G. P. Arnold. “Magnetic Structure of Europium.” In: *Phys. Rev.* 135 (1A July 1964), A176–A180. DOI: 10.1103/PhysRev.135.A176.

[216] I. Turek et al. “First-principles study of the electronic structure and exchange interactions in bcc europium.” In: *Phys. Rev. B* 68 (22 Dec. 2003), p. 224431. DOI: 10.1103/PhysRevB.68.224431.

[217] R. Pradip et al. “Lattice Dynamics of EuO: Evidence for Giant Spin-Phonon Coupling.” In: *Phys. Rev. Lett.* 116 (18 May 2016), p. 185501. DOI: 10.1103/PhysRevLett.116.185501.

[218] Stefan Grimme et al. “A consistent and accurate ab initio parametrization of density functional dispersion correction (DFT-D) for the 94 elements H-Pu.” In: *The Journal of Chemical Physics* 132.15 (Apr. 2010), p. 154104.

[219] Benoit Van Troeye, Marc Torrent, and Xavier Gonze. “Interatomic force constants including the DFT-D dispersion contribution.” In: *Phys. Rev. B* 93 (14 Apr. 2016), p. 144304. DOI: 10.1103/PhysRevB.93.144304.

[220] H. Krakauer, M. Posternak, and A. J. Freeman. “Linearized augmented plane-wave method for the electronic band structure of thin films.” In: *Phys. Rev. B* 19 (4 Feb. 1979), pp. 1706–1719. DOI: 10.1103/PhysRevB.19.1706.

[221] David Miller, S. D Mahanti, and Phillip Duxbury. “Charge density wave states in tantalum dichalcogenides.” In: *Physical Review B* 97 (Jan. 2018). DOI: 10.1103/PhysRevB.97.045133.

[222] D J Eaglesham, R L Withers, and D M Bird. “Charge-density-wave transitions in 1T-VSe2.” In: *Journal of Physics C: Solid State Physics* 19.3 (Jan. 1986), p. 359. DOI: 10.1088/0022-3719/19/3/006.

[223] B. Giambattista et al. “Scanning tunneling microscopy of atoms and charge-density waves in 1T-$TaS_2$, 1T-$TaSe_2$, and 1T-$VSe_2$.” In: *Phys. Rev. B* 41 (14 May 1990), pp. 10082–10103. DOI: 10.1103/PhysRevB.41.10082.

[224] Vladimir N. Strocov et al. “Three-Dimensional Electron Realm in $VSe_2$ by Soft-X-Ray Photoelectron Spectroscopy: Origin of Charge-Density Waves.” In: *Phys. Rev. Lett.* 109 (8 Aug. 2012), p. 086401. DOI: 10.1103/PhysRevLett.109.086401.

[225] Manuel Bonilla et al. “Strong room-temperature ferromagnetism in VSe2 monolayers on van der Waals substrates.” In: *Nature Nanotechnology* 13.4 (Apr. 2018), pp. 289–293. ISSN: 1748-3395. DOI: 10.1038/s41565-018-0063-9.

[226] S. Kumar and U. Schwingenschlögl. “Thermoelectric Response of Bulk and Monolayer MoSe2 and WSe2.” In: *Chemistry of Materials* 27.4 (Feb. 2015), pp. 1278–1284. ISSN: 0897-4756. DOI: 10.1021/cm504244b.

[227] Thibault Sohier, Matteo Calandra, and Francesco Mauri. "Two-dimensional Fröhlich interaction in transition-metal dichalcogenide monolayers: Theoretical modeling and first-principles calculations." In: *Phys. Rev. B* 94 (8 Aug. 2016), p. 085415. DOI: 10.1103/PhysRevB.94.085415.

[228] Thibault Sohier, Matteo Calandra, and Francesco Mauri. "Density functional perturbation theory for gated two-dimensional heterostructures: Theoretical developments and application to flexural phonons in graphene." In: *Phys. Rev. B* 96 (7 Aug. 2017), p. 075448. DOI: 10.1103/PhysRevB.96.075448.

[229] Thibault Sohier et al. "Breakdown of Optical Phonons' Splitting in Two-Dimensional Materials." In: *Nano Letters* 17.6 (2017). PMID: 28517939, pp. 3758–3763. DOI: 10.1021/acs.nanolett.7b01090.

[230] Silvana Radescu, Denis Machon, and Patrice Mélinon. "Origin of dynamical instabilities in some simulated two-dimensional materials: GaSe as a case study." In: *Phys. Rev. Mater.* 3 (7 July 2019), p. 074002. DOI: 10.1103/PhysRevMaterials.3.074002.

[231] U. Monteverde et al. "Under pressure: Control of strain, phonons and bandgap opening in rippled graphene." In: *Carbon* 91 (2015), pp. 266–274. ISSN: 0008-6223. DOI: https://doi.org/10.1016/j.carbon.2015.04.044.

[232] Xinjie Wang and David Vanderbilt. "First-principles perturbative computation of dielectric and Born charge tensors in finite electric fields." In: *Phys. Rev. B* 75 (11 Mar. 2007), p. 115116. DOI: 10.1103/PhysRevB.75.115116.

[233] Mike Folk et al. "An overview of the HDF5 technology suite and its applications." In: *Proceedings of the EDBT/ICDT 2011 Workshop on Array Databases*. AD '11. Uppsala, Sweden: Association for Computing Machinery, 2011, pp. 36–47. ISBN: 9781450306140. DOI: 10.1145/1966895.1966900.

# Publications

Parts of this thesis, in particular intermediary results for the validation in chapter 6 have been published in the *IOPscience* journal *Electronic Structure* as part of:

Gerhorst, Christian-Roman; Neukirchen, Alexander; Klüppelberg, Daniel A; Bihlmayer, Gustav; Betzinger, Markus; Michalicek, Gregor; Wortmann, Daniel; Blügel, Stefan (1 March 2024). ”Phonons from density-functional perturbation theory using the all-electron full-potential linearized augmented plane-wave method FLEUR”. Electronic Structure. **6** (1): 017001. [94]

# Data Availability Statement

The datasets generated and/or analyzed in this work are available on zenodo.org under the DOI 10.5281/zenodo.14840419.

# Acknowledgments

Writing this thesis was a lengthy and arduous task, that would not have been possible without the help and guidance of a lot of smart, competent, and helpful people.

My first shoutout goes to my supervisor Prof. Dr. Stefan Blügel, who gave me a place in the institute and was a wellspring of ideas for tackling problems and opening up new directions in my thesis.

I deeply thank Prof. Dr. Carsten Honerkamp for spontaneously agreeing to be my second referee after just a quick phone call.

Dr. Gustav Bihlmayer was, as my direct supervisor, an integral part of keeping the thesis on track and an incredibly reliable source of wisdom for the history, physics, and numerics of the FLAPW method and electronic structure in general. For this I thank him wholeheartedly.

In general, I thank the members of the phonon task-force, that helped me further the implementation in FLEUR through regular meetings and in-depth discussions on its technicalities. Notable among them are Dr. Daniel Wortmann, who I relied on a lot for questions in the debugging process, and Dr. Gregor Michalicek, who through his meticulous proofreading of this manuscript has helped consolidate the results of my time as a PhD student into one coherent work.

I extend my hand in gratitude to my friend and former office mate Robin Hilgers, with whom I shared many car rides and lengthy office talks about everything and nothing. Thanks for taking my mind of work and keeping me sane, mate!

More recently, my thanks go to my carpool consisting of Antonia, Thorben, Thomas, and Friedrich. For many nice talks and many kilometers driven and, for the latter two, also for taking over and further developing the complex topic of DFPT in FLAPW and testing my knowledge of the finer details of my own work by asking valuable questions and double checking the ideas that went into it.

Aside from this I thank the many nice people at the PGI-1/IAS-1 for relaxing lunch breaks and good off-topic talks. A special thanks goes to our secretary Yasmin Ergüven, without whom it would be impossible for anything or anyone in the institute to work in an orderly fashion.

Last, but most certainly not least, I thank my family, my friends, and all the people outside the institute that shaped my life and me as a person. Without you all having my back, it would never have been possible to write this thesis. Or my master's. Or my bachelor's. Or in fact

anything else I have achieved up to this point. This thesis is the conclusion of a long and winding way on which you have accompanied and supported me. And no matter how much I try - I could never repay you for it in full.

# Eidesstattliche Erklärung

**Alexander Neukirchen**

erklärt hiermit, dass diese Dissertation und die darin dargelegten Inhalte die eigenen sind und selbstständig, als Ergebnis der eigenen originären Forschung, generiert wurden.

Hiermit erkläre ich an Eides statt

1. Diese Arbeit wurde vollständig oder größtenteils in der Phase als Doktorand dieser Fakultät und Universität angefertigt;

2. Sofern irgendein Bestandteil dieser Dissertation zuvor für einen akademischen Abschluss oder eine andere Qualifikation an dieser oder einer anderen Institution verwendet wurde, wurde dies klar angezeigt;

3. Wann immer andere eigene- oder Veröffentlichungen Dritter herangezogen wurden, wurden diese klar benannt;

4. Wenn aus anderen eigenen- oder Veröffentlichungen Dritter zitiert wurde, wurde stets die Quelle hierfür angegeben. Diese Dissertation ist vollständig meine eigene Arbeit, mit der Ausnahme solcher Zitate;

5. Alle wesentlichen Quellen von Unterstützung wurden benannt;

6. Wenn immer ein Teil dieser Dissertation auf der Zusammenarbeit mit anderen basiert, wurde von mir klar gekennzeichnet, was von anderen und was von mir selbst erarbeitet wurde;

7. Ein Teil dieser Arbeit wurde zuvor veröffentlicht und zwar in:

Gerhorst, Christian-Roman; Neukirchen, Alexander; Klüppelberg, Daniel A; Bihlmayer, Gustav; Betzinger, Markus; Michalicek, Gregor; Wortmann, Daniel; Blügel, Stefan (1 March 2024). ”Phonons from density-functional perturbation theory using the all-electron full-potential linearized augmented plane-wave method FLEUR”. Electronic Structure. **6** (1): 017001.

8. Die dieser Arbeit zugrundeliegenden Daten sind unter dem DOI 10.5281/zenodo.14840419 verfügbar.

_____

Datum, Unterschrift